INVERSION OF SURFACE PARAMETERS USING

POLARIMETRIC SAR

Dissertation

zur Erlangung des akademischen Grades
Doctor rerum naturalium
(Dr. rer. nat.)

vorgelegt dem Rat der Chemisch-Geowissenschatlichen Fakultät der
Friedrich-Schiller-Universität Jena

von

Dipl. Geogr. Irena Hajnsek

geboren am

22.04.1970 in Ljubljana (Slowenien)

Reviewer

1. Prof. Dr. C. C. Schmullius, FSU Jena, Germany
2. Prof. Dr. E. Pottier, Universität Rennes I, France
3. Prof. Dr. W.-M. Boerner, University of Illionois at Chichago, USA

Tag der öffentlichen Verteidigung   17.10.2001

External Reviewer

1. Dr. S. R. Cloude, AEL Consultants, Cuper, Scotland
2. Dr. J.-S. Lee, Naval Research Laboratory, Washington, USA
3. Dr. A. Moreira, DLR – HR, Germany

Dedicated to the women working in the domain of science

Resnica,
ki jo govoriš, nima preteklosti
in ne prihodnosti.
Ona je,
in to je vse,
kar je potrebno

Truth,
which is spoken, has no past
and no future
it is
and that is all
what is required

Abstract

In this dissertation on the *Inversion of Surface Parameters using Polarimetric SAR*, the potential of implementing recent advances made in Polarimetric Synthetic Aperture Radar to surface parameter estimation is investigated. The sensitivity of microwave scattering to the dielectric properties and the geometric structure of bare soil surfaces makes radar remote sensing a challenge for a wide range of environmental issues related to the condition of natural surfaces. Especially, the potential for retrieving soil moisture with a high spatial and/or temporal resolution represents a significant contribution to hydrological and ecological modelling, as well as to economic optimisation of agricultural procedures.

The classical point measurement methods for, *soil moisture* content and *surface roughness*, are described. The ground data acquisition as well as the SAR data acquisition campaign were performed with the E-SAR of the German Aerospace Center at Oberpfaffenhofen (DLR-OP-IHR) over two test sites in Germany, the Elbe-Auen and the Weiherbach region. The basic principles of SAR and radar polarimetry are introduced in order to provide the conceptual framework for the inversion of surface parameters from fully polarimetric SAR data, which includes the critical assessment of various novel polarimetric concepts.

The prevalent methods for estimating the surface parameters from polarimetric SAR data are critically reviewed. The small perturbation model and two semi-empirical models are forming the basis of a comparative analysis. These two semi-empirical models were chosen in order to provide an overview of the evolution of ideas and techniques in the area of quantitative surface parameter estimation utilising partially polarimetric SAR image data takes. Further, the potential of polarimetric techniques recently developed in different application areas are investigated with regard to their suitability to improve the performance of the introduced inversion algorithms. First, the potential for applying the polarimetric decomposition techniques was addressed in order to repress the disturbing influence of secondary scattering processes, resulting from rough surface scatter. Then, the potential to estimate terrain slopes from fully polarimetric data utilising polarimetric techniques only is investigated and discussed as an attractive alternative to the standard method of using a-priori terrain information.

A new model for the inversion of surface parameters from polarimetric SAR image data takes, the *Extended Bragg Model*, is introduced. The main advantages and disadvantages of this alternate model are discussed. Finally, future perspectives on how to extend the model by implementation of recent advances in polarimetric SAR interferometry are presented.

Keywords: Surface Parameters Inversion, Soil Moisture Estimation, Surface Roughness Estimation, Synthetic Aperture Radar (SAR), SAR Polarimetry

Kurzfassung

In dieser Arbeit wurde das Potential vom polarimetrischen Synthetischen Apertur Radar - *SAR* zur Bestimmung von geophysikalischen Oberflächenparametern untersucht. Die Abhängigkeit des Rückstreusignals von den dielektrischen und geometrischen Eigenschaften einer vegetationslosen Bodenoberfläche wird in der Radarfernerkundung zur Bestimmung von Oberflächenparametern verwendet. Die Oberflächenparameter, volumetrische Bodenfeuchte und Oberflächenrauhigkeit, liefern als Eingangsparameter einen signifikanten Beitrag für hydrologische und ökologische Modelle und sind mit ihrer hohen räumlichen und zeitlichen Auflösung dienlich bei der Optimierung von landwirtschaftlichen Verfahren.

Die klassischen Punktmessungen zur Bestimmung der Oberflächenparameter, volumetrische Bodenfeuchte und Oberflächenrauhigkeit, werden beschrieben. Die Flugzeugkampagne und die gleichzeitig durchgeführten Geländeaufnahmen wurden auf zwei Testgebieten in Deutschland, an der Elb-Aue und im Weiherbachtal durchgeführt. Die Flugzeugkampagne fand mit dem E-SAR des Deutschen Zentrums für Luft- und Raumfahrt (DLR-OP-HR) statt. Die Grundlage für die Invertierung von Oberflächenparametern bilden das SAR und die polarimetrische Konstellation des SAR, deren grundlegende Prinzipien und neue Konzepte vorgestellt werden.

Ausgehend von der exakten Lösungsfindung der Maxwell Gleichungen bis hin zur Entwicklung von empirischen Modellen zur Bestimmung von Oberflächenparametern, wurden drei richtungsweisende Verfahren kritisch untersucht. Hierzu gehören das Small Perturbation Model und zwei semi-empirische Erweiterungen. Die ausgewählten semi-empirischen Erweiterungen stellen einen Überblick in der Entwicklung von Modellen und Techniken von teilpolarisierten SAR Daten dar. Ferner wurde das Potential neuer polarimetrischer Techniken untersucht, die auf die polarimetrischen SAR Daten angewendet wurden, um damit die Bedingungen für die anschließende Anwendung der semi-empirischen Modelle zu verbessern. Zum einen kamen polarimetrische Zerlegungstechniken von Streumechanismen zur Anwendung, die die störenden sekundären Streumechanismen reduzieren und zum anderen konnten mit Hilfe der polarimetrischen Informationen topographische Höhenunterschiede ohne *a-priori* Wissen extrahiert werden, um die Daten zur Bestimmung von Oberflächenparametern zu korrigieren.

Ein neu entwickeltes Oberflächenmodel, *Extended Bragg Model*, zur Invertierung der Oberflächenparameter mit seinen Vor- und Nachteilen wurde vorgestellt. Dieses Model weist die geringsten Invertierungsungenauigkeiten auf.

Schlüsselwörter: Oberflächenparameter-Bestimmung,   Volumetrische   Bodenfeuchte, Oberflächenrauhigkeit, Synthetisches Apertur Radar (SAR), SAR Polarimetrie

Preface

At the initiation of writing my dissertation, a good friend told me that writing a thesis document is like writing down the story of all the experiences that have grown out of the previous three years of work. This gave me the courage required to commit to paper - the sometimes - difficult task of approaching the topic of *Fully Polarimetric SAR Analysis* from a geographer's perspective. But, before I start with writing my '*research story*', I would first like to thank all those who provided help and guidance during its formulation.

The thesis describes work carried out, as part of a BMBF project sponsored by the German Ministry of Education and Research, at the German Aerospace Center (DLR), Institute of Radio Frequency Technology and Radar Systems in Oberpfaffenhofen (DLR-OP-IHR); a dissertation fellowship at the German Aerospace Center; and another dissertation fellowship contract with the European TMR Polarimetry Network carried out in parts at St. Andrews in Scotland under the guidance of Dr. Shane R. Cloude, and at Rennes in France under the supervision of Professor Dr.-Ing.-Habil. Eric Pottier.

Foremost, among those I would like to thank, are my supervisor and former Group Leader at DLR, Dr. Christiane Cornelia Schmullius (now Professor with the University of Jena), for her introducing me to the field of radar remote sensing. Together with Prof. Dr. Peter Ergenzinger, the supervisor of my Diploma thesis, she was the main source of inspiration for choosing my thesis topic, and helped me to grow from being a student, to become a more mature and responsible scientist. I am also deeply indebted to my second supervisor, Prof. Dr.-Ing.-Habil. Eric Pottier from the University of Rennes I, for the support he provided particularly during the final stages of my doctoral research studies. Despite the differences in our background, his patient and clear explanations helped guiding me through the *polarimetric labyrinth*. His personal support from the very beginning was a rare privilege. I know, he will not like to hear it; but when he was working until three in the morning almost every day, he was appearing to me like a *TIRED OLD PROFESSOR*, yet the old Professor was still very young and never said NO to any inquisitive disturbances. Thanks again "*beloved T.O.P*"! A very special thanks is going to my third supervisor, Prof. Dr. Wolfgang-Martin Boerner from the University of Illinois at Chicago. He was not only my scientific supervisor but also like a favourite uncle to me and he always motivated me with his never-ending enthusiasm to any kind of application in polarimetry. His comments, even if sometimes very demanding - he was never 100% satisfied - were essential in improving the final version of this work. I hope his dream of a better understanding of our Earth in the frame of the Collaboratorium Terra Digitalis would come true one day.

This work could not have been completed without the critical review and constructive comments from my external reviewers: Foremost, Prof. Dr. Shane Robert Cloude from the University of Dundee, Scotland, who erased my intense fear of complex mathematics, and to whom I am grateful for guiding me through the first steps of gaining competency in radar polarimetry, which absorbed some time for me to understand; Dr. Jong-Sen Lee from the Naval Research Laboratory, Washington DC, for his profuse help particularly regarding polarimetric speckle filtering, and for his human touch as well as his cordial induction to the polarimetry family; Dr.-Ing. Alberto Moreira, Leader of the SAR Technology Division of the Institute of Radio Frequency Technology and Radar Systems at DLR, who extended me the

X

Zusammenfassung

Die flugzeug- und satelliten-gestützte Fernerkundung der Erde stellt seit vielen Jahren eine anerkannte und viel genutzte Informationsquelle für kartographische, geodätische und geowissenschaftliche Fragestellungen dar, die auch bereits seit geraumer Zeit zur aktuellen und großräumigen Erfassung von Umweltveränderungen genutzt wurde. Die Fernerkundung ermöglicht die Abbildung und Untersuchung von der Erdoberfläche und Atmosphäre in Abhängigkeit vom Reflexions- und Absorbtions-specktrum der interessierenden Objekte in verschiedenen räumlichen, zeitlichen und spektralen Auflösungen sowie mit unterschiedlicher radiometrischer Empfindlichkeit.

„Das Ziel dieser Arbeit ist es, geophysikalische Oberflächenparameter, wie volumetrische Bodenfeuchte und Oberflächenrauhigkeit, mit Hilfe der polarimetrischen Radarfernerkundung quantitativ zu bestimmen".

Natürliche Böden können durch ihre materielle Beschaffenheit und geometrischen Eigenschaften beschrieben werden. Der entscheidende Oberflächenparameter zur Bestimmung der Materialeigenschaften eines natürlichen Bodens stellt die volumetrische Bodenfeuchte m_v dar. Einen Bezug dieses Parameters zum Rückstreusignal des Radars ist durch den Realteil der komplexen Dielektrizitätskonstante ε' gegeben. Die geometrischen Eigenschaften eines natürlichen Bodens können durch zwei Parameter, die RMS Höhe s und die Autokorrelationslänge l, die ein Maß für die vertikale und horizontale Rauhigkeit darstellen, beschrieben werden. Einen Bezug zum Rückstreusignal wird durch die Wellenlänge λ ($k= 2\pi/\lambda$) zu ks und kl gegeben.

Eine attraktive Alternative zu klassischen Methoden stellt die großflächige und räumliche hochauflösende Oberflächenparameterbestimmung mittels der Radarfernerkundung dar. Mit klassischen Methoden ist die Erfassung der beschriebenen Oberflächenparameter sehr arbeits- und zeitaufwendig. Am Beispiel von zwei Testgebieten, dem Elbe-Auen-Vorlandbereich und das Weiherbach-Wassereinzugsgebiet, wurden auf unterschiedlich großen, landwirtschaftlich genutzten Feldern Stechzylinder-Proben zur Messung von volumetrischer Bodenfeuchte gewonnen und mit einem zwei-dimensionalen Rauhigkeitsmessgerät zur Messung von Oberflächenrauhigkeit angewendet. Die landwirtschaftlichen Felder im Elb-Auen Gebiet zeichnen sich durch trockene und mäßig bis rauhe Oberflächen aus, wobei das Weiherbach Gebiet feuchte und glatte Flächen aufweist. Die Geländemessungen weisen insgesamt ein breites Spektrum von Bodenfeuchte $7 < m_v$ [vol. %] < 37 (z. B. $7 < \varepsilon' < 22.5$) und Oberflächenrauhigkeitswerten $1 < s$ [cm] < 3.5 (z. B. $0.3 < ks < 0.95$) auf.

Ersatzweise können Oberflächenparameter mit der Methode der Radarfernerkundung erhoben werden. Zur Aufnahme mit dem Radar wurde das flugzeuggetragene Experimentelle SAR-System (E-SAR) des Deutschen Zentrums für Luft- und Raumfahrt e. V. (DLR), welches am Institut für Hochfrequenztechnik und Radarsysteme in Oberpfaffenhoffen, entwickelt worden ist, ausgewählt. Das E-SAR wurde mit dem Ziel aufgebaut, einen modifizierbaren Meß-Sensor zur SAR-Verfahrenserprobung und für grundsätzliche Signaturmessungen verfügbar zu haben. Es arbeitet in verschiedenen Frequenzbereichen und Polarisationen. Zum Zweck der Oberflächenparameterbestimmung kam die voll-polarimetrische L-Band-Konstellation zur Anwendung.

Die polarimetrische Radarfernerkundung ist ein relativ neues Werkzeug zur Beschreibung der Topographie zur Erfassung von geophysikalischen Oberflächenparametern. Die Entwicklung von neuen Techniken und Modellen zur Bestimmung von objektspezifischen Parametern, wie Oberflächenrauhigkeit, Bodenfeuchte und Objektart, stellt seit Jahren ein bedeutendes wissenschaftliches Thema dar. Seit den siebziger Jahren fanden zahlreiche Untersuchungen zur qualitativen und quantitativen Bestimmung von Objektparametern aus Radarsensoren sowohl von Satelliten als auch flugzeuggetragenen Systemen statt. Für die quantitative Bestimmung der modellrelevanten Boden- und Bestandsparameter werden die Rückstreu-Eigenschaften hinsichtlich ihrer Größenrelation, Ausrichtungsgenauigkeit, Polarisations-, Frequenz- und Einfallswinkelabhängigkeit in Bezug zu den erhobenen Geländeparametern interpretiert. Untersuchungen dieser Art wurden oft zunächst mit Scatterometern, später auch mit abbildenden Systemen durchgeführt. Aus der Vielzahl der Untersuchungen kann schlussfolgernd festgestellt werden, dass zwischen dem Radarsignal und dem Bodenwassergehalt in Volumenprozente, Gewichtsprozente oder Prozente der Feldkapazität ein exponentieller bzw. für engere Wertebereiche ein linearer Zusammenhang besteht. Die ersten Anwendungen fanden mit Regressionsanalysen, dann mit Rückstreu-Modellen und später mit Inversions-Modellen statt. Die ersten Ergebnisse zeigten:

- Die Regressionsanalysen sind regional unterschiedlich und erlauben keine Übertragung auf andere Regionen. Die regionalen Unterschiede ergeben sich aus den verschiedenen geologischen Ausgangssubstraten für die Bodenbildung, die sich hinsichtlich der Textur, Struktur, Humusgehalt, Quellungs- und Schrumpfungs-eigenschaften und auch der Reliefposition unterscheiden. Die meisten Untersuchungen dieser Art wurden in Gebieten mit geringer räumlicher Variabilität der Substrate durchgeführt, die Idealvoraussetzungen für solche Untersuchungen darstellen.
- Der Einsatz von Rückstreumodellen ist meist an Hand von wenigen Referenzdaten überprüft worden, da Radarsysteme mit unterschiedlichen geometrischen Auflösungen, Frequenzen, Polarisationen und Einfallswinkeln nicht zur Verfügung standen (Flugzeug, Shuttle oder Satellit).
- Die Inversionsmodelle stecken hinsichtlich der Genauigkeit noch in den Anfängen und bedürfen der weiteren wissenschaftlichen Erforschung. Am vielversprechendsten waren hier Untersuchungen mit polarimetrischen SAR-Daten.

Die Abhängigkeiten des Rückstreuquerschnittes von den drei Hauptparametern Oberflächenrauhigkeit, Autokorrelationslänge (ks und kl) und relative Dielektrizitätskonstante (ε') ermöglichen mit Hilfe von Modellen eine Invertierung dieser Parameter. Die Modelle weisen unterschiedliche Möglichkeiten auf, diese Parameter zu extrahieren, und werden in der Literatur kontrovers diskutiert. Die Vielzahl der komplex ineinander wirkenden Einflussparameter erschweren die Erfassung der Zusammenhänge in einfachen und anwendbaren Modellen. So wurden mehrskalige komplexe Rauhigkeitsmodelle entwickelt, deren Anzahl der statistischen Inputparameter die Anzahl der Outputparameter bis um ein Neunfaches übersteigen können. Die Anwendbarkeit solcher Modelle ist nur mit *a priori*-Wissen über das betrachtete Medium möglich, welches ein unabhängiges und objektives Modellieren erschwert und nicht zur automatischen Bestimmung der Bodenparameter dienlich ist. Allen Modellen ist gemeinsam, dass sie sehr große Abweichungen in der Genauigkeit bei der Validierung aufzeigen. Eines des wichtigsten Aufgabenstellungen dieser Arbeit war, die Frage zu beantworten: ***Ist es möglich die Oberflächenparameter, volumetrische Bodenfeuchte und Oberflächenrauhigkeit, unabhängig voneinander, mit einer hohen quantitativen Genauigkeit aus polarimetrischen Radardaten zu bestimmen ?***

Die polarimetrische Radarfernerkundung spielt eine bedeutende Rolle in der Oberflächenparameter-Bestimmung. Das Basis-Konzept von Rückstreumodellen bildet die polarimetrische Konstellation des Radars. Entwickelt worden sind theoretische, empirische und semi-empirische Rückstreu- und Invertierungs-Modelle zur Ermittlung dieser Parameter auf unbewachsenen Oberflächen. Bis zum heutigen Stand der Forschung sind polaimetrische Invertierungs-Modelle über bewachsenen Oberflächen noch im sehr frühen Entwicklungsstadium und werden hier nicht weiter behandelt.

In dieser Arbeit werden drei Invertierungs-Modelle am Beispiel von zwei Testgebieten beschrieben und ihre Vor- und Nachteile ausgiebig diskutiert. Eines der weit verbreitesten und am häufigsten angewandten ist das sehr einfach zu implementierende theoretische ‚*Small Perturbation Model*' (SPM). Das SPM erlaubt durch das Vorhandensein einer sehr kleinen Rauhigkeitskomponente $ks < 0.3$ eine direkte Ableitung der komplexen Dielektrizitätskonstante aus dem Verhältnis der gleich-polarisierten Rückstreu-Amplituden, σ_{HH}/σ_{VV}. Die Haupteinschränkung dieses Models ist der sehr kleine Gültigkeitsbereich für die Oberflächenrauhigkeit und die abnehmende Sensitivität der Bodenfeuchte bei $m_v > 20$ [vol %]. Für natürliche Bodenoberflächen ist der Anteil der Oberflächenrauhigkeit meist zu groß, als dass dieses Modell eine Relevanz in der Praxis zugemessen werden könnte. Nichtsdestotrotz stellte das Modell die Grundlage für weitere Entwicklungen dar. Eine Erweiterung des Gültigkeitsbereiches für den Parameter der Oberflächenrauhigkeit und damit eine bessere Anpassung an die natürlichen Oberflächenrauhigkeitsverhältnisse leisten die semi-empirischen Modelle.

Die semi-emprischen Modelle leiten ihre Algorithmen einerseits über physikalisch-mathematische Überlegungen und andererseits durch Regressionen über einen ausgewählten

Datensatz zum Erhalt von Modellierkonstanten her. Im Gegensatz zu den theoretischen Modellen sind die semi-empirischen und empirischen Modelle für einen größeren und weiteren Anwendungsbereich in Bezug auf Oberflächen- und Systemparameter konzipiert. Auf den rauhigkeitsbeschreibenden Parameter der Autokorrelationslänge *kl* wird verzichtet. Angenommen wird, dass dieser schwer zu definierende Parameter, sowohl im Gelände wie auch im mathematischen Sinn, keinen gravierenden Einfluss auf die Radarrückstreuung hat, wie auch in einigen Studien schon nachgewiesen wurde (ZRIBI 1999).

Der Vorteil der semi-empirischen Modelle ist ihre einfache Handhabung, während ihr Nachteil immer noch eine eingeschränkte Übertragbarkeit zu anderen Testgebieten darstellt:

- Der semi-empirische Ansatz von OH *et al*. (1992) benötigt zu den co-polarisierten auch das kreuz-polarisierten Verhältnis zur Invertierung von Oberflächenparametern. Dabei werden die physikalisch-mathematischen Überlegungen des SPM übernommen und der Wertebereich für die Oberflächenrauhigkeit *ks* erweitert.
- Im Gegensatz zum empirischen Modell von DUBOIS *et al*. (1995), das nur das ko-polarisierte Verhältnis betrachtet und somit immer noch eine höhere Sensitivität in der Bestimmung der volumetrischen Bodenfeuchte m_v zeigt.
- Beide Modelle gehen von der Voraussetzung aus, dass nur Oberflächenstreuung vorhanden ist. Deshalb findet im Vorfeld eine Ausscheidung der Anteile statt, die der Bedingung $\sigma_{HH}^0 / \sigma_{VV}^0$ < 1 and $\sigma_{VH}^0 / \sigma_{VV}^0$ < -11 dB nicht genügen und auf Mehrfach- und Volumenstreuung hindeuten. Die Anwesenheit von Mehrfach- und Volumenstreuung kann hervorgerufen werden durch Vegetation auf den Feldern, durch kleine Autokorrelationslängen und hohe Oberflächenrauhigkeiten sowie durch Depolarisationseffekte im Boden selbst. Diese Mechanismen bedingen eine hohe Anzahl der ungültigen Anteile und können somit nicht als repräsentativ für statistische Auswertungen gelten.

Die semi-empirischen Modelle, basierend auf dem SPM, erhöhen den Gültigkeitsbereich für die Oberflächenparameter, stellen aber immer noch eine zu hohe Fehlerquelle zur quantitativen Bestimmung dar. Ein weiterer Nachteil stellt die Invertierung erst eines Oberflächenparameters dar, meist m_v, um dann im zweiten Schritt den zweiten Parameter, *ks*, bestimmen zu können. Zusätzlich ist die Anwendbarkeit dieser Modelle mit Regressionskonstanten, die über einem speziellen Testgebiet erstellt wurden, sehr fraglich.

Zur Minderung der Einflüsse von Mehrfach- und Volumenstreuung wurden verschiedene „*Polarimetrische Dekomposition-Techniken*" verwendet. Die Idee der polarimetrischen Dekomposition ist die Trennung von übereinanderlagernden Streumechanismen vom Rückstreusignal. Diese Technik ermöglicht es, die drei Hauptstreumechanismen des Rückstreusignals des Radars, *Oberflächen-, Mehrfach- und Volumenstreuung*, zu separieren und diese Methode als Vorverarbeitungsschritt für die anschließende Anwendung des theoretischen und der semi-empirischen Modelle zu verwenden.

Zur Anwendung kamen die Eigenvektor-Dekomposition von der Koherenz-Matrix (Cloude 1986) und die modellbasierte Dekomposition (Freeman & Durden 1998). Die Genauigkeit der Invertierungsergebnisse mit der Methode der Eigenvektor-Dekomposition konnte insgesamt verbessert werden. Nach der Eigenvektor-Dekomposition werden die Streumechanismen in drei voneinander unabhängigen Matrizen getrennt. Die Matrizen entsprechen hauptsächlich den folgenden Anteilen oder Komponenten: Die erste entspricht der Oberflächenstreuung, die zweite der Mehrfachstreuung, und die dritte der Volumenstreuung. Die Verwendung nur der ersten Komponente zur Anwendung des SPM verbesserte die Genauigkeit der m_v-Messung signifikant, insbesondere über leicht bewachsenen Oberflächen. Die Anwendungsergebnisse der semi-empirischen Modelle zeigte nur beim Dubois-Modell für ks eine (signifikante) starke Verbesserung. Dies liegt daran, dass im Dubois-Modell nur mit ko-polarisierten Rückstreusignalen gearbeitet wird und mit der Entfernung von Mehrfach- und Volumenstreuung eine ideale Voraussetzung geschaffen wurde. Im Gegensatz zum Oh-Modell, das mit Kreuz-Polarisationen arbeitet und dieses nicht in der ersten Komponente enthalten ist. Allgemein ist darauf hinzuweisen, dass mit der Regressionskonstante auch ein gewisser Anteil von Mehrfachstreuung in den semi-empirischen Modellen berücksichtigt wird. Daraus folgend wurden die semi-empirischen Modelle auf die erste und zweite Komponente angewendet und eine nochmals verbesserte quantitative Bestimmung von beiden Oberflächenparametern, m_v und $ks,$ konnte erzielt werden. Ein anderer Versuche die Modell-Bedingungen zu verbessern, konnte mit der modellbasierten Dekomposition erreicht werden. Hierbei wird eine Trennung der Streumechanismen, basierend auf drei einfachen Streumodellen, bewirkt. Die erste Komponente, die Oberflächenstreuung, wird mit dem SPM modelliert und kann somit direkt zur Invertierung der volumentrischen Bodenfeuchte herangezogen werden. Dieses Verfahren zeigte die höchst erzielte Genauigkeit der m_v Bestimmung mit dem SPM.

Ein weiterer wichtiger Faktor zu Verbesserung der Modellergebnisse ist das Kompensieren von topographischen Effekten. Topographische Effekte werden normalerweise durch die Ermittlung des lokalen Einfallswinkels mittels eines digitalen Geländemodelles (DGM) korrigiert. In dieser Arbeit wurde ein kürzlich entwickeltes Modell angewendet, das nur die polarimetrischen Information des Radar zur Korrektur von topographischen Variationen benötigt, und als POL-DEM in der offenen Literatur bekannt ist. Hierzu wird der Orientierungwinkels ermittelt, der als Winkel beschrieben ist, bei der die lineare Antennen-Polarisation solange gedreht werden muss, bis sie horizontal zur tangentialen Ebene der Bodenoberfläche ist. Das Rückstreusignal wird nun um den negativen Wert des Orientierungswinkels in der Entfernungsrichtung gedreht. Dieses Verfahren zur Korrektur von topographischen Variationen von SCHULER *et al*. 1998, POTTIER *et al*. 1999 und LEE *et al*. 2000 wurde auf das Weiherbach-Einzugsgebiet angewendet und mit DGM-korrigierten Ergebnissen verglichen. Die Invertierungsergebnisse der semi-empirischen Modelle unter Verwendung der Orientierungswinkel-Methode weisen eine geringe aber doch spürbare Verbesserung der Ergebnisse auf. Daraus folgt allgemein, die Genauigkeiten der Korrektur mit dem DGM kann nicht mit der polarimetrischen Winkel-Methode ersetzt werden, jedoch kann es aber bei Nichtvorhandensein eines DGM als wertvolles Annäherungsverfahren verwendet werden.

Trotz der erhöhten Genauigkeiten der Invertierungsergebnisse mit den beschriebenen Vorverarbeitungsschritten ist die gewünschte Genauigkeit von < 5 % nicht erreicht worden. Deshalb wurde ein neues Invertierungsverfahren entwickelt, das auf der modellbasierten Eigenvektor-Dekomposition basiert, der *„Extended Bragg Methode (EX-Bragg)"* (CLOUDE *et al.* 1999). EX-Bragg beruht auf der Basis des SPM und erweitert die *ks* Komponente mit einem eingeführten theoretischen Winkel. Ein großer Vorteil dieser Methode ist die unabhängige Bestimmung der Oberflächenparameter. Mit diesem Verfahren konnten die höchsten Invertierungsgenauigkeiten erzielt werden, somit wurde der Gültigkeitsbereich von m_v auf 40 [vol. %] und *ks* < 1 erweitert. Zwei Nachteile dieses Verfahren sind: der Einfluss von Phasenrauschen und Vegetation sowie hohe Oberflächenrauhigkeiten.

Diese Einflüsse auf die Genauigkeit von Invertierungsergebnissen zeigen auch die erwähnten theoretischen sowie semi-empirischen Modelle. Allgemein kann festgehalten werden, dass der Einfluß von Vegetation nicht allein durch Verwendung der polarimetrischen Radarfernerkundung gelöst werden kann. Hierzu müssen weitere Methoden entwickelt werden, um ein zufriedenstellendes Ergebnis zu erlangen. Mit größter Wahrscheinlichkeit kann festgestellt werden, dass eine Anwendung von Radar-Daten für die flächendeckende Ermittlung des Bodenwassergehaltes als Start- und Kontrollwert für Bodenwasserhaushalts- und Gebietswasserhaushaltsmodelle oder als Unterlage für regionale Planungen vom heutigen technischen Standpunkt möglich ist und eine nützliche Alternative zu den aufwendigen klassischen Punktmessungen darstellt.

Referenzen

CLOUDE, S. R., 'Group Theory and Polarisation Algebra', *OPTIK*, vol.75, no. 1, pp. 26-36, 1986.

CLOUDE, S. R., HAJNSEK, I. & PAPATHANASSIOU, K. P., 'An Eigenvector Method for the Extraction of Surface Parameters in Polarimetric SAR', *Proceedings of the CEOS SAR Workshop*, Toulouse 1999, ESA SP-450, pp. 693 – 698, 1999.

DUBOIS, P. C. VAN ZYL, J. J. & ENGMAN, T., 'Measuring Soil Moisture with Imaging Radars*', IEEE Transactions on Geoscience and Remote Sensing*, vol. 33, no. 4, pp. 916-926, 1995.

FREEMAN, A. & DURDEN, S. L., 'A Three-Component Scattering Model for Polarimetric SAR Data', *IEEE Transactions on Geoscience and Remote Sensing*, vol. 36, no. 3, pp. 963-973, 1998.

LEE, J. S., D. L. SCHULER & T. L. AINSWORTH, 'Polarimetric SAR Data Compensation for Terrain Azimuth Slope Variation', *IEEE Transactions on Geoscience and Remote Sensing*, vol. 38, no. 5, part I, pp. 2153-2163, 2000.

OH, Y., SARABANDI, K. & ULABY, F. T., 'An Empirical Model and an Inversion Technique for Radar Scattering from Bare Soil Surfaces', *IEEE Transactions on Geoscience and Remote Sensing*, vol.30, no. 2, pp. 370-381, 1992.

POTTIER, E., SCHULER, D. L., LEE, J.-S., & AINSWORTH, T. L., 'Estimation of the Terrain Surface Azimuthal/Range Slopes Using Polarimetric Decomposition of Polsar Data', *Proceeding IGARSS'99*, Hamburg, pp. 2212-2214, 1999.

SCHULER, D. AINSWORTH, T., LEE, J. S. & DE GRANDI, G., 'Topographic Mapping Using Polarimetric SAR data', *International Journal of Remote Sensing*, vol. 34, no. 5, pp. 1266-1277, 1998.

ZRIBI, M., CIARLETTI, V. & VIDAL-MADJAR, D., 'An Inversion Model of Soil Roughness Based on Two Radar Frequency Measurements', Proceedings IGARSS'99, Hamburg, pp. 2425 - 2427, 1999.

Content

Abstract, Kurzfassung

Preface

Zusammenfassung

Content

List of Figures, List of Tables, List of Symbols, List of Abbreviation

1 Introduction

2 Soil Surface Parameters

3 Estimation of Ground Measured Soil Surface Parameters

4 Remote Sensing Using Airborne Synthetic Aperture Radar Data

5 Polarimetric Concepts for Microwave Remote Sensing

6 Inversion of Surface Parameters Using Classical Approaches

7 Inversion of Surface Parameters Using Polarimetric Pre-Processing Techniques

8 Inversion of Surface Parameters Using Extended Bragg Scattering Model

9 Conclusion and Outlook

List of Figures

List of Tables

List of Symbols

Chapter 2

$\Gamma(h, v)$	Fresnel coefficient for different polarisations, v vertical and h horizontal
δp	penetration depth
$\varepsilon = \varepsilon_r$	complex dielectric constant
ε'	real part of the dielectric constant
ε''	imaginary part of the dielectric constant
εw	dielectric constant of pure water
$\varepsilon w\infty$	dielectric constant of pure water at the high-frequency limit
θ	local incidence angle
λ	wavelength
ρb	bulk density of the soil
ρw	density of water
$\rho(x)$	surface correlation function
τw	relaxation time of pure water
l	surface correlation length
k	wavenumber
ks	surface roughness in relation with the wavelength
S	degree of saturation
s	surface roughness,
m_v	volumetric soil moisture
R	water content, volume fraction
Rm	water content, mass basis
Rv	water content, conversion from mass basis to volume fraction
rms height	surface roughness, defined as the standard deviation of the height variations

Chapter 4

$\beta°$	radar brightness
DN	digital number
C	calibration constant
RCS	radar cross section

Chapter 5

α	scattering alpha-angle
β	scattering beta-angle
λ	eigenvalue
ρ	complex polarisation ratio
$\sigma°$	normalised radar cross section
ϕ_0	absolute phase reference
χ	polarimetric ellipticity angle
ψ	polarimetric orientation angle
ω	angular frequency
A	scattering anisotropy
A_0	wave amplitude
$\vec{E}(\vec{r},t)$	electric field vector (real)
$\vec{\bar{E}}(\vec{r})$	electric field vector (complex)
$\vec{e}$	eigenvector
H	scattering entropy
$\vec{k}$	propagation vector
$\vec{k}_P$	scattering vector (Pauli basis)

$\vec{k}_L$	scattering vector (Lexicographic basis)
TP	total power
P	appearance probability for scattering process
[C]	covariance Matrix
[D]	transformation matrix Pauli to Lexicographic Basis
[J]	wave coherency matrix
[S]	scattering matrix
[T]	coherency matrix
[U_2]	2x2 special unitary matrix (complex)
[U_3]	3x3 special unitary matrix (complex)
[R_2]	2x2 LOS rotation matrix (real)
[R_3]	3x3 LOS rotation matrix (real)

Chapter 6

Rp	Bragg scattering coefficient for parallel
Rs	Bragg scattering coefficient for perpendicular
p	co-polarised backscattering ratio
q	cross-polarised backscattering ratio

Chapter 7

[T_D]	coherency matrix with dihedral scattering contributions
[T_S]	coherency matrix with surface scattering contributions
[T_V]	coherency matrix with volume scattering contributions

Chapter 8

β	angle in the plane perpendicular to the scattering plane
β_1	width of distribution of the average angle β
C_1, C_2, C	describing the Bragg components in the Extended-Bragg Model
γ_{LLRR}	Left-Right circular coherence
σ_N	additive noise amplitude

List of Abbreviation

AOI	angle of incidence
DEM	digital elevation model
DN	digital number
EM	electromagnetic wave
E-SAR	Experimental Synthetic Aperture Radar
GIS	geographical information system
GOM	geometric optics model
IEM	integral equation model
IPU	international physical union
KA	Kirchhoff Approximation
LIA	local incidence angle
LOS	line of sight
NDVI	normalised difference vegetation index
OAC	orientation angle correction
PAR	parallel to the row direction
POM	physic optics model
PPR	perpendicular to the row direction
RCS	radar cross section
RLA	radar look angle
SAR	synthetic aperture radar
SLC	single complex SAR data
SPM	small perturbation model
TDR	Time Domain Reflectometry

Chapter 1

Introduction

 One of the defining social themes of these days is ecological awareness. Ecology stands today at the interface between science and public policy. Pressure groups, citizens, and policy-makers draw on ecological research to form opinions on questions facing our planet: how to deal with climate change, biodiversity, population control and other pressing matters. Therefore, the issue of how ecological information is gathered and how that information is applied to environmental stress change monitoring, becomes tremendously relevant nowadays (GALLAGHER *et al.* 1995).

Earth's solid surface represents an essential part of our ecosystem and because of its diversity a huge number of bio- & geo-physical parameters is required for its detailed description and/or monitoring. An important element of the earth's surface is the soil. Soils can be parameterised in terms of its consistency, and its dielectric and geometric properties. The dielectric properties of soils are expressed – *apart from its consistency* - primarily by its moisture content. On the other hand, the soil roughness describes the geometric characteristics of the soil surface.

The *soil moisture content* plays an essential role in predicting, estimating and modelling major ecological processes such as evaporation, transpiration, surface runoff and ground water replenishment. Even the contamination of river or ground water with undesirable water pollutants is indirectly influenced by the soil water movement. Soil moisture deficit or surplus are often key factors affecting the temporal and spatial dynamics of vegetation systems. Thus, a knowledge of temporal and spatial fluctuations of soil moisture content is relevant to a wide spectrum of applications, for example: the prediction of plant growth, determination of the proper time for sowing, the identification of agricultural areas with accelerated soil erosion or water logging and the monitoring of dynamic soil processes acting on the surface (physical, chemical and biological). Furthermore, it serves as input parameter for hydrological and meteorological modelling and enables to identifying environmentally sensitive areas.

On the other hand, knowledge of the *surface roughness* is important for monitoring soil erosion. The erosion of soil and rock by water, wind and ice is a natural process. Geological erosion over long periods of time has provided the parent material from which soil is built. Human activity has greatly accelerated the rate of natural erosion. Expanding populations and their demand for land-based resources has led to rapid conversion of forest and grassland to rural, urban, industrial, and other uses. Such changes remove the protective land cover under which soils slowly develop their pedological and biological characteristics. The hazard induced by such changes depends on climate and topographic factors, and on the type of exposed soil material. Inappropriate methods of forestry/land clearing or agricultural land management, as

well as overgrazing of pasture or savannah lands lead to accelerated rates of soil erosion, threading the sustainability of such land use (RIQUIER 1982).

Classical methods in soil physics are based on point measurements to estimate these two surface parameters. The most critical factor, besides the enormous time and working effort, is the extrapolation of point samples to catchment (or sub-regional) scale processes. According to DOOGE (1988), hydrology as scientific discipline spans fifteen orders of magnitude, ranging from the scale of cluster of water molecules (10^{-8} m) to the global hydrological cycle (10^7 m). In practice, hydrological studies have traditionally favoured the catchment scale, or what DOOGE refers to as the meso-scale or the lower end of the macro-scale. The greatest error in the parameterisation occurs on the interface between different scales of hydrological to climatic or ecological models. Such mismatch problems have an important implication for the credibility of impact studies driven by the output of models. In order to bridge the scales between different science applications, e.g. climate hydrology and ecology models, methods for both observing and representing sub-grid-scale heterogeneity, as well as linking parameter/state variables across disparate scales, are in great need.

The linking and the integration of geophysical laws at different scales is a challenge in the field of surface dependent processes. Prior to the 1970's, environmental monitoring was mainly focused on local-scale processes and measurements. This favoured observation scale reflects the tradition of applied hydrology, the relative simplicity with which such data can be collected and the available technology of the time for data storage and interrogation. According to BEVEN (1995) '*hydrological science is constrained by the measurement techniques that were available at the present time. Hydrological theory reflects the scale at which measurements are relatively easy to make'. Or in other words the distinction should be made between the characteristic 'observation scale' and the 'process scale'.* With the global appreciation on the global dimension to environmental changes, there have been moves to rationalise existing monitoring networks (RODDA 1995) and to undertake co-ordinated, international measurement campaigns such as the *Global Energy and Water Cycle Experiment, GEWEX* (Anon. 1993).

However, remotely sensed (from space or airborne sensors) information provides today new opportunities to hydrologists and ecologists from monitoring extended processes with a spatial resolution from about a meter up to a global scale. Remote sensing techniques provide data for hydrological model parameter estimation, computation of geo-physical parameters and for real–time forecasting. Indeed, remote sensing is capable of quantifying some of the key hydrological parameters for water balance modelling (precipitation, evaporation, snow cover, runoff, soil moisture and surface roughness).

Several remote sensing techniques (HENDERSON & LEWIS 1998) are available today to measure a variety of surface parameters at meso-scales to macro-scales. For the distribution of soil moisture content and surface roughness, the development of airborne or spaceborne gamma-

ray, near to far infrared, thermal infrared spectrometers, passive radiometers and active radar systems, promises to yield estimates of high accuracy and high spatial resolution.

Radar remote sensing with its sensitivity to the dielectric and geometric characteristics of objects, its weather independent imaging capability and its potential to acquire subsurface information, in dependence of the frequency band used, is one of the most promising approaches for surface parameter estimation.

1.1 State-of-the-Art

Electromagnetic (EM) wave scattering on rough dielectric surfaces has been the subject of intensive studies for many decades. Many experimental measurements have been accumulated and many approaches have been developed in order to predict and interpret experimental data. Despite the large amount of research efforts the general surface scattering problem is analytically not completely solved. The following approaches can be categorised as approximate solutions, and hence with a more or less restricted applicability or exact but too general to be of practical importance (BECKMANN & SPIZZICHINO 1963).

In the following, a brief survey of the history of surface scattering investigations and a review of the current status of soil moisture content and surface roughness retrieval algorithms will be given. The original algorithms used for these two surface parameters originated in different research areas at different times. The estimation of the surface roughness and the complex dielectric constant originated with the development of electromagnetic scattering theory. A long time later, with increasing interest from the environmental community in soil moisture retrieval, simple semi-empirical and empirical methods were developed.

Soil Moisture Content

Knowledge about the sensitivity of backscattered signals in dependence of the complex dielectric properties of the illuminated object, initiated the first attempts to relate the backscattered signal to soil moisture content. In the seventies, first qualitative and later quantitative soil moisture content estimation algorithms, from air- or space-borne radar data, were developed mainly on an empirical basis. In this context, several non-linear relationships have been explored, depending on system parameters such as frequency, polarisation and local incidence angle. For different test sites, different regression models have been developed implying problems in their transferability to other data sets or regions (WANG & SCHMUGGE 1980, DE LOOR *et al.* 1982, DOBSON *et al.* 1985, TROCH *et al.* 1993, WEVER *et al.* 1995).

In parallel, a second research direction followed the approach of modelling the backscattering behaviour of rough surfaces in order to establish its relationship to surface parameters. Having

established this relation in terms of a scattering model, the inversion of the scattering model allows the estimation of the surface parameters from their backscattering behaviour. Several surface scattering models have been developed providing information about the general behaviour of wave scattering from natural terrain. However, the complexity and wide variety of natural surfaces make it difficult to model exactly these surfaces and their backscattering behaviour as a function of frequency, polarisation and illumination geometry. Consequently, the validity range of the developed scattering models is more or less restricted and the results obtained are in most cases ambiguous. A brief summary about the existing scattering models, estimating both surface parameters, is given next.

Surface Roughness

One the earliest mathematical formulations of wave scattering from rough surfaces was that of Lord RAYLEIGH (1877). This work leads to the so-called Rayleigh criterion for determining the degree of surface roughness. The scattering of electromagnetic waves from statistically rough surfaces was further investigated by MANDEL'SHTAM (1913) with regard to the molecular scattering of light on liquid surfaces. In the early fifties the field of rough surface scattering began to expand, with FEINBERG (1944 - 1946) investigating the coherent component of scattered electromagnetic waves for small surface height irregularities; RICE (1951) applying his perturbation vector theory for the scattering of electromagnetic waves on a two-dimensional randomly rough surfaces, with DAVIES (1954) developing a simpler theory for scalar waves and ANTOKOL'SKII (1948), BREKHOVSKIKH (1951) and ISAKOVICH (1952) formulating the Kirchhoff tangent plane approximation. Further developments of the theory went along the lines of the *Small Perturbation Approximation (SPM)* and the *Kirchhoff Approximation (KA)* (SILVER 1947, SANCER 1968).

The most often quoted reference book on wave scattering from rough surfaces is that of BECKMANN & SPIZZICHINO (1963), providing a review of wave scattering theory from rough surfaces based on the Kirchhoff solution to the scalar wave scattering problem from periodic and random surfaces. Even though it was written close to half a century ago, this treatise is still concidered today as one of the most valuable text. Another review from BASS & FUKS (1979) considers both perturbation and Kirchhoff theory including more complicated problems such as surface self-shadowing and multiple scales of surface roughness, and provides an excellent summary of Soviet (SSSR) Russian contributions, unknown for a long time in the West. Further reviews on wave interactions with random media – as natural rough surfaces – are included in the books of ISHIMARU (1978) and ULABY *et al*. (1982). A more recent text from OGILVY (1991) provides a good numerical overview of wave scattering from random rough surfaces, and it includes simulation results. Finally, a more updated review of theoretical wave scattering models from random media, their extensions and applications can be found in the treatise by FUNG (1994). Due to the large amount of studies on this subject matter it is impossible to refer to all on what is available in the open literature. Therefore, only these major

publications have been referenced in that they provide a good overview of the relevant literature.

A more recent highly acclaimed theoretical "scalar" scattering model is the Integral Equation Model (IEM) developed by FUNG (1994), and its simplification by SHI *et al*. (1997). This offers an alternative approach for the retrieval of surface parameters and is valid for a wider range of surface conditions when compared to other earlier theoretical models. Therefore, it has been given considerable credit by the remote sensing community, far more than any other recently developed theoretical model designed to bridge the gap between SPM and KA. However, the exact formulation is confusing, as three different approaches are involved (FUNG 1992, FUNG 1994, HSIEH *et al*. 1997, CHEN *et al*. 2000). The first two references address the original version of the model, the third reference is the first amendment, while the fourth addresses a later version. However, as recently pointed out (ELFOUHAILY 2001) the IEM lacks of theoretical consistency as it does not include correctly the SPM. This is a compulsory condition if an improvement over any other previous theoretical study is intended. The model does not satisfy the requirements proposed in the book by MITTRA *et al*. (1973) on which the study is based. Thus, only in the case of perfectly conducting surfaces and backscattering the IEM seems to agree with SPM. Furthermore, the model is theoretically inconsistent and, even for backscattering from perfectly conducting surfaces, it is not expected to improve SPM or KA (ALVAREZ-PEREZ 2001). Apart from these limitations, even more important is its weakness for cross-polarisation modelling (ALVAREZ-PEREZ 2001), which limits the application of scalar IEM on single or dual co-polarised data.

1.2 Scope, Problem Formulation & Organisation of the Thesis

The scope of this thesis is to answer the questions: **How accurate and under what conditions can soil-moisture and roughness be estimated from fully polarimetric SAR data? Which are the main limitations; and where lie the challenges for radar remote sensing concerning the quantitative estimation of these two key surface parameters?** An actual answer to these questions is expedient considering the recent advances accomplished in sensor technology, data processing and data analysis techniques and the progress in physical understanding of microwave scattering gained from the large amount of novel polarimetric SAR radar data (BOERNER *et al*. 1998), which have become available in the last few years. The answer to these questions today is even more important in order to understand the potential of near-future radar spaceborne missions such as PALSAR (http://yyy.tksc.nasda.go.jp/Home/Projects/ALOS/tback_e.html) and RADARSAT-2 (http://www.rsi.ca/) planned to operate in a fully polarimetric mode at L and C bands, respectively.

Upon assessing the state-of-the-art on the pertinent literature on radar remote sensing of soils, the semi-empirical models of OH *et al*. (1992) and of DUBOIS *et al*. (1995) were selected to analyse the problems of surface parameter estimation and to provide an accuracy assessment. The insufficiency of either model for dealing primarily with depolarisation effects caused by rough surfaces and/or vegetation covers plus S/N degradation, dictated the search for other more effective correction models and methods. Utilising recent advances of SAR polarimetry, the target matrix decomposition concepts of CLOUDE (1986), CLOUDE & POTTIER (1996, 1997) and of FREEMAN & DURDEN (1998) were chosen first; and then the polarimetric DEM extraction method of SCHULER *et al*. (1999), POTTIER *et al*. (1999) and of LEE *et al*. (2000) for dealing with these two major problems. Although partially effective, the corrections were still not satisfactory for expanding the validity range of the two semi-empirical models. Whereupon an alternate new model, based on the Bragg-Model (BORGEAUD & NOLL 1994, MATTIA *et al*. 1997), was formulated. This new *Extended Bragg-Model* was chosen for extensive further testing. The complete detailed formulations of the various subtasks of this dissertation study are outlined in the introductions to the associated chapters as summarised below.

In *Chapter 2*, the two most essential surface parameters, the *soil moisture content* and the *surface roughness* are introduced in order to define, describe and to present the classical methods to measure them. The description of the used test sites, the Elbe-Auen and the Weiherbach region, and the performed ground measurements are summarised in *Chapter 3*. Simultaneously to the ground measurement campaigns an airborne E-SAR flight campaign has been performed over the two test sites, the Elbe-Auen and the Weiherbach region, with the implementation of fully polarimetric (scattering matrix) L-band (λ = 23 cm) SAR. In *Chapter 4*, the basic principles of synthetic aperture radar and their imaging geometry are introduced, which will be of relevance later on for this study in order to understand the impact of topography on the quantitative estimation of surface parameters. As mentioned before, polarimetry plays an important role in the quantitative estimation of surface parameters from surface scattering models. Therefore, the basic wave and scattering polarimetric concepts are presented in *Chapter 5*. In *Chapter 6*, a critical review of three surface scattering inversion models, the small perturbation model (SPM) and two semi-empirical models addressed by OH *et al*. (1992) and DUBOIS *et al*. (1995) are given respectively, for estimating soil moisture and surface roughness from polarimetric SAR data. These models are chosen in order to provide an overview of the evolution of ideas and techniques in the area of quantitative surface parameter estimation. In *Chapter 7*, the potential of polarimetric techniques recently developed in different application areas is investigated with regards to their suitability to improve the performance of the introduced inversion algorithms. In the first part, the potential of polarimetric decomposition techniques to reduce the disturbing influence of secondary scattering processes is discussed. In the second part, the potential to estimate terrain slopes from fully polarimetric data is investigated and discussed as an attractive alternative to the standard method of using a-priori terrain information. A new alternate model for the inversion of surface parameters from polarimetric SAR image data takes is introduced in *Chapter 8*. The main advantages and disadvantages of this extended Bragg model are discussed. Finally,

Chapter 9 summarises the obtained results, and draws conclusions from a concise and comprehensive comparative analysis of the pertinent methods addressed in this dissertation research study. Thereupon, utilising the findings, it provides perspectives for future investigations utilising novel results of advancing polarimetric SAR interferometry (CLOUDE & PAPATHANASSIOU 1998, PAPATHANASSIOU 1999) and tomography (REIGBER & MOREIRA 2000, REIGBER 2001).

1.3 References to Chapter 1

ALVAREZ-PEREZ, J. L., 'Two novel studies of electromagnetic scattering in random media in the context of radar remote sensing', PhD thesis, Nottingham, in print, 2001.

ANTOKOL'SKII, M. L., Reflection of waves from a perfectly reflecting rough surface, DAN SSSR, vol. 62, pp. 203-206, 1948.

BASS, F. G. & FUKS, I. M., 'Wave Scattering from Statistically Rough Surfaces', *International Series in Natural Philosophy*, vol. 93, p. 525, 1979.

BECKMANN, P. & SPIZZICHINO A., 'The Scattering of Electromagnetic Waves from Rough Surfaces', Oxford: Pergamon, Reprinted 1978 by Artech House Inc., Norwood, Massachusetts, USA, p. 503, 1963.

BEVEN, K. J., 'Linking parameters across scales: subgrid parameterisations and scale dependent hydrological models', in Kalma, J. D. & Sivapalan, M. (eds*) Scale Issues in Hydrological Modelling*, Chichester: Wiley, pp. 263-282, 1995.

BOERNER, W.-M. *et al.*, 'Polarimetry in Radar Remote Sensing: Basic and Applied Concepts', Chapter 5 in F. M. Henderson and A.J. Lewis (ed.), 'Principles and Applications of Imaging Radar', vol. 2 of Manual of Remote Sensing, (ed. R. A. Reyerson), Third Edition, John Willey & Sons, New York, 1998.

BORGEAUD, M., S. V. NGHIEM, R. T. SHIN & AND J. A. KONG, 'Theoretical Models for Polarimetric Microwave Remote Sensing of Earth Terrain*, Journal of Electromagnetic Waves and Applications*, vol. 3, no.1,pp. 61-81, 1989.

BREKHOVSKIH, L. M., 'Radio wave diffraction by a rough surface', DAN SSSR, vol. 79, no. 4, pp. 585-588, 1951.

CLOUDE, S. R., 'Polarimetry: The Characterisation of Polarimetric Effects in EM Scattering', PhD. Thesis, University of Birmingham, Faculty of Engineering, UK, October 1986

CLOUDE, S. R. & K. PAPATHANASSIOU, "Polarimetric SAR Interferometry", *IEEE Transactions on Geoscience and Remote Sensing*, vol. 36, pp. 1551-1565, Sep. 1998

CLOUDE, S. R. & POTTIER, E., 'An Entropy Based Classification Scheme for Land Applications of Polarimetric SAR', *IEEE Transactions on Geoscience and Remote Sensing*, vol. 35, no. 1, pp. 68-78, 1997.

CLOUDE, S. R. & POTTIER, E., 'A Review of Target Decomposition Theorems in Radar Polarimetry', *IEEE Transactions on Geoscience and Remote Sensing*, vol. 34, no. 2, pp. 498–518, 1996.

CHEN, K.S., WU, T.D., TSAY, M.K. &FUNG, A. K., 'A Note on the Multiple Scattering in an IEM Model', *IEEE Transactions on Geoscience and Remote Sensing ,*vol. 38 , no. 1, pp. 249-256, 2000.

DAVIES, H., 'The Reflection of electromagnetic waves from a rough surface', *Proceedings of IEEE*, Pt. 4, vol. 101, no. 7, pp. 209-214, 1954.

DE LOOR, G. B., HOOGEBOOM, P. & ATTEMA, E. P. W., 'The Dutch Rove Program', *IEEE Transactions on Geoscience and Remote Sensing*, vol. 20, no. 1, pp. 3-11, 1982.

DOBSON, M. C., ULABY, F. T., EL-RAYES, M. & HALLIKAINEN, M. T., 'Microwave dielectric behaviour of wet soil. Part II: Dielectric mixing models', *IEEE Transactions on Geoscience and Remote Sensing*, vol. 23, pp. 35-46, 1985.

DOOGE, J. C. I., 'Hydrology in perspective', *Hydrological Sciences Journal*, vol. 33, pp. 61-85, 1988.

DUBOIS, P. C. VAN ZYL, J. J. & ENGMAN, T., 'Measuring Soil Moisture with Imaging Radars', *IEEE Transactions on Geoscience and Remote Sensing*, vol. 33, no. 4, pp. 916-926, 1995

ELFOUHAILY, T., THOMPSON D. R., FREUND, D. E. VANDERMARK, D. & CHAPRON, B., 'A new bistatic model for electromagnetic scattering from perfectly conducting random surfaces: numerical evaluation and comparison with SPM', *Waves in Random Media*, vol. 11, pp. 33-43, 2001

FEINBERG, E. L., Radio wave propagation along a real surface, J. Phys. USSR, vol. 8, pp. 317-330, 1944, vol. 9, pp. 1-6, 1945 and vol. 10, pp. 410-418, 1946

FERRO-FAMIL, L., 'Teledetection Multi-Frequentielle et Multi-Temporelle D'Environnements Naturels a Partir de Donnes SAR Polarimetriques', *Doctoral Thesis from the University of Nantes*, France, no. 0366, pp. 220, 2000.

FUNG, A. K., LI, Z. & CHEN, K. S., 'Backscattering from a randomly rough surface', *IEEE Transactions on Geocience and Remote Sensing*, vol. 30, no. 2, pp. 356-369, 1992.

FUNG, A. K., 'Microwave Scattering and Emission Models and their Applications', Arctech House Norwood USA, p. 573, 1994.

GALLAGHER, R. B., FISCHMAN, J. & HINES, P. J., 'Big questions for a small planet', *Science*, vol. 269, p. 283, 1995.

HSIEH, C-Y., FUNG, A. K., NESTI, G., SIEBER, A. J. & COPPO, P., 'A further study of the IEM surface scattering model', *IEEE Transactions on Geoscience and Remote Sensing*, vol. 35, no. 4, 901-909, 1997

ISAKOVICH, M. A., 'Wave scattering from a statistically rough surface', Otchet FIAN SSSR, Akustich. Lab., 1953, Trudy Akust. in-ta AN SSSR, no. V, pp. 152-251, 1969.

ISHIMARU, A., 'Wave Propagation and Scattering in Random Media: Single Scattering and Transport Theory', vol. I, 'Multiple Scattering, Turbulence, Rough Surfaces and Remote Sensing', New York: Academic Press, 1978.

KLEMES, V., 'A hydrological Perspective', *Journal of Hydrology*, vol. 100, pp. 3 – 28, 1988.

LEE, J. S., D. L. SCHULER & T. L. AINSWORTH, 'Polarimetric SAR Data Compensation for Terrain Azimuth Slope Variation', *IEEE Transactions on Geoscience and Remote Sensing*, vol. 38, no. 5, part I, pp. 2153-2163, 2000.

MANDEL'SHAM, L. I., 'Irregularities in a free liquid surface', *Poln. sobr. trudov* (collected works), vol. 1, pp. 246-260, 1948, first pub. as 'Über die Rauhigkeit freier Flüssigkeitsoberflächen', *Ann. Physik*, vol. 41, no. 8, pp. 609-624, 1913.

MATTIA, F., LE TOAN, T., SOUYRIS, J. C., DE CAROLIS, G., FLOURY, N., POSA, F. & PASQUARIELLO, G., 'The Effect of Surface Roughness on Multi-Frequency Polarimetric SAR data', *IEEE Transactions on Geoscience and Remote Sensing*, vol. 35, no. 4, pp. 954-965, 1997.

MITTRA, R., POGGIO, A. J. & MILLER, E. K., 'Integral Equation Solution of three dimensional scattering problems', *Computer Techniques for Electromagnetics*, Pergamon, 1973.

OGILVY, J. A. & FOSTER, J. R., 'Rough surfaces: Gaussian or exponential statistics', *Phys. Rev. D: Appl. Phys.,* vol. 22, pp. 1243-1251, 1989.

OH, Y., SARABANDI, K. & ULABY, F. T., 'An Empirical Model and an Inversion Technique for Radar Scattering from Bare Soil Surfaces', *IEEE Transactions on Geoscience and Remote Sensing*, vol.30, no. 2, pp. 370-381, 1992.

PAPATHANASSIOU, K. P., *"Polarimetric SAR Interferometry", Dr.-Tech. Thesis,* TU Graz, 1999 February 25, DLR-FB 99-07, 1999

PAPATHANASSIOU, K. P., CLOUDE, S. R. & REIGBER, A., 'Estimation of Vegetation Parameters using Polarimetric SAR Interferometry, Part I and Part II', *Proceedings of CEOS SAR Workshop 1999*, CNES, Toulouse, France, 26-29 October 1999.

POTTIER, E., SCHULER, D. L., LEE, J.-S., & AINSWORTH, T. L., 'Estimation of the Terrain Surface Azimuthal/Range Slopes Using Polarimetric Decomposition of Polsar Data', Proceeding IGARSS'1999, Hamburg, pp. 2212-2214, 1999

RAYLEIGH, LORD, 'The Theory of Sound', Scientific Papers, vol. 6 in 3, New York: Dover, 1964, first edition 1877.

RICE, S. O., 'Reflection of electromagnetic waves from slightly rough surfaces', *Comm. Pure Appl. Math.*, vol. 4, no. 2/3, pp. 351-378, 1951.

REIGBER, A.; "Airborne SAR Tomography", Dissertation for degree of Dr.-Ing., University of Stuttgart, Germany, September 2001

REIGBER, A.; MOREIRA A, *"First demonstration of airborne SAR tomography using multibaseline L-band data"*, IEEE Transactions on Geoscience and Remote Sensing, Volume: 38 Issue: 5 Part: 1, Sept. 2000, Page(s): 2142 -2152

RIQUIER, J., 'A world assessment of soil degradation', *Nature and Resources*, vol. 18, pp. 18-21, 1982.

RODDA, J. C., 'Guessing or assessing the world's water resources', *Journal of the Institute of Water and Environmental Managers*, vol. 9, pp. 360-368, 1995.

SANCER, M. I., 'An Analysis of the Vector Kirchhoff Equations and the Associated Boundary Line Charge', *Radio Science*, vol. 3, pp. 141-144, 1968.

SCHULER, D. AINSWORTH, T., LEE, J. S. & DE GRANDI, G., 'Topographic Mapping Using Polarimetric SAR data', *International Journal of Remote Sensing*, vol. 34, no. 5, pp. 1266-1277, 1998

SHI, J., WANG, J., HSU, A. Y., O'NEILL, P. E. & ENGMAN, E., 'Estimation of Bare Surface Soil Moisture and Surface Roughness Parameters Using L-band SAR Image Data', *IEEE Transactions on Geoscience and Remote Sensing*, vol. 35, no. 5, pp. 1254-1264, 1997.

SILVER, S., 'Microwave Antenna Theory and Design', McGraw-Hill Book Company, New York, 1947.

TROCH, P. A., MANCINI, M., PANICONI, C. & WOOD, E. F., 'Evaluation of a distributed catchment scale water balance model', *Water Resources Research*, vol. 29, no. 6, pp. 1805-1817,1993.

TURNER, M.G., 'Spatial and temporal analysis of landscape patterns', *Landscape Ecology*, vol. 4, pp. 21-30, 1990.

ULABY, F, MOORE, R., & FUNG, A., 'Microwave Remote Sensing: Active and Passive I – III', Addison-Wesley Publication, pp. 2162, 1981-1986.

WANG, J. R. & SCHMUGGE, T. J., 'An empirical model for the complex dielectric permittivity of soil as a function of water content', *IEEE Transactions on Geoscience and Remote Sensing*, vol. 18, pp. 288-295, 1980.

WEVER, T. & HENKEL, J., 'Assessment of MAC-Europe AIRSAR data for soil moisture retrieval. MAC-Europe'91', *Final Results Workshop*, 4-6 October, Lenggries, Germany, ESA-WPP-88, pp. 83-88, 1995.

WILBY, R. L. & SCHIMMEL, D. S., 'Eco-Hydrology. Plants and Water in Terrestrial and Aquatic Environments', Routledge, 1999, p.402.

Chapter 2

Soil Surface Parameters

The purpose of this chapter is to outline the main parameters that characterise the dielectric and geometric behaviour of natural soil surfaces, to review briefly the physical and chemical processes, which influence them and to introduce the parameters used for their description and parameterisation, and finally to describe why they need to be measured.

2.1 Soil Water Content

The relatively thin mantel of soil over the land surface of the earth is a porous material of widely varying properties. Its solid phase consists of the inorganic products of weathered rock or transported material together with the organic products of the flora and fauna that inhabit soil. Hence, time, parent material, climate, vegetation, and topography are all relevant parameters to determine the properties of soil.

Soil can be seen as a three phase system of *solid particles*, *soil water* and *soil air* within spatial and time variations of the soil matrix. Soil particles are classified according to the grain size into sand, silt and clay in the descending order. The soil water in the soil matrix represents the porosity part and consists of a portion V_g / V_t (volume of gas/bulk volume of a quantity of soil) occupied by soil air and another V_l / V_t (volume of liquid/total volume of a quantity of soil) occupied by soil water. The amount of water in soil is expressed in

water content, volume fraction	$R = V_l / V_t$	(2.1)
water content, mass basis	$R_m = m_v / m_s$	(2.2)
degree of saturation	$S = V_l / (V_l + V_g)$	(2.3)

Combining Eq. (2.1) and Eq. (2.2), the following relation is obtained for converting from the mass basis to the volume fraction, which is generally more useful in field studies:

$$R_v = R_m \rho_b / \rho_w \qquad (2.4)$$

In Eq. (2.4) it is assumed that the density of water is unaffected by being adsorbed in soil so that m_v / V_l is equal to ρ_w, the density of pure free water. The volume fraction, R, is equivalent to a depth fraction representing the ratio of the depth of water to the depth of the soil profile that contains it. This form is used when examining gains and loses of water in the field, because precipitation and evaporation are also expressed as depth of waters.

Water content as a volume fraction ranges from zero at oven dryness to a value at pore space saturation. For agronomic and hydrological purposes, two intermediate stages are commonly recognised during the drying of wet soil. The wetter of these is the field capacity, which is the water content found when a thoroughly wetted soil has drained for about two days. It is determined in the field under conditions that prevent evaporation and allow good drainage. The drier stage, the permanent wilting point, is the water content found when test plants growing on the soil wilt and do not recover if their leaves are kept in a humid atmosphere overnight. Field capacity and the wilting point are used for marking the upper and lower levels of the water of the soil on which water is ordinarily available for plants. As experiments with nonorganic soils show, they both tend to increase with increasing clay in the soil. It could be also shown that at field capacity the degree of saturation of the sandy soil is much lower than that of the clayey soil. This is due to a larger amount of pore space in the sandy soil, which is made up of relatively large pores that drain readily. The conclusion is that the size distribution of pores influences water retention, water movement and aeration, and hence, is often more important than the size distribution of particles (SCHEFER & SCHACHTSCHABEL 1992).

2.1.1 Soil Water Retention

Soil water is held within the soil matrix by absorption at surfaces of particles and capillaries in the pores. The surface absorption is influenced by the specific surface area and its exchangeable cations. Clay particles in particular are able to adsorb water actively and swelling can occur actively. Surfaces of quartz grains are not so reactive and only limited surface absorption can occur in a bed of sand. However, water can be drawn into the pores between the grains by capillaries. It is not always possible to distinguish which of these two mechanisms, surface or capillary absorption, controls water retention. The relation between water content R, and suction S, is a basic property of a soil that is important enough to warrant the special name moisture characteristic or sometimes denoted as water-retention curve. Examples of curves $R(S)$ for three soils drying from saturation are given in Fig. 2.1. They show that sandy soils release more of their water at low suctions than clayey soils do. Furthermore, a sandy medium of fairly uniform particle size releases most of its water over a small range of suction. Commonly, suctions of 1 and 150 m are selected as useful reference points on the curve corresponding in an approximate way to the water content at field capacity and at the permanent wilting point, respectively, in many soils. However, they differ physically from these in being well-defined equilibrium values. The amount of water held by a soil at a given suction is influenced by a number of properties of the soil including its texture, structure, organic content, and the nature of its clay minerals. Regression equations have been established to show the effect of these properties on water content at various suctions. GUPTA and LARSON (1979) have tabulated regression coefficients for predicting water content from the sand, silt, clay, and organic matter contents, and bulk density of each of several suctions. Hence, the moisture characteristics of a soil can be estimated if these properties are known. An obstacle to

these methods is that pore space geometry is not well represented in the criteria used. Clay and organic content and area of surface relate well to surface absorption but the size distribution of pores, which greatly affects water retention by capillary absorption, is inadequately represented and can be in fact obtained from the moisture characteristic itself (MARSHALL 1999).
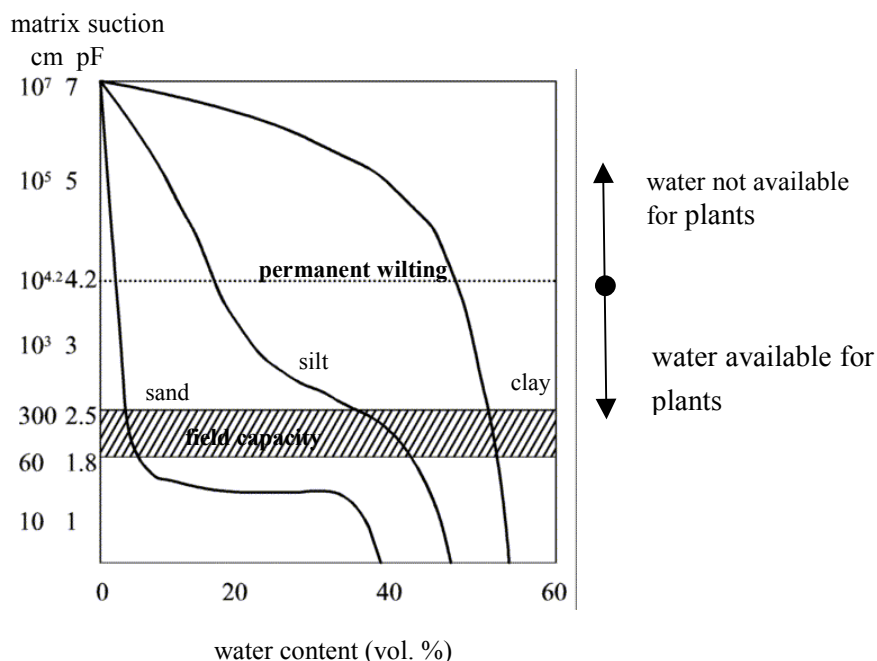
Fig. 2.1: The relation between water content and suction for a sand, a silt and a loamy soil
(SCHEFFER & SCHACHTSCHABEL 1994)

2.1.2 Properties of Water

Even if it is not easy to clearly separate mechanisms, which are responsible for attracting water to the soil, the nature of each of these mechanisms influence the way soil behaves. For example, water attracted by reactive clay minerals will cause a swelling of the soil but on the other hand when water is attracted by capillaries into the pores of a sandy soil no swelling occurs. Therefore, it is necessary to consider the interaction between water and soil, and also the properties of water itself that affects this interaction.

Water has unusual properties and behaviour compared to other fluids, mainly because of its strongly polarised molecular structure. The single electron of each hydrogen atom is involved in bounding it to the oxygen atom, thus leaving a positive charge on both hydrogen atoms. Since the two hydrogen atoms are arranged towards one side of the oxygen atom. The water acts as an electrical dipole with a positive pole due to hydrogen atoms and a negative pole due to the oxygen atom. Furthermore, one molecule of water can link up with another through hydrogen bounding thus allowing some degree of association between molecules in liquid water. HORNE (1968), in a review study on the structure of water, cities as one example the

effect of hydrostatic pressure upon the viscosity of a liquid should increase with pressure. However, in water it first decreases and only after applying sufficient pressure it reaches about 100 MPA. This is explained by considering that the cluster of hydrogen-bonded molecules are progressively eliminated by increasing the pressure until the water behaves like a normal liquid. Among the many unusual properties of water two are of special importance in soil physics, its high surface tension and its heat capacity.
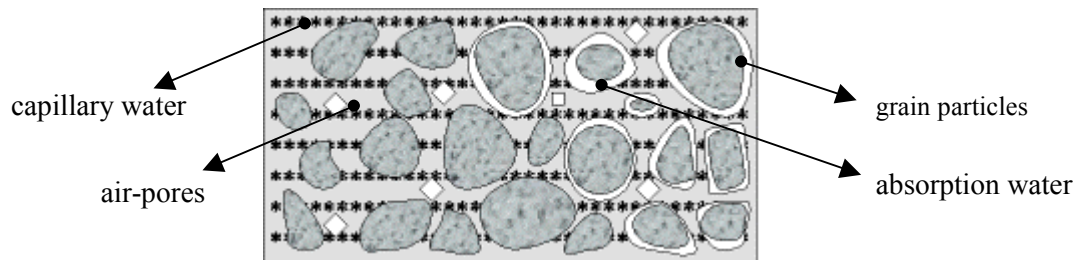
Fig. 2.2: Top view of existing soil water forces in the unsaturated zone

Because the centres of positive and negative charges inside the water molecules are separated, water molecules are attracted and oriented by the electrostatic field of a charged ion and this results in the hydration of solute ions. As evidence of the rearrangement of water molecules that accompanies hydration, there is commonly a reduction in the overall volume, known as electrostriction, when salt is added to water. Hydration of ions can occur in soil too, when polarised water molecules interact with the exchangeable cations, which is a major mechanism in water absorption at the first stage of soil wetting. Other possible mechanisms of absorption at this first stage are intermolecular attractions between the solid surface and water over a short range due to van der Waals forces, and second hydrogen bounding of water molecules to oxygen atoms on the solid surface. LOW & WHITE (1970) consider that hydrogen bounding gives rise to a partially bounded network of water molecules originating at the oxygen atoms of the mineral surface and extending outward with decreasing effectiveness for a distance of 5 nm or more. However, the existence of any long-range structure in water at interfaces is debatable in the literature (CONWAY 1977).

In the following, the main physical and chemical properties of the soil matrix and the way they are influenced by the presence of water will be described. This is important in order to understand the relation between soil moisture content and the dielectric properties of the soil matrix.

2.1.3 Complex Dielectric Constant

The phenomenon by which that non-conducting materials can also be influenced from electrical fields was first observed by M. Faraday, who named them dielectrica. The key parameter that describes the behaviour of a non-conductor in an electrical field is the complex dielectric constant, which is dependent on numerous parameters, such as frequency, temperature, salinity and ferromagnetic substances. Charged particles, under the impact of an external electrical field, are getting out of balance, while the free electrons of a conductor move until the electrical field inside the conductor vanishes. This only partially happens in dieletrica, where the free charges are moving till the back force in the solid body equalises the force affected by the external electrical field. Since, positive and negative particles are contrarily linked, they form electric dipoles. This process is also called dielectric polarisation (MARSHALL *et al*. 1999). Two main mechanisms can be distinguished, deformation and orientation polarisation, which are responsible for the polarisation of dielectrica. During the orientation of the dipole the energy of a dielectrica is stored. One part of this energy is stored as thermal and the other part is lost due to the internal friction. The dielectrica of a material thus define the amount of electric energy, which can be stored, adsorbed and lead through the medium.

In the electromagnetic wave theory, the real component of the complex dielectric constant is described as refraction or reflection of a wave at the interface between two different media (Snellius Law). The refraction index is a function of the incident angle and the velocity of the transmitted wave, which is related to the refractive angle and the velocity of propagation in the boundary layer of the wave. The refraction index is defined as the square root of the complex dielectric constant of the denser medium and is a dielectric constant, if related to the vacuum or the air. The complex dielectric constant is a measure of the medium response to an electromagnetic wave. This response is composed of two parts, the real and the imaginary (STRATTON 1941, VON HIPPEL 1954*)*, where the complex dielectric constant is given by

$$\varepsilon = \varepsilon' - j\varepsilon'' \tag{2.5}$$

where ε' is referred to the permittivity of the material, whereas ε'' is referred to the dielectric loss factor of the material and describes the feasibility of a medium to adsorb a wave and to transform its energy into another form. Throughout this dissertation write-up ε' will refers to the average relative dielectric constant of the material. For most natural surfaces $\varepsilon'' << \varepsilon'$ (VON HIPPEL 1954*)*.

The attenuation length of electrical field in a given medium is characterised by the imaginary part of its complex dielectric constant. Under the assumption that a propagating wave has exponential attenuation with depth, the penetration depth δp of the wave into the medium is known as the skin depth and is given by (ULABY *et al*. 1986, SCHANDA 1986):

$$\delta_p = \frac{\lambda \sqrt{\varepsilon'}}{2\pi\varepsilon''} \qquad (2.6)$$

The penetration depth of a slightly lossy medium δp is per definition about 1/e (e = Euler's Number $\approx$ 2.7183) of the input value attenuated (SCHANDA 1986). From Eq. (2.6) follows that at longer wavelengths, the penetration depth increases, while at the same time for a fixed wavelength the penetration depth into a medium in general increases with decreasing dielectric constant.

The dielectric constant of most dielectric natural media is between 1 and 6, and increases with increasing water content. Finally, free liquid water (ULABY 1986) has a dielectric constant up to 81 towards low frequencies. This is the reason for the very high sensitivity of microwaves to the moisture contained in the observed bodies, depending on the molecules rotation, e.g. freezing, tight binding to a soil particle, etc., which therefore reduces the ε of water.

The behaviour of ε in homogeneous media, such as pure water and ice, are fairly well understood. The frequency dependency of the dielectric constant of pure water is given by the well-known Debye (1929) equation

$$\varepsilon_w = \varepsilon_{w\infty} + \frac{\varepsilon_{w0} - \varepsilon_{w\infty}}{1 + j2\pi f\tau_w} \qquad (2.7)$$

where ε_{w0} is a static dielectric constant of pure water and $\varepsilon_{w\infty}$ presents a high-frequency (or optical) limit of ε_w, both formulations are dimensionless. τ_w is the relaxation time of pure water measured in seconds and f the electromagnetic frequency given in Hz (VON HIPPEL 1954).

In case of a dry soil, the real part of the dielectric constant ε', varies over the range between two and four; representative values for the imaginary part ε'' lie below 0.05 (ULABY 1986). Since the first water added to dry soil is tightly bound to the surface of the soil particles, it will cause only a small increase of the soil's ε. As more water is added, above the transition value of moisture, the soil's ε rapidly increases due to the behaviour of water molecules as described in Section 2.1.2. Because the matrix forces, acting on water molecules, decrease rapidly with increasing distance from the soil surface, the water molecules located several layers away from the soil particles are able to move free within the soil (SCHMUGGE 1980).

Many empirical and theoretical models have been suggested in the literature to relate the dielectric constant of the mixture to that of its constituents. An extensive investigation in the frequency range between 1.4 and 18 GHz can be found in VON HIPPEL (1954) and in HALLIKAINEN *et al*. (1985). The behaviour of the experimental measurements have been summarised by polynomial expressions dependent on the volumetric soil water content and the percentage of sand and clay contained in the soil. However, the soil particles have been classified according to USGS (United States Geological Survey) and are, therefore not directly

transferable to the European soil classification system. To eliminate the dependence upon adjustable parameters, DOBSON *et al*. (1985) developed a physical soil model that depends only on measurable soil characteristics and does not require adjustable parameters to fit the experimentally measured data. The model is based on two parameters: the bound water fraction and the free water fraction, according to the pore-size distribution calculated from the particle-size distribution. Studies from TOPP *et al*. (1980), DE LOOR (1982), SHIVOLA (1989) and STACHEDER (1996) on the permittivity of dielectric mixtures indicate that for a frequency range of 1 to 10 GHz a two component refractive index formula which considers only the volumetric fraction of dry matter and free water is a sufficient good working approach for most soil types. Based on these conclusions, in this study, the developed polynomial relation by TOPP *et al*. (1980) of the third order was used for the conversion from the volumetric soil water content m_v to the real part of the dielectric constant ε', and vice versa (see Section. 2.1.5.2). Measurements and evaluation of the imaginary part ε'' of the complex dielectric constant are not considered in this study because of its almost negligible influence on the total amount of ε.

2.1.4 Soil Water Measurement

Methods for measuring the mass of the soil water have been already applied in the 15th Century. Today the most common method for measuring soil moisture is with regard to the mass, volume or saturation of the soil. At this phase of development, it should be mentioned that the measurements of soil moisture content is on the one hand one of the most inaccurate methods in principle, but on the other hand one of the relatively accurate ones in soil physics. The definition of the material state at which the soil can be labelled as dry poses the main problem (GARDNER 1986).

There is a large number of methods available to measure directly and indirect the soil moisture content as described in the literature (STACHEDER 1996, PRIETZSCH 1998, MARSHALL 1999). In principle, direct and indirect methods to measure the soil moisture content can be distinguished. The direct methods include all measured processes in which the soil water is removed with evaporation, extraction, or chemical reactions. The indirect methods use the functional relations existing between the physical or chemical properties of the soil matrix and the moisture of the soil. In this study two methods were used, the gravimetric method, which is a direct method, and time domain reflectometry, as indirect approach. Both of them are described in the following.

2.1.4.1 Gravimetric Method

The most usual direct method to evaluate the water content of a soil sample is to estimate the mass difference before and after drying it in an oven at 150° C until a constant mass is reached.

The mass difference m_v corresponds to the water loss of the sample during the drying process. However, the endpoint of the drying processes does not correspond to a completely water-free sample, but to a balanced state between vapour pressure of the material and water vapour partial pressure in the drying region. From this point of view the state for which the material is called dry, is a subjective term. The water content on a mass basis is described in Eq. (2.2).

The unit of the gravimetric water content is [g/g] and expresses the weight in percent after multiplication with 100 of the soil water [weight %]. If the soil water content is expressed in volumetric percent [vol. %], the bulk density of the soil has to be taken into account. For these, the soil samples are taken with a predefined volume. The water content as a volume fraction R, is obtained from R_m by means of Eq. (2.4), where ρ_b is the dry bulk density of the soil, and ρ_w is the density of the water, which for most applications is expressed as [vol. %] or 1 Mgm^{-3}.
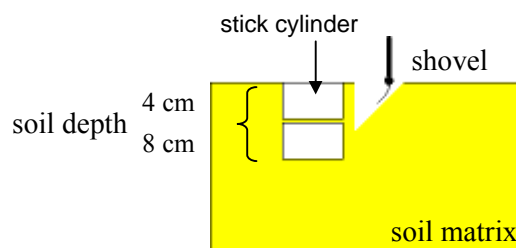
Fig. 2.3: Stick cylinder scheme

This procedure was introduced by GRADNER (1986). Despite arbitrary features of the method, it is the standard with which other estimations of soil moisture content are compared. A disadvantage of the method is that the sampling of experimental areas interferes with continuing experiments. When holes are bored and roots are cut, infiltration and drainage behaviour are effected. A large number of samples may be required because water can be distributed unevenly in the field due to the effect of soil texture and/or structure variability on its retention and movement. Additionally, the method is very time- and work-consuming. Since the amount of water lost, increases with the drying temperature in any inhomogeneous soils that contain clay or organic matter, the oven temperature must be controlled within a range about 100 – 110°C. A variation of about 10 per cent or more has been found in field samples in several experiments as quoted by HOLMES *et al*. (1967). If one consider also the water lost due to evaporation, with a rate of 1-4 mm day $^{-1}$, then the variability of soil makes the moisture sampling approach unattractive.

2.1.4.2 Time Domain Reflectometry

The principle of time domain reflectometry is the measurement of the capacitance of the soil matrix, which depends on the water content of the surrounding medium. The electric capacitance in between two conductors, with the length of 15 cm, placed in the soil depends upon the water content of the soil because the dielectric constant of water (ε' $\approx$ 80) is much

larger than that of the dry soil ($\varepsilon' \approx 5$) or the air ($\varepsilon' \approx 1$), which replaces the water as the soil dries. The technique of time domain reflectometry (TDR) circumvents a direct capacitance measurement and is valid for a wide range of soil types (sand and silt). The geometric arrangement for the insertion into the soil is a parallel, two-electrode configuration with the spacing between the insertion rods, that form the transmission line, is 50 mm. Their length determines the depth in the soil to which the pulse is conducted and the result is effectively the volumetric fraction of water in the soil to the chosen depth.

Electric transmission line theory leads to the expression for the propagation velocity of an electromagnetic wave in a slightly long transmission line as

$$V = c[\tfrac{1}{2}\varepsilon'\{1 + (1 + \tan^2\delta)^{1/2}\}]^{-1/2} \tag{2.12}$$

where c is the speed of light, and $\tan\delta = \{\varepsilon'' + (\sigma_{dc}/\omega\varepsilon_0)\}/\varepsilon'$. The remaining symbols are explained as: ε' is the real part of the complex dielectric constant, ε'' is the imaginary part, σ_{dc} is the zero-frequency electrical conductivity of the medium, ω is the angular frequency, and ε_0 is the free-space permittivity. Measurement at a very high frequency makes $\tan\delta$ tend to zero, so that

$$V = c / (\varepsilon')^{1/2}. \tag{2.13}$$

This leads to

$$t = 2L\varepsilon^{1/2} / c \quad \text{and} \quad \varepsilon = (ct / 2L)^2. \tag{2.14} \, \text{(2.15)}$$

Here t is the time taken for the propagation of an electromagnetic pulse launched along a transmission line of length L and reflected back to the origin. The variation of the dielectric constant of soil with the water content, R, can approximately be estimated by adding the three contributions $R\varepsilon$ (water), $\phi\varepsilon$(air) and $[1 - (R + \phi)]\varepsilon$ (soil), where R is the volume fraction of water, ϕ the same for the air-filled pores, and $[1 - (R + \phi)]$ is the volume fraction of the soil. In principle, then it is to be expected that R would have a functional dependence upon ε, as determined for the soil in question. TOPP *et al*. (1980) established such a relationship to be

$$R = -a + b\varepsilon - c\varepsilon^2 + d\varepsilon^3 \tag{2.16}$$

Volumetric soil moisture content m_v

$$m_v = -5.3 \cdot 10^{-2} + 2.92 \cdot 10^{-2}\,\varepsilon' - 5.5 \cdot 10^{-4}\,\varepsilon'^2 + 4.3 \cdot 10^{-6}\,\varepsilon'^3 \tag{2.17}$$

Real part ε' of the complex dielectric constant ε

$$\varepsilon' = 3.03 + 9.3\,m_v + 146\,m_v^2 - 76.7\,m_v^3. \tag{2.18}$$

The experimental values of the variables were determined for ε by pulse travel-times, Eq. (2.15), and for R by gravimetric measurements and the use of dry bulk densities. This empirically determined third order polynomial expression for the dielectric constant is independent of type, bulk density, texture, salinity and temperature of the soil and is confirmed in several investigations (DALTON & VAN GNEUCHTEN 1986, WHALLEY 1993). Thus, up to now this function is used in several studies and is regarded as an universal calibration function even if actual investigations indicate a limited validity for all soil types valid. HERKELRATH *et al*. (1991), for example, received significantly divergent results for soils with organic matter. After intensive investigations with inorganic and organic soil types, ROTH *et al.* (1992) suggest to use two different calibration functions - for inorganic and organic soil.
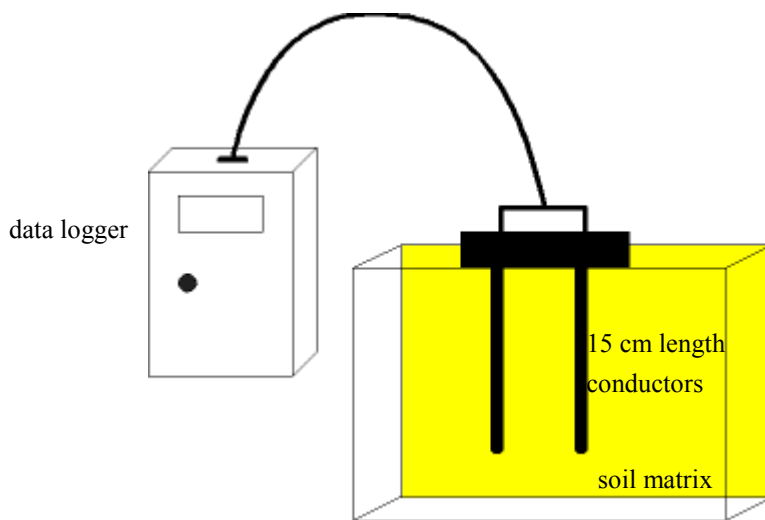
Fig. 2.4: Time domaine reflectometry scheme

The accuracy of the obtained time domain measurements is varying about of ± 1.3 [vol %]. In principle, all studies notice a slight underestimation of soil water content for clay enriched soil and for soil mixed with high organic matter. Some authors explained this phenomenon with dielectric properties of bounded water (DOBSON 1985, HALLIKAINEN 1985). Minerals and swelling clay have a high surface tension and are for this reason able to adsorb a high amount of water. Hydration of the exchangeable cations is largely responsible for this absorption and for the accompanying increase in the interlayer spacing. As consequence of this process, the minerals and clay swell macroscopically. With continuing absorption, it becomes plastic and it is further explained, as follows, by the development of a diffuse layer of ions. If the solution midway between two parallel surfaces has a higher electrolyte concentration than that of an outer solution bathing the clay, water will be attracted osmotically, and the distance between the surfaces will consequently increase. The exchangeable cations, unable to move freely out to the bathing solution, act as being retained by a semi-permeable membrane. The water dipoles are strongly bounded so that they no longer rotate or polarise. Thus, the dielectric constant of bounded water is significantly smaller than of free water and cannot anymore be measured

using time domain reflectometry. This is in contrary to the oven drying methods where the bounding forces can be dissolved in the water. Therefore, the use of an universal calibration function may lead to an underestimation of soil water content. Using an universal calibration function for the measurement of soil moisture content should be critically observed. For some soil types, especially mineral and clay rich soil, the use of a soil specific calibration function is needed.

2.2 Geometric Properties

The solid phase of soil consists of particles with various shapes and sizes, packed together in different ways. The packing may be dense or open, and the particles may behave either as heterogeneous individuals or as clusters in aggregates. The amount of pore space and size of the pores vary in a complementary way. These are all aspects of the structure of soil, which is defined as the arrangement of the solid particles and of the pore space located between them (MARSHALL 1962(a)).

The structure of soil depends on the size distribution of the primary particles and the forces affecting their arrangement. Swelling and shrinking, freezing and thawing, the water movement, the growth and decay of plant roots, and the action of earthworms and other animals can all serve in rearranging the particles. Chemical and biological processes mobilise and deposit materials that hold them together as aggregates. The resulting structure and especially the size, shape and arrangement of the aggregates is influenced by weather conditions and can lead to desegregation.

Structure itself directly affects many of the properties of soil. Water retention and conductance are dependent on pore space and pore size. It influences tillage operations because the properties of individual particles are more or less masked in stable aggregates, which can give a favourable physical condition to soil that would otherwise be intractable. It affects the environment of roots through its effects on water and oxygen supply and soil strength. Growth of plants can severely be retarded or totally prevented by structure that is grossly unfavourable to water or air movement or resistant to seedling emergence or root growth.

All these processes and descriptions of the soil structure make clear that natural surfaces always has some kind of roughness. The scale of the roughness may range from geological scales as found, for example, for mountains down to sub-nano meter scales as found, in e.g., vacuum deposition experiments. Rough surfaces can be divided into two main categories, the deterministic and the randomly rough surfaces. The first are periodic surfaces with a given profile and periodic irregularities. Historically, this class of rough surfaces was first investigated due to the simplicity of a non-statistical approach and thus enabling the simplification of the theory. Natural surfaces are categorised into the class of random rough

surfaces, which are characterised by random irregularities on the surface and are best described by the statistical distribution of their deviation from a certain mean level.

Randomly rough surfaces seen in terms of the application on bare agricultural fields are defined as the relief developed from the soil tillage without taking the straightened soil structure, as furrows and seat grooves, into account. Synonym to this term also the term micro-relief is found in the literature. In relation to the size, the genesis and the impact of the soil, four types of relief can be distinguished (RÖMKENS & WANG 1984):

- Relief size 0 - 2 mm, consisting of single particles and unequally distributed micro aggregates;
- Relief size 2 - 100 mm, consisting of large unequally distributed aggregates caused by tillage;
- Relief size 100 - 200 mm, consisting of furrows and grooves developed through systematic and equally distributed tillage;
- Relief size > 100 m, disposition formed through geological activities.

Even if the relief types are through their attributes not always clearly distinguishable, all of them have an impact on soil processes, known as soil erosion (HELMING 1992). In this study, the relief size of 2 to 100 mm over bare agricultural fields is of interest.

The influence of chemical, physical and biological processes, as well as the tillage, on the micro relief was the object of several earlier studies and is summarised in the studies of MARSHALL *et al.* (1996). Some authors have shown that with the tillage the micro-relief becomes finer (ALLMARAS *et al.* 1967). Others could verify that roots and fungal hyphae are responsible for the stable soil crumbs, pressing soil particles together as they expand during growth and ramifying the soil thoroughly, separating some parts and compressing others, drying it, and incorporating inorganic matter within it. Further, some of the products from the decomposition of roots and other organic matter by micro-organisms act as binding agents (OADES 1993, TISDALL 1994). The physical agents of cracks that separate natural aggregates are mainly caused due to the movement of the soil with shrinking and swelling. In a hypothetical model, proposed by EMERSON (1959), the microstructure of the smallest unit of soil aggregates consists of clay domains, linked to each other, and of quartz grains held together by electrostatic bounds. Furthermore, the changes of weather conditions influence the micro-relief, as for example, overland flow, rain, wind and ice. They are all involved in the processes of soil erosion.

The characterisation and categorisation of roughness on agricultural fields depends on the soil type, on the region, the time where the roughness measurements are performed, and on the seeded crop type. This makes a consistent classification of roughness over a large area, as for example over the full extent of Germany, difficult, if not truly impossible. Furthermore, different tillage methods affect the roughness of cultivated fields differently and cause varying

depths on a field. Three main tillage methods applied widely in all regions, can be discriminated, being, in order of decreasing roughness: ploughed, harrowed and seedbeded. Ploughed fields are deeply gashed in the soil crumb and often the first soil layer is turned up side down, where on harrowed fields the soil crumb is raked, and for the seedbed fields the soil crumb is flattened. For the preparation of crop seeding, the different tillage methods, ploughing, harrowing and seeding, are successively performed to enable a optimal nutriment composition for the grow of the seedlings.

2.2.1 Surface Roughness Estimation

The second important parameter besides the complex dielectric constant, which influences the scattering behaviour of natural surfaces, is roughness. In the following, surface roughness will be defined through statistical parameters and the existing methods to measure them will be addressed.

2.2.1.1 Statistic Description of Surface Roughness

Randomly rough surfaces are usually described in terms of their deviation from a smooth 'reference surface'. There are essentially two aspects describing the nature of a randomly rough surface: the spread of heights about the reference surface and the variation of these heights along the surface. A variety of equivalent statistical distributions and parameters may be used to parameterise these two surface properties. In this investigations, the parameter set of the root mean square height RMS, s and the surface correlation length, l, associated to the surface correlation function are considered the best for the parametric description of the natural surfaces. The RMS height, s, is used to describe the vertical surface roughness and is defined as the standard deviation of the surface height variation in cm,

$$RMS_{\text{height}} = s = \sqrt{\frac{\sum_{i=1}^{n}(z_i - \bar{z})^2}{n-1}} \qquad (2.19)$$

On the other hand, the surface correlation function $\rho(x)$ and the associated correlation length, l, are parameters used for the horizontal description of the surface roughness. In the discrete case, the normalised surface correlation function for a spatial displacement $x' = (j-1)\Delta x$ is given by

$$p(x') = \frac{\sum\limits_{i=1}^{N+1-j} z_i z_{j+i-1}}{\sum\limits_{i=1}^{N} z_i^2} \tag{2.20}$$

where z_{j+i-1} is a point with the spatial displacement from the point x_i (Fung 1994). The surface correlation length is defined as the displacement x' for which $\rho(x')$ between two points inhibits values smaller than 1/e (Euler's Value ≈ 2.7183)

$$p(l) = 1/e \tag{2.21}$$

Thus, the surface correlation describes the statistical independence of two points on a surface and increases with the correlation between two neighbouring points. For a smooth surface $l = \infty$.

For characterisation of a surface with two parameters, the RMS height, s, and the surface correlation length, l, describe the natural surface only as a two-dimensional stationary randomly rough surface. Both statistical parameters, s and l, are independent from each other according to the single scale roughness theory (BECKMANN & SPIZZICHINO 1963). l can be large or small for a high or low s. Experimental data acquired over natural surfaces show, that most bare soil surfaces are characterised by large spatial variations, making it difficult to determine consistent roughness parameters for modelling and inversion purposes. The most delicate point is the measurement of the correlation length, which is highly variable (MATTIA & LE TOAN 1999).

Two critical points should be mentioned here, which are controversially discussed in the literature: One is the question about how long should be the measurement distance for a accurate estimation of the surface correlation length; the second question is about the shape of the correlation function used for electromagnetic modelling.

Regarding the first question, OH & KAY (1998) demonstrated that the variability of l estimates decreases with profile length, and that a mean estimate of l with a precision of $\pm 10 \%$ requires a profile length of 200 l. Their results also illustrate that the correlation length estimates, at short profile lengths, are biased towards values smaller than the true underlying value of l, and that this bias decreases with increasing profile length. Additionally, DAVIDSON et al. (2000) observed for a short profile, of about 1 m, a correlation between s and l, which is not in accordance with the single scale roughness theory. They explained this phenomenon with the relative size of the clods associated with the different tillage states and conclude that this result provides a method of reducing the number of unknowns related to the surface roughness.

The theory of wave scattering from rough surfaces often assumes that surface correlation functions for natural surfaces have mainly two shapes, a Gaussian or an exponential

distribution function. Measurements sometimes suggest that surface correlations have an close to the origin exponential shape and change to Gaussian for points further apart (OGLIYV & FOSTER 1989).

Alternatively, to the single scale roughness description, several authors proposes multiscale roughness description. There are two main approaches: the two scale roughness models, with the small and large scale roughness (SHIN & KONG 1984, BAUDOIN *et al.* 1990) and the excessive number of investigations on random fractals approaches (KELLER *et al.* 1987, SHEPARD *et al.* 1995, MATTIA & LE TOAN 1999, DAVIDSON *et al.* 2000).

Being aware of the mentioned problems with the single scale approach, this dissertation uses the classical single scale roughness approach to describe the randomly natural rough surfaces. In particular, only the RMS height for the randomly rough surface description will be used. Due to the mentioned difficulties to estimate the surface correlation length accurately, concerning the field measurements as well as the mathematical formulation, some of the theoretical and the most empirical EM models are not considering *l*. Furthermore, some studies demonstrated that *l* has only a weak influence on the radar backscatter, about 1 dB in L- and C-bands, respectively, and can be therefore neglected (ZRIBI *et al.* 1999).

The relation of the ground measured RMS height and the surface correlation length to the EM wave are given in terms of the actual wavelength λ ($k=2\pi/\lambda$) with ks and kl. Therefore, the ks and kl are decreasing with increasing wavelength. The values for ks, for example, are ranging between 0 and 1 for the L-Band with a center wavelength of about 23 cm.

2.2.1.2 Methods for the Surface Roughness Estimation

Several methods for the estimation of the surface roughness have been developed in the last fifty years, which may be separated into two main categories: the two-dimensional and three-dimensional methods. In the dissertation of HELLMING (1992), the most common methods are very well summarised.

The first measurements for the estimation of surface roughness were made mechanically using long and thin steel needles attached on a normalised board. These vertical movable needles are mapping the relief of the ground, which are presented on a scale grid attached on the board (KUIPERS 1957, BURWELL *et al.* 1963). The distance of the needles was initially varying between 50 to 100 mm. This technique has been improved in order to increase its measurement and operational efficiency. The distance between the needles was reduced down to 5 mm to increase the estimation accuracy, while on the other hand, the digitalisation of photographs from the needle positions or recording the distance of the vertical movement with a potentialmeter was performed to decrease the evaluation time (CURRENCE & LOVELY 1971).

The main advantage of these needle board profilometer techniques is the simple handling and the readily obtained overview of the impact of tillage to the soil surface. The main disadvantage of this technique lies in the disturbance of the soil surface by the needles, preventing the repetition of the measurements. Beyond this, the low spatial resolution, with 5 mm point measurement distance and a vertical resolution of > 1 mm appealed not sufficient for detailed relief investigations. Especially critical is the technical limitation of the length of needle profilometers up to 1.5 m, a fact that makes surface correlation length estimations imprecise.

In the last years, several new methods were developed for measuring surface roughness with high resolution, untouchable and fast. These methods are using optical sensors and are based on photogrammetry or triangulation. The method of photogrammetry consist in transmitting light and measuring its reflection from the surface. These measurement acquisition is fast but the processing of the recorded images and the generation of digital surface elevation models requires a time consuming manual processing (JESCHCKE 1990). Another disadvantage of this method is the disturbing influence of surrounding light as well as the influence of the colour and the moisture content of the soil during the measurement. The laserprofiler method is more robust to surrounding influences, so that the measurements can be collected readily. The transmitted laser pulses are reflected on the soil surface and are recorded with a photodiode. High sampling speed and a high spatial resolution, ranging from 1 to 5 mm with a vertical precision of ± 1.5 mm, are the main advantage of such systems, but the high cost and time effort to construct and install the system are the main disadvantages (HELMING 1992, DAVIDSON 2000). Traditional laser profilers are capable to measure only short profile lengths, from 1 up to 2 m. New generation laser profilers are capable to acquire roughness profiles up to 25 m with a very high location precision (DAVIDSON 2000). Such long profiles are necessary for an accurate estimation of the surface correlation length, and surface characterisation (periodicity, stationarity, homogeneity) while for measuring the RMS height they are of second importance.

In this study for the estimation of surface roughness the classical needle profilometer, constructed at the German Aerospace Center, Institute for Radio Technology and Radar Systems, at Oberpfaffenhofen, (DLR-OP-IHR) was chosen (HAJNSEK 1999, NEUSCH 2000). The needle board is 1.5 m long and 0.60 m high. The distances in between the needles are between 0.5 and 1 cm (see Fig. 2.5). Low cost, simple handling and sufficient spatial resolution to measure the RMS height predetermined the decision for this technique. The description of the measurement procedure is given in *Chapter 3*.
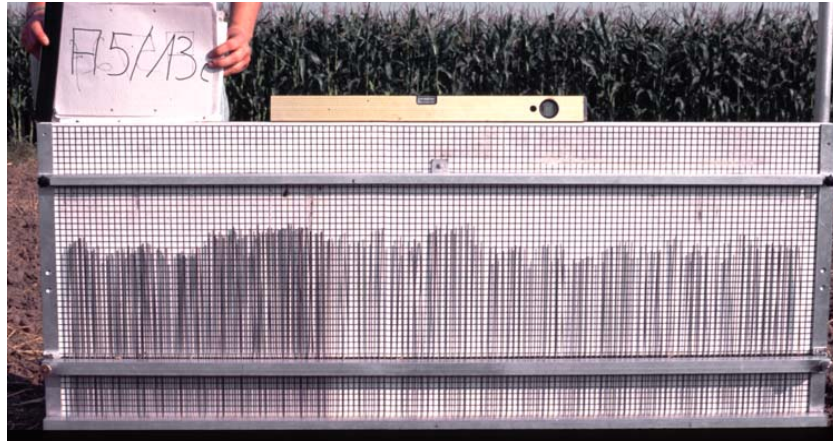
Fig. 2.5: Surface roughness profile measurements
with a needle board on a bare agricultural field.

2.2.2 Nature of Surface Scattering

Natural surfaces can be considered as rough, and the roughness is the dominant factor for the scattering behaviour of an EM wave. The roughness of any scattering surfaces is not an intrinsic property of that surface but depends on the properties of a wave being transmitted. Both, the frequency and the local angle of incidence of the transmitted wave, determine how rough or smooth any surface appears to be. The relation of the EM wave in terms of its wavelength λ to the statistical roughness parameter s, as described in the previous section, is given by ks. Thus with increasing wavelength, the roughness term is decreasing, consequently, the indication of relative roughness for any surfaces is depending on the wavelength as $k = 2\pi / \lambda$. Also the local incidence angle plays an important role for defining the roughness condition of a surface. In the near field of the propagating EM wave, the surface appears rougher than in the far field, which can be compared with the reflection of the sunset over the sea. (BECKMANN & SPIZZICHINO 1963).
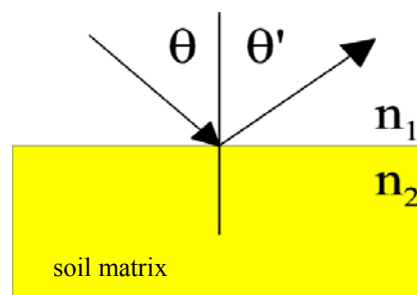
Fig. 2.6: Fresnell reflection scheme

In case of an ideal smooth surface the characteristics of the reflection can be described by the well known Fresnel Reflectivity Γ. The Fresnel Reflectivity, named after the French Engineer and Physicist Augustin Jean Fresnel (1788-1827), characterises the reflection of a transmitted wave at the interface between two dielectric media n, for example the air n_1 and a homogeneous soil n_2. The Fresnel coefficient Γ is a function of the angle of the transmitted θ and reflected wave θ', and the dielectric constant of the scatterer.

$$\Gamma_h(\theta) = \frac{\mu \cos\theta - \sqrt{\mu\varepsilon - \sin^2\theta}}{\mu \cos\theta + \sqrt{\mu\varepsilon - \sin^2\theta}} \qquad \Gamma_v(\theta) = \frac{\varepsilon \cos\theta - \sqrt{\mu\varepsilon - \sin^2\theta}}{\varepsilon \cos\theta + \sqrt{\mu\varepsilon - \sin^2\theta}} \qquad (2.22)$$

where Γ_h and Γ_v is the horizontal and vertical polarisation of the EM wave and μ is always for non-ferromagnetic media, as natural surfaces, equal to one. The response of the horizontal polarisation increases with increasing the local incidence angle. The vertical polarisation decreases to zero at a certain angle, the so called Brewster Angle - the angle under which the transmitted wave is completely absorbed by the dielectric medium - and increases then suddenly with further increase of the local incidence angle.

Considering a constant wavelength and fixed local incidence angle, the interaction of a transmitted EM wave with a surface of different roughness conditions can be in general treated as the rougher the surface, the more diffuse the scattering or the smoother the surface, the more directional the scattering. The Fresnel reflectivity, as described above, considers an ideal smooth surface boundary. In the natural environment the surface condition varies from medium to rough. The backscattered EM wave on a surface consists of two components, a reflected or coherent and a scattered or incoherent one. The coherent component reacts as a specular reflection on a smooth surface and thus in a case of a monostatic radar there is no scatter return (see Fig. 2.7). The incoherent component is a diffuse scatterer and distributes the scattering power in all directions. As the surface becomes rougher, the coherent component becomes negligible and the incoherent component consists of only diffuse scattering.
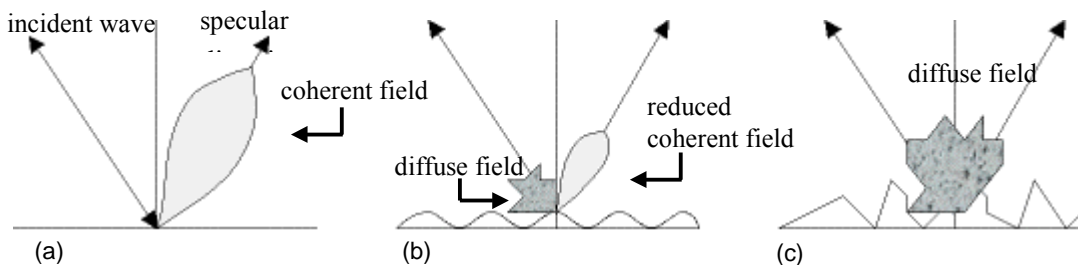
Fig. 2.7: Rates of roughness components demonstrated on a (a) smooth,
(b) rough and (c) very rough surface.

Defining a surface from an electromagnetic point of view as smooth or rough, as before mentioned, is obviously somewhat arbitrary. Nevertheless, in the literature there can be found

two main criteria to define a smooth surface, the Rayleigh and the Frauenhofer criterion, respectively. Considering a plane monochromatic wave transmitted at some angle θ onto a rough surface (see Fig. 2.8), it is a simple matter to calculate the phase difference $\Delta\phi$ between two rays scattered from separate points on the surface:

$$\Delta\phi \;=\; 2h\frac{2\pi}{\lambda}\cos\theta \tag{2.23}$$

where h is the standard deviation of the roughness height regarding to a reference height and θ the local incident angle.
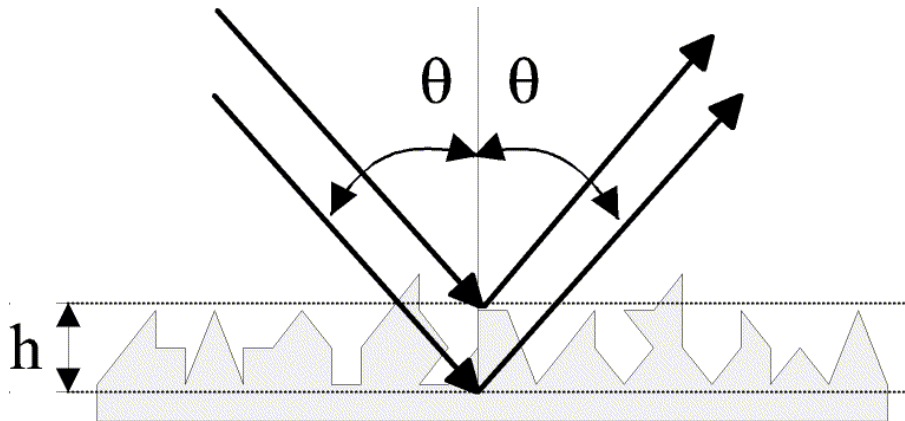
Fig. 2.8: Diagram for determining the phase difference between two parallel waves scattered from different points on a rough surface (SCHANDA 1980).

The Rayleigh criterion states that if the phase difference $\Delta\phi$ between two reflected waves is less than $\pi/2$ radians, than the surface may be considered as smooth, and is defined by Eq. (2.24)

$$h < \frac{\lambda}{8\cos\theta} \tag{2.24}$$

The usage of a more stringent criterion, which is adapted to the EM wave region, is proposed in ULABY et al. (1982) and is called Frauenhofer criterion (Eq. (2.25)). This criterion considers a surface as smooth, if the phase difference is $\Delta\phi < \pi/8$

$$h < \frac{\lambda}{32\cos\theta} \tag{2.25}$$

2.3   Synopsis

In *Chapter 2* the main soil surface parameters, namely the moisture and the surface roughness, are defined and described.

The first part deals with the mathematical formulation of the soil moisture content and its state and influence on the soil matrix. Two main mechanisms, the absorption and the capillary hold the soil water in the soil matrix. The amount of water held by the soil matrix is influenced by a number of properties including its texture. Thus, a soil with a high amount of clay particles holds more water than a soil with a high amount of sand particles. To understand the mechanisms between the water and the solid state of the soil matrix some properties of the soil water have been explained. As it is well known that EM wave propagation is sensitive to the dielectric constant, therefore the relation to the soil moisture content and the mean electric properties of the soil matrix have been presented. In this thesis, two methods are described to estimate the soil moisture content, the gravimetric and the time domain reflectometry methods.

In the second part, the geometric properties, in particular the surface roughness of bare agricultural fields, are primarily defined and classified in three main roughness categories: ploughed, harrowed and seedbeded. The statistical description of the random roughness from a single scale surface is given by the vertical, the RMS height s; and the horizontal parameter, the surface correlation length l. The relation between the ground measured parameters to the EM wave is given by the wavelength ($k=2\pi/\lambda$). Alternatively to the single scale description of a surface, several authors propose multiscale roughness descriptions; for example the two scale roughness models and the random fractal approaches. In this thesis the classical single scale roughness description of a surface is chosen and particular only the RMS height s will be used due to difficulties for estimating the surface correlation length accurately. Two types of measurement techniques for surface roughness, the two-dimensional, with a needle board, and three-dimensional, with a laser profilometer are discussed. Their advantages and disadvantages have been presented. In the last section, the variation of the EM wave scattering behaviour with roughness, smooth to rough, have been presented.

2.4　References to Chapter 2

ALLMARAS, R. R, BURWELL, R.E & R.F. HOLT, 'Plow-layer porosity surface roughness from tillage as affected by initial porosity and soil moisture at tillage time', *Soil Sci. Soc. Am. P.*, vol. 31, pp. 550-556, 1967.

BECKMANN, P. & SPIZZICHINO A., 'The scattering of electromagnetic waves from rough surfaces', Pergamon Press, p. 503, 1963.

BEAUDOIN, A. LE TOAN, T. & GWYN, Q. H. J., 'SAR observations and modelling of the C-band backscatter variability due to multi scale geometry and soil moisture', *IEEE Transactions on Geoscience and Remote Sensing*, vol. 28, no. 5, pp. 886-895, 1990.

BURWELL, R. E., ALLMARAS, R. R. & AMEMIYA, M., 'A field measurement of total porosity and surface microrelief of soils', J. of Soil Science, vol. 34, pp. 577 – 597, 1963.

CONWAY, B. E., 'The state of water and hydrated ions at interfaces', *Adv. Colloid Interface Sci.*, vol. 8, pp. 91 – 211, 1977.

CURRENCE, H. D. & W. G. LOVELY, 'An automatic soil surface profilometer', Trans ASAE, vol. 14, pp. 69-71, 1971.

DALTON, F. N. & VAN GNEUCHTEN, M. Th., 'The TDR method for measuring soil water content and salinity, *Geoderma*, vol. 38, pp 237 – 250, 1986.

DE LOOR, G. P., 'The dielectric properties of wet materials', *Proceedings of IGARSS 82*, Muenchen, TP – 1, 1 – 5, 1982.

DAVIDSON, M. W. J., LE TOAN, T., MATTIA, F., SATALINO, G., MANNINER, T. & BORGEAUD, M., 'On the characterisation of agricultural soil roughness for radar remote sensing studies', *IEEE Transactions on Geocience and Remote Sensing,* vol. 38, no. 2, pp. 630-640, 2000.

DOBSON, M. C. ULABY, F. T., HALLIKAINEN, M. T. & EL-RAYES, M A., 'Microwave Dielectric Behaviour of Wet Soil – Part II: Empirical Models and Experimental Observations', *IEEE Transaction on Geoscience of Remote Sensing*, vol. 23, no. 1, pp. 35 – 46, 1985.

EMMERSON, W. W., 'The determination of the stability of soil crumbs', *J. Soil Sci.*, no. 5, pp. 233 – 50, 1954.

FUNG, A. K., 'Microwave Scattering and Emission Models and their Applications', Arctech House Norwood USA, p. 573, 1994.

GARDNER, W. H., 'Water content', in: Methods of soil analysis, part 1, 2nd edn., ed. A. Klute, *Agronomy*, vol. 9, pp. 493 – 544, 1986.

GUPTA, S. C., & LARSON, W. E., 'Estimating soil water retention characteristics from particle size distribution, organic matter percent, and bulk density', *Water Resour. Res.*, vol. 15, pp. 1633-1635, 1979.

HAJNSEK, I., 'Pilotstudie Radarbefliegung der Elbaue', Endbericht TP. I.2, p. 93, 1999, in: Verbundvorhaben Morphodynamik der Elbe, FKZ 0339566 des BMBF, in: *Interner Bericht* DLR 551-1/2001.

HALLIKAINEN, M. T., ULABY, F. T., DOBSON, M. C., EL-RAYES, M A., & WU, L.-K., 'Microwave Dielectric Behaviour of Wet Soil – Part I: Empirical Models and Experimental Observations', *IEEE Transactions on Geoscience and Remote Sensing*, vol. 23, no. 1, pp. 25 – 33, 1985.

HELMING. K., 'Die Bedeutung des Mikroreliefs für die Regentropfenerosion', Bodenökologie und Bodengeneses, Dissertation an der Technischen Universität Berlin, Selbstverlag, no. 7, p. 155, 1992.

HERKELRATH, W. N., HAMBURG, S. P. & MURPHY, F., 'Automatic, real-time monitoring of soil moisture in a remote field area with TDR', *Water Resour. Res.*, vol. 27, no. 5, pp. 857-864, 1991.

HOLMES, J. W., TAYLOR, S. A., & RICHARDS, S. J., 'Measurement of soil water', in: *Irrigation of agricultural Lands*, eds. R.M. Hagan, H.R. Haise, and T.W. Edminster. Agronomy, no. 11, pp. 275 – 303, 1967.

HORNE, R. A., 'The structure of water and aqueous solutions', *Surv. Prog. Chem.*, vol. 4, pp. 1 – 43, 1968.

JESCHCKE, W., 'Digital close-range photogrammetry for surface measurement', *IAPRS*, Zürich, vol. 28-5, pp. 1058-1065, 1990.

KELLER, J. M., CROWNOVER, R. & CHEN, R., 'Characteristics of natural sciences related to the fractal dimension', *IEEE Trans. On Pattern Anal. And Mach. Intell.,* vol. 9, no. 5, 1987.

KUIPERS, H., 'A reliefmeter for soil cultivation studies', *Neth. J. of Agric. Sci.*, pp. 255-262, 1957.

LOW, P. F., & WHITE, J. L., 'Hydrogen bounding and polywater in clay-water systems', *Clays and Clay Minerals*, vol. 18, pp. 63 – 66, 1970.

MARSHALL, T. J., HOLMES, J. W. & ROSE, C. W., 'Soil Physics', *Cambridge University Press*, third edition, p. 453, 1999.

MARSHALL(A), T. J., 'The nature, development and significance of soil structure', *Trans. Int. Soc. Soil Sci.* Comm. IV and V, NZ, pp. 243-57, 1962(a).

MATTIA, F. & LE TOAN, T., 'Backscattering properties of multi scale rough surfaces'*, J. Electromagn. Waves Applicat.*, vol. 13, pp. 491-526, 1999.

MULAEM, Y., & FRIEDMAN, S. P., 'Theoretical prediction of electric conductivity in saturated and unsaturated soil', *Water Resour. Res.*, vol. 27, no.10, pp. 2771 – 2777, 1991.

NEUSCH, T., 'Multi-Frequency and Multi-Polarization Synthetic Aperture Radar Data for Modelling Hydrological Parameters', Aachen Shaker, no. 5, pp. 128, 2000.

OADES, J. M., 'The role of biology in the formation, stabilisation and degradation of soil structure', *Geoderma*, vol. 56, pp. 377-400, 1993.

OGILVY, J. A. & FOSTER, J. R., 'Rough surfaces: Gaussian or exponential statistics', *Phys. Rev. D: Appl. Phys.,* vol. 22, pp. 1243-1251, 1989.

OH, Y. & KAY, Y. C., 'Conditions for precise measurement of soil surface roughness', *IEEE Transactions on Geoscience and Remote Sensing*, vol. 36, pp. 691-695, 1998.

PRIETZSCH, C., 'Vergleichende Analyse von SAR-Daten für die Regionalisierung des Wassergehaltes im Oberboden', *Dissertation*, Mathematisch- Naturwissenschaftlichen Fakultät, Universität Potsdam, p.159, 1998.

RHOADES(A), J. D. RAATS, P. A. C., & PRATHER, R. J., 'Effects of liquid-phase electrical conductivity, water content and surface conductivity on bulk soil electrical conductivity', *Soil. Sci. Soc. Am. J.*, vol. 40, pp. 651 – 653, 1976.

RHOADES, J. D. & VAN SCHILFGAARDE, J, 'An electrical conductivity probe for determining soil salinity', *Soil. Sci. Soc. Am. J.*, vol. 40, pp. 647 – 651, 1976.

ROTH, C. H., MALICKI, M. A. & PLAGGE, R., 'Empirical evaluation of the relationship between soil dielectric constant and volumetric water content as the basis for calibrating soil moisture measurements by TDR', *J. Soil. Sci.*, vol. 43, pp. 1 – 13, 1992.

RÖMKENS, M. J. M & J. Y. WANG, 'The effect of tillage on surface roughness', *ASAE*, Paper 84, p. 2026, 1984

SCHANDA, E., 'Physical Fundamentals of Remote Sensing', Berlin, 1986.

SCHEFFER, F. & SCHACHTSCHABEL, P., 'Lehrbuch der Bodenkunde', 13. durchgesehene Aufl. von P. Schachtschabel, H.-P. Blume, G. Brümmer, K.-H. Hartge und U. Schwertmann, Enke Verlag, pp. 491, 1992.

SCHMUGGE, T., 'Effect on soil texture on the microwave emission from soils', *IEEE Transactions on Geoscience and Remote Sensing*, vol. 18, pp. 353 – 361, 1980.

SHEPARD, M. K, BRACKETT, R. A. & ARVIDSON, E., 'Self-affine (fractal) topography: surface parametrization and radar scattering', *J. of Geophy. Res.*, vol. 100, no. E6, pp. 11, pp.709-11,718, 1995.

SHIN, T. R. & KONG, J. A., 'A backscatter model for a randomly pertubated periodic surface', *IEEE Transactions on Geoscience and Remote Sensing,* vol. 20, no. 4, 1982.

SHIVOLA, A, 'Properties of dielectric mixtures with layered spherical inclusions', in: *Microwave Radiometry and Remote Sensing Applications*, ed. P. Pampaloni (Utrecht, VSP), pp. 115 – 123, 1989.

STACHEDER, M., 'Die Time Domain Reflectometry in der Geotechnik: Messung von Wassergehalt elektrischer Leitfähigkeit und Stofftransport', *Schr. Angew. Geol. Karlsruhe*, vol. 40, I – XV, pp 170, 1996.

STRATTON, J. A., 'Electromagnetic Theory', McGraw-Hill Book Company, New York, 1941.

TISDALL, J. M., 'Possible role of soil micro-organisms in aggregation in soils', *Plant and Soil*, vol. 159, pp. 115-21, 1994.

TOPP, G. C., DAVIS, J. L., & ANNAN, A. P., 'Electromagnetic Determination of soil water content: Measurements in Coaxial Transmission Lines', *Water Resour Res.,* vol. 16, no. 3, pp. 574 – 582, 1980.

ULABY, F, MOORE, R., & FUNG, A., 'Microwave Remote Sensing: Active and Passive I – III', Addison-Wesley Publication, pp. 2162, 1981-1986.

VON HIPPEL, A., 'Dielectrics and Waves', vol. I and II, pp. 284, 1954, reprint 1995.

WHALLEY, W. R., 'Considerations on the use of time domaine reflectometry (TDR) for measuring soil water content', *J. Soil. Sci.*, vol. 44, pp. 1 – 9, 1993.

ZRIBI, M., CIARLETTI, V. & VIDAL-MADJAR, D., 'An Inversion Model of Soil Roughness Based on Two Radar Frequency Measurements', Proceedings IGARSS'99, Hamburg, pp. 2425 - 2427, 1999.

Chapter 3

Estimation of Ground Measured
Soil Surface Parameters

This chapter describes the test sites and the ground measurements used later on for the validation of the surface parameter inversion models. The ground measurements were performed over bare agricultural fields including measurements for soil moisture content and surface roughness. Two test sites are chosen in Germany, the Elbe-Auen floodplain area of the Lower River Elbe and the hilly area of the Weiherbach watershed. Both test sites were selected for ongoing research programs in different scientific areas. For the validation of the estimated surface parameters from polarimetric SAR data, it is necessary to define precisely the method used for the estimation of the ground measurements. Often, the explanation for a low correlation between ground-measured and estimated parameters, has not been related to the estimation methods but is a result of insufficient or deficient ground parameter measurement methods.

3.1   Floodplain of the River Elbe

The floodplain of the River Elbe located in North-Eastern Germany is subject of a compound system project funded by the German Ministry of Research (BMBF). The main objectives of the project called "*Morphodynamics of the River Elbe*" are the ecology of the river itself and its floodplain. The River Elbe originates in the Czech Republic and flows through Germany into the North Sea. This region has been chosen due to its conservation value and the large number of related ongoing research programs in geomorphology, soil sciences, hydrology and hydraulics (HAJNSEK 2001).

The actual floodplain of the River Elbe in the recent natural-space unit developed in the Holocene, about 15 000 to 20 000 BC. Characteristics for this time are periodic displacements of the main river channel as a result of misaligned sand and mud banks. Until the time of the beginning of river regulation, a natural equilibrium with dynamic erosion and sedimentation processes controlled the nature of the floodplain. The natural dynamic processes started to be disturbed in the Middle Ages with the introductions of dyke constructions. The river valley of today is a wide corridor of intensive land and water use. Since settlements and infrastructures cannot continuously move in response to flood or drought, floodplains have become regulated by human interventions with more or less respect to the natural dynamics according to culture and severity of natural impacts. The main technical encroachments on the River Elbe occurred in form of channel straightening, erosion mitigation, extensive flood protection, irrigation
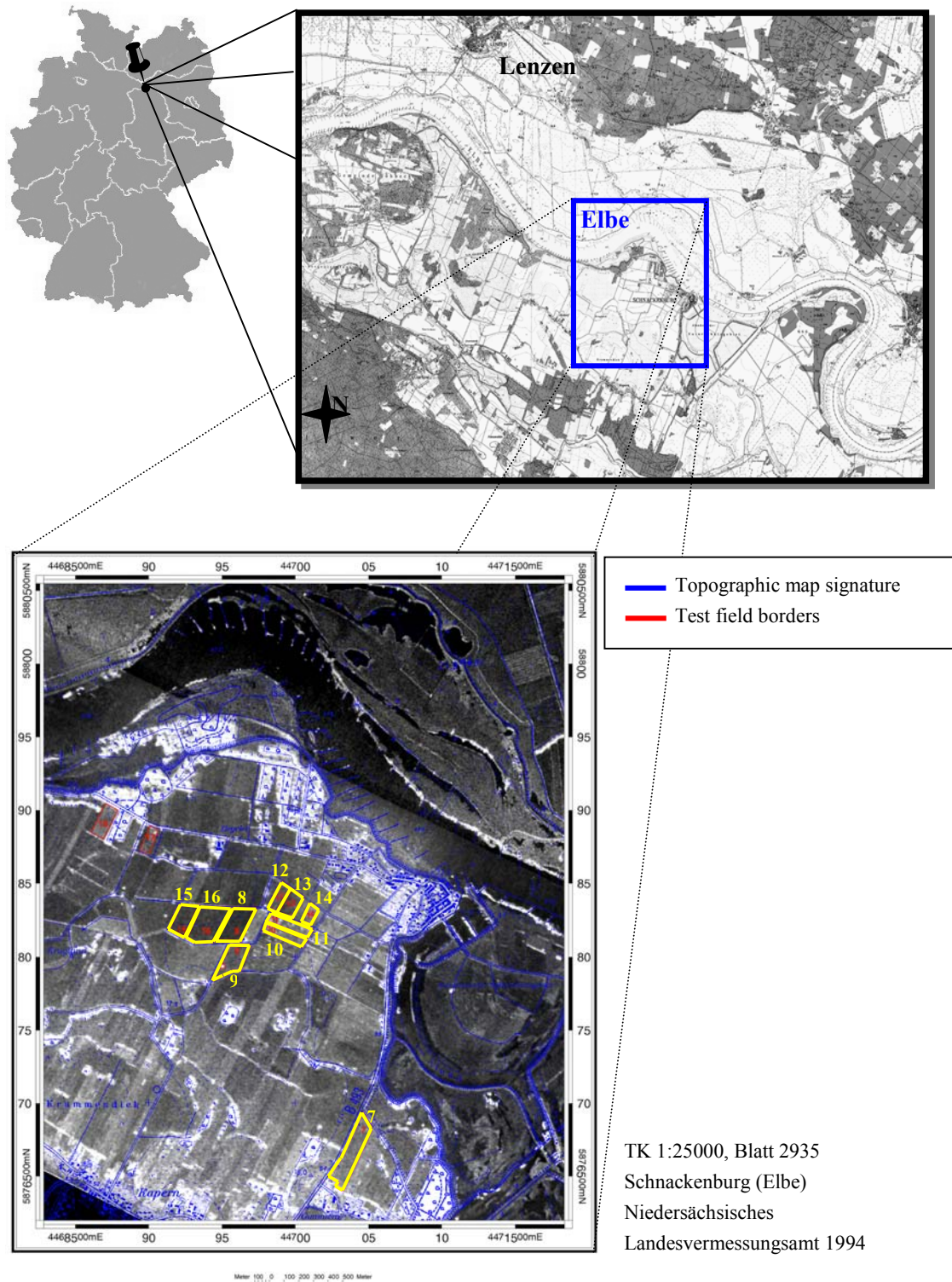
Fig. 3.1: Topographic map of the River Elbe test site with the test field A5/7 to A5/16

and/or drainage structures. Despite several ameliorations in the floodplain of the river, some tracks of natural dynamics in the fertile plain can be recognised. In areas inside the river channel, during low water level, natural deposit structures as scour, gutter, holes and sandbanks become visible, and some of the few natural fertile plains were preserved, over the years. Thus, the river Elbe test site gives the unique possibility to examine on the one hand the high

structural variety of a '*natural*' and on the other hand one, a strongly by human activities coined and shaped landscape on a relatively small area.

The test site is situated in the region of the "*Lower Central Elbe*" between 53°6'N 11°24'E – 53°N11°40'E and 53°0'N 11°24'E – 53°0'N11°40'E, and extends from river km 465 by Cumlosen to river km 485 by Lenzen. The region has a size of 15 km (air line) length and 5.4 km (air line) width. The size of the test site was chosen in accordance with the illuminated swath dimensions of the SAR sensor and lies in the 'Three-Land-Corner' of Brandenburg, Sachsen-Anhalt and Niedersachsen, in the districts of Prignitz, Alt-Markt and Wendland respectively.

The test site extends from the city Lenzen in the North-West to the small village Cumlosen in the North-East and from the small river Aland in the South-East to the settlement Restorf in the South-West. The following landscape units can be found in this area: meadows, pastures (within and outside the dyke), agriculturally used areas (field and grassland surfaces), fertile plains (within and external of the dyke), urbane settlements (farmsteads to cities), and the river Elbe. The largest urbane settlements in the area are, to the right of the river, the city Lenzen and, to the left of the river, the city Schnackenburg. The Elbe flows centrally through the test area, dividing the observed landscape into right and left sections.

3.1.1 Geography of the Test Site

The Elbe test site can be separated into three main geomorphologic units (DUPHORN & SCHNEIDER 1983):

- old moraine landscapes on the west and north site of the test area which were formed before approx. 250 000 to 130 000 years.
- the river valley, which was eroded between 15 000 and 20 000 BC due to the melting water of the last ice age ('*Weichsel Ice Age*'), as well as appropriate deposits on the adjoining terrace.
- the Elbe floodplain, which is mainly covered with sand and smaller particles as clay and silt, was formed during the Holocene.

The Elbe is an alluvial river, i.e. one that flows on a thick accumulation of alluvial deposits created by the river itself in earlier stages of its creation. A characteristic of alluvial rivers is that they experience overbank floods with a frequency ranging between annual and biennial occurrences during the season of large water surplus above the watershed. Overbank flooding of an alluvial river normally inundates parts or all of a floodplain that is bounded on either side by rising slopes called bluffs. The meandering river channel itself with abandoned sections of former river channels, meander-like developed narrow necks, which are then cut by shortening the river course, are dominating the floodplain. The cutoff followed quickly by deposition of

sand and silt across the end of the abandoned channel producing an oxbow lake. The oxbow lake is gradually filled with organic matter produced by aquatic plants. Eventually the oxbows are converted into swamps.

However, the sedimentation processes were not only restricted by the widely distributed channel network of the river but also by periodic flooding inducing the sediment freight to higher situated areas of the flood plain. Thereby, a frequently layer-wise deposition of alternate river sand and silk took place. Since the sedimentation rate was larger in the depressions, a gradual smoothing-out of the floodplain was obtained.

During periods of overbank flooding, when the entire floodplain is inundated, water spreads from the main channel over adjacent floodplain deposits. As the current suddenly slackens, a sudden skip of flow energy is associated with it and the sand and silt are deposited in a zone adjacent to the channel. The result is an accumulation known as a natural lee. Because deposition is heavier closest to the channel and decreases away from the channel, the lee surface slopes away from the channel (SCHEFFER & SCHACHTSCHABEL 1992). This explains the often appearing sand bank barriers close to the river, and behind them the extended flat and lower situated backswamps.

The finer proportion of the sediment freight, as clay loam, covers today a wide area of the river floodplain, only some sand lenses are still rising up to the surface. The particle size distribution of the flooded earth depends on the water flow conditions at the time of the deposit, which causes laminated sediments with varying grain sizes. The thickness of the laminates varies often over short distances between five and 20 dm. Individual authors have proposed different natural processes as the reasons for the sedimentation of silt and clay. However, the most important factors are on the one hand the influence of man-induced deforestation, and on the other hand field-structural uses, both causing the decrease of the river flow velocity.

The relatively high clay proportion of the soils in the investigation area causes special unfavourable local conditions for agricultural land use. Clay soils are characterised by large volume of the particle, but only a small proportion of coarse and middle-sized grain. Thus, they frequently are moderately to poorly aerated and possess a relatively small proportion of plant-available water (SCHEFFER & SCHACHTSCHABEL 1992). The major part of the water is bound firmly in the micro pores as dead water. Particularly, during missing structure formation, clay soils possess smaller water conductivity, so that the clay loam lamination acts as an impermeable layer. In the area under investigation, because of such impermeable, clay loam layers, widespread strained groundwater conditions occur.

The handling of such clay-loam soils depict special agricultural tillage processes. They are to be processed only in a certain dampness state and are therefore considered as '*minute soils*'. In both the damp and in the dry state, land processing and cultivation reacquires considerable efforts. In the damp state the soil is plastic (highly viscose) and sticking. In this state, the soil

lubricates, and these negative soil characteristics are still further accentuated by soil compression due to heavy traffic loads. On the other hand, in the dry state, clay-loam aggregates are difficult to destroy (SCHEFFER & SCHACHTSCHABEL 1992). Thus, the water regime of a region determines the characteristics of different types of soils (FLEMMING 1997).

The human intervention leads not only to the disturbance of the water balance in the ground but also to the prevention of the emergence of new soils. The drainage of the soil in the flood plain once developed is adjusted particularly by dykes and drainage trenches.

Field Nr.	Soil-texture-classes (%)	Field Nr.	Soil-texture-classes (%)
A5/7	S (70) Sl (20) Ls (10)	A5/12	Sl (90) L (10)
A5/8	Cl (70) L (10) Sl (20)	A5/13	Sl (40) Sl (60)
A5/9	L (35) Sl (30) Cl (20) Sl (15)	A5/14	Sl (100)
A5/10	Sl (55) L (30) S/C (10)	A5/15	C (90) Sl (10)
A5/11	L (25) Sl (20) S/C (10) Sl (45)	A5/16	L (100)

Tab. 3.1: Soil-texture-classes from the Elbe test fields (S = sand, C = clay and L = loam)

The knowledge of the texture of a soil is important because it largely determines the water retention and transmission properties of the soil. Soil-texture-classes are based on varying proportions of sand, silt and clay, expressed in percentages. Pure sand soils drain too rapidly, while for predominantly clay soils, the individual pore space is too small for adequate drainage. On soils with high clay and silt content, root penetration may be difficult. As mentioned in *Chapter 2*, the water storage capacity of sand is very low, for clay high; and loams hold intermediate amounts. Sand transmits the water downward more rapidly, and clay more slowly. Thus, for planning of the quantity of irrigation water to be applied, these factors must be taken into account. Sand reaches its full capacity very rapidly, and any additional water beyond it is wasted. On the other hand, clay-rich loams take water up very slowly, retain it longer, and, if irrigation is too rapid, water will be lost by surface runoff. In this sense, sandy soils require more frequent watering than clay-rich soils. Furthermore, the organic content of a soil also strongly affects its water-holding capacity. Intermediate loam textures are generally best suited as agricultural soils because they drain well, but also have favourable water-retention properties.

The soil-texture-classe found inside the test site are listed in Tab. 3.1. The appraisal classification is based on the 'Deutsche 'Reichsbodenschätzung Karte'. (Niedersächsisches Landesverwaltungsamt-Landesvermessung (1993): A Soil Type Map on the basis of the soil estimation (1976). Katasteramt Lüchow, Blatt 2935). Further detailed publications on the soil type in the test area are available in MEYER & MIELICH (1983), SCHWARZ, GOENGROEFT & MIELICH (1997, 1999). According to the German soil classification scheme the characteristic soil types in this region are *Rambla*, *Paternia* and *Vegen*. On locations with high ground water level, primarily *Auengleye*, *Auennassgleye* and *Auenmoorgleye* soils can be found. Besides the pedologically important effects and factors as type of sedimentation, duration of flooding and

ground water level changes, also the seasonal changes of the river water level are of importance for the interpretation of different ecological states of the river's floodplain. The seasonal high water level of the river influences seriously the backswamps, so that differences are found for different locations.

3.1.2 Ground Measurements

Ground data has been collected in August 1997 over ten agricultural test fields with different roughness conditions, from slightly rough to truly rough (see Fig. 3.3). Soil moisture measurements have been performed on five different locations at each test field. Roughness measurements have been done twice for each direction over each test field. Due to the presence of vegetation on three of the fields, only seven bare fields remained finally suitable for the investigations in this study. The measured values for soil moisture range over these fields from m_v [vol %] 7.5 to 31 (i.e., $4.5 << \varepsilon' << 18$), while the surface roughness ks ranges from 0.3 up to 0.5 (i.e., $1 << s$ [cm]$<< 3.5$). The fields are viewed with incidence angle ranging from 48 to 50 degree.

20. August. 1997							
Field Nr.	**Field Cover**	**Field Cultivation**	**Cover Density [%]**	**Cover Height [cm]**	**mv 0-4 cm [vol. %]**	**mv 4-8 cm [vol. %]**	**s**
A5/7	potatoes	seed	90-100	65-80	4.80	6.16	---
A5/8	bare	deep ploughed	---	---	20.97	31.12	1.877
A5/9	sugar beet	seed	100	40-60	17.13	28.76	---
A5/10	bare	harrowed	---	---	21.12	18.54	1.663
A5/11	sugar beet	seed	80	30-40	9.76	14.31	---
A5/12	willow beet	seed	80	20	10.27	14.64	1.400
A5/13	bare	coarse harrowed	---	---	9.98	19.53	2.096
A5/14	bare	coarse harrowed	---	---	7.48	21.18	2.770
A5/15	willow beet	seed	50	25-50	17.10	25.48	1.120
A5/16	bare	ploughed	---	---	11.36	23.35	3.494

Tab. 3.2: Cover, cultivation, cover density, cover height, soil moisture content and surface roughness of the river Elbe-Auen test site, see location at Fig.3.1.

3.1.2.1 Soil Moisture Content

Soil moisture samples were taken after a long dry climatic period at two different depths, 0 - 4 cm and 4 - 8 cm, using traditional gravimetric sampling and time domain reflectometry (TDR). Due to the very dense and hard soil only few TDR measurements could be successively performed. Therefore, only gravimetrically measured soil samples will be used as reference for the quantitative comparison of soil moisture inversion from the radar data. The mean soil moisture values m_v [vol %] in the soil depth from 0 - 4 cm vary between 5 to 28 [vol %], while in the deeper soil layer, 4 - 8 cm, between 5 to 31 [vol %]. The measured values are compiled in Fig. 3.2. As expected, the upper soil layer is observed to be dryer and shows a higher spatial variation over the fields, compared to the deeper soil layers. The upper soil layer exhibit the highest variations from 1 [vol. %] to 20 [vol. %] and the lower soil layers only a variation between 1 [vol. %] to 8 [vol. %] (SCHEFFER & SCHACHTSCHABEL 1992).
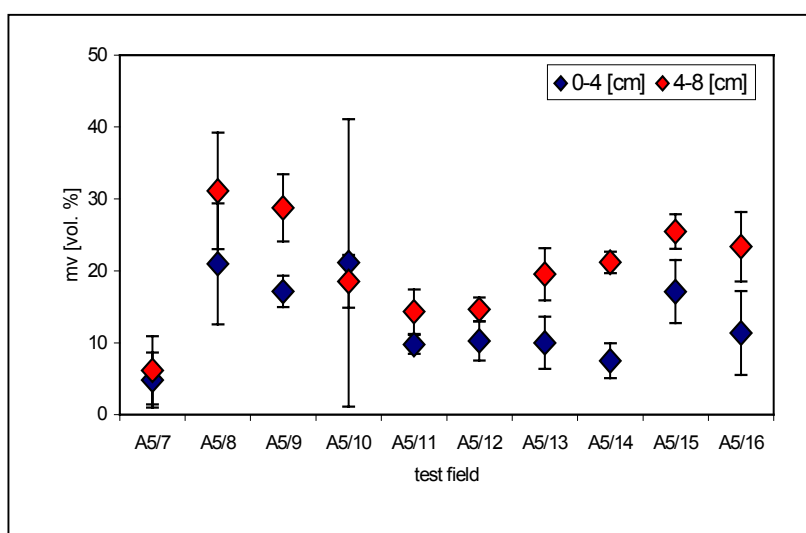
Fig. 3.2: Volumetric moisture content for 10 test fields taken in August 1997

The high moisture variation in the agricultural fields in August during a constant dry climatic period may be explained by different storage, bound capability and texture of the soils. The highest difference in the volumetric content between the upper and the deeper soil layer is observed for bare fields, which are deeply ploughed or coarsely harrowed (A5/8, 13, 14, 16). For such fields a much dryer crust and a wetter lower soil layer are characteristic. In contrast, covered fields show a smaller gradient in the volumetric moisture in the vertical direction, certainly due to the weaker evaporation of the top soil layer.

Furthermore, a correlation between the soil moisture content and the soil texture can be recognised. The driest agricultural fields have a higher sand fraction (A5/11, 12, 13, 14, 18). However, for the transformation of the measured soil moisture contents into the corresponding real parts of the dielectric constant, using the algorithm proposed by TOPP *et al.* (1980), no influence resulting from the soil type or texture is accounted for (see *Chapter 2*).

3.1.2.2 Surface Roughness

Four different agricultural soil cultivations can be identified under the test fields: seeded, harrowed, coarsely harrowed and deeply ploughed fields. The soil roughness was estimated by using a needelboard (0.60 m wide and 1.5 m long) in four directions: perpendicular (PPR) and parallel to the ridges (PAR), as well as perpendicular (PPF) and parallel (PAF) to the nominal flight direction. From each measurement set, a picture was taken and the needles were digitised at 5 cm intervals. The height difference of the digitised points to the average height leads to the calculation of the roughness variation. The resulting RMS heights have been averaged over each field. The measured results are compiled in Fig. 3.3.
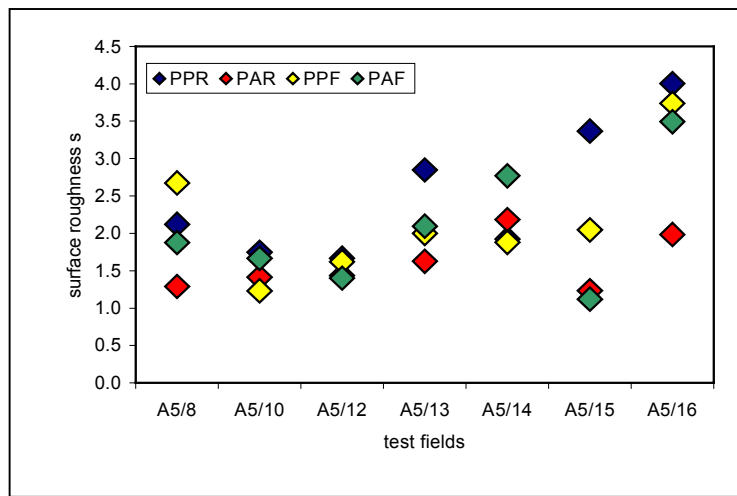
Fig. 3.3: Surface Roughness measurements in four directions: perpendicular (PPR) and parallel to the row direction (PAR); perpendicular (PPF) and parallel to the flight direction (PAF) for the Elbe-Auen test site.

As already mentioned due to dense vegetation cover on three fields, roughness measurements could only be done on seven test sites. In general, the measured roughness values, RMS heights *s*, do not differ significantly in the different directions. The *s* values for the PPR, which shows the highest variations, vary from 1.7 cm to 4 cm, the PAR from 1.2 cm to 2.1 cm, which exhibits the smallest variation, the PPF from 1.2 cm to 3.7 cm and the PAF from 1.1 cm to 3.5 cm, are nearly in the same range. The impact of the row direction to the backscattered signal was known from former studies. The study of CHAMPION & FAIVRE (1996) describes that a crucial roughness factor influences the backscattered signal, concluding that the position of the RMS height to the azimuth angle plays a significant role. Therefore, only the roughness measured in the PAF direction were used for the quantitative comparison of the inversion results.

Field ID	AOI	s cm	ks	ε' 0-4 cm	ε' 4-8 cm	m_v 0-4 cm	m_v 4-8 cm
A5/8	48.18	1.88	0.5	10.69	17.75	20.97	31.12
A5/10	49.20	1.66	0.45	10.79	9.28	21.12	18.54
A5/12	50.03	1.4	0.38	5.44	7.28	10.27	14.64
A5/13	50.03	2.1	0.57	5.34	9.84	9.98	19.53
A5/14	49.99	2.77	0.75	4.51	10.82	7.48	21.18
A5/15	48.29	1.11	0.3	8.51	13.61	17.10	25.48
A5/16	48.56	3.5	0.95	5.86	12.19	11.36	23.35

Tab. 3.3: Ground measurements for the Elbe-Auen test site and their conversion into ε' and *ks*

3.2 Hilly Area of the Watershed Weiherbach

The watershed of Weiherbach is located on a hilly terrain in South-West. Since 1989, the Weiherbach area has been the subject of a multi disciplinary research project entitled "*Modelling of Water and Solute Transport in Small Rural Catchments*". The main goal of this project is the collection of basic surface and water information as terrain topography, water networks, soil chemistry, geological behaviour, land use and their implementation into a geographic information system (GIS) (BÄHR & VÖGTLE 1999). This test site has been chosen due to its hilly topography as a complementary site to the flat Elbe-Auen test site for the validation of the developed inversion algorithms.

It is situated in the Kraichgau region, approximately 30 km north-east of Karlsruhe in the German State of Baden. The Weiherbach Valley is composed mainly of agricultural fields, farms and small forest parcels. Its main characteristic is a homogenous loess cover of up to 30 m that covers most of the area. The catchment has an undulating surface with some terrain slopes and is affected by erosion. This leads to typical hill slopes catenaries with eroded soils, low in clay and organic carbon at the top and soils, developed from fine accumulated material at the bottom. Another important feature of the loess soils is the abundance of macropores, mainly large wormholes, that greatly influence the solute transport in those soils under certain hydrological conditions.

The test area is surrounded by the small city Neuenbürg in North-West, by the city Kraichtal in the West and by the small village Münzesheim in the South-East. The entire test area is about 6 km^2 in area extent.
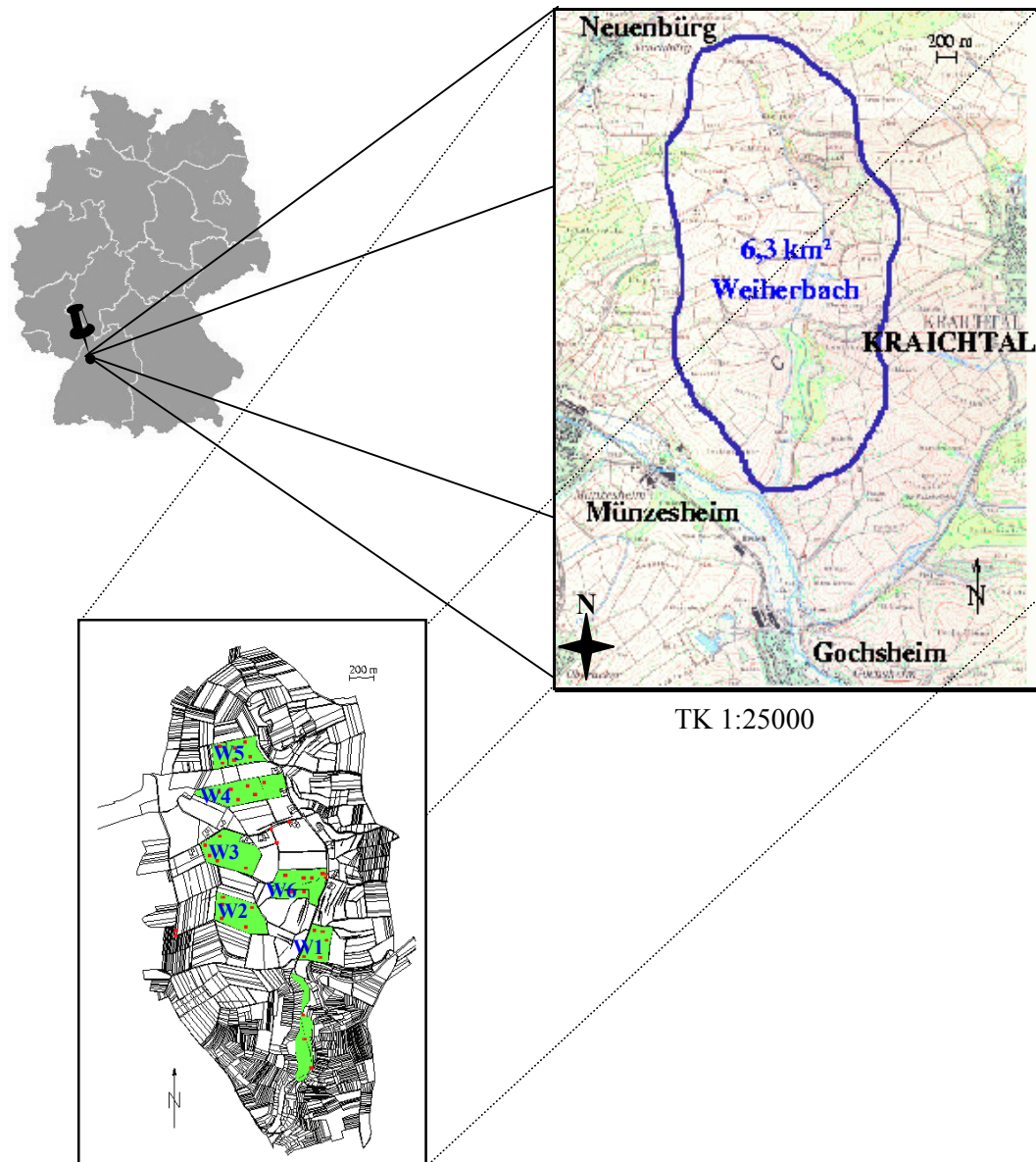
Fig. 3.4: Topographical map of the Watershed Weiherbach with test fields W1 to W6

3.2.1 Geography of the Test Site

The watershed is embedded in a flat and widespread terrain, which is bordered by 100 m high steps. Above these steps a flat terrain starts again. From a geomorphological point of view, the system is a so-called step-layer-landscape, a tectonic composition of geomorphologic alternately hard and smooth layers, which are the result of a continuous sedimentation during the geological era of the Mesozoic. Therefore, in this region two main geological units can be found

- the most commonly and mighty layer of the Sandstone, where a thickness up to 500 m is measured at various locations, and

- the younger, and more in the East-South easterly region, located layer of Limestone.

During the quaternary ice ages in Northern and Southern Germany, the landscape was formed by the growing and melting periods of glaciers. At those periods the landscape formed by the disposal of debris, arising from snowmelt and frost, which were only sparsely covered with vegetation. In this arctic dry areas or tundra - at that time -, the rich silt material was blown throughout middle Europe, and was deposited during lowering of the wind speed or on the wind calm – *lee* - sides of the mountains. The deposit is called loess (löß) and reaches some 100 m of thickness. Predominantly, it is composed of a silt fraction of 65-80 %, a clay fraction 10-25 % and a sand fraction of 10-25 % (with fine and middle sand) in central Europe. In most cases, the loess is carbonate rich, yellow coloured and has a significant grain size maximum between 10 and 60 μm in diameter.

Under the humid climatic conditions, following the ice ages, the high carbonate fraction was washed out, and the yellow loess has been transformed through iron oxide and clay, forming the yellow-braun loess-clay. From these loess soils, the most fertile agricultural soils types developed, i.e., the Parabraun-Soils, the Schwarz-Soils and Pararendzina. Pararendzina, Parabraunsoil and Kolluvisols are the most common soils of the agricultural fields in the Weiherbach test area (WEIBLEIN & SCHILLINGER 1996).

Small rivers and their erosive forces transform the landscape locally into a hilly terrain, with steep walls along the small river channels. Erosive processes also influence the soil succession: on the top of the slopes and on the slope itself pure loessy soils, very rich in silt, are present; while in the depressions the transported clay and humus-rich materials can be found. The top layer (< 40 cm) of the loess soil on the deposition is much smaller in grain size than that of the lower soil layer, and it shows therefore, a higher permeability. In the Weiherbach test area four distinctive paelosoil types (loess covers) can be found, which reaches a thickness from a few decimetre up to 4 m.

A soil texture map was supplied by a team of geologists involved in the Weiherbach project. This team elaborated the soil texture map in the system of the 'Bodenkundliche Kartieranleitung' 1982 (BK'82), which was based on soil estimation data acquired for this area by the finance department (WEIBLEN & SCHILLINGER 1996). The soil texture map distinguishes the three texture size fractions: clay, silt and sand. Seven main soil texture classes could be distinguished on the six test fields. The soil texture classes, listed in Tab. 3.4, consider only the first 20 cm of the top layer of soil. Finally, the watershed Weiherbach itself is predominantly composed of silt loam soils, i.e. including high amount of clay components.

Field Nr.	clay fraction (%)	silt fraction (%)	sand fraction (%)
W1	11	79	10
W2	14	76	10
W3	15	75	10
W4	18	75	7
W5	21	70	10
W6	24	70	7

Tab. 3.4: Soil textures occurring in the Weiherbach test fields

3.2.2 Ground Measurements

During the ground measurement campaign in April 1997, six bare agricultural fields were chosen for validation purposes within the Weiherbach watershed. They had a varying soil moisture, $14 < m_v$ [vol. %] < 37 corresponding to i.e., $7 < \varepsilon' < 22.5$ and surface roughness for a wavelength of 23 cm, at $0.4 < ks < 0.5$ (i.e., $1.5 < s < 1.9$) values. The ground measurements for the Weiherbach watershed test sites were performed similar to those for the Elbe-Auen test sites using screened board measurements perpendicular to the flight directions for collecting surface roughness data and using gravimetric sampling as well as time domain reflectometry (TDR) for the moisture estimation.

Field Nr.	Field Cover	Field Cultivation	Cover Density [%]	Cover Height [cm]	mv 0-4 cm vol. %	mv 4-8 cm vol. %	mv 0-16 cm vol. %	s
				17. April. 1997				
W1	winter wheat	seed	43	22	27.77	32.47	27.53	1.70
W2	bare	---	---	---	27.11	35.15	30.53	1.49
W3	winter wheat	seed	45	22	29.65	36.95	26.37	1.78
W4	winter wheat	seed	5	---	21.79	29.41	27.58	1.45
W5	bare	ploughed	0	---	14.79	25.99	21.41	1.89
W6	winter wheat	seed	48	< 22	21.76	25.68	28.10	1.56

Tab. 3.5: Cover, cultivation, cover density and cover height of the Weiherbach test site.

3.2.2.1 Soil Moisture Content

During the flight campaign, moisture measurements were taken using time-domain reflectometry at the depth of 0 - 15 cm and by assessing the classical gravimetric method in three different depths 0 - 4 cm, 4 - 8 cm and 0 - 15 cm. In order to establish a common reference measurement basis between the two test sites (Elbe-Auen and Weiherbach), only the gravimetric measurements are used for the validation of the inversion results. As shown in Fig. 3.5, the mean volumetric moisture constant, over the six test fields does not vary as much as over the river Elbe-Auen test fields. The variation of m_v for the top soil layer lies between 14 and 29 [vol %], for the deeper layer, 4 - 8 cm, it is between 25 and 37 [vol %], and for the deepest soil layer a variation from 21 to 30 [vol %] is measured. For the Weiherbach test sites the error bars indicate a smaller moisture variation over the fields than in the Elbe-Auen test site. The measurements for the Weiherbach test area indicate, in general, wetter soil conditions due to the seasonal rainy period in April. In the week of the flight campaign the weather conditions were unsteady with some short precipitation events.
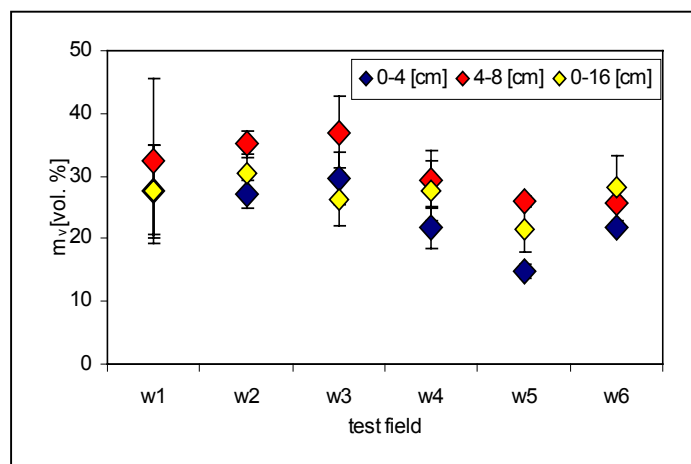
Fig. 3.5: Volumetric moisture content measurements for the Weiherbach test fields

The vertical volumetric moisture distribution of the soil fields, presented in Fig. 3.5, is characterised by the water storage capability of the individual fields. During a rain event the top layer saturates faster and then, after a certain time delay, the water infiltrates into deeper layers. After the rain event, the top layer dries out much faster due to evaporation than the soil layers located underneath. In case of the Weiherbach test fields the driest soil layer, two to three days after a rain event, is the top layer, the wettest lies within 4 - 8 cm depth, while deeper lying layers are moderately wet. These observations are in agreement with research results on the soil behaviour of the Weiherbach project (NEUSCH 2000).

3.2.2.2 Surface Roughness

The performed surface roughness measurements on the agricultural test fields are limited to only one direction, namely parallel to the nominal flight direction. As presented in Tab. 3.6 the surface roughness variation over the six test fields is not significant. In comparison to the Elbe-Auen test fields, the Weiherbach test fields are much smoother with a RMS height ranging from 1.45 to 1.89 cm.

Field ID	RMS height s	Field ID	RMS height s
W1	1.70	W4	1.45
W2	1.49	W5	1.89
W3	1.78	W6	1.56

Tab. 3.6: Surface Roughness measurements for each test field for the Weiherbach test site

Field ID	AOI	s cm	ks	ε' 0-4 cm	ε' 4-8 cm	m_v 0-4 cm	m_v 4-8 cm
W1	47.05	1.70	0.46	15.23	18.82	27.7	32.47
W2	43.42	1.49	0.41	14.76	21.01	27.11	35.15
W3	42.89	1.78	0.48	16.63	22.53	29.65	36.95
W4	43.93	1.45	0.39	11.2	16.44	21.79	29.41
W5	43.41	1.89	0.51	7.35	13.97	14.79	26
W6	45.65	1.56	0.42	11.18	13.75	21.76	25.68

Tab. 3.7: Ground measurements for the Weiherbach test site and their conversion into ε' and *ks*

3.2.2.3 Digital Elevation Model

A digital elevation model with a grid size of 12.5 m was provided by the University of Karlsruhe. It is interpolated down to a 2.5 m raster in order to match the resolution of the L-band radar images.
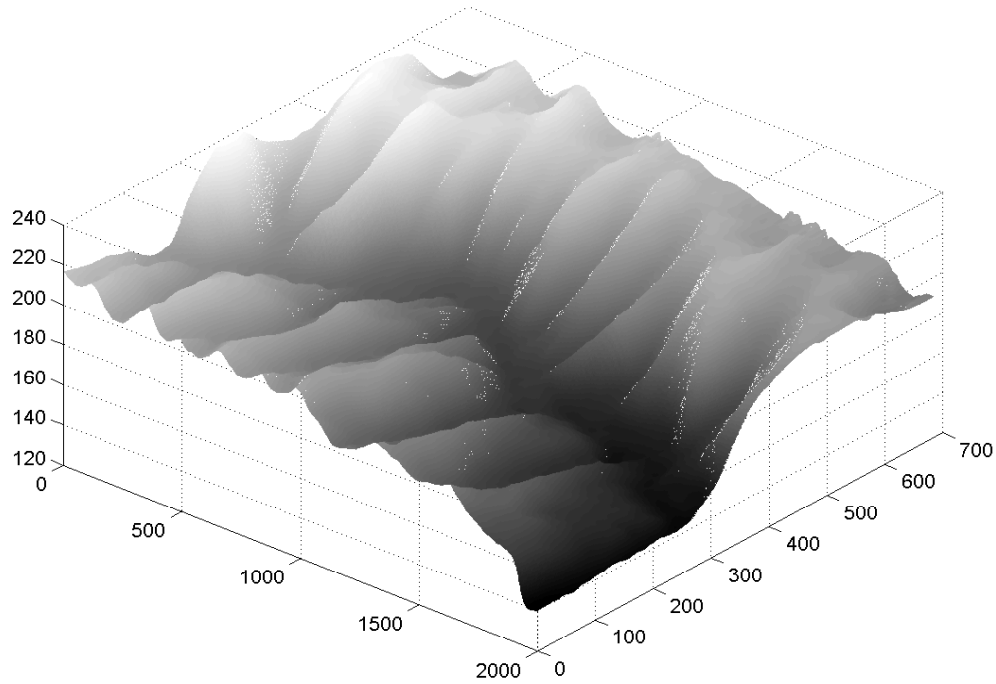
Fig. 3.6: Digital Elevation Model from the Weiherbach Watershed

The absolute topographic height above sea level of the test site lies between 180 m up to 203 m and varies about 100 m over the entire test site. As seen in Fig. 3.4, the Weiherbach test site is divided by a small river into two natural space units. Nearly all test fields are located on the more flat west site, except of field W1, which lies on the east site of the river. Three of the fields are tilted to the north, W2 – W4; two are tilted to the east, W5 and W6; and one, W1, to the south-west direction. Their slope variations range from 0.3 to 1.8 degrees, and they are much steeper in the range direction (see Tab. 3.8).

Field ID	Height [m]	Azimuth – Slope [degree]	Range – Slope [degree]
W1	181	-0.21	-1.77
W2	193	0.57	-0.33
W3	198	0.52	-0.40
W4	203	0.95	-0.11
W5	199	0.47	0.58
W6	180	0.56	0.56

Tab. 3.8: Variation in height, azimuth-slope and range-slope for the Weiherbach watershed

W1

W2

W3

W4

W5

W6
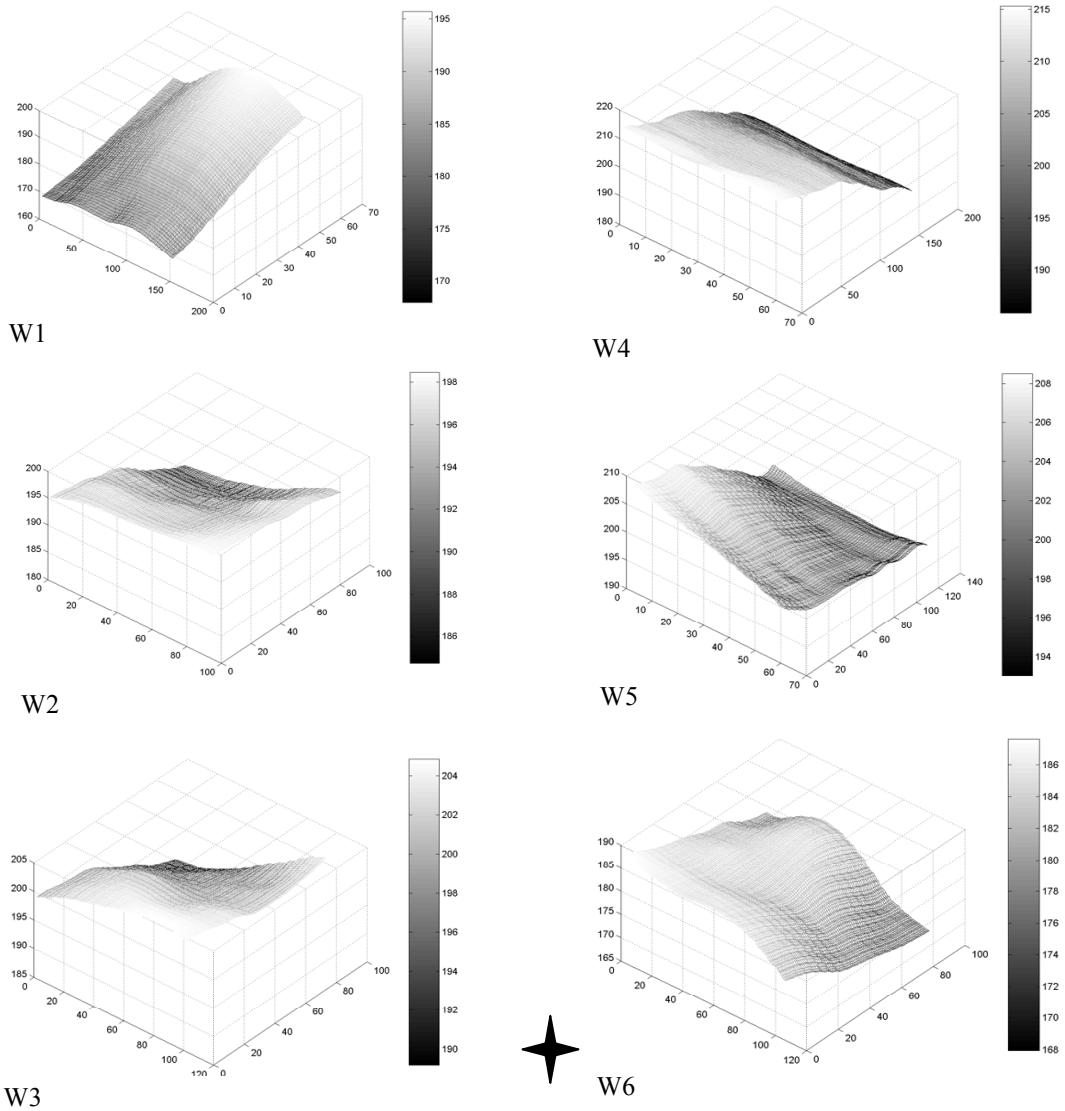
Fig. 3.7: Representation of the six test fields in their DEM co-ordinate system

3.3   References to Chapter 3

BÄHR, H. –P. & VÖGTLE, T. H.,'GIS for Environmental Monitoring', *E. Schweizerbartsch'sche Verlagsbuchhandlung*, Stuttgart, 1999.

CHAMPION, I. & FAIVRE, R., 'The field row direction relative to the radar azimuth considered as an apparent surface roughness for smooth bare fields', *Int. J. Remote Sensing*, vol. 17, no. 16, pp. 3305-3311, 1996.

DUPHORN, K. & SCHNEIDER, U., 'Zur Geologie und Geomorphologie des Naturparks Elbufer-Drawehn', *Abh. Naturwiss. Ver. Hamburg*, HF vol. 25, pp. 9-40, 1983.

FLEMMING, A., 'Die Bedeutung des Grabensystems für den Gebietswasserhaushalt im geplanten Rückdeichungsgebiet Lenzen (Elbe)', Diplomarbeit im Fachbereich Geographie der Universität Hamburg, 1997, unpublished.

GRÖNGRÖFT, A., SCHWARZ, R., & MIELICH, G., 'Verbreitung und Eigenschaften der Auenböden in dem geplanten Rückdeichungsgebiet Lenzen – erste Ergebnisse', *Auenreport* 3, 3 Jg., pp. 58-65, 1997.

HAJNSEK, I., 'Pilotstudie Radarbefliegung der Elbaue', Endbericht TP. I.2, p. 93, 1999, in: Verbundvorhaben Morphodynamik der Elbe, FKZ 0339566 des BMBF, in: *Interner Bericht* DLR 551-1/2001.

MEYER, H. & MIELICH, G., 'Einfluß periodischer Hochwässer auf Genese, Verbreitung und Standorteigenschaften der Böden in der Pevestorfer Elbaue (Kreis Lüchow-Dannenberg)', *Abh. Naturwiss. Ver. Hamburg*, vol. 25, pp 41-73, 1983.

NEUSCH, T., 'Multi-Frequency and Multi-Polarization Synthetic Aperture Radar Data for Modelling Hydrological Parameters', Aachen: *Shaker Verlag*, Karlsruhe, Universitäre. Dissertation., p. 128, 2000.

SCHEFFER & SCHACHTSCHABEL, 'Lehrbuch der Bodenkunde', 13. Auflage, *ENKE Verlag*, 1992.

SCHWARZ, R., GRÖNGRÖFT, A. & MIELICH, G., 'Auwirkung von Eindeichung und Melioration auf den Wasserhaushalt von Auenböden – aufgezeigt am Beispiel zweier Grünlandstandorte an der unteren Mittelelbe bei Lenzen', *Auenreport-Sonderheft* 1, pp. 41-5, 1999.

TOPP, G. C., DAVIS, J. L., & ANNAN, A. P., 'Electromagnetic Determination of soil water content: Measurements in Coaxial Transmission Lines', *Water Resour Res.,* vol. 16, no. 3, pp. 574 – 582, 1980.

WEIBLEN, B. & SCHILLINGER, M., 'Erstellung einer Bodenartenkarte auf Basis von Daten der Bodenschätzung', *Zwischenbericht des Weiherbachprojektes*, 1996.

Chapter 4

Remote Sensing Using
Airborne Synthetic Aperture Radar Data

The scope of this chapter is to introduce briefly the basic principles of Synthetic Aperture Radar (*SAR*). Synthetic Aperture Radar imaging is today a well developed remote sensing technique for providing large scale, high resolution radar reflectivity images of the Earth's surface. More detailed information can be found in several standard texts as for example in TOMIYASU (1978), HOVANESSIAN (1980), ELACHI (1988), CURLANDER & MCDONOUGH (1990), HENDERSON & LEWIS (1998) OLIVER & QUEGAN (1998), FRANCESCHETTI & LANARI (1999), SOUMEKH (1999), and KLAUSING & HOLPP (2000).

4.1　SAR Principles

There are two main categories of remote sensing imaging systems: passive and active. While passive systems make use of naturally emitted, reflected or scattered radiation from Earth's surface, active systems are equipped with a transmitting unit and receive the signal backscattered or reflected from the illuminated terrain. An important class of active imaging sensors are radar systems operating in the microwave region of the electromagnetic spectrum. The active operating mode makes these sensors independent from external illumination sources and additionally the fact of operating at the microwave region reduces drastically the impact of clouds, fog and rain on the resulting images. Thus, active radar imaging systems allow widely day and night all-weather imaging, an important requirement for continuos global scale monitoring.

Imaging radar systems provide a two-dimensional image of the radar reflectivity of a scene by illuminating it with microwave pulses and receiving the scattered field. There are two possible operation scenarios for such radar systems. The first one is to use the same system for transmitting and receiving. In this case receiver and transmitter are located at the same position and therefore this configuration is widely known as monostatic configuration. It is the classical operation scenario for space and airborne radar systems up to now. In the second scenario receiver and transmitter are spatially separated from each other by using one active (i.e. transmitting) system to illuminate the scene and one or more passive (i.e. receiving only) systems for receiving the scattered field. Such bi/multi-static configurations were up to now used only for indoor laboratory radar measurements but may become a prospective alternative for cost-effective future spaceborne multistatic implementations such as the Cart-Wheel concept (MASSONNET 1999).
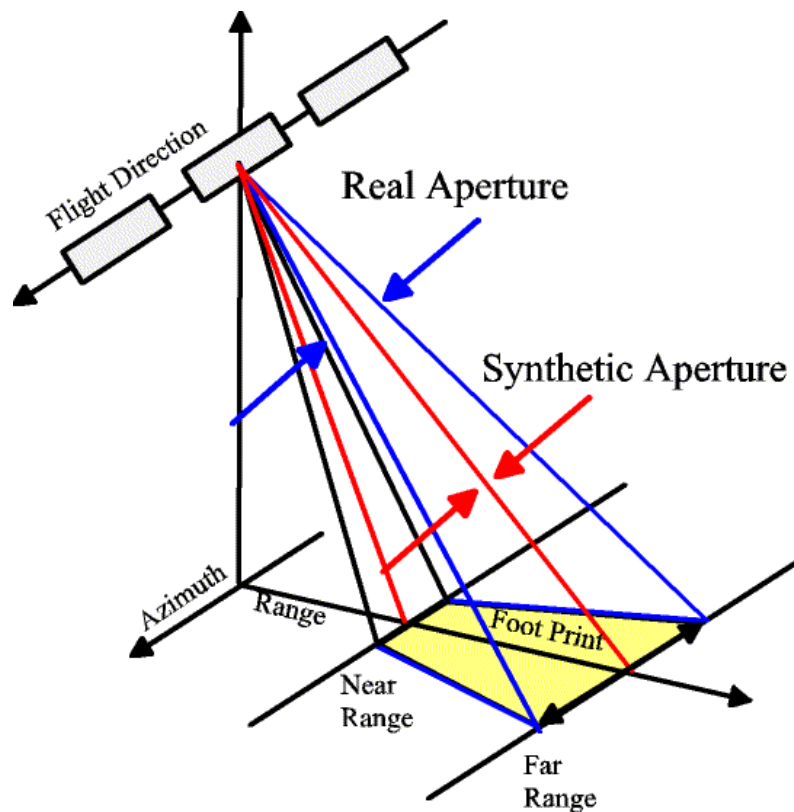
Fig. 4.1: SAR geometry

In a simplified description, a monostatic radar system consists of a pulsed microwave transmitter, an antenna which is used for transmission and reception, and a receiver unit. It is mounted on a moving platform such as an aeroplane, the space-shuttle or a satellite and operated in a side-looking geometry (see Fig. 4.1). Accordingly, the antenna beam is directed slant-wise towards the ground and – in the most conventional implementation - orthogonal to the moving direction, which is referred to as range or cross-track direction. The transmitted pulse is radiated by the antenna towards the ground along the antenna beam directions. The spot on the ground illuminated by a single pulse is referred to as the antenna footprint, the entire image strip as the image swath. The backscattered signal is received by the receiver-antenna and the receiver unit. The platform motion in the flight direction provides the scanning in the direction of the sensor trajectory, which is referred to as azimuth or along-track direction.

One of the most important quality criteria of an imaging sensor is its spatial resolution. It is a measure of how close two point-like objects can be located to each other in order to still be separated in the image. For radar imaging sensors, the spatial resolution is given for range and azimuth separately. In range direction it is inversely proportional to the bandwidth of the transmitted signal. Consequently, a wider bandwidth results into a higher range resolution. The constrains on the achievable range resolution are mainly given by the bandwidth limitation of the antennas. Today, the achievable range resolutions are about 1 to 10 meters for spaceborne

systems while airborne systems are capable to achieve resolutions on the order of tenths of centimetres (MOREIRA 1999, BAMLER & HARTL 1998).

More challenging is the quest for achieving reasonably high resolution in the azimuth direction. The first generation of radar imaging systems were so-called *Rreal Aperture Radars* (RAR), characterised by a azimuth resolution depending on the operating frequency, the size of the real antenna, and the distance between sensor and the object to be imaged. Due to technical and operational constrains on both, the size of the used antenna and the transmitted frequency, the achievable resolution was poor and varied inside the image. The solution to these limiting problems was given by the next generation of radar sensors operating according to the concept of *synthetic antenna* or *synthetic aperture*. The basic idea of this concept is to simulate a very long antenna by moving a small real antenna along the flight direction. The coherent integration of the received signals along the flight track allows synthesising a long virtual- antenna and leads to images with high spatial azimuth resolution independent of- the operating frequency and the distance to the scene. This break-through enabled the operation of high resolution SAR systems not only on airborne but also on spaceborne platforms (HENDERSON & LEWIS 1998). The constrains on the spatial resolution of SAR systems are given today by practical limitations on the transmitted power, and data rate, leading to resolutions of several meters for spaceborne sensors and on the order of one meter or better for airborne radars.

4.2 SAR System Parameters

A natural scene is characterised in terms of its three-dimensional reflectivity function describing the density distribution of scatterers in the scene. The SAR imaging process can be regarded as the projection of this three-dimensional scene reflectivity function onto the two-dimensional range-azimuth image space. In this sense, the physical information content of the SAR image is nothing more than the band-limited projection of the scene reflectivity into the SAR image geometry. The reflectivity function of the scene depends mainly on the frequency, polarisation and the imaging geometry. Consequently, the physical information content of SAR images depends also on the choice of these diversified parameters (BOERNER & VERDI 2000). Imaging radar systems are operating within the microwave region of the electromagnetic spectrum, i.e. at frequencies from 3 MHz up to 300 GHz with corresponding wavelengths from 100 m down to 1 mm. Civil radar systems nowadays operate commonly at X (f ~10 GHz or λ ~ 3 cm), C (f ~ 6 GHz or λ ~ 5 cm), S (f ~ 3 GHz or λ ~ 10 cm), L (f ~ 2 GHz or λ = 15 cm) and P (f ~ 0.5 GHz or λ ~ 60 cm). With respect to polarisation conventional SAR systems operate using linearly polarised antennas (usually horizontally or/and vertically) in a single-, dual- or fully polarimetric mode. In the single-polarisation mode the pulse transmission is performed at a single polarisation, defined by the polarisation of the antenna, and the backscattered signal is received at the same polarisation (BOERNER *et al*. 1998).
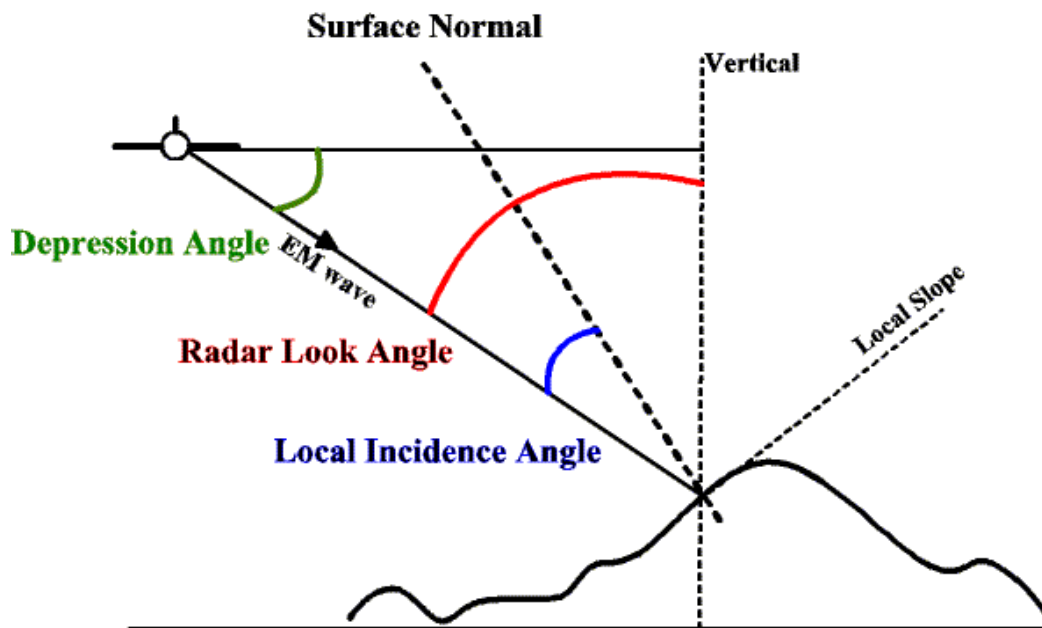
Fig. 4.2: Angle relations for a terrain with slope variations.

The most common mode of dual-polarised sensors is to transmit at a single polarisation and to receive at two orthogonal polarisations. Finally, the complete polarimetric information in form of the scattering matrix is measured by fully polarimetric systems capable of both transmitting and receiving at two orthogonal polarisations, retaining the relative polarisation phase information. The information content of fully polarimetric data is discussed in detail in *Chapter 5*.

An important feature of radar remote sensing is the penetration capability of microwaves into material media. The penetration depth is a function of the density and the moisture content of the penetrated medium, as well as frequency and polarisation dependent. Thus, again the information content depends on the used frequency and polarisation. For example, considering a dry medium, shorter wavelengths (X- or C-band, $\lambda \sim 3$ or ~ 5 cm) interact mainly with its upper layer and consequently the obtained radar image contains information about this part of the medium. On the other hand, by using a sensor operating at lower frequencies (L- or P-band, $\lambda \sim 23$ or ~ 63 cm), the incident wave penetrates more into the medium, and the obtained image may contain information about deeper layers.

The knowledge of the imaging geometry is essential for the physical interpretation of the image. Especially important is the radar look angle (RLA), defined as the angle between the vertical of the antenna to the ground and the range direction. On the one hand, the scattering process itself depends on the direction of the incident wave. On the other hand it effects directly the projection defining the mapping of the scene into the SAR image. Because of this projection, information about the spatial structure of the scene is lost. All points in the scene located at the same range distance to the sensor are mapped into the same position in the image independently of their height. This leads to the characteristic geometry distortion effects in

SAR images. For flat planar scenes without topographic variations all points in the scene are located at the same height so that the geometric-distortion is caused only by the RLA variation over range. The geometrical relationship between scene and corresponding SAR image is given completely by the radar look angle. However, in the case of topographic variations inside the scene, the geometric- distortions become appreciable- leading to the three of the following effects in the image:

- the *shadow effect* results from the radar illumination on a front side of a mountain while casting a shadow behind. The shadow area- does not produce any backscattered signal in the far-field region, and no signal contribution to the image is generated;
- the *foreshortening effect* results from many scatterers along the slope returning at nearly the same time and are mapped onto the hill base in range direction. This causes the effect to appear very bright at the front side of a hill - also known as '*front-porching effect*';
- the *layover effect* results from mapping the top of the hill before the bottom of the hill in case of very steep slopes.

In this case, the geometrical relationship between scene and SAR image depend from both: the RLA and the terrain topography. The distortions effects can be corrected by backprojecting the SAR image onto an available digital elevation model of the scene (SCHREIER 1993).

4.3   Radar Backscattering Coefficient

In the previous section, SAR was treated as an imaging instrument. In this section we consider SAR as a measurement instrument. The procedure to establish the relation between the pixel values of a SAR image and the physical measurable is called radiometric calibration. It can be viewed- as a two-step process: 1. relative calibration that accounts for the relative relationship within the image, and 2. absolute calibration in order to establish absolute measurables comparable between different SAR images and imaging geometries.

For distributed scatterers, the intensity information of the SAR image is expressed in terms of the radar brightness and the radar backscattering coefficient. The radar brightness $\beta°$ corresponds to the average Radar-Cross Section (RCS) per unit image area (i.e., per pixel) in dB and is the standard radiometric product for uncalibrated radar images. It results directly from the amplitude of the received signal expressed in terms of the digital number DN as

$$\beta^0 = 10 \cdot \log_{10}\left(\frac{DN^2}{C}\right) \qquad (4.1)$$

where C is the absolute calibration constant, which in the case of E-SAR is 60 dB.

The radar backscattering coefficient, also known as sigma nought σ^0, is defined as the average radar cross section per unit ground area in dB. Hence, σ^0 can be obtained by normalising β° to the ground patch corresponding to the projection of each pixel onto the ground

$$\sigma^0 = \beta^0 \cdot \sin\theta. \tag{4.2}$$

The angle θ is the local incidence- angle or the *Angle of Incidence* (AOI), defined as the angle between the incident radar beam to the surface normal. The radiometric resolution express the ability of a SAR sensor to discriminate differences in σ^0, and indicates therefore its quality as a measurement instrument.

From Eq. 4.2 follows that the knowledge of the local incidence angle is important in order to obtain the normalised intensity measurable. The values of σ^0 depend on the physical and electrical properties of the scatterer, on the wavelength, the polarisation, on the the radar look angle.

For flat terrain the local incidence angle corresponds to the radar look angle, which can be estimated directly from the imaging geometry as

$$\theta = ar\cos\left(\frac{h - \bar{z}}{Ro}\right) \tag{4.3}$$

where h is the flight altitude above mean sea level and $\bar{z}$ the averaged terrain elevation and Ro the slant-range distance to the scatterer. However, in the presence of terrain variations, the local incidence angle is no longer given by the radar look angle. In this case the relative orientation of the terrain – in terms of its surface normal – is required to estimate the local incident angle. In general, this information cannot be extracted from a single SAR image itself. The most common way to account for it is by using an available elevation model of the imaged terrain.

The obtained backscattering coefficient for the 10 Elbe-Auen test fields are varying from -13 to -26 dB for L_{HH}, from -14 to -26 dB for L_{VV} and from -21 to -40 dB for L_{HV}. As expected, for surface scatterers the general trend is VV > HH > HV. The backscattering coefficients for the 6 Weiherbach fields are much higher, varying from –11 to -17 dB for L_{HH}, from –8 to –13 dB for the L_{VV} and from –23 to –27 dB for the L_{HV}, where VV > HH > HV. Considering only the backscattering coefficients, the influence of the object parameters becomes evident against the background at which the two test sites are recorded during two different seasonal states, the wet spring and the dry summer, and most likely also during different times of the day with little attention pay to meteorological conditions.

4.4 Speckle

SAR images display a characteristic granular noise over distributed scatterers, which is inherent to all kinds of coherent imaging systems operating at wavelengths smaller than the spatial resolution. This, so called speckle phenomenon, is a consequence of the interference of the individual scattering processes occurring within the resolution cell. Distributed scatterers may be modelled to consist of a large number of elementary scatterers randomly distributed as indicated in Fig. 4.3 (GODMANN, MADSEN, NEZRY 1991, LOPES 1993, LEE *et al.* 1994). In this context, the total scattered field is given by the coherent superposition of the contribution of each of these elementary scatterers. The phase of each such elementary contribution depends on the location of the corresponding scatterer inside the resolution cell. As their locations vary from pixel to pixel the resulting total scattered field varies in amplitude and phase accordingly (see Fig. 4.4) leading to the characteristic speckle pattern.

Speckle is not noise, in the sense that the same imaging configuration leads to the same speckle pattern. On the other hand, it limits the radiometric resolution and therefore the subsequent ability to discriminate between different intensity levels. Speckle can be reduced by averaging (multi-looking), taking into account the loss of spatial resolution. This averaging can be performed by using different approaches, for example: 1) by averaging adjacent pixels in the SAR image (spatial domain multi-looking), 2) by dividing the synthetic aperture into segments, process them separately to individual images, and thereafter average them incoherently (frequency domain approach).
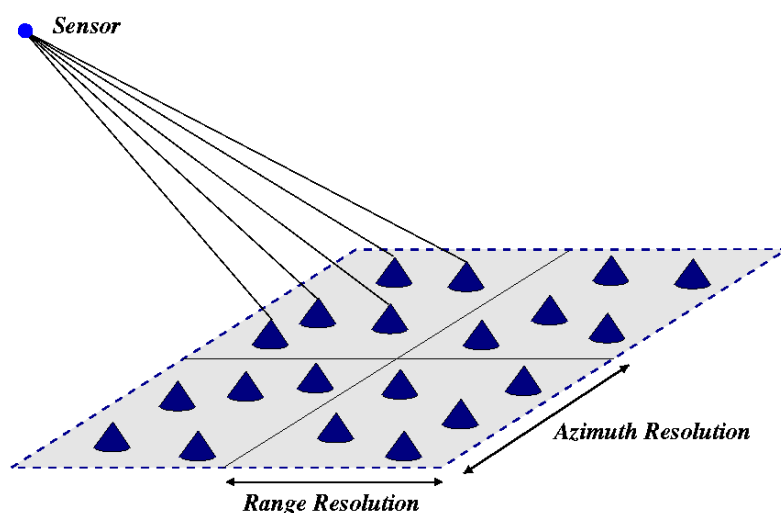
Fig. 4.3: Schematic representation of distributed scatterers and imaging geometry

Several filter algorithms have been developed fulfilling more or less satisfactorily the requirements of the users (NEZRY 1991, LOPES 1993, TOUZI 1994, QUEGAN 1995). In this dissertation research - polarimetric speckle filters developed by LEE *et al.* (1994) were- used. The Lee-Filter approach- relies on the multiplicative noise model, and estimates the speckle

variance based on the local image statistics (LEE 1991). A particular, specifically designed Lee-filter was implemented in its refined version in order to filter homogenous areas, while preserving edges and textures. The filter has been applied with a 7x7 window and a coefficient of variation of 0.5, which corresponds to 4 look images.
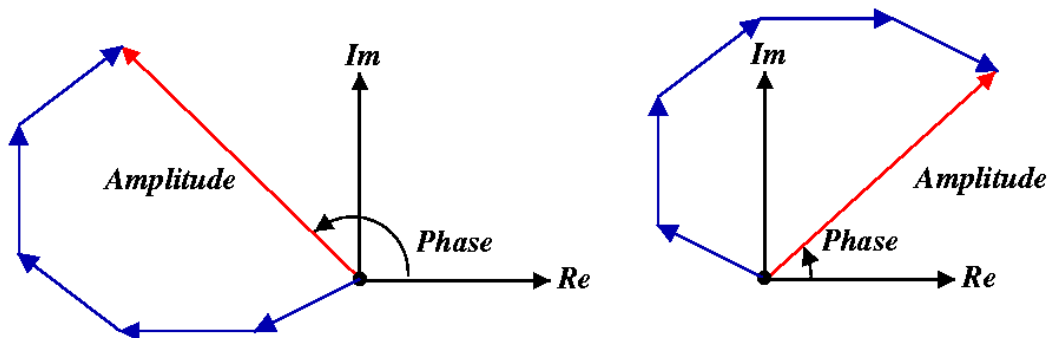
Fig. 4.4: Speckle Phenomenon: Total scattering field as coherent superposition of elementary scattering contributions for different resolution cells.

4.5   Experimental Data

The airborne Experimental Synthetic Aperture Radar (E-SAR) System, developed at the German Aerospace Center, Institute of Radio Frequency Technology and Radar Systems in Oberpfaffenhofen (DLR-OP-IHR/SAR), operates at five microwave bands (X, C, S, L, P) in a dual polarisation mode at X- and C-band, in a single polarisation mode at S-band, and fully polarimetric modes in L- and P-bands, respectively (MOREIRA 1998).

E-SAR Technical Parameters

RF-Band	X-Band	C-Band	S-Band	L-Band	P-Band
RF-centre frequency	9.6 GHz	5.3 GHz	3.3 GHz	1.3 GHz	450 MHz
Transmit peak power	2500 W	750 W	2 kW	400 W	200 W
Receiver noise figure	4.0 dB	4.0 dB	5 dB	8.5 dB	4.0 dB
Antenna gain	17.5 dB	17 dB	16 dB	15 dB	12 dB
Azimuth beamwidth	17°	19°	12°	18°	30°
Elevation beamwidth	30°	33°	32°	35°	~ 60°
Antenna Polarization	H and V	H and V	H and V	H and V	H and V
IF-centre frequency	300 MHz	300 MHz	300 MHz	300 MHz	300 MHz
Max. Signalbandwidth	100 MHz	100 MHz	100 MHz	100 MHz	50 or 18 MHz
System bandwidth	120 MHz	120 MHz	120 MHz	100 MHz	60 or 25 MHz

Tab. 4.1: System parameters of the DLR's E-SAR (2001)

For the investigations in the frame of this study only the L-band configuration in the fully polarimetric (HH,VV,HV,VH) mode was chosen. At L-band, the spatial resolution of the single look complex data (SLC) is in azimuth about 0.75 m and in range about 1.5 m. The data were acquired in April and August of 1997 along two 15 km long and 3.2 km wide strips (see Figure 4.5). Corner reflectors were positioned in the test area for calibration purposes. The most important system parameters are listed in Table 4.1. More detailed and updated information is provided on the following web page http://www.op.dlr.de/ne-hf/projects/ESAR/.

(a)   (b)
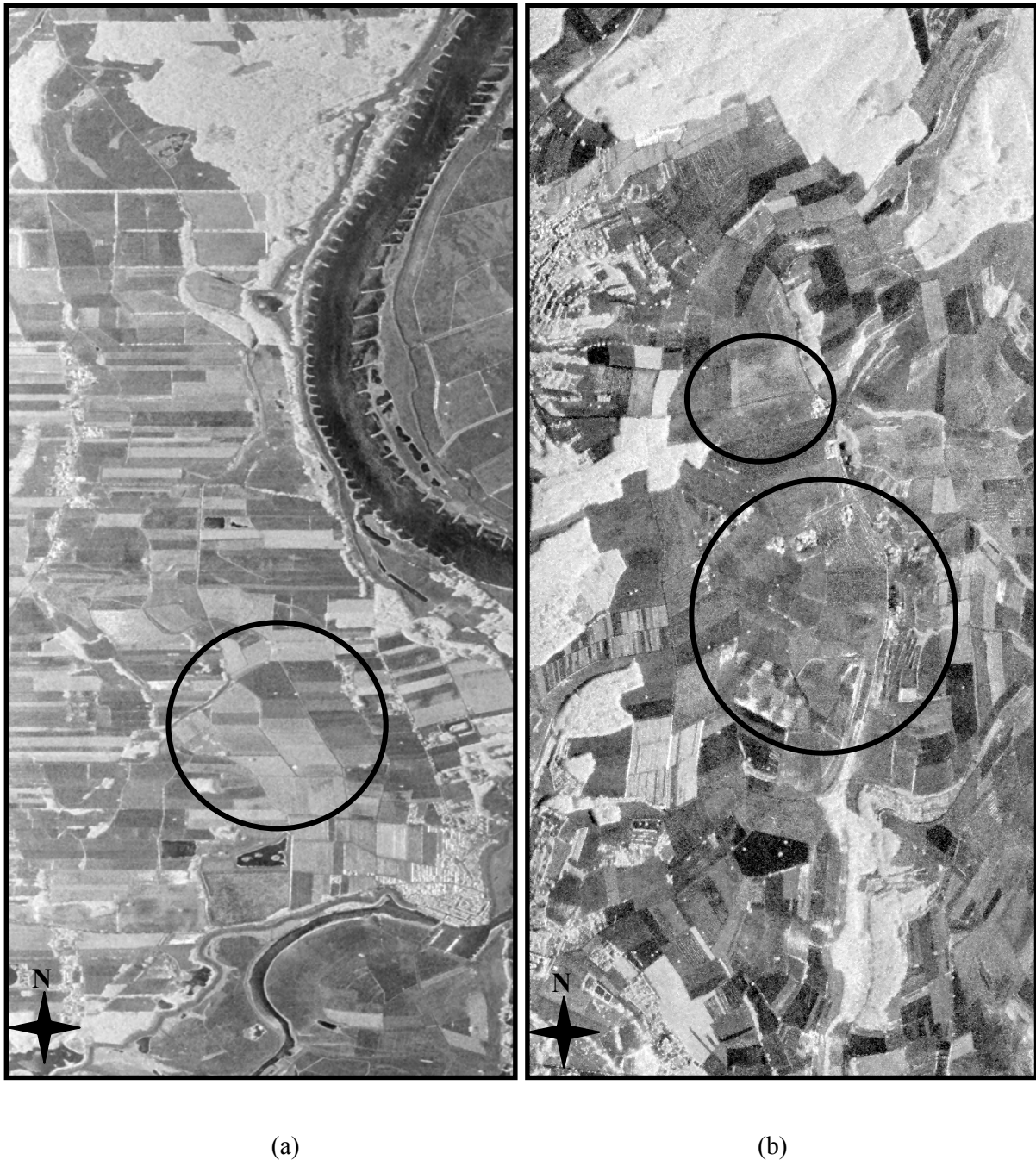
Fig. 4.5: Total Power Images at L-Band ($|HH|^2+|VV|^2+2|HV|^2$)
of the two test sites (a) Elbe-Auen and (b) Weiherbach.

4.6 References to Chapter 4

BAMLER, R. & HARTL, P., 'Synthetic Aperture Interferometry - A-State-of-the Art-Review', *Inverse Problems*, IOC Publ., Vol. 14, R1 - R54, 1998

BOERNER, W. M. ET AL., 'Polarimetry in Radar Remote Sensing: Basic and Applied Concepts', Chapter 5 in F. M. Henderson, and A.J. Lewis, (ed.), "Principles and Applications of Imaging Radar", vol. 2 of Manual of Remote Sensing, (ed. R. A. Reyerson), Third Edition, John Willey & Sons, New York, 1998.

BOERNER, W-M & VERDI, J. S., 'Recent Advances in Polarimetric-Interferometric SAR - theory & technology and its applications', CEOS-WGCV-99, Toulouse, France, 26 - 29 October 1999, ESA-SP-450, pp. 379 - 396, 2000.

CURLANDER, J.C. & MCDONOUGH, R.N., 'Synthetic Aperture Radar: Systems and Signal Theory", John Willey & Sons, New York, 1991.

FRANCESCHETTI & LANARI, 'Synthetic Aperture Radar Processing', CRC Press, p. 307, 1999.

ELACHI, C., 'Spaceborne Radar Remote Sensing: Applications and Techniques', *IEEE Press*, New York, NY,1988.

GOODMAN, J. W., 'Some fundamentals properties of speckle', *Journal of Optical Society of America*, vol. 66, no. 11, pp. 1145-1149, 1976.

HENDERSON, F. M. & LEWIS, A. L. (ed.), 'Principles & Applications of Imaging Radar', Manual of Remote Sensing, Third edition, vol. 2, p. 866, 1998.

HOLECZ, F., 'Postprocessing von SAR-Satellitenbilddaten', Remote Sensing Laboratories, Zürich, vol. 23, p. 150, 1993.

HOVANESSIAN, F.T., 'Introduction to Synthetic Array and Imaging Radars', Artech House, Inc., Norwood, MA, 1980.

KLAUSING, H. & HOLPP, W. (ed.), 'Radar mit realer und synthetischer Apertur: Konzeption und Realisierung', Oldenburg Verlag München, p.399, 2000.

LEE, J. S., GRUNES, M. R. & MANGO, S. A., 'Speckle reduction in multi-polarisation, multi-frequency SAR imagery', IEEE Geoscience and Remote Sensing, vol. 29, no. 4, pp. 535-544, 1991.

LEE, J. S. & JURKEVICH, I., 'Speckle Filtering of Synthetic Aperture Radar Images: A Review', *Remote Sensing Reviews*, vol. 8, pp. 313-340, 1994.

LOPES. A., NEZRY, E, ROUZI, R. & LAUR, H., 'Structure detection and statistical adaptive speckle filtering in SAR images', *International Journal of Remote Sensing*, vol. 14, no. 9, pp. 1735-1758, 1993.

NEZRY, E., LOPES, A. TOUZI, R., 'Detection of structural and textural features for SAR images filtering', *Proceedings IGARSS'91*, Espoo, Finland, vol. IV, pp. 2162-2172, 1991.

MADSEN, S. N., 'Spectral theory: Modelling, Analysis, and Applications Related to Synthetic Aperture Radar data', Ph.D. thesis, Technical University of Denmark, Denmark, Nov. 1986.

MASSONNET, D., 'Capabilities and Limitations of the Interferometric Cartwheel', *Proceedings of the CEOS SAR Workshop*, Toulouse 1999, ESA SP-450, pp. 251-262, 1999.

MOREIRA, A., 'Synthetic Aperture Radar'', Chapter in Book ', 'Radar mit realer und Syntetischer Apertur', Oldenburg Verlag, Munich, 1999 (88 pages)

MOREIRA, A., 'The E-SAR System: Specification of a high resolution Multi-look real time processor', DLR Interner Bericht,R-551-11-11/86, Radar Group, 1998 November 04.

OLIVER, C. & QUEGAN, S., 'Understanding Synthetic Aperture Radar Images', Artech House, p. 479, 1998.

QUEGAN, S. & RHODES, I., 'Statistical Models for Polarimetric Data: Consequences, Testing and Validity', International Journal of Remote Sensing, vol. 16, pp. 1183-1210, 1995.

RANEY, R. K., FREEMAN, T., HAWKINS, R. W. & BAMLER, R, 'A Plea for Radar Brightness', *Proceedings IGARSS'94*, vol. II, pp. 1090-1092, 1994.

SCHREIER, G. (ed.), 'SAR Geocoding: Data and Systems', Wichmann, Karlsruhe, p.435, 1993.

SOUMEKH, M., 'Synthetic Aperture Radar Signal Processing with MATLAB Algorithms', New York: John Wiley & Sons, 1999.

TOMIYASU, K., 'Tutorial Review of Synthetic Aperture Radar', *Proceedings IGARSS'78*, vol. 66, no. 5, 563-583, 1978.

TOUZI, R., & LOPES. A., 'The Principle of Speckle Filtering in Polarimetric SAR Imagery', *IEEE Transactions of Geoscience and Remote Sensing*, vol. 32, pp. 1110-1114, 1994.

ULANDER, L. M. H. & HAGBERG, J. O., 'Radiometric and Interferometric Calibration of ENVISAT-1 ASAR', European Space Agency Contract Report No. PO/133382, no. 172, p. 114, 1995.

WAITE, W. P., 'Historical Development of Imaging Radar', In: Geoscience Applications of Imaging Radar Systems, RSEMS (Remote Sensing of the Electro Magnetic Spectrum), (A. J. Lewis, ed.), Association of American Geographers, vol. 3, no. 3, pp. 1-22, 1976.

Chapter 5

Polarimetric Concepts for Microwave Remote Sensing

In this chapter the basic polarimetric concepts used in this dissertation study are introduced. The reviewed definitions and mathematical formulations are necessary to describe the polarimetric scattering problem for point and distributed scatterers and are essential for modelling and inversion of surface parameters from polarimetric data in the next chapters. There are two main conceptual formalisms in polarimetry. The first one is a real space formalisms based on the Stokes Vector for the description of the polarimetric properties of waves and on the Mueller matrix, (in backscattering also known as Kennaugh matrix) for the polarimetric description of the scatterer (BORN & WOLF 1985, COLLET 1993, GUISSARD 1994, BOERNER *et al*. 1993, BOERNER *et al*. 1998). The second one is a complex space formalism based on the Jones vector for the analysis of wave polarisation and on the covariance or coherency matrix for the description of the scattering process (KENNAUGH 1954, BOERNER *et al*. 1998). Both formalisms are equivalent. The real space formulations and concepts can be transformed unambiguously into the corresponding complex space formulations and concepts, and vice versa. However, due to the fact that SAR data are measured and processed in the complex domain, in the following the complex space formalism is chosen for use in this study; whereas for an ellipsometric, hyperspectral analysis the real space formalism is commonly preferred (BORN & WOLF 1985), but not further discussed here.

5.1 Polarisation Description of Plane EM Waves

The solution of the wave equation (derived from Maxwell´s equations) for linear source-free homogeneous media leads to the simplest form of electromagnetic waves with constant amplitude on a plane perpendicular to the direction of propagation. Such waves are known as plane waves (STRATTON 1941, JACKSON 1975, JONES 1989, CHEN 1983). The instantaneous real electric field vector of such a wave $\vec{\underline{E}}(\vec{r},t)$ propagating into the direction $\vec{k}$ at a given location, defined by the position vector $\vec{r}$ and a given time t, can be written as

$$\vec{\underline{E}}(\vec{r},t) = \underline{E}(\vec{r})\cos(\omega t) \tag{5.1}$$
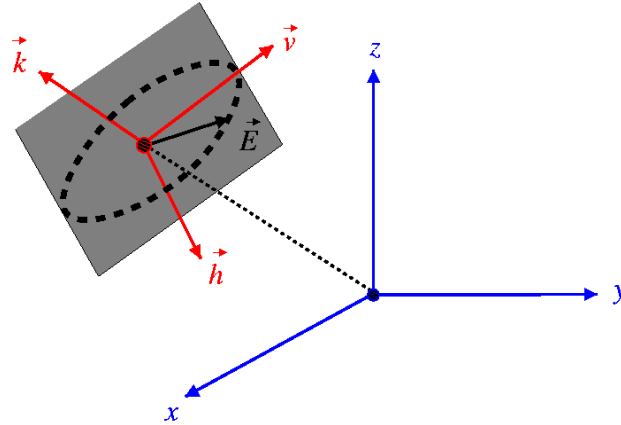
Fig. 5.1: Plane wave propagating in $\vec{k}$ direction.

where $\underline{\vec{E}}(\vec{r})$ is the real amplitude of the electric field and ω is the angular frequency of the wave. In the case for which the electric field vector varies in time with a single angular frequency the wave is called monochromatic. The corresponding complex representation of the electric field, which is independent of time, is according to the IPU (International Physical Union) convention given by

$$\vec{E}(\vec{r}) = \vec{E} \cdot e^{(i\vec{k}\vec{r})} \tag{5.2}$$

where $\vec{E}$ is the constant complex amplitude vector of the electric field. Introducing a right handed orthogonal coordinate system $(\vec{h}, \vec{v}, \vec{k})$ (see Fig. 5.1), the complex amplitude vector $\vec{E}$ can be decomposed into two orthogonal complex components E_h and E_v as

$$\vec{E} = E_h \vec{h} + E_v \vec{v} \tag{5.3}$$

Polarisation is in general, related to the vectorial nature of waves. It describes the behaviour of the field vector in time. As a physical property of the wave, the polarisation is independent of the coordinate system used to describe it. However, the definition of polarisation requires a reference coordinate system and a direction of propagation. Concerning a EM monochromatic plane wave, the polarisation describes the orientation of the electric field vector, in the plane perpendicular to the direction of propagation, as a function of time. In general, the tip of the electric field vector moves on this plane in time along an ellipse, which is known as the polarisation ellipse (BORN & WOLF 1985, MOTT 1993, COLLET 1993, BOERNER et al. 1998).

The shape of the polarisation ellipse expresses the polarisation state of the plane wave. It can be completely described in terms of two angles, the orientation angle ψ and the ellipticity angle χ.
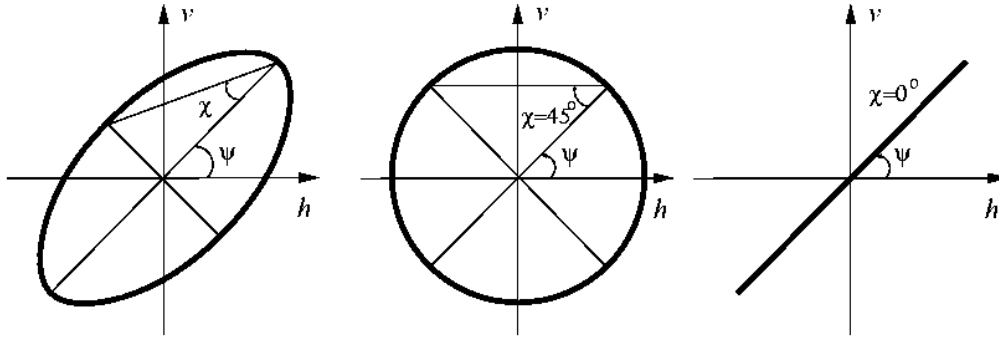
Fig. 5.2: Representation of the polarisation ellipse in the ($\vec{h}$, $\vec{v}$) plane.

The orientation angle ψ, defined as the angle between the major axis of the ellipse and the x-axis, expresses the inclination of the ellipse and is limited between 0° and 180°. The ellipticity angle χ, defined as the ratio between two minor semi-axes of the ellipse (*a* and *b* axis),

$$\tan \chi = \pm \frac{b}{a} \qquad (5.4)$$

describes the shape of the ellipse and varies by definition between – 45° and 45°. At $\chi = 0°$ the ellipse degenerate to a straight line with inclination given by the orientation angle ψ, corresponding to linear states. In this case, $\psi = 0$ defines horizontally polarised waves, while $\psi = 90°$ expresses vertically polarised waves. For $\chi = \pi/4$, the ellipse becomes a circle, describing circular polarisation states. Ellipticity angles between 0° and 45° describe elliptical polarised waves. The ellipticity angle χ defines also the sense of rotation of the *E* vector. If $\chi < 0$, then the rotation is right-handed, otherwise, for $\chi > 0$, the rotation is left-handed (in the IPU System of Conventions). Note that the sense of rotation is related to the direction of wave propagation and thus depends on its definition (MOTT 1992) as compiled in Tab. 5.1.

	Horizontal	Vertical	Linear +45°	Linear at +135°	Left Circular	Right Circular
Orientation ψ	90°	0°	45°	135°	0° to 180°	0° to 180°
Ellipticity χ	0°	0°	0°	0°	45°	-45°
Complex Ratio ρ	∞	0	1	-1	i	$-i$

Tab. 5.1: Polarisation descriptors for characteristic polarisation states

In general, a plane monochromatic electromagnetic wave has potentially four degrees of freedom. Two of them are needed for the description of the polarisation state of the wave. As already mentioned, the two polarisation angles constitute such a real pair of parameters for the description of the polarimetric state of the wave in terms of the shape of the polarisation ellipse. Apart from the polarisation state, two additional parameters are necessary for a complete wave

description: the wave amplitude A_0, corresponding to the wave intensity and the size of the polarisation ellipse and an initial absolute phase reference ϕ_0. Both of them are wave characteristics and not polarisation parameters, i.e. they are not essential for the definition of the polarimetric state of the wave, and will be occasionally ignored in the following.

In Eq. (5.3), the complex amplitude of the electric field $\vec{E}$ is represented as a linear combination of two orthogonal linear polarisations $\bar{h}$ and $\bar{v}$ weighted by their corresponding complex amplitudes E_h and E_v. This description of the electric field vector may be considered as a component representation of the electric field vector in a two-dimensional complex space with respect to the $\{\bar{h}, \bar{v}\}$ basis. In this context, an alternative representation of a monochromatic plane wave in the two-dimensional complex space as a linear combination of two arbitrary orthonormal polarisation states can be introduced. Accordingly, defining two orthonormal polarisation states, denoted by $\vec{\varepsilon}_m$ and $\vec{\varepsilon}_n$, which establish a polarisation reference basis $\{\vec{\varepsilon}_m, \vec{\varepsilon}_n\}$, a given plane wave $\vec{E}$ can be decomposed into its projections onto the basis polarisations as

$$\vec{E} = E_m \vec{\varepsilon}_m + E_n \vec{\varepsilon}_n \qquad \text{where} \quad \vec{\varepsilon}_m \vec{\varepsilon}_m = \vec{\varepsilon}_n \vec{\varepsilon}_n = 1 \quad \text{and} \quad \vec{\varepsilon}_m \vec{\varepsilon}_n = 0 \qquad (5.5)$$

Using the complex amplitudes E_m and E_n, the plane wave can be alternately represented in terms of a two-dimensional complex vector $\vec{E}_{mn}$

$$\vec{E}_{mn} := \begin{bmatrix} E_m \\ E_n \end{bmatrix} \qquad (5.6)$$

called the Jones vector as first introduced by Jones (JONES 1941, JONES(a) 1941, GRAVES 1956), which describes completely a coherent plane wave (also known as the Sinclair vector in radar polarimetry when using the IEEE Standard notation). In order to demonstrate the equivalence between the real and complex space representation of a plane wave. The Jones vector can be addressed in terms of the orientation angle ψ, the ellipticity angle χ, the wave amplitude A_0 and the initial phase ϕ_0 as (FERRO-FAMIL 2000)

$$\vec{E}_{mn} = A_0 e^{-i\phi_0} \begin{bmatrix} \cos\psi & -\sin\psi \\ \sin\psi & \cos\psi \end{bmatrix} \begin{bmatrix} \cos\chi \\ -i\sin\chi \end{bmatrix} \qquad (5.6a)$$

Based on the Jones vector, a complex polarisation descriptor can be introduced, namely the complex polarisation ratio ρ, defined as the ratio of the orthogonal complex electric field components (BOERNER et al. 1981, KOSTINSKI & BOERNER 1986, AZZAM & BASHARA 1988, BOERNER et al. 1998)

$$\rho \ := \ \frac{E_n}{E_m} = \frac{a_n}{a_m} e^{i(\delta_n - \delta_m)} \ = \ \tan a \cdot e^{(i\delta)} \tag{5.7}$$

where $\tan \alpha \ = \ \alpha_n / a_m$ with $0 \ < \ \alpha \ < \ \pi/2$ and $\delta \ = \ \delta_n - \delta_m$ with $0 < \delta < 2\pi$. The two angles α and δ, are known as the Deschamps parameters (DESCHAMPS 1941), and constitute an alternative two parameters real set for the description of the polarisation state of a wave in terms of an amplitude ratio and a phase difference.

As a complex scalar, the complex polarisation ratio ρ has two degrees of freedom, expressed by the two Deschamps angles, and allows the mapping of polarisation states onto the two-dimensional complex plane. It should be pointed out that with the information of the polarisation ratio the absolute magnitude and phase of the polarisation ellipse is lost. According to Eq. (5.7) linear polarisations are represented by a real ρ ($\delta = 0$ or $\chi = 0$), while elliptic polarisations are represented by a complex ρ (i.e., $\delta \neq 0$ or $\chi \neq 0$). The complex polarisation ρ can be expressed as a function of the polarisation angles χ and ψ as (BORN & WOLF 1985)

$$\rho \ = \ \frac{\cos 2\chi \sin 2\psi \ + \ i \sin 2\chi}{1 \ + \ \cos 2\chi \cos 2\psi} \tag{5.8}$$

Tab. 5.1 summarises the descriptions in terms of χ and ψ as well as ρ referred to a Cartesian basis for some characteristic polarisation states.

5.2 Change of Polarisation Basis

As discussed in the previous section, a monochromatic plane wave can be expressed as a linear combination of two orthonormal linear polarisation states defining the reference polarisation basis. The representation of the wave depends, of course, on the choice of the reference basis. Here, it is important to realise that the polarisation of a wave is independent of any reference basis, but its representation depends on the chosen reference frame. As the only requirement for building up such a basis is orthogonality, an infinite number of such bases can be used for the wave description. In the following, the change of the wave representation as a consequence of changing the reference basis is addressed. For this, two orthonormal polarisation bases $\{\bar{\varepsilon}_m, \ \bar{\varepsilon}_n\}$ and $\{\bar{\varepsilon}_i, \ \bar{\varepsilon}_j\}$ are considered, for which a given plane wave $\bar{E}$ can be represented as follows

$$\bar{E} = \bar{\varepsilon}_m E_m \ + \ \bar{\varepsilon}_n E_n = \bar{\varepsilon}_i E_i \ + \ \bar{\varepsilon}_j E_j \tag{5.9}$$

The corresponding Jones vectors are

$$\bar{E}_{mn} = \begin{bmatrix} E_m \\ E_n \end{bmatrix} \quad \text{and} \quad \bar{E}_{ij} = \begin{bmatrix} E_i \\ E_j \end{bmatrix} \tag{5.10}$$

The transformation of the Jones vector from the $\{\bar{\varepsilon}_m, \ \bar{\varepsilon}_n\}$ basis into the corresponding Jones vector in the $\{\bar{\varepsilon}_i, \ \bar{\varepsilon}_j\}$ basis is a linear transformation in the two-dimensional complex space. Thus, it will be controlled by a 2x2 complex transformation matrix $[U_2]$

$$\bar{E}_{ij} = [U_2]\bar{E}_{mn} \tag{5.11}$$

The transformation matrix $[U_2]$ is a special unitary 2x2 complex matrix, i.e. $[U_2]$ is unitary and has a unit determinant. Both constraints are required to ensure that the amplitude of the wave remains the same (unitarity) and that the phase of the wave is consistently defined in the new polarisation basis (det ($[U_2]$)=1) (BOERNER *et al.* 1998). $[U_2]$ can be expressed in terms of the orientation angle ψ, the ellipticity χ and the initial phase ϕ_0 as (FERRO-FAMIL 2000)

$$[U_2] = \begin{bmatrix} \cos\psi & -\sin\psi \\ \sin\psi & \cos\psi \end{bmatrix} \begin{bmatrix} \cos\chi & i\sin\chi \\ i\sin\chi & \cos\chi \end{bmatrix} \begin{bmatrix} e^{-i\phi_0} & 0 \\ 0 & e^{i\phi_0} \end{bmatrix} \tag{5.11a}$$

or in terms of the complex polarisation ratio ρ of the first Jones vector of the new basis (BOERNER *et al.* 1998)

$$[U_2] = \frac{1}{\sqrt{1+\rho\rho^*}} \begin{bmatrix} 1 & -\rho^* \\ \rho & 1 \end{bmatrix} \begin{bmatrix} \exp(-i\delta) & 0 \\ 0 & \exp(i\delta) \end{bmatrix} \tag{5.11b}$$

where

$$\delta = \arctan(\tan(\psi)\tan(\chi)) \ - \ \phi_0 \tag{5.12}$$

The angle δ represents a phase reference for the new basis states and is required for the determination of the initial phase of the Jones vector in the new reference basis.

5.3 Partially Polarised Waves

Until now completely polarised monochromatic plane waves were considered. As stated above, the polarisation state of such waves is completely described in terms of a single polarisation ellipse or a single Jones vector. A second important class of waves are the so-called quasi monochromatic or partially polarised waves. Such waves can be considered as wave packets of multiple frequencies of a bandwidth centered at the mean wave frequency. In contrast to completely polarised waves for which both the amplitude and the phase of the electric field are independent of time and space, partially polarised waves are characterised by temporally and

/or spatially varying electric field amplitude, phase and polarisation. Thus, the electric field vector no longer describes a well defined ellipse but one that varies in time. In this case, polarisation can be defined only in the sense of statistical averaging over time.

To advance the analysis of partially polarised waves, the concept of a wave coherency matrix was introduced (BORN & WOLF 1985). This matrix is defined, using the outer product of the corresponding Jones vector averaged over a coherency time (BORN & WOLF 1985, MOTT 1992, BOERNER *et al*. 1998), as

$$[J] = \left\langle \vec{E}_{mn} \cdot \vec{E}_{mn}^+ \right\rangle = \begin{bmatrix} \left\langle E_m E_m^* \right\rangle & \left\langle E_m E_n^* \right\rangle \\ \left\langle E_n E_m^* \right\rangle & \left\langle E_n E_n^* \right\rangle \end{bmatrix} = \begin{bmatrix} J_{mm} & J_{mn} \\ J_{nm} & J_{nn} \end{bmatrix} \tag{5.13}$$

Formally, the coherency matrix is a 2x2 hermitian positive semi definite matrix, whose elements are proportional to the second order moments of the elements of the complex Jones vector. The diagonal elements of the matrix corresponds to the intensities of each of them so that the trace of [*J*] equals the total intensity of the wave. The off-diagonal elements contain the cross-correlation between the elements of the Jones vector and express the amount of correlated structure in the field. In absence of any correlation between E_m and E_n, are find that $J_{mn} = J_{nm} = 0$, and [*J*] becomes diagonal with equal diagonal elements. In this case, the wave does not contain any polarised structure and is called totally unpolarised. Such a wave has only one degree of freedom, namely its amplitude. On the other hand, if $J_{mn}J_{nm} = J_{mm}J_{nn}$, (i.e., det([*J*]) = 0) the correlation between E_m and E_n is maximum, and the wave is completely polarised. In this case, the wave has four degrees of freedom. Between these two extreme cases lies the general case of partial polarisation (det([*J*]) > 0) with a certain amount of correlation between E_m and E_n.

It becomes evident that the description of partially polarised waves requires, apart from the two parameters needed to describe the polarisation state, also the degree of polarisation (BORN & WOLF 1985, MOTT 1992, BOERNER *et al*. 1998). Consequently, they can not be described by a Jones vector, which contains only two degrees of freedom, but require for their complete description the complete wave coherency matrix. Finally, it has to be noted that as the trace and the determinant of a hermitian matrix are invariants under unitary transformations, both the total wave intensity as well as the degree of polarisation are not affected under polarisation basis transformations.

5.4 The Polarimetric Scattering Problem

Up to now the description of the polarimetric properties of plane waves has been discussed. The next step is to consider the polarimetric properties of the interaction of waves with scattering objects. In general the scattering process can be addressed as follows: A fully polarised

monochromatic plane wave $\vec{E}^i$ is emitted by a transmitting antenna, with a defined polarisation state, and propagates in direction of $\vec{k}_i$ towards a scatterer. In a right-handed orthogonal coordinate system $(\vec{h}_i,\ \vec{v}_i,\ \vec{k}_i)$ located at the transmitting antenna, the transmitted wave can be written as

$$\vec{E}^i = E_h^i \vec{h}_i + E_v^i \vec{v}_i ,$$ (5.14)

The wave interacts with the scatterer, which may change its polarisation and/or degree of polarisation, and becomes scattered with a directional characteristic depending on the scatterer. A receiving antenna, located in a direction $\vec{k}_s$ in the far field region of the scatterer (where the scattered wave is considered to be a plane wave), receives the scattered wave $\vec{E}^s$. In a right-handed orthogonal coordinate system $(\vec{h}_s,\ \vec{v}_s,\ \vec{k}_s)$, located at the receiving antenna, the received wave can be written as

$$\vec{E}^s = E_h^s \vec{h}_s + E_v^s \vec{v}_s .$$ (5.15)

Two conventions to define the scattered wave coordinate system $(\vec{h}_s,\ \vec{v}_s,\ \vec{k}_s)$ with respect to the incident wave coordinate system $(\vec{h}_i,\ \vec{v}_i,\ \vec{k}_i)$ can be found in the literature (ULABY & ELACHI 1990, LÜNEBURG 1995). The first one is known as the *Forward Scattering Alignment* convention and is mainly used in bistatic scattering problems. The second one is known as the *Back-Scattering Alignment* convention is preferred used in radar backscattering problems, and it is the one explicitly used in this study (BOERNER *et al.* 1998).

The scattering process can be regarded as a transformation of the incident wave into the scattered wave performed by the scatterer. This transformation may change the polarisation state of the wave and its degree of polarisation. Using the Jones vector representation for the incident and scattered waves (actually, the Sinclair backscattering vector is here implemented)

$$\vec{E}^i = \begin{bmatrix} E_h^i \\ E_v^i \end{bmatrix} \quad \text{and} \quad \vec{E}^s = \begin{bmatrix} E_h^s \\ E_v^s \end{bmatrix} .$$ (5.16)

this transformation can be represented by a 2x2 complex matrix [S] as

$$\vec{E}^s = [S]\vec{E}^i \rightarrow \begin{bmatrix} E_h^s \\ E_v^s \end{bmatrix} = \frac{e^{ikr}}{r} \begin{bmatrix} S_{HH} & S_{HV} \\ S_{VH} & S_{VV} \end{bmatrix} \begin{bmatrix} E_h^i \\ E_v^i \end{bmatrix} ,$$ (5.17)

This 2x2 complex matrix is known as the radar scattering matrix [*S*] and is the basic concept of radar polarimetry (SINCLAIR 1950, KENNAUGH 1949-1954, VAN DE HULST 1985, KOSTINSKI & BOERNER 1986, MOTT 1992, BOERNER *et al.* 1998).
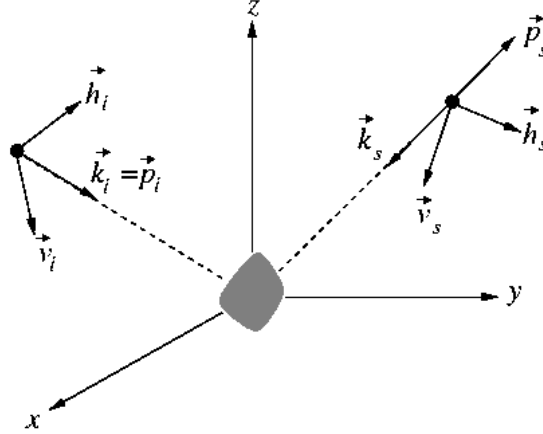
Fig. 5.3: BSA scattering geometry

$$[S] = \frac{e^{ikr}}{r} \begin{bmatrix} S_{HH} & S_{HV} \\ S_{VH} & S_{VV} \end{bmatrix},$$

(5.18)

The factor e^{ikr}/r expresses the wave attenuation occurring during the travel time from the transmitter to the scatterer and as well as the corresponding phase shift (k is the wave number) and is not of interest for conventional polarimetric applications. However, in SAR interferometry and polarimetric interferometry, this phase shift becomes important as it allows the estimation of the three-dimensional location of the scatterer.

The four elements of the scattering matrix S_{ij} (i, $j = H$ or V) are known as the complex scattering amplitudes and are related to the corresponding radar cross section values σ_{ij}^0 as in the $\{H, V\}$ polarisation basis (KENNAUGH 1952):

$$S_{HH} = c \cdot e^{-i\varphi_{HH}} \sqrt{\sigma_{HH}^0}$$
$$S_{HV} = c \cdot e^{-i\varphi_{HV}} \sqrt{\sigma_{HV}^0}$$
$$S_{VH} = c \cdot e^{-i\varphi_{VH}} \sqrt{\sigma_{VH}^0}$$
$$S_{VV} = c \cdot e^{-i\varphi_{VV}} \sqrt{\sigma_{VV}^0}$$

(5.19)

where c is scalar calibration factor. The span of $[S]$, which is defined by the sum of the squares of the absolute values of the complex scattering amplitudes, corresponds to the total power scattered by the scatterer, which is an invariant (BOERNER *et al.* (1982)):

$$TP := |S_{HH}|^2 + |S_{HV}|^2 + |S_{VH}|^2 + |S_{VV}|^2 \tag{5.20}$$

Ignoring an absolute phase factor, the scattering matrix contains in the general bistatic case seven independent parameters, four amplitudes and three relative phases. In the monostatic case, where receiver and transmitter are located at the same position, the $[S]$ matrix becomes symmetric in a reciprocal scattering medium, i.e. $S_{HV} = S_{VH}$ and is known as the symmetric Sinclair matrix (VAN DE HULST 1957, MOTT 1992). This symmetry holds, for all reciprocal propagation and scattering media. Consequently, the number of independent parameters in $[S]$ is reduced in backscattering down to five parameters expressed by three amplitudes and two relative phases.

Eq. (5.17) underlines the power of the scattering matrix concept: For a given frequency and scattering geometry, the scattering matrix depends only on the scatterer and not on the polarisation of the wave used for its measurement. Changing the polarisation of the incident wave, the scattered wave changes accordingly, while $[S]$ remains the same. Note that the form of the scattering matrix depends of course on the choice of the basis used to describe the incident and scattered waves, a fact which is discussed later on in Section 5.7

The scattering matrix can be measured by transmitting two orthogonal polarisations on a pulse to pulse basis and receiving the scattered waves in two orthogonal polarisations (commonly the same as used for transmission). Most polarimetric systems operate in the *H*, *V* basis where by transmitting in a first cycle a *H* polarised wave and receiving in the *H* and *V* polarisations the S_{HH} and S_{VH} scattering coefficients are measured, while the remaining coefficients S_{HV} and S_{VV} are measured in a second cycle where a *V* polarised wave is transmitted and *H* and *V* polarisations are received.

5.5 Scattering Vector

In order to extend the concept of the scattering matrix to describe the scattering behaviour of distributed scatterers, the concept of the scattering vector is introduced in this section. Alternatively to the matrix formulation of Eq. (5.18), the polarimetric scattering problem can be addressed in a vectorial formulation using the concept of system vectors (BOERNER & AL-ARINI 1981, KOSTINSKI & BOERNER 1986, BEBBINGTON 1992, CLOUDE & POTTIER 1996). This approach replaces the scattering matrix $[S]$ by an equivalent four-dimensional complex scattering vector k_4 defined by

$$[S] = \begin{bmatrix} S_{HH} & S_{HV} \\ S_{VH} & S_{VV} \end{bmatrix} \rightarrow \vec{k}_4 := V([S]) = \frac{1}{2} Trace([S]\psi) = [k_0, \ k_1, \ k_2, \ k_3]^T \qquad (5.21)$$

where V ([S]) is the matrix vectorisation operator, *Trace* ([S]) is the sum of the diagonal elements of [S] and ψ is a complete set of 2x2 complex basis matrices under a hermitian inner product (CLOUDE 1986). There are several basis sets that can be used for the vectorisation of [S]. Two of them are usually used in the literature: the first one ψ_L is known as the lexicographic basis, which corresponds to a straightforward ordering of the elements of [S]

$$\psi_L := \left\{ 2 \begin{bmatrix} 1 & 0 \\ 0 & 0 \end{bmatrix}, \ 2 \begin{bmatrix} 0 & 1 \\ 0 & 0 \end{bmatrix}, \ 2 \begin{bmatrix} 0 & 0 \\ 1 & 0 \end{bmatrix}, \ 2 \begin{bmatrix} 0 & 0 \\ 0 & 1 \end{bmatrix} \right\}, \qquad (5.22)$$

Performing the vectorisation of [S] by using the lexicographic basis matrices, we obtain the corresponding scattering vector as

$$\vec{k}_{4L} = [S_{HH}, \ S_{HV}, \ S_{VH}, \ S_{VV}]^T \qquad (5.23)$$

The advantage of the resulting scattering vector is that its elements are given by the amplitudes of the scattering matrix, and thus, are directly related to the system measurables.

The second important basis used for the vectorisation of the scattering matrix is given by the set of the four Pauli spin matrices ψ_P as

$$\psi_P : \left\{ \sqrt{2} \begin{bmatrix} 1 & 0 \\ 0 & 1 \end{bmatrix}, \ \sqrt{2} \begin{bmatrix} 1 & 0 \\ 0 & -1 \end{bmatrix}, \ \sqrt{2} \begin{bmatrix} 0 & 1 \\ 1 & 0 \end{bmatrix}, \ \sqrt{2} \begin{bmatrix} 0 & -i \\ i & 0 \end{bmatrix} \right\} \qquad (5.24)$$

The vectorisation of [S] carried out by using the Pauli matrices basis set, leads to the Pauli scattering vector for the bistatic case with the explicit form

$$\vec{k}_{4P} = \frac{1}{\sqrt{2}} [S_{HH} + S_{VV}, \ S_{HH} - S_{VV}, \ S_{HV} + S_{VH}, \ i(S_{HV} - S_{VH})]^T \qquad (5.25)$$

The advantage of using the Pauli matrix basis lies in the straightforward physical interpretation of the Pauli matrices in terms of elementary scattering mechanisms as well as relative polarisation plane preservation.

♦ The first Pauli matrix can be interpreted as the scattering matrix of an isotropic "odd"-bounce scatterer. Such scatterers are characterised by $S_{HH} = S_{VV}$ and $S_{HV} = S_{VH} = 0$. Spheres, flat surfaces or trihedral corner reflectors are typically scatterers of this type.

♦ The second Pauli matrix is also diagonal but generates a π phase difference between the diagonal elements. It indicates isotropic "even"-bounce scattering which is characterised by $S_{HH} = -S_{VV}$ and $S_{HV} = S_{VH} = 0$ as from dihedral corner reflectors.

♦ The third Pauli matrix can be interpreted as the scattering matrix of an isotropic "even"-bounce scatterer with a relative orientation of $\pi/4$ with respect to the horizontal, because it may be obtained from the second Pauli matrix by rotation of the $(\bar{\varepsilon}_H, \bar{\varepsilon}_V)$ reference basis by $\pi/4$.

♦ The fourth Pauli matrix represents a scatterer, which transforms all incident polarisation states into their orthogonal states. As it is asymmetric, i.e. $S_{HV} \neq S_{VH}$, it does not appear in backscattering, unless the medium is not reciprocal (Faraday rotation effect).

Thus, the Pauli scattering vector is closely related to the physics of wave scattering (CLOUDE 1986). A second important advantage of the Pauli compared to the Lexicographic scattering vector relies on the close relationship between the Pauli matrices and its manipulations. This relationship leads to a simplified formation of line of sight rotation (LOS) relations in terms of scatterers, antenna and the Pauli scattering vector as they will be discussed in Section 5.8.

In the case of backscattering from a reciprocal scatterer, one of the elements of the target vector is redundant, and the reduced three-component scattering vector are usually introduced for a simplified formulation. As follows in case of the lexicographic scattering vector

$$\bar{k}_{3L} = \left[S_{HH}, \sqrt{2}S_{HV}, S_{VV} \right]^T \tag{5.26}$$

and the corresponding three dimensional Pauli scattering vector

$$\bar{k}_{3P} = \frac{1}{\sqrt{2}} \left[S_{HH} + S_{VV}, S_{HH} - S_{VV}, 2S_{HV} \right]^T \tag{5.27}$$

The factor $\sqrt{2}$ in Eq. (5.26) is required in order to keep the norm (total power) of the three dimensional vector consistent with its four dimensional representation (BOERNER *et al.* 1982).

The transformation of the three-dimensional scattering vector from its Pauli basis into its lexicographic basis representation, and vice versa, is given by

$$\bar{k}_{3P} = [D_3]\bar{k}_{3L} \qquad \text{and} \qquad \bar{k}_{3L} = [D_3]^{-1}\bar{k}_{3P} \tag{5.28}$$

where [D$_3$] is a 3x3 special unitary matrix (BOERNER *et al.* 1998)

$$[D_3] = \frac{1}{\sqrt{2}} \begin{bmatrix} 1 & 0 & 1 \\ 1 & 0 & -1 \\ 0 & \sqrt{2} & 0 \end{bmatrix} \qquad \text{and} \qquad [D_3]^{-1} = [D_3]^T = \frac{1}{\sqrt{2}} \begin{bmatrix} 1 & 1 & 0 \\ 0 & 0 & \sqrt{2} \\ 1 & -1 & 0 \end{bmatrix} \qquad (5.29)$$

The scattering vector contains exactly the same information as the scattering matrix, and thus, it is also characterised by five degrees of freedom. The main advantage of using the scattering vector instead of the scattering matrix is that it enables the introduction of a scattering covariance matrix (similar to the concept of the wave covariance matrix discussed in Section 5.3), in order to describe statistical scattering effects which cannot be described by a single scattering matrix (CLOUDE 1997, PAPATHANASSIOU 1999).

In the remaining of this work, only the scattering problem in backscattering will be considered because it is the relevant case for conventional SAR remote sensing applications. In this case, the scattering problem becomes three-dimensional and therefore only the three-dimensional formulation for the scattering vector and the coherency/covariance matrices will be used. Thus in the following the subscript 3 will be dropped.

5.6 Distributed Scatterers

Up to now only deterministic scatterers were considered, described completely by a single scattering matrix or alternatively by a single scattering vector. However, in most Geoscience radar applications, the scatterers are embedded in a dynamic environment and are, therefore, affected by spatial and/or time variations (AZZAM & BASHARA 1989). These scatterers, called partial scatterers, can no longer be completely described by a single scattering matrix. One important class of partial scatterers are spatially distributed scatterers, as most of the natural terrain surfaces are. They may be considered to be composed statistically homogeneous of randomly distributed deterministic scattering centres. The scattering behaviour of each of these individual scattering centres is completely described by a single scattering matrix $[S_i]$. On the strength of the finite resolution of such radar systems, the measured scattering matrix consists of the coherent superposition of the individual scattering matrices $[S_i]$ of all scattering centers residing in the resolution cell. For another resolution element of the same scatterer, the measured scattering matrix $[S_i]$ may be different due to the different spatial disposition of the individual scattering objects. Note that this is the same physical effect as the generation of speckle discussed in section 4.4.

To advance the analysis of partial scatterers in the complex domain, the concept of a scatterer covariance or coherency matrix has been introduced. The 3x3 polarimetric covariance matrix $[C_3]$ is defined by using the outer product of the 3 dimensional lexicographic scattering vector (BOERNER & EL-ARINI 1981, BOERNER et al. 1998, TRAGL 1990, LÜNEBURG et al.1991)

$$[C] := \left\langle \vec{k}_L \cdot \vec{k}_L^+ \right\rangle = \begin{bmatrix} \left\langle |S_{HH}|^2 \right\rangle & \sqrt{2}\left\langle S_{HH}S^*_{HV} \right\rangle & \left\langle S_{HH}S^*_{VV} \right\rangle \\ \sqrt{2}\left\langle S_{HV}S^*_{HH} \right\rangle & 2\left\langle |S_{HV}|^2 \right\rangle & \sqrt{2}\left\langle S_{HV}S^*_{VV} \right\rangle \\ \left\langle S_{VV}S^*_{HH} \right\rangle & \sqrt{2}\left\langle S_{VV}S^*_{HV} \right\rangle & \left\langle |S_{VV}|^2 \right\rangle \end{bmatrix} \quad (5.30)$$

where $<\dots>$ indicates spatial averaging, assuming homogeneity of the random scattering medium. Homologous, the 3x3 polarimetric coherency matrix $[T_3]$ is defined by using the outer product of the 3 dimensional Pauli scattering vector (CLOUDE 1992)

$$[T] := \left\langle \vec{k}_P \cdot \vec{k}_P^+ \right\rangle = \begin{bmatrix} \left\langle |S_{HH}+S_{VV}|^2 \right\rangle & \left\langle (S_{HH}+S_{VV})(S_{HH}-S_{VV})^* \right\rangle & 2\left\langle (S_{HH}+S_{VV})S^*_{HV} \right\rangle \\ \left\langle (S_{HH}-S_{VV})(S_{HH}+S_{VV})^* \right\rangle & \left\langle |S_{HH}-S_{VV}|^2 \right\rangle & 2\left\langle (S_{HH}-S_{VV})S^*_{HV} \right\rangle \\ 2\left\langle S_H(S_{HH}+S_{VV})^* \right\rangle & 2\left\langle S_{HV}(S_{HH}-S_{VV})^* \right\rangle & 4\left\langle |S_{HV}|^2 \right\rangle \end{bmatrix} (5.31)$$

$[C]$ and $[T]$ are two equivalent ways for the description of distributed scatterers and contain the same information. Both matrices are by definition hermitian positive semi definite, which implies that they have real non-negative eigenvalues and orthogonal, and are in general of full rank 3. The rank of a matrix is defined as the maximum number of linearly independent columns (or rows) of the matrix (BROYDEN 1975). With respect to the physical information content of the coherency (or covariance) matrix, the rank of [T] (or [C]) can be regarded as the amount of linear independent contribution in which [T] can be decomposed. A rank 3 coherency matrix implies the existence of 3 linearly non-zero eigenvectors. The physical interpretation of the eigenvalues and eigenvectors will be discussed in following sections. Without ensemble averaging both matrices have rank 1. Finally, for deterministic scatterers as point scatterers, the ensemble averaging becomes irrelevant as the corresponding matrices are of rank 1.

Both matrices describe completely a reciprocal partial scatterer. They contain nine independent parameters, three real power values in the main diagonal and three off-diagonal complex cross-correlations, which contain the information of correlation between the complex elements of $[S]$ over the spatial averaging. The relation between $[C]$ and $[T]$ can be established by using the transformation of the corresponding scattering vectors in Eq. (5.28) (CLOUDE 1986)

$$[T] = \left\langle \vec{k}_P \cdot \vec{k}_P^+ \right\rangle = \left\langle [D_3]\vec{k}_L \cdot \vec{k}_L^+[D_3]^+ \right\rangle = [D_3]\left\langle \vec{k}_L \cdot \vec{k}_L^+ \right\rangle[D_3]^+ = [D_3][C][D_3]^+ \quad (5.32)$$

Performing the matrix multiplication, the elements of $[T]$ can be expressed in terms of the elements of $[C]$ as

$$[T] = \frac{1}{2}\begin{bmatrix} c_1+c_6+c_3^*+c_3 & c_1-c_3+c_3^*-c_6 & \sqrt{2}(c_2+c_5^*) \\ c_1+c_3-c_3^*-c_6 & c_1+c_6-c_3^*-c_3 & \sqrt{2}(c_2-c_5^*) \\ \sqrt{2}(c_5+c_2^*) & \sqrt{2}(c_2^*-c_5) & 2c_4 \end{bmatrix}, \ [C] = \begin{bmatrix} c_1 & c_2 & c_3 \\ c_2^* & c_4 & c_5 \\ c_3^* & c_5^* & c_6 \end{bmatrix} (5.33)$$

Similarly, the transformation of $[T]$ into $[C]$ is obtained by using again Eq.(5.28)

$$[C] = \langle \vec{k}_L \cdot \vec{k}_L^+ \rangle = \langle [D_3] \vec{k}_P \cdot \vec{k}_P^+ [D_3]^+ \rangle = [D_3] \langle \vec{k}_P \cdot \vec{k}_P^+ \rangle [D_3]^+ = [D_3][T][D_3]^+ \quad (5.34)$$

and the elements of $[C]$ can be expressed in terms of the elements of $[T]$ as

$$[C] = \frac{1}{2} \begin{bmatrix} t_1 + t_4 + t_2^* + t_2 & \sqrt{2}(t_3 + t_5) & t_1 - t_4 + t_2^* - t_2 \\ \sqrt{2}(t_3^* + t_5^*) & 2t_6 & \sqrt{2}(t_3^* - t_5^*) \\ t_1^* - t_4^* - t_2 - t_2^* & \sqrt{2}(t_3 - t_5) & t_1 + t_4 - t_2^* - t_2 \end{bmatrix}, \quad [T] = \begin{bmatrix} t_1 & t_2 & t_3 \\ t_2^* & t_4 & t_5 \\ t_3^* & t_5^* & t_6 \end{bmatrix} (5.35)$$

Since the transformations in Eq. (5.32) and Eq. (5.33) are unitary similarity transformations, both matrices have the same eigenvalues but different eigenvectors. Both matrices are in general of full rank 3, i. e., they have three nonzero eigenvalues.

There is a final note to be made on the formation of the coherency (or covariance) matrix. Compared to the scattering matrix data, coherency (or covariance) matrix data have a reduced resolution because of the spatial averaging needed for the formation of the $[T]$ (or $[C]$) matrix. This loss of resolution is especially critical for point scatterers as for distributed scatterers the loss is compensated by a reduced speckle noise because of the multilooking effect. This trade-off between high resolution required for point scatterers and reduced speckle noise over distributed scatterers can be resolved by applying an adaptive polarimetric speckle filter instead of a box filter for the formation of the coherency (or covariance) matrix, which was first introduced by J.-S. Lee (LEE *et al.* 1999). Such filters perform a multilooking filtering process on distributed scatterers, leading to a matrix with rank greater than one, while point scatterers or edges remain unfiltered leading thus, as expected, to a rank one matrix.

In the following of this work, the scattering problem will be addressed only in terms of the Pauli scattering vector and the coherency scattering matrix.

5.7   Basis Transformations of the Scattering Matrices

As already discussed, the scattering matrix depends on the choice of the reference basis used to describe the polarisation state of the incident and scattered waves. In this section, the effect of changing the polarisation reference basis on $[S]$ will be addressed (BOERNER *et al* 1998).

5.7.1 Scattering Matrix Transformation

In Section 5.2, the effect of changing the polarisation reference basis of the Jones Vector of a plane wave has been described by a 2x2 special unitary matrix $[U_2]$

$$[U_2] = \frac{1}{\sqrt{1+\rho\rho^*}} \begin{bmatrix} 1 & -\rho^* \\ \rho & 1 \end{bmatrix} \begin{bmatrix} \exp(-i\delta) & 0 \\ 0 & \exp(i\delta) \end{bmatrix} \text{ with } [U_2]^{-1} = [U_2]^+ \qquad (5.36)$$

The same $[U_2]$ matrix describes the analogous change of basis transformation of the $[S]$ matrix as changing the polarisation basis of $[S]$ does not mean anything more but changing the polarisation basis of the corresponding incident and scattered Jones vectors.

In this sense, the basis transformation of the scattering matrix $[S]_{HV}$ referred to the $\{\bar{\varepsilon}_H, \bar{\varepsilon}_V\}$ into the scattering matrix basis $[S]_{IJ}$ referred to the $\{\bar{\varepsilon}_I, \bar{\varepsilon}_J\}$ polarisation basis can be written as (BOERNER *et al*. 1998, POTTIER 1998)

$$[S]_{IJ} = [U_2][S]_{HV}[U_2]^T \qquad (5.37)$$

According to Eq.(5.37) the knowledge of the scattering matrix in one polarisation basis allows us to derive the scattering matrix in any other orthonormal polarisation basis by using the change of basis transformation. This is exactly the great advantage of polarimetric radar systems over conventional radar sensors operating in a single or dual polarisation mode. The individual components of the scattering matrix in the new polarisation basis are then given as complex linear combinations of the elements of the scattering matrix in the original measured basis. Performing the matrix multiplication of Eq. (5.37),

$$\begin{bmatrix} S_{II} & S_{IJ} \\ S_{JI} & S_{JJ} \end{bmatrix} = \frac{1}{1+\rho\rho^*} \begin{bmatrix} 1 & -\rho^* \\ \rho & 1 \end{bmatrix} \begin{bmatrix} \exp(-i\delta) & 0 \\ 0 & \exp(i\delta) \end{bmatrix} \begin{bmatrix} S_{HH} & S_{HV} \\ S_{VH} & S_{VV} \end{bmatrix} \begin{bmatrix} \exp(-i\delta) & 0 \\ 0 & \exp(i\delta) \end{bmatrix} \begin{bmatrix} 1 & \rho^* \\ -\rho & 1 \end{bmatrix} (5.38)$$

the components of the scattering matrix in the new polarisation basis, characterised by a complex polarisation ratio ρ, are obtained as a function of the elements of the scattering matrix in the original basis as

$$S_{II} = \frac{1}{1+\rho\rho^*}\left[S_{HH}\cdot e^{-i2\delta} - \rho^* S_{HV} - \rho^* S_{VH} + \rho^{*2}S_{VV}\cdot e^{i2\delta}\right]$$

$$S_{IJ} = \frac{1}{1+\rho\rho^*}\left[\rho S_{HH}\cdot e^{-i2\delta} + S_{HV} - \rho\rho^* S_{VH} - \rho^* S_{VV}\cdot e^{i2\delta}\right]$$

$$\qquad (5.39)$$

$$S_{JI} = \frac{1}{1+\rho\rho^*}\left[\rho S_{HH}\cdot e^{-i2\delta} - \rho\rho^* S_{HV} + S_{VH} - \rho^* S_{VV}\cdot e^{i2\delta}\right]$$

$$S_{JJ} = \frac{1}{1+\rho\rho^*}\left[\rho^2 S_{HH}\cdot e^{-i2\delta} + \rho S_{HV} + \rho S_{VH} + S_{VV}\cdot e^{i2\delta}\right]$$

In the case of backscattering from reciprocal media, $S_{HV} = S_{VH}$ and $S_{ij} = S_{ji}$, Eq. (5.39) reduces to

$$S_{II} = \frac{1}{1 + \rho\rho^*}\left[S_{HH} \cdot e^{-i2\delta} - 2\rho^* S_{XX} + \rho^{*2} S_{VV} \cdot e^{i2\delta}\right]$$

$$S_{IJ} = \frac{1}{1 + \rho\rho^*}\left[\rho S_{HH} \cdot e^{-i2\delta} + (1 - \rho\rho^*) S_{XX} - \rho^{*2} S_{VV} \cdot e^{i2\delta}\right] \qquad (5.40)$$

$$S_{JJ} = \frac{1}{1 + \rho\rho^*}\left[\rho^2 S_{HH} \cdot e^{-i2\delta} + 2\rho S_{XX} + S_{VV} \cdot e^{i2\delta}\right]$$

There are three invariants under the change of basis transformation as given in Eq. (5.38): The first one is the span of [S], which is defined as the sum of squares of absolute values of its elements and corresponds to the total power (TP) according for the presentation of scattering power under the change of basis transformations. The second is the difference of its off diagonal elements, i.e. $S_{HV} - S_{VH} = S_{ij} - S_{ji}$, which guarantees the symmetry of the scattering matrix. Finally, in all polarisation bases. The fact that det $([U_2]) = 1$, implies finally the determinant invariance of the scattering matrix, i.e. det $([S]_{HV}) = $ det $([S]_{IJ})$.

$$S_{LL} = \frac{1}{2}\left[S_{HH} + 2iS_{XX} - S_{VV}\right]$$

$$S_{LR} = \frac{1}{2}\left[i(S_{HH} + S_{VV})\right] \qquad (5.41)$$

$$S_{RR} = \frac{1}{2}\left[-S_{HH} + 2iS_{XX} + S_{VV}\right]$$

As an example, the transformation of the scattering matrix from the linear $\{\bar{\varepsilon}_H, \ \bar{\varepsilon}_V\}$ basis into the Left-/Right-handed circular polarisation basis $\{\bar{\varepsilon}_L, \ \bar{\varepsilon}_R\}$ is demonstrated in the following (KROGAGER 1993, KROGAGER & BOERNER 1996). According to the discussion in Section 5.1, left circular polarisation can be expressed in terms of the polarisation angles $\psi_L = 0°$, $\chi_L = 45°$. The corresponding complex polarisation ratio is obtained by substituting the values for the polarisation angles into Eq. (5.8) as $\rho = i$ while from Eq. (5.12) follows that $\delta = 0$. Using this polarisation ration in Eq. (5.40) the elements of the scattering matrix in the Left-/Right-handed circular polarisation basis follow as

5.7.2 Scattering Vector and Coherency Matrix Transformation

The corresponding change of basis transformation for the Pauli scattering vector $\vec{k}_P$ is given by (BOERNER & EL-ARINI 1981, CLOUDE 1986)

$$\vec{k}_{P_{IJ}} = [U_{3P}]\vec{k}_{P_{HV}} \quad \text{or} \quad \begin{bmatrix} S_{II} + S_{JJ} \\ S_{II} - S_{JJ} \\ 2S_{IJ} \end{bmatrix} = [U_{3P}] \begin{bmatrix} (S_{HH} + S_{VV}) \\ (S_{HH} - S_{VV}) \\ 2S_{HV} \end{bmatrix} \tag{5.42}$$

where

$$[U_{3P}] = \frac{1}{1+\rho\rho^+} \begin{bmatrix} \cos(2\delta) + \Re(\rho^2 e^{-2i\delta}) & -i\sin(2\delta) - i\Im(\delta^2 e^{-2i\delta}) & 2i\Im(\rho e^{-2i\delta}) \\ -i\sin(2\delta) + i\Im(\rho^2 e^{-2i\delta}) & \cos(2\delta) - \Re(\rho^2 e^{-2i\delta}) & 2\Re(\rho e^{-2i\delta}) \\ 2i\Im(\rho) & -2\Re(\rho) & 1 - |\rho|^2 \end{bmatrix} \tag{5.43}$$

Finally, the change of basis transformation for the 3x3 covariance and coherency matrices can be evaluated straightforwardly using the corresponding transformations for the 3-dimensional scattering vectors derived in the previous section. Using Eq. (43), we obtain for the coherency matrix

$$[T]_{IJ} = \left\langle \vec{k}_{P_{HV}} \cdot \vec{k}_{P_{HV}}^+ \right\rangle = \left\langle [U_{3P}]\vec{k}_{P_{HV}} \cdot \vec{k}_{P_{HV}}^+ [U_{3P}]^T \right\rangle = [U_{3P}] \left\langle \vec{k}_{P_{HV}} \cdot \vec{k}_{P_{HV}}^+ \right\rangle [U_{3P}]^T = [U_{3P}][T]_{HV}[U_{3P}]^{-1} \tag{5.44}$$

The corresponding expression for the covariance matrix can be obtained by substituting Eq. (5.44) into Eq. (5.28) (PAPATHANASSIOU 1999).

5.8 Line of Sight Rotation

Having discussed the effect of changing the polarisation basis in the previous section, this section concerns the transformation caused by rotating the scattering object or the antenna used for transmission and reception about the *Line-of Sight* (LOS). The LOS is defined as the line which connects the antenna phase centre with the scatterer.

5.8.1 Scattering Matrix Rotation

Consider a scattering matrix

$$[S] = \begin{bmatrix} S_{HH} & S_{HV} \\ S_{VH} & S_{VV} \end{bmatrix} \tag{5.45}$$

If the scatterer is rotated about the *Line of Sight* (LOS) by an angle θ, the scattering matrix is transformed into $[S(\theta)]$ by the following unitary transformation (HUYNEN 1970)

$$[S(\theta)] = [R_2(\theta)][S][R_2(\theta)]^{-1} \tag{5.46}$$

$[R_2(\theta)]$ is a real 2x2 unitary rotation matrix, given by

$$[R_2(\theta)] = \begin{bmatrix} \cos\theta & \sin\theta \\ -\sin\theta & \cos\theta \end{bmatrix} \quad \text{where} \quad [R_2(\theta)]^{-1} = [R_2(\theta)]^T \tag{5.47}$$

Performing the matrix multiplication of Eq. (5.46)

$$[S(\theta)] = \begin{bmatrix} S_{HH}(\theta) & S_{HV}(\theta) \\ S_{VH}(\theta) & S_{VV}(\theta) \end{bmatrix} = \begin{bmatrix} \cos\theta & \sin\theta \\ -\sin\theta & \cos\theta \end{bmatrix} \begin{bmatrix} S_{HH} & S_{HV} \\ S_{VH} & S_{VV} \end{bmatrix} \begin{bmatrix} \cos\theta & -\sin\theta \\ \sin\theta & \cos\theta \end{bmatrix} \tag{5.48}$$

we obtain the elements of the rotated scattering matrix

$$
\begin{aligned}
S_{HH}(\theta) &= S_{HH}\cos^2\theta + S_{HV}\cos\theta\sin\theta + S_{VH}\cos\theta\sin\theta + S_{VV}\sin^2\theta \\
S_{HV}(\theta) &= -S_{HH}\cos\theta\sin\theta + S_{HV}\cos^2\theta - S_{VH}\sin^2\theta + S_{VV}\cos\theta\sin\theta \\
S_{VH}(\theta) &= -S_{HH}\cos\theta\sin\theta - S_{HV}\sin^2\theta + S_{VH}\cos^2\theta + S_{VV}\cos\theta\sin\theta \\
S_{VV}(\theta) &= S_{HH}\sin^2\theta - S_{HV}\cos\theta\sin\theta - S_{VH}\cos\theta\sin\theta + S_{VV}\cos^2\theta
\end{aligned}
\tag{5.49}
$$

In the case of backscattering from reciprocal media $S_{HV} = S_{VH} = S_{XX}$ and $S_{HV}(\theta) = S_{VH}(\theta) = S_{XX}(\theta)$, Eq. (5.49) reduce to

$$
\begin{aligned}
S_{HH}(\theta) &= S_{HH}\cos^2\theta + S_{XX}\cos\theta\sin\theta + S_{VV}\sin^2\theta \\
S_{XX}(\theta) &= -S_{HH}\cos\theta\sin\theta + S_{XX}\left(\cos^2\theta - \sin^2\theta\right) + S_{VV}\cos\theta\sin\theta \\
S_{VV}(\theta) &= S_{HH}\sin^2\theta - S_{XX}\cos\theta\sin\theta + S_{VV}\cos^2\theta
\end{aligned}
\tag{5.50}
$$

Considering the special case for which the cross-polarised component is zero, i.e. $S_{XX} = 0$, as is the case for example for Bragg surface scatterers, Eq. (5.50) further reduces to

$$
\begin{aligned}
S_{HH}(\theta) &= S_{HH}\cos^2\theta + S_{VV}\sin^2\theta \\
S_{XX}(\theta) &= -S_{HH}\cos\theta\sin\theta + S_{VV}\cos\theta\sin\theta \\
S_{VV}(\theta) &= S_{HH}\sin^2\theta + S_{VV}\cos^2\theta
\end{aligned}
\tag{5.51}
$$

Eq. (5.51) makes evident that the rotated scattering matrix has non-zero cross-polarisation, which are induced by the LOS rotation. Thus, it is important to distinguish between cross-polarisation induced by the scattering process itself, which is uncorrelated with the co-polarised scattering components, and rotation induced cross-polarisation, which correlates completely

with the co-polarised components. It is exactly this correlated cross-polarised component introduced by the LOS rotation which is used for the determination of the azimuthal slopes discussed in Chapter 7 (SCHULER *et al.* 1999, LEE *et al.* 1999, POTTIER *et al.* 1999).

5.8.2 Scattering Vector and Coherency Matrix Rotation

From Eq. (5.50) and using following trigonometric identities

$$\cos^2\theta - \sin^2\theta \ = \ \cos 2\theta \qquad \text{and} \qquad \cos\theta\sin\theta \ = \ \frac{1}{2}\sin 2\theta \qquad (5.52)$$

the corresponding rotated Pauli scattering vector $\vec{k}_{3P}(\theta)$ can be written as

$$\vec{k}_P(\theta) = \begin{bmatrix} S_{HH}(\theta) + S_{VV}(\theta) \\ S_{HH}(\theta) - S_{VV}(\theta) \\ 2S_{XX}(\theta) \end{bmatrix} = \begin{bmatrix} (S_{HH} + S_{VV}) \\ (S_{HH} - S_{VV})\cos 2\theta - 2S_{XX}\sin 2\theta \\ (S_{HH} - S_{VV})\sin 2\theta + 2S_{XX}\cos 2\theta \end{bmatrix} = \begin{bmatrix} 1 & 0 & 0 \\ 0 & \cos 2\theta & \sin 2\theta \\ 0 & -\sin 2\theta & \cos 2\theta \end{bmatrix} \begin{bmatrix} (S_{HH} + S_{VV}) \\ (S_{HH} - S_{VV}) \\ 2S_{XX} \end{bmatrix} (5.53)$$

The relationship between rotated and original Pauli scattering vector is then given by

$$\vec{k}_P(\theta) = [R_{3P}(\theta)]\vec{k}_P \qquad \text{where} \quad [R_{3P}(\theta)] = \begin{bmatrix} 1 & 0 & 0 \\ 0 & \cos 2\theta & \sin 2\theta \\ 0 & -\sin 2\theta & \cos 2\theta \end{bmatrix} \qquad (5.54)$$

Note that, according to Eq. (5.53), the $(S_{HH} + S_{VV})$ component of the Pauli scattering vector remain invariant under LOS rotations (KENNAUGH 1954, HUYNEN 1970).

Finally, the LOS rotation transformation for the 3x3 covariance and coherency matrices can be evaluated straightforwardly using the corresponding transformations for the scattering vectors derived in the previous section. Using Eq. (5.54) we obtain for the coherency matrix

$$[T(\theta)] = \left\langle \vec{k}_{3P}(\theta) \cdot \vec{k}_{3P}(\theta)^+ \right\rangle = [R_{3P}(\theta)]\left\langle \vec{k}_P \cdot \vec{k}_P^+ \right\rangle[R_{3P}(\theta)]^T = [R_{3P}(\theta)][T][R_{3P}(\theta)]^{-1} \quad (5.55)$$

The corresponding expression for the coherency matrix rotation can be obtained by substituting Eq. (5.55) into Eq. (5.28).

It has to be noted, that the rotation of a scatterer by an angle θ about the LOS is equivalent to rotating the antenna used for transmission and reception by an angle $-\theta$. The antenna rotation leads to a rotated reference basis for reception and transmission. In this sense, the LOS transformations can be regarded as a special subspace of change of basis transformations

described by a unitary transformation matrix with a single degree of freedom, namely the rotation angle θ (POTTIER 1998) .

5.9 Symmetry Properties of Distributed Scatterers

As discussed in section 5.6 distributed scatterers are characterised by the superposition of elementary scattering centres and are completely described by their coherency matrix [T]. In the most general case, where no assumption about the distribution of the elementary scattering centres inside the resolution cell of such scatterers are made, [T] contains three real elements in the diagonal and three complex off diagonal elements. Thus, it can be described by nine parameters. Symmetry assumptions about the distribution of the elementary scattering centres in such partial scatterers leads to a simplification of the scattering problem and allows quantitative conclusions about their scattering behaviour (NGHIEM et al. 1992, CLOUDE & POTTIER 1996, CLOUDE 1998). If the scattering matrix of a particle in a particular position and for a particular direction is known, then the scattering matrix of its mirrored or rotated image in certain symmetrical positions is also known. VAN DE HULST (1981) was the first one formulating symmetry properties of the scatterer and implementing it on the Müller matrix. Accordingly, in the following three special cases of symmetries are considered in terms of the coherency matrix.
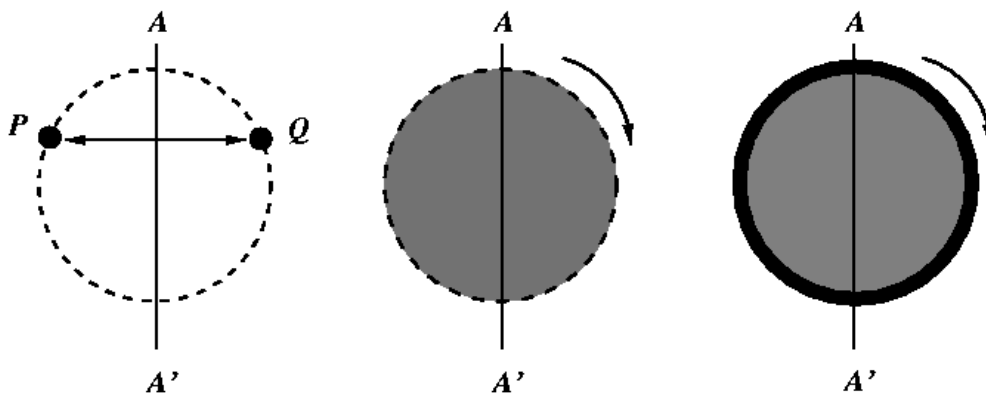
Fig. 5.4: On reflection (left), rotation (middle) and the azimuthal (right) symmetry.

5.9.1 Reflection Symmetry

Reflection symmetric media are characterised by a symmetry plane, which contains the *radar line of sight* indicated with AA′ in Fig. 5.4. This implies that for any scatterer *P* located at the one side of the plane characterised by a scattering matrix/vector

$$[S_P] = \begin{bmatrix} S_{HH} & S_{XX} \\ S_{XX} & S_{VV} \end{bmatrix} \quad \text{and} \quad \vec{k}_P = \frac{1}{\sqrt{2}}[S_{HH} + S_{VV}, S_{HH} - S_{VV}, 2S_{XX}]^T \quad (5.56)$$

there is an mirrored scatterer *Q* at the other side of the plane with scattering matrix/vector given by (VAN DE HULST 1985)

$$[S_Q] = \begin{bmatrix} S_{HH} & -S_{XX} \\ -S_{XX} & S_{VV} \end{bmatrix} \quad \text{and} \quad \vec{k}_Q = \frac{1}{\sqrt{2}}[S_{HH} + S_{VV}, S_{HH} - S_{VV}, -2S_{XX}]^T \quad (5.57)$$

$[S_P]$ and $[S_Q]$ differ only in the sign of the off-diagonal elements. Accordingly, the coherency matrix $[T]$ of such a medium can be written as the superposition of the coherency matrices for both symmetrical components

$$[T] = [T_P] + [T_Q] = \left\langle \vec{k}_P \cdot \vec{k}_P^+ \right\rangle + \left\langle \vec{k}_Q \cdot \vec{k}_Q^+ \right\rangle \quad (5.58)$$

where the averaging for $[T_P]$ is performed over the scatterers located on the one side of the plane and for $[T_Q]$ over the mirrored with respect to the symmetry plane scatterers

$$[T] = \begin{bmatrix} t_1' & t_2' & t_3' \\ t_2'^* & t_4' & t_5' \\ t_3'^* & t_5'^* & t_6'' \end{bmatrix} + \begin{bmatrix} t_1' & t_2' & -t_3' \\ t_2'^* & t_4' & -t_5' \\ -t_3'^* & -t_5'^* & t_6'' \end{bmatrix} = \begin{bmatrix} t_1 & t_2 & 0 \\ t_2^* & t_4 & 0 \\ 0 & 0 & t_6 \end{bmatrix} \quad (5.59)$$

From Eq. (5.59) follows that the coherency matrix of reflection symmetric media contains only five non-zero elements. The correlation between the co- and cross-polarisation vanishes as a consequence of the opposite sign of the corresponding elements of $[T_P]$ and $[T_Q]$.

$$\left\langle (S_{HH} + S_{VV})S_{XX}^* \right\rangle = \left\langle (S_{HH} - S_{VV})S_{XX}^* \right\rangle = 0 \quad (5.60)$$

The coherency matrix can be completely described by five parameters corresponding to the three real elements on the diagonal and the remaining a complex cross-correlation between the co-polarised channels. Smooth surface scatterers are typical reflection symmetric scatterers.

5.9.2 Rotation Symmetry

Rotation-symmetric media are media with a spatial distribution of elementary scattering centres, which do not change when the medium is rotated about the LOS axis. In other words, the scattering behaviour of such media is invariant under LOS rotations. The coherency matrix $[T]$ remain the same when the medium is rotated about the LOS by any angle θ

$$[T(\theta)] = [R_3(\theta)][T][R_3(\theta)]^{-1} \tag{5.61}$$

where $[R_3(\theta)]$ is the in Section 5.8 introduced 3x3 unitary LOS rotation matrix

$$[R_3(\theta)] = \begin{bmatrix} 1 & 0 & 0 \\ 0 & \cos 2\theta & \sin 2\theta \\ 0 & -\sin 2\theta & \cos 2\theta \end{bmatrix} \quad \text{and} \quad [R_3(\theta)]^{-1} = [R_3(\theta)]^{T} \tag{5.62}$$

The three complex eigenvectors $\vec{e}_{Ri}$ of the rotation matrix $[R_3(\theta)]$ (CLOUDE & POTTIER 1996, CLOUDE 1998)

$$\vec{e}_{R1} = \begin{bmatrix} 1 \\ 0 \\ 0 \end{bmatrix}, \quad \vec{e}_{R2} = \frac{1}{\sqrt{2}}\begin{bmatrix} 0 \\ 1 \\ i \end{bmatrix}, \quad \vec{e}_{R3} = \frac{1}{\sqrt{2}}\begin{bmatrix} 0 \\ 1 \\ -i \end{bmatrix} \tag{5.63}$$

are by definition invariant under rotations about the LOS

$$[R_3(\theta)]\ \vec{e}_{Ri} = \lambda_{Ri}\vec{e}_{Ri} \tag{5.64}$$

where the λ_{Ri} denote the corresponding eigenvalues. Consequently, a rotation-invariant coherency matrix must be constructable from a linear combination of the outer products of these eigenvectors (CLOUDE & POTTIER 1996)

$$[T] = f_1\left(\vec{e}_{R1}\cdot\vec{e}_{R1}^{+}\right) + f_2\left(\vec{e}_{R2}\cdot\vec{e}_{R2}^{+}\right) + f_3\left(\vec{e}_{R3}\cdot\vec{e}_{R3}^{+}\right) \qquad \rightarrow \tag{5.65}$$

$$[T] = f_1\begin{bmatrix} 1 & 0 & 0 \\ 0 & 0 & 0 \\ 0 & 0 & 0 \end{bmatrix} + f_2\begin{bmatrix} 0 & 0 & 0 \\ 0 & 1/2 & i/2 \\ 0 & -i/2 & 1/2 \end{bmatrix} + f_3\begin{bmatrix} 0 & 0 & 0 \\ 0 & 1/2 & -i/2 \\ 0 & i/2 & 1/2 \end{bmatrix} = \begin{bmatrix} f_1 & 0 & 0 \\ 0 & (f_2+f_3)/2 & i(f_2-f_3)/2 \\ 0 & -i(f_2-f_3)/2 & (f_2+f_3)/2 \end{bmatrix} \tag{5.66}$$

The eigenvalues of $[T]$ are f_1, f_2 and f_3 implying that $[T]$ is of rank 3. From Eq. (5.66) follows that the coherency matrix of rotation symmetric media contains only five non-zero elements, with two equal elements along the diagonal

$$\left| \left\langle \left(S_{HH} - S_{VV} \right)^2 \right\rangle \right| = 4 \left| \left\langle S_{XX}^2 \right\rangle \right| \tag{5.67}$$

The correlation between $(S_{HH} - S_{VV})$ and S_{XX} does not vanish as it is the case for reflection-symmetric media.

$$\left\langle \left(S_{HH} - S_{VV} \right) S_{XX}^* \right\rangle \neq 0 \tag{5.68}$$

On the other hand, the correlation between $(S_{HH} + S_{VV})$ and the other two components $(S_{HH} - S_{VV})$ and S_{XX}, becomes zero

$$\left\langle \left(S_{HH} + S_{VV} \right) \left(S_{HH} - S_{VV} \right)^* \right\rangle = \left\langle \left(S_{HH} + S_{VV} \right) S_{XX}^* \right\rangle = 0 \tag{5.69}$$

From Eq. (5.66) follows that the coherency matrix of rotation symmetric media is completely described by four parameters. Rotation symmetry is in general a typical for distributed scatterers and characterises gyrotropic random media, as given for example by a random distribution of helixes.

5.9.3 Azimuthal Symmetry

When both, reflection and rotation symmetry are present, the medium is said to be azimuthally symmetric. For such a medium all planes including the LOS direction are *reflection symmetry* planes. The corresponding coherency matrices must satisfy, at the same time, the conditions of reflection and rotation symmetry. Accordingly, the coherency matrix of such a medium can be regarded as of being composed of two reflection symmetric terms, where each of them is rotation symmetric

$$[T] = \begin{bmatrix} f_1 & 0 & 0 \\ 0 & (f_2 + f_3)/2 & i(f_2 - f_3)/2 \\ 0 & -i(f_2 - f_3)/2 & (f_2 + f_3)/2 \end{bmatrix} + \begin{bmatrix} f_1 & 0 & 0 \\ 0 & (f_2 + f_3)/2 & -i(f_2 - f_3)/2 \\ 0 & i(f_2 - f_3)/2 & (f_2 + f_3)/2 \end{bmatrix} = \begin{bmatrix} f_1 & 0 & 0 \\ 0 & (f_2 + f_3) & 0 \\ 0 & 0 & (f_2 + f_3) \end{bmatrix} \tag{5.70}$$

It follows that the resulting coherency matrix is a diagonal matrix with two equal diagonal elements

$$\left| \left\langle \left(S_{HH} - S_{VV} \right)^2 \right\rangle \right| = 4 \left| \left\langle S_{XX}^2 \right\rangle \right| \tag{5.71}$$

All correlation elements of $[T]$ become zero

$$\left\langle \left(S_{HH} + S_{VV}\right)\left(S_{HH} - S_{VV}\right)^{*} \right\rangle = \left\langle \left(S_{HH} + S_{VV}\right)S_{XX}^{*} \right\rangle = \left\langle \left(S_{HH} - S_{VV}\right)S_{XX}^{*} \right\rangle = 0 \qquad (5.72)$$

Consequently, azimuthally symmetric media are completely described by only two parameters. In this case, the Pauli matrices lead directly to the eigenvectors of $[T]$. The degenerated eigenvalues are given by $\left| \left\langle \left(S_{HH} + S_{VV}\right)^{2} \right\rangle \right|$, and $\left| \left\langle \left(S_{HH} - S_{VV}\right)^{2} \right\rangle \right| = 4 \left| \left\langle S_{XX}^{2} \right\rangle \right|$. Uniform random volumes are typical azimuthally symmetric scatterers. Note that often in the literature rotation symmetry is erroneously refereed as azimuthal symmetry!

Summarising, the less restrictive reflection symmetry reduces the number of parameters in $[T]$ from nine to five, rotation symmetry reduces further the number of parameters down to four, while the higher symmetric form of azimuthal symmerty yields a diagonal coherency matrix with only two independent parameters. The corresponding covariance matrix $[C]$ for the three described symmetry cases where first derived by NGHIEM *et al.* (1988) using a direct expansion of the elements of $[C]$.

5.10   Polarimetric Entropy / Anisotropy / Alpha Angle

In this section, polarimetric parameters used for the extraction of physical information about the scattering process properties of distributed scatterers are introduced and discussed.

5.10.1   The Diagonalisation of the Coherency matrix

Since the coherency matrix $[T]$ is hermitian positive semi-definite, it can always be diagonalised by an unitary similarity transformation of the form (CLOUDE 1986, CLOUDE 1992, CLOUDE & POTTIER 1995)

$$[T] = [U_{3}][\Lambda][U_{3}]^{-1} \qquad \text{where} \quad [\Lambda] = \begin{bmatrix} \lambda_{1} & 0 & 0 \\ 0 & \lambda_{2} & 0 \\ 0 & 0 & \lambda_{3} \end{bmatrix}, \qquad [U_{3}] = \left[\bar{e}_{1}, \bar{e}_{2}, \bar{e}_{3}\right]^{T} \qquad (5.73)$$

$[\Lambda]$ is the diagonal eigenvalue matrix with elements the real nonnegative eigenvalues, $0 \le \lambda_{1} \le \lambda_{2} \le \lambda_{3}$ of $[T]$, and $[U_{3}]$ is the unitary eigenvector matrix with columns corresponding to the orthonormal eigenvectors $\bar{e}_{1}, \bar{e}_{2}$ and $\bar{e}_{3}$ of $[T]$. The idea of the eigenvector approach is to use the diagonalisation of the coherency matrix $[T]$ of a distributed scatterer, which is in general of rank 3, in order to decompose it into the non-coherent sum of three independent coherency matrices $[T_{i}]$

$$[T]=[U_3][\Lambda][U_3]^{-1}=\lambda_1\left(\bar{e}_1\cdot\bar{e}_1^+\right)+\lambda_2\left(\bar{e}_2\cdot\bar{e}_2^+\right)+\lambda_3\left(\bar{e}_3\cdot\bar{e}_3^+\right)=[T_1]+[T_2]+[T_3] \qquad (5.74)$$

The matrices $[T_i]$ are of rank 1 complying a deterministic scattering contribution, characterised by a single scattering matrix. In this sense, Eq. (5.74) may be interpreted as the decomposition of $[T]$ into three single scattering components described by $[T_1]$, $[T_2]$ and $[T_3]$. The contribution of each one in terms of power is given by the appropriate eigenvalue. The sum of the three eigenvalues expresses the total power TP received from the scatterer

$$TP = \lambda_1 + \lambda_2 + \lambda_3 \qquad (5.75)$$

The information about which 'kind' of scatterers are presented by $[T_1]$, $[T_2]$ and $[T_3]$ is contained in the corresponding eigenvectors. The exact interpretation of the eigenvectors in terms of scattering mechanisms will be discussed in the next section. The physical basis of the eigenvector decomposition is provided by the orthogonal nature of the eigenvectors and the statistical significance of diagonal coherency matrices. The former guarantees always the existence of a set of orthonormal basis matrices in which the expansion of $[T]$ leads to a diagonal coherency matrix. The choice of the basis matrices is then dictated by the eigenvectors. On the other hand, the absence of off-diagonal terms establishes the statistical independence between component vectors.

There are two important physical features arising directly from the eigenvalues of the coherency matrix. The first one is the polarimetric scattering entropy H defined by using the logarithmic sum of the eigenvalues of $[T]$ (CLOUDE 1986)

$$H := \sum_{i=1}^{3} - P_i \log_3 P_i \qquad (5.76)$$

P_i expresses the appearance probabilities for each contribution, defined from the eigenvalues of $[T]$ as

$$P_i := \frac{\lambda_i}{\sum_{j=1}^{3} \lambda_j} = \frac{\lambda_i}{\lambda_1 + \lambda_2 + \lambda_3} \qquad \text{so that} \quad P_1 + P_2 + P_3 = 1. \qquad (5.77)$$

According to its definition the entropy ranges from 0 to 1. It can be interpreted as a measure of the randomness of the scattering, or in other words, it expresses the number of effective scattering processes occurring: An entropy of 0 indicates a rank 1 $[T]$ matrix with only one nonzero eigenvalue, i.e. $\lambda_2 = \lambda_3 = 0$. This implies a non-depolarising scattering process described by a single scattering matrix. At the other extreme an entropy of 1 indicates the presence of three equal nonzero eigenvalues, i.e. $\lambda_1 = \lambda_2 = \lambda_3$. It characterises a random noise scattering process, which depolarises completely the incident wave regardless of its

polarisation. However, most distributed natural scatterers lie in between these two extreme cases, having intermediate entropy values.

The second one is the polarimetric scattering anisotropy defined as the normalised difference between the appearance probabilities of the second and the third scattering component (CLOUDE 1986, POTTIER 1998)

$$A := \frac{P_2 - P_3}{P_2 - P_3} = \frac{\lambda_2 - \lambda_3}{\lambda_2 + \lambda_3} \tag{5.78}$$

A ranges also from 0 to 1 and expresses the relation between the secondary scattering processes. For a deterministic scatterer with entropy $H = 0$ the anisotropy becomes zero as well as in the case of a pure noise scatterer with entropy $H = 1$. For scatterers characterised by intermediate entropy values, a high anisotropy indicates the presence of only one strong secondary scattering process, while a low anisotropy indicates the appearance of two equally strong scattering processes. In this sense, the anisotropy provides complementary to the entropy information and facilitates the interpretation of the scatterer.

The great advantage of these two parameters arises from the invariance of the eigenvalue problem under unitary transformations: The same scatterer leads to the same eigenvalues and consequently to the same entropy and anisotropy values independently on the basis used to measure the corresponding scattering matrix.

5.10.2 Interpretation of Scattering Mechanisms

As discussed in the previous section, the diagonalisation of $[T]$, according to Eq. (5.73), produces a set of three orthogonal components at first without a given physical significance. The objective of this section is the physical interpretation of the resulting components and the corresponding eigenvectors of $[T]$. The unitary matrix $[U_3]$ in Eq. (5.73) is a general unitary matrix with $3^2-1=8$ degrees of freedom (CLOUDE 1986). Because the unitary matrix $[U_3]$, which describes the change of polarisation basis transformation, possesses only two degree of freedom, Eq. (5.73) cannot be interpreted as a simple change of polarisation basis transformation, and the corresponding eigenvectors cannot be considered as conventional polarisation states.

The important idea for the physical interpretation of the eigenvector decomposition is the assosiation of unitary complex vectors with polarimetric scattering mechanisms. For this, a scatterer with scattering matrix / vector given by

$$[S] = \begin{bmatrix} S_{HH} & S_{HV} \\ S_{HV} & S_{VV} \end{bmatrix} \quad \text{and} \quad \bar{k}_P = \frac{1}{\sqrt{2}} \begin{bmatrix} S_{HH} + S_{VV}, S_{HH} - S_{VV}, 2S_{XX} \end{bmatrix}^T \tag{5.79}$$

where *XX* means *HV* = *VH* is considered. The scattering vector $\vec{k}_P$ can be normalised in order to obtain a associated unitary vector $\vec{e}$

$$\vec{e} = \frac{1}{\left|\vec{k}_P\right|}\vec{k}_P \tag{5.80}$$

Furthermore, an arbitrary three-dimensional unitary vector $\vec{e}$ has five degrees of freedom, and can therefore be written in terms of five angles (CLOUDE 1995, CLOUDE 1997)

$$\vec{e} = \frac{1}{\left|\vec{k}_P\right|}\vec{k}_P = \begin{bmatrix} \cos\alpha\,\exp\left(i\phi_1\right) \\ \sin\alpha\,\cos\beta\,\exp\left(i\phi_2\right) \\ \sin\alpha\,\sin\beta\,\exp\left(i\phi_3\right) \end{bmatrix} = \frac{1}{\sqrt{2}\left|\vec{k}_P\right|}\begin{bmatrix} S_{HH} + S_{VV} \\ S_{HH} - S_{VV} \\ 2S_{XX} \end{bmatrix} \tag{5.81}$$

According to the *Scattering Vector Reduction Theorem* (CLOUDE 1997), it is always possible to generate this arbitrary scattering mechanism, represented by the associated complex unitary vector $\vec{e}$ by starting from the identity vector $[1,0,0,]^T$ and applying a set of three ordered matrix transformations

$$\vec{e} = \begin{bmatrix} \exp\left(i\phi_1\right) & 0 & 0 \\ 0 & \exp\left(i\phi_2\right) & 0 \\ 0 & 0 & \exp\left(i\phi_3\right) \end{bmatrix}\begin{bmatrix} 1 & 0 & 0 \\ 0 & \cos\beta & -\sin\beta \\ 0 & \sin\beta & \cos\beta \end{bmatrix}\begin{bmatrix} \cos\alpha & -\sin\alpha & 0 \\ \sin\alpha & \cos\alpha & 0 \\ 0 & 0 & 1 \end{bmatrix}\begin{bmatrix} 1 \\ 0 \\ 0 \end{bmatrix} \tag{5.82}$$

The first matrix contains the scattering phase angles and accounts for the phase relations between the elements of the vector $\vec{e}$. For convenience it will be ignored in the following. The second and third matrices represent canonical forms of plane rotations. In this sense a change about $\Delta\alpha$ and $\Delta\beta$ of the parameterisation angles corresponds to a change from one scattering mechanism $\vec{e}$ to another $\vec{e}'$. The transformation matrices for the α and β angles are simple plane rotations given by

$$\vec{e}' = \begin{bmatrix} 1 & 0 & 0 \\ 0 & \cos\Delta\beta & -\sin\Delta\beta \\ 0 & \sin\Delta\beta & \cos\Delta\beta \end{bmatrix}\vec{e} \quad\text{and}\quad \vec{e}' = \begin{bmatrix} \cos\Delta\alpha & -\sin\Delta\alpha & 0 \\ \sin\Delta\alpha & \cos\Delta\alpha & 0 \\ 0 & 0 & 1 \end{bmatrix}\vec{e} \tag{5.83}$$

The comparison of Eq. (5.82) with Eq. (5.53) makes evident that the second transformation matrix in Eq. (5.82) represents physically a rotation of the scatterer about the radar *LOS* by an angle $\beta/2$. This correspondence is valid as long as we use the Pauli basis for the vectorisation of the scattering matrix, and follows directly from the nature of the Pauli matrices, which relates physical rotations to matrix transformations (CLOUDE 1986, CLOUDE (a) 1986).

The third matrix cannot be associated with a physical rotation. However, α represents an internal degree of freedom of the scatterer. It is continuous within a range of $0° \leq \alpha \leq 90°$ and is associated with the 'type' of scattering mechanism. This becomes evident by substituting different α angle values into Eq. (5.82) and interpreting the generated $\vec{e}$ in terms of the scattering vectors, assuming for simplicity $\beta = 0$.

i) For $\alpha = 0°$

$$\vec{e} = \begin{bmatrix} 1 & 0 & 0 \\ 0 & 1 & 0 \\ 0 & 0 & 1 \end{bmatrix}\begin{bmatrix} 1 \\ 0 \\ 0 \end{bmatrix} = \begin{bmatrix} 1 \\ 0 \\ 0 \end{bmatrix} = \frac{1}{\sqrt{2}|\vec{k}_P|}\begin{bmatrix} S_{HH} + S_{VV} \\ S_{HH} - S_{VV} \\ 2S_{HV} \end{bmatrix} \tag{5.84}$$

$\vec{e}$ corresponds to the scattering vector of an isotropic surface, i.e. a surface where $|HH| = |VV|$, and HH and VV are in phase.

ii) For $\alpha = 90°$

$$\vec{e} = \begin{bmatrix} 0 & 1 & 0 \\ 1 & 0 & 0 \\ 0 & 0 & 1 \end{bmatrix}\begin{bmatrix} 1 \\ 0 \\ 0 \end{bmatrix} = \begin{bmatrix} 0 \\ 1 \\ 0 \end{bmatrix} = \frac{1}{\sqrt{2}|\vec{k}_P|}\begin{bmatrix} S_{HH} + S_{VV} \\ S_{HH} - S_{VV} \\ 2S_{HV} \end{bmatrix} \tag{5.85}$$

the obtained $\vec{e}$ is associated with the scattering vector of an isotropic dihedral and the phase difference between HH an VV is 180°, i.e. a dihedral with $|HH| = |VV|$.

iii) For $\alpha = 45°$

$$\vec{e} = \begin{bmatrix} 1/\sqrt{2} & 1/\sqrt{2} & 0 \\ 1/\sqrt{2} & 1/\sqrt{2} & 0 \\ 0 & 0 & 1 \end{bmatrix}\begin{bmatrix} 1 \\ 0 \\ 0 \end{bmatrix} = \begin{bmatrix} 1/\sqrt{2} \\ 1/\sqrt{2} \\ 0 \end{bmatrix} = \frac{1}{\sqrt{2}|\vec{k}_P|}\begin{bmatrix} S_{HH} + S_{VV} \\ S_{HH} - S_{VV} \\ 2S_{HV} \end{bmatrix} \tag{5.86}$$

the obtained $\vec{e}$ corresponds to the scattering vector of a horizontally oriented dipole scatterer, where $S_{HH} = 1$ and $S_{VV} = S_{HV} = 0$. To illustrate now the effect of β, keeping $\alpha = 45°$, $\beta = 90°$ is applied

$$\vec{e} = \begin{bmatrix} 1 & 0 & 0 \\ 0 & -1 & 0 \\ 0 & 0 & -1 \end{bmatrix}\begin{bmatrix} 1/\sqrt{2} & 1/\sqrt{2} & 0 \\ 1/\sqrt{2} & 1/\sqrt{2} & 0 \\ 0 & 0 & 1 \end{bmatrix}\begin{bmatrix} 1 \\ 0 \\ 0 \end{bmatrix} = \begin{bmatrix} 1/\sqrt{2} \\ -1/\sqrt{2} \\ 0 \end{bmatrix} = \frac{1}{\sqrt{2}|\vec{k}_P|}\begin{bmatrix} S_{HH} + S_{VV} \\ S_{HH} - S_{VV} \\ 2S_{HV} \end{bmatrix} \tag{5.87}$$

$\vec{e}$ corresponds now to a vertically oriented dipole scatterer where $S_{VV} = 1$ and $S_{HH} = S_{HV} = 0$. For intermediate values of α, anisotropic scattering mechanisms are represented; for which $|HH|$ and $|VV|$ are no longer equal (as they are for $\alpha = 0°$ and $\alpha = 90°$). The range of possible variations in scattering mechanism can be illustrated by the variation of α along the real line as shown in Fig. 5.5. It is important to note that the type of scatterer is defined by its α-angle

independently of its orientation $\beta/2$, hence it does not matter if there is a misalignment between radar and scatterer coordinates. Tab. 5.2 contains the values of the five angles for a range of canonical scattering mechanism, which are of interest in radar polarimetry.

$$\alpha=0^o \qquad \alpha=45^o \qquad \alpha=90^o$$

Isotropic Surface $\qquad$ Dipol $\qquad$ Isotropic Dihedral

$$[S]=a\begin{bmatrix} 1 & 0 \\ 0 & 1 \end{bmatrix} \qquad [S]=a\begin{bmatrix} 1 & 0 \\ 0 & 0 \end{bmatrix} \qquad [S]=a\begin{bmatrix} 1 & 0 \\ 0 & -1 \end{bmatrix}$$

Anisotropic Surfaces $\qquad$ Anisotropic Dihedrals
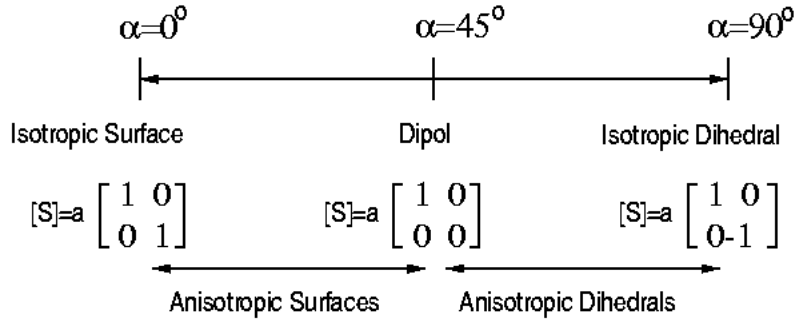
Fig. 5.5: Schematic representation of the α-angle interpretation

Considering these aspects the general $[U_3]$ transformation of the scattering vector $\bar{k}$ describe not only polarimetric basis transformations, but linear combinations of three orthogonal coherent scattering mechanisms, which correspond to changes in the selected scattering mechanisms (CLOUDE 1996). Accordingly, the physical interpretation of the diagonalisation of $[T]$ is the generation of a set of complex projections of the scattering vector onto three orthogonal scattering mechanisms given by the three eigenvectors of $[T]$. Now the origin of the eight degrees of freedom in the general $[U_3]$ matrix becomes evident.

Sphere	$\alpha=0°$	$\beta=\infty$	$\phi1=\psi$	$\phi2=\phi3=\infty$
Dihedral at $\theta°$	$\alpha=90°$	$\beta=2\theta°$	$\phi1=\infty$	$\phi2 - \phi3=0$
Dipole at $\theta°$	$\alpha=45°$	$\beta=2\theta°$	$\phi1=\psi$	$\phi2=\phi3=\psi$
Surface at $\theta°$	$\alpha=0°$	$\beta=2\theta°$	$\phi1\approx0°$	$\phi2\approx\phi3=0°$
Helix	$\alpha=90°$	$\beta\pm45°$		$\phi2 - \phi3=-90°$

Tab. 5.2: Parameter values of canonical scatterers (∞ indicates no fixed values)

Each one of the three eigenvectors $\bar{e}_i$ contains five parameters. This leads to 15 parameters. However, the constraint that the three mechanisms must be orthogonal, provides six equations. This reduces the number of parameters down to nine. Finally, the phase of the determinant should be zero, according the special unitarity of $[U_3]$, in order to establish the correct phase relationships between the components. This finally leaves us with eight independent parameters of $[U_3]$.

5.10.3 Parameter Estimation

The eigenvector decomposition of a rank 3 $[T]$ matrix leads to three eigenvalues and three eigenvectors. The entropy H and anisotropy A can be estimated straightforwardly from the eigenvalues using Eq. (5.76) and Eq. (5.78), respectively. On the other hand, for each one of the eigenvectors

$$\vec{e}_1 = \begin{bmatrix} e_{1_1} \\ e_{1_2} \\ e_{1_3} \end{bmatrix}, \qquad \vec{e}_2 = \begin{bmatrix} e_{2_1} \\ e_{2_2} \\ e_{2_3} \end{bmatrix}, \qquad \vec{e}_3 = \begin{bmatrix} e_{3_1} \\ e_{3_2} \\ e_{3_3} \end{bmatrix} \qquad (5.88)$$

the corresponding α_i - angle is obtained, according to Eq. (81), from the absolute value of the first element as

$$\alpha_1 = \arccos\left(|e_{11}|\right) \qquad \alpha_2 = \arccos\left(|e_{21}|\right) \qquad \alpha_3 = \arccos\left(|e_{31}|\right) \qquad (5.89)$$

while the corresponding β_i - angle is obtained using the ratio between the absolute values of the second and third eigenvector elements as

$$\beta_1 = \arctan\left(\frac{|e_{13}|}{|e_{12}|}\right) \qquad \beta_2 = \arctan\left(\frac{|e_{23}|}{|e_{22}|}\right) \qquad \beta_3 = \arctan\left(\frac{|e_{33}|}{|e_{32}|}\right) \qquad (5.90)$$

In the same manner three sets of scattering angles can be obtained as

$$\phi_{1_1} = \arctan\left(\frac{\mathrm{Im}(e_{1_1})}{\mathrm{Re}(e_{1_1})}\right) \quad \phi_{1_2} = \arctan\left(\frac{\mathrm{Im}(e_{1_2})}{\mathrm{Re}(e_{1_2})}\right) \quad \phi_{1_3} = \arctan\left(\frac{\mathrm{Im}(e_{1_3})}{\mathrm{Re}(e_{1_3})}\right)$$

$$\phi_{2_1} = \arctan\left(\frac{\mathrm{Im}(e_{2_1})}{\mathrm{Re}(e_{2_1})}\right) \quad \phi_{2_2} = \arctan\left(\frac{\mathrm{Im}(e_{2_2})}{\mathrm{Re}(e_{2_2})}\right) \quad \phi_{2_3} = \arctan\left(\frac{\mathrm{Im}(e_{2_3})}{\mathrm{Re}(e_{2_3})}\right) \quad (5.91)$$

$$\phi_{3_1} = \arctan\left(\frac{\mathrm{Im}(e_{3_1})}{\mathrm{Re}(e_{3_1})}\right) \quad \phi_{3_2} = \arctan\left(\frac{\mathrm{Im}(e_{3_2})}{\mathrm{Re}(e_{3_2})}\right) \quad \phi_{3_3} = \arctan\left(\frac{\mathrm{Im}(e_{3_3})}{\mathrm{Re}(e_{3_3})}\right)$$

Thus, 15 angles extracted from the eigenvectors, which built up the general unitary matrix $[U_3]$ are obtained. However, as discussed before, $[U_3]$ matrices contain only 8 independent parameters. Consequently, the 15 extracted angles are not independent from one another. This makes an interpretation of each individual α_i and β_i problematic. To overcome this problem, the interpretation is performed in terms of a dominant scattering mechanism: As the distributed scatterer is modelled to be decomposed into three elementary scattering processes, which occur with a probability P_i and with each one corresponding to an α_i and β_i angle, the best estimate in a maximum likelihood sense of the α and β angles are given by their mean values

$$\alpha = P_1\alpha_1 + P_2\alpha_2 + P_3\alpha_3$$
$$\beta = P_1\beta_1 + P_2\beta_2 + P_3\beta_3$$

(5.92)

These α and β angles for the dominant scattering mechanism, together with the entropy and anisotropy values, have been used for the classification of natural scatterers from fully polarimetric SAR data (LEE 1999, POTTIER 1998)

5.10.4 Experimental Data Analysis

Closing this chapter, a first order interpretation of polarimetric entropy, anisotropy and alpha angle maps obtained from polarimetric experimental data at L-band form the Elbe-Auen test site is given. (see Fig. 5.6). The description of the floodplain of the Elbe-Auen as well as the total power L-band image can be found in *Chapter 3*. The landscape is composed mainly of agricultural fields, small urban areas, grass land, bushes, small forest areas and the Elbe-Auen channel as well as the arbitrary channel of the small Aland river. The agricultural area consists of different crop types and bare fields. On the basis of these different types of scatterers - bare surfaces, grass land, fields covered with crops, and forested and urban areas - the behaviour of the polarimetric entropy, anisotropy and alpha angle is analysed.
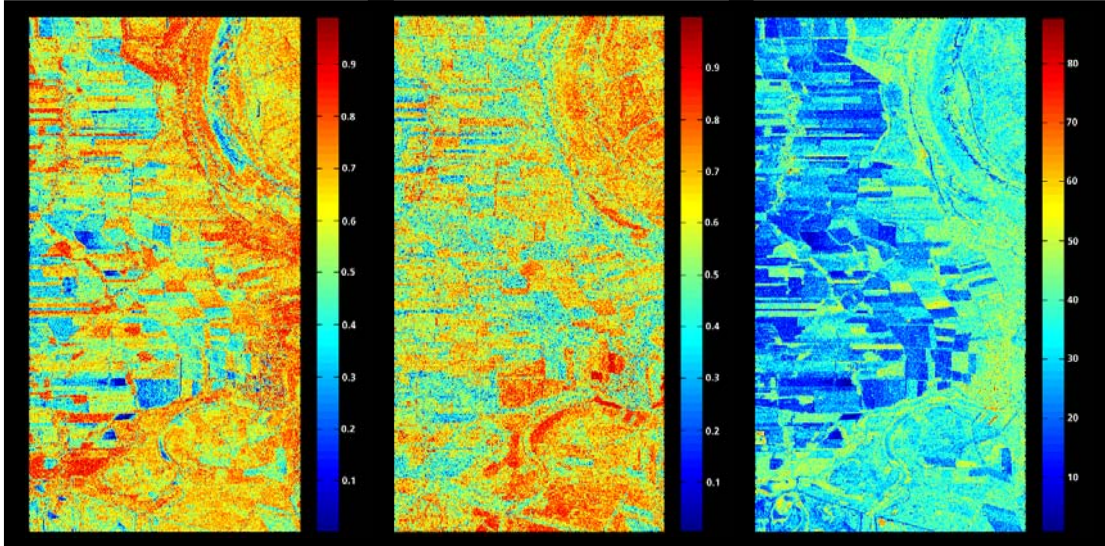
Fig. 5.6: Polarimetric entropy (left), alpha angle (middle)
and anisotropy (right) maps for the Elbe-Auen.

The bare surface and the river channel, as seen in Fig. 5.6, have low entropy values ranging from 0 to 0.4, anisotropy which ranges from 0 to 1, and low alpha angle values ranging from 0° to 40°. The low values for H indicate the presence of a single dominant scattering mechanism, while the low α values indicate to an anisotropic surface scattering. The anisotropy varies over

its whole definition range, from low values over high roughness areas for which the presence of secondary scattring effects is expected, to high values over small roughness areas for which the scattering process becomes quasi-deterministic.
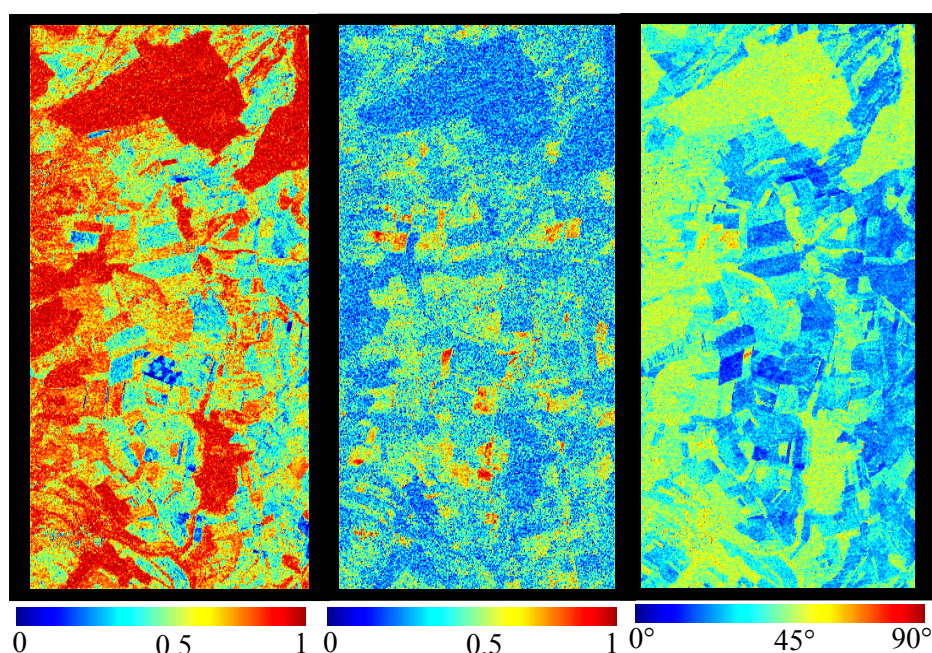
Fig. 5.7 Polarimetric entropy (left), anisotropy (middle)
and alpha angle (right) maps for the Weiherbach.

The scattering from grass land and agricultural fields covered with vegetation at L-band, include components from the vegetation as well as from the underlying soil surface. Thus, the presence of secondary scattering processes is expected. Indeed such scatterers are characterised by a medium range of H and α and again A covers a whole range between 0 and 1. The H ranges from 0.4 to 0.6, and α ranges from 43° to 55°. The medium H values are characteristic for the present of two (or more) scattering mechanisms. The corresponding α value indicate dipol-like scattering processes.

Finally, forest and urban areas show high H values and high α values but again a value of A, which is ranging from 0 to 1. High H ranges from 0.6 up to 1 indicating the superposition of three scattering mechanisms in accordance with the expectations at L-band. The high α values ranging from 55° up to 90° indicate dominant dihedral scattering. High anisotropy values indicate the presence of two main scattering mechanisms, while low anisotropy values indicate three scattering mechanisms.

Polarimetric parameters	bare surface	grassland	forest
Entropy H	0 to 0.5	0.5 to 0.8	0.8 to 1
Alpha Angle α	0° to 43 °	43° to 55°	55° to 90 °
Anisotropy A	0 to 1	0 to 1	0 to 1

Tab. 5.3: Ranges of the statistical polarimetrical parameters.

5.11 Synopsis

In *Chapter 5*, the main concept of wave and scattering SAR polarimetry has been presented. It will be of relevance to the next chapters concerning the estimation of soil surface parameters from polarimetry SAR data. It starts with the definition of polarisation and the description of polarised plane EM waves in a spherical co-ordinate system. In the real domain, only two parameters are to describe the shape of the polarisation ellipse needed, the orientation angle and thereby the polarisation state of the wave, ψ and the ellipticity angle χ. For the description of the polarisation in the two-dimensional complex space, the Jones vector representation was introduced and used for the definition of the complex polarisation ratio ρ. The inherent change of the reference basis by using the unitary transformation matrix $[U_2]$ is discussed.

The polarimetric scattering problem in backscattering characterisations has been addressed by introducing the Sinclair matrix $[S]$. The Sinclair matrix describes the resolution cell of deterministic scatterers to receive information about distributed scatterers. In order to facilitate this, the scattering vector was introduced. The outer product of the scattering vector builds the well known covariance or coherency matrix, which contains the same information as the Kennaugh matrix and additionally information about a number of resolution cells. In *Chapter 7*, only the coherency matrix will be considered for the modelling and inversion of surface parameters. For the ease of the reader, the tools for the transformation from the covariance $[C]$ into the coherency matrix $[T]$, and vice versa, are presented in the next chapter.

The change of basis transformation for the scattering matrix, the scattering vector, and the coherency matrix, from an arbitrary reference basis into another has been introduced and then exemplary applied on the transformation from the HV linear basis into the left/right circular basis. This transformation will be relevant for the extraction of the orientation angle for the correction of topographic induced slopes.

The symmetry properties of the scattering matrix allows a simplification of the scattering problem and permits a quantitative conclusion about their scattering behaviour. Three special cases of symmetries: reflection, rotation and azimuthal symmetry, have been discussed. Each of them characterises typical remote sensing scatterers: the reflection symmetry, for example, is usually found over bare agricultural fields. On the other hand, the rotation symmetry properties are not prevalent found in nature. They are describing the random distribution of helixes and the azimuthal symmetry, which appears if both symmetries are present, and is usually found at shorter wavelength over dense forest canopies.

Finally, three statistical polarimetric parameters:, the entropy, the anisotropy and the alpha angle have been introduced. Their definitions and physical interpretations on two test sites, the Elbe-Auen and the watershed Weiherbach have been presented.

5.12   References to Chapter 5

AZZAM, R. M. & N. M. BASHARA, 'Ellipsometry and Polarized Light', North Holland, Amsterdam,1989 Third Edition, *Harcourt Brace Jovanovich College Publishers*, Orlando, 1988.

BEBBINGTON, D. H. O., 'Target Vectors: Spinorial Concepts', *in Proceedings of 2nd International Workshop on Radar Polarimetry*, IRESTE, University of Nantes, France, pp. 26-36, Sep. 1992

BOERNER, W. M. & M. B. EL-ARINI, 'Polarisation Dependence in Electromagnetic Inverse Problem', *IEEE Transactions on Antennas and Propagation*, vol. 29, no. 2, pp. 262-271, 1981.

BOERNER, W.-M., C. L. LIU & X. ZHANG, 'Comparison of Optimisation Procedures for 2x2 Sinclair, 2x2 Graves, 3x3 Covariance, and 4x4 Mueller (Symmetric) Matrices in Coherent Radar Polarimetry and its Application to Target Versus Background Discrimination in Microwave Remote Sensing', *EARSeL Advances in Remote Sensing*, vol. 2, no. 1, pp. 55-82, 1993.

BOERNER, W. M. ET AL., 'Polarimetry in Radar Remote Sensing: Basic and Applied Concepts', Chapter 5 in F. M. Henderson, and A.J. Lewis, (ed.), "Principles and Applications of Imaging Radar", vol. 2 of Manual of Remote Sensing, (ed. R. A. Reyerson), Third Edition, John Willey & Sons, New York, 1998.

BORGEAUD, M., S. V. NGHIEM, R. T. SHIN & AND J. A. KONG, 'Theoretical Models for Polarimetric Microwave Remote Sensing of Earth Terrain'*, Journal of Electromagnetic Waves and Applications*, vol. 3, no.1, pp. 61-81, 1989.

BROYDEN, C. G., 'Basic Matrices: An Introduction to Matrix Theory and Practice', Macmillian Press, London, pp. 211, 1975.

BORN, M. & E. WOLF, 'Principles of Optics', Sixth Edition, Pergamon Press, New York, 1985

CHEN, H. C., 'Theory of Electromagnetic Waves: A Coordinate-Free Approach', McGraw-Hill Book Company, New York, 1983.

CLOUDE, S. R., 'Group Theory and Polarisation Algebra', *OPTIK*, vol.75, no. 1, pp. 26-36, 1986.

CLOUDE, S. R., 'Polarimetry: The Characterisation of Polarimetric Effects in EM Scattering', PhD. Thesis, University of Birmingham, Faculty of Engineering, UK, October 1986

CLOUDE, S. R., 'Uniqueness of Target Decomposition Theorems in Radar Polarimetry', in W. – M. Boerner et al. (eds.) Direct and Inverse Methods in Radar Polarimetry*, Kluwer Academic Publishers*, Netherlands, pp. 267-398, 1992.

CLOUDE, S. R. & E. POTTIER, 'Concept of Polarisation Entropy in Optical Scattering'*, Optical Engineering*, vol. 34, no. 6, pp. 1599-1610, 1995.

CLOUDE, S. R. & E. POTTIER, 'A Review of Target Decomposition Theorems in Radar Polarimetry', *IEEE Transactions on Geoscience and Remote Sensing*, vol. 34, no. 2, pp. 498-518, 1996

CLOUDE, S. R. & E. POTTIER, 'An Entropy Based Classification Scheme for Land Applications of Polarimetric SAR', *IEEE Transactions on Geoscience and Remote Sensin*g, vol. 35, no.1, pp. 68-78, 1997.

CLOUDE, S. R., 'Wide Band Radar Inversion Studies Using the Entropy-Alpha Decomposition', Proceedings SPIE'97, vol. 3120, Wideband Interferometric Sensing and Imaging Polarimetry, pp. 118-129, *SPIE's 42nd Annual Meeting*, San Diego, 27 July-1 August 1997.

CLOUDE, S.R., 'Symmetry, Zero Correlations and Target Decomposition Theorems', *Proceedings 4th Int. Workshop on Radar Polarimetry*, PIERS, pp. 58-66, 1998.

COLLET, E., 'Polarized Light: Fundamentals and Applications', Marcel Dekker, Inc., New York, 1993.

DESCHAMPS, G.A., 'Geometrical Representation of the Polarisation of a Plane Electromagnetic Wave', *Proceedings of the IRE*, vol. 39, no. 5, pp. 540-544, 1951.

FERRO-FAMIL, L., 'Teledetection Multi-Frequentielle et Multi-Temporelle D'Environnements Naturels a Partir de Donnes SAR Polarimetriques'*, Doctoral Thesis from the University of Nantes*, France, no. 0366, pp. 220, 2000.

GUISSARD, A., 'Mueller and Kennaugh Matrices in Radar Polarimetry', *IEEE Transactions on Geoscience and Remote Sensing*, vol. 32, no. 3, pp. 590-597, 1994.

GRAVES, C. D., 'Radar Polarization Power Scattering Matrix', *Proceedings of the IRE*, vol. 44, no. 5, pp. 248-252, 1956.

HUYNEN, J. R., 'Phenomenological Theory of Radar Targets', Ph. D. thesis, University of Technology, Delft, The Netherlands, December 1970.

JACKSON, D. J., 'Classical Electrodynamics', John Willey & Sons, New York, 1975.

JONES, D. S, 'Acoustic and Electromagnetic Waves', Oxford Science Publications, Oxford, 1989.

JONES, R. C., 'A new Calculus for the Treatment of optical Systems I. Description and Discussion', *Journal of the Optical Society of America*, vol. 31, pp. 488-493, 1941.

JONES, R. C., 'A new Calculus for the Treatment of optical Systems II. Description and Discussion', *Journal of the Optical Society of America*, vol. 31, pp. 493-499, 1941.

KENNAUGH, E. M., 'Effects of the Type of Polarisation on Echo Characteristics', Reports 381-1 to 394-24, Antenna Laboratory, The Ohio State University Research Foundation, Columbus, OH, 1949-1954.

KOSTINSKI, B. & W. M. BOERNER, 'On the Foundation of Radar Polarimetry', *IEEE Transactions on Antennas and Propagation*, vol. 34, no. 12, pp. 1395-1404, 1986.

KROGAGER, E., 'Aspects of Polarimetric Radar Imaging', PhD. Thesis, Technical University of Denmark, Electromagnetics Institute, Lyngby, DK, March 1993.

KROGAGER, E., & W. M. BOERNER, 'On the Importance of Utilizing Polarimetric Information in Radar Imaging Classification', AGARD Proc. 582-17, 1-13, April 1996

LEE, J. S., M. R. GRUNES, T. AINSWORTH, D. LU, D. L. SCHULER, & S. R. CLOUDE, 'Unsupervised Classification Scheme of Polarimetric SAR Images by Applying Target Decomposition Theorems and Complex Wishard Distribution', *IEEE Transactions on Geoscience and Remote Sensing*, vol. 34, no. 5, pp. 2249-2258, 1999.

LEE, J. S., M. R. GRUNES & G. DE GRANDI, 'Polarimetric SAR speckle filtering and its implication on classification', *IEEE Transactions on Geoscience and Remote Sensing,* vol. 37, no. 5, pp.2363-2373, 1999.

LEE, J. S., D. L. SCHULER & T. L. AINSWORTH, 'Polarimetric SAR Data Compensation for Terrain Azimuth Slope Variation', *IEEE Transactions on Geoscience and Remote Sensing*, vol. 38, no. 5, part I, pp. 2153-2163, 2000.

LORENTZ, H.A., 'The Theorem of Poynting Concerning the Energy in the Electromagnetic Field and Two General Propositions Concerning the Propagation of Light', English translation in Collected Papers, vol. 3, pp.1-11, Martinus Nijhoff, The Hague, 1936.

LÜNEBURG, E., ZIEGLER, V., SCHROTH, A. & K. TRAGL, 'Polarimetric Covariance Matrix Analysis of Random Radar Targets', AGARD-CP-501, Target and Cluster Scattering and their Effects on Millitary Radar Performance, Ottawa, pp. 27.1-27.12, 1991.

LÜNEBURG, E., 'Backscattering & Forward Propagation', Manuscript of Polarimetric Short Course, Seattle, July 1995.

MOTT, H., 'Antennas for Radar and Communications: A Polarimetric Approach', John Willey & Sons, New York, 1992.

NGHIEM, S. V., S. H. YUEH, R. KWOK, AND F. K. LI, 'Symmetry Properties in polarimetric Remote Sensing', *Radio Science*, vol. 23, no. 4, pp. 713-720, 1988.

POTTIER, E., D. L. SCHULER, J. S. LEE & T. L. AINSWORTH, 'Estimation of the Terrain Surface Azimuthal/Range Slopes Using Polarimetric Decomposition of Polsar Data', *Proceedings of IGARSS'99*, Hamburg, Germany, 1999.

POTTIER, E., 'Unsupervised Classification Scheme of POLSAR Images based on the Complex Wishard Distribution and the H/A/alpha Polarimetric Decomposition Theorem', *Proceedings 4th Int. Workshop on Radar Polarimetry*, PIERS, pp. 535-547, 1998.

SCHULER, D. L., J.S. LEE & T. L. AINSWORTH, 'Comparision of Terrain Azimuthal Slope Effects in Geophysical Parameter Studies Using Polarimetric SAR Data', Remote Sens. Environ, vol. 69, pp. 139-155, 1999.

SINCLAIR, G., 'The Transmission and Reception of Elliptically Polarized Waves', *Proceedings of the IRE*, vol. 38, no. 2, pp. 148-151, 1950.

TRAGL, K., 'Polarimetric Radar Backscattering from Reciprocal Random Targets', *IEEE Transactions on Geoscience and Remote Sensing*, vol. 28, no. 5, pp. 856-864, 1990.

ULABY, F. T. & ELACHI, C., 'Radar Polarimetry for Geocience Applications', Artech House, Inc., Norwood, MA, 1990.

VAN DE HULST, H., 'Light Scattering by Small Particles', Sixth Edition, Dover Press, New York, 1985.

VAN ZYL, J. J., 'On the Importance of Polarization in Radar Scattering Problems', Ph.D. thesis, California Institute of Technology, Pasadena, CA, December 1985.

Chapter 6

Inversion of Surface Parameters
Using Classical Approaches

T his chapter is the first of three chapters concerning the estimation of soil parameters from
polarimetric SAR data. In this first chapter, a critical review of three approaches for the
estimation of soil roughness and soil moisture content is given in order to provide the status of
surface parameter estimation. The three methods are introduced in chronological order. First,
the small perturbation surface scattering model - which is together with the Kirchhoff scattering
model the most common model for computing scattering from randomly rough surfaces - is
considered. Then, two extensions of the Small Perturbation Model, developed in order to
improve the performance of the Small Perturbation Model as well as its practical applicability,
are introduced. The first one is the semi-empirical extension addressed by OH *et al.* in 1992 and
the second is the empirical extension proposed by DUBOIS *et al.* in 1995. These three
approaches are selected not only because of their wide prevalence in the radar remote sensing
community but also in order to give an overview of the evolution of ideas and techniques in the
area of quantitative soil surface parameter estimation, although those methods are not
necessarily the best for the estimation as it will be shown in *Chapter 7* and *8*.

6.1 Theoretical Surfaces Scattering Models

The scattering problem of electromagnetic waves from randomly rough surfaces, which has
been an actual research topic over decades, is still not satisfactorily solved and no exact closed-
form solutions exist hitherto. However, for many practical applications, approximate solutions
are sufficient. Various approximate methods for wave scattering at rough surfaces of a more or
less general form have been developed. In the field of radar, the most common approximate
methods have been the Kirchhoff Approximation (KA) and the Small Perturbation Model
(SPM).

The KA is valid when the surface roughness dimensions are large compared to the wavelength,
and is therefore more suitable for applications with short wavelengths, as for example at X- or
C-band and for large surface correlation lengths ($kl > 6$). In this case, the scattering at a point
on the surface may be considered as scattering at the tangential plane to this point. Even with
this approximation it is not possible to obtain an analytic solution, and additional assumptions
are necessary. Therefore, two modifications of the KA have been addressed: The Geometric
Optics Model (GOM) and the Physic Optics Model (POM). The GOM represents the low

frequency solution of the KA, the obtained scattering coefficients depend mainly on the surface slope, and is valid for high surface roughness conditions ($ks > 2$). In contrast, the POM represents the high frequency solution of the KA, where the obtained scattering coefficients depend on the surface roughness and the surface correlation length, and it is valid for high surface roughness $ks > 0.25$.

On the other hand, the SPM assumes that the variation in surface height is small compared to the wavelength and is therefore more appropriate for applications with long wavelengths, as at S-, L- or P-band. Although valid only within a limited range of rough surface parameters, it is one of the classical and most widely used solutions of the rough surface scattering. It has been used extensively in many practical applications and the analytic conditions for its validity have been investigated in detail in several studies (BECKMANN & SPIZZICHINO 1963, CHEN & FUNG 1988).

6.1.1 Small Perturbation Model

6.1.1.1 Model Description

A perfectly smooth surface has zero backscatter at oblique incidence. However, in the Bragg scattering region, where the variation of surface height is small relative to the wavelength (i.e., for ks values $\ll 0.3$) the presence of roughness can be seen as a perturbation of the smooth surface scattering problem. In this case, the backscatter coefficients are obtained by the small perturbation or Bragg scattering model which is derived directly from Maxwell's equations (OH *et al.* 1992). According to this model, the random surface is decomposed into its Fourier spectral components, each one corresponding to an idealised sinusoidal surface. The scattering is mainly due to the spectral component of the surface which matches (i.e. is in resonance) with the incidence wavelength and angle of incidence (AOI). The scattering matrix [*S*] for a Bragg surface is of the form

$$[S] = \begin{bmatrix} S_{HH} & S_{HV} \\ S_{VH} & S_{VV} \end{bmatrix} = m_s \begin{bmatrix} R_S(\theta, \ \varepsilon) & 0 \\ 0 & R_P(\theta, \ \varepsilon) \end{bmatrix} \tag{6.1}$$

where m_s is the backscatter amplitude containing the information about the roughness condition of the surface, and R_S and R_P are the Bragg scattering coefficients perpendicular and parallel to the incidence plane, respectively. Both are functions of the complex permitivity ε and the local incidence angle θ

$$R_S = \frac{\cos\theta - \sqrt{\varepsilon - \sin^2\theta}}{\cos\theta + \sqrt{\varepsilon - \sin^2\theta}} \qquad R_P = \frac{(\varepsilon - 1)(\sin^2\theta - \varepsilon(1 + \sin^2\theta))}{(\varepsilon\cos\theta + \sqrt{\varepsilon - \sin^2\theta})^2} \qquad (6.2)$$

One of the most important statements of the SPM arrives directly from Eq. (6.1), the co-polarised ratio R_s / R_p depends only on the complex permitivity and the local incidence angle, and is independent of surface roughness. Fig.(6.1) shows the dependency of the co-polarised ratio on the soil moisture content according to Eq.(6.1), for incidence angles ranging from 25 up to 60 degrees. For dry surfaces, the co-polarised ratio is high and decreases with increasing moisture content. A strong variation of the ratio for all incidence angles can be observed for soil moisture values ranging from $0 < m_v < 20$ [vol. %] which saturates for m_v values > 20 [vol %]. This indicates that the SPM is insensitive to very wet surfaces and therefore, its inversion yields prospectively too large uncertainties for moisture content estimates above the saturation level. Several studies have experimentally verified the sensitivity of R_s / R_p to soil moisture content in the case of slightly rough surfaces as well at its saturation above $m_v = 20$ [vol %] (CHEN & FUNG 1988).
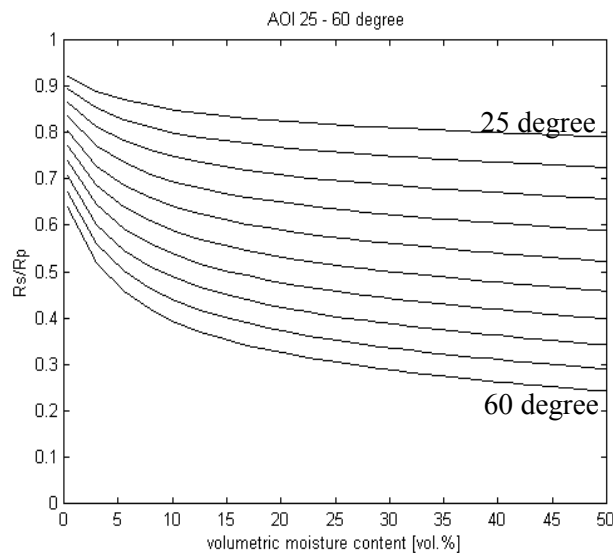
Fig. 6.1: Modelled co-polarised ratio versus soil moisture

However, for the most natural bare surfaces the validity range for roughness conditions of the SPM is too strict in order to be of practical importance. To demonstrate this, the roughness and moisture content values of all test fields from both test sites, Elbe-Auen and Weiherbach, are shown in Fig. 6.2. The roughness values are plotted against the corresponding moisture values, measured in two depths of 0 - 4 cm and 4 - 8 cm. The fact that only one of the test fields lies in the Bragg region, indicates the limited applicability of the SPM for the inversion of surface parameters under realistic conditions in radar remote sensing.

107
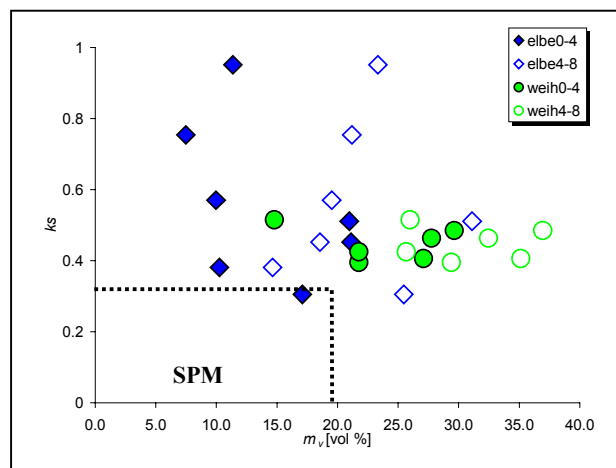
Fig. 6.2: Validity range of the SPM, surface roughness versus soil moisture content, for the Elbe-Auen and Weiherbach test sites.

6.1.1.2 Model Inversion

Even if the roughness conditions of the test fields are not covered by the validity range of SPM, the analysis of the inversion behaviour of the model and the comparison of the estimated parameters with the ground measurements allow helpful insights in the general problem of surface parameter estimation. Therefore, the inversion of soil moisture content by using the SPM is performed and discussed in the following. Due to the insufficiency of the model to describe the given roughness conditions the inversion of ks is not performed.

The inversion of m_v by means of the SPM is straightforward: The formation of the R_s / R_p ratio leads directly to a non-linear equation, which for a given incidence angle, depends only on ε_r. Resolving for ε_r and converting it to m_v, it leads to the desired estimation of the soil moisture content.

6.1.1.3 Experimental Data Analyses

In general, the co-polarised ratios observed in experimental data from natural surfaces are significantly higher than those predicted from the SPM, primarily due to the presence of roughness and in several orders of speckle and/or noise effects on the SAR data. To demonstrate this, the relation of the measured to the modelled values according to the SPM ratios using the dielectric constant, estimated from the ground measurements, and the

corresponding local incidence angle over the test fields is shown in Fig. 6.3. Due to this underestimation, the fields are interpreted dryer than they really are.
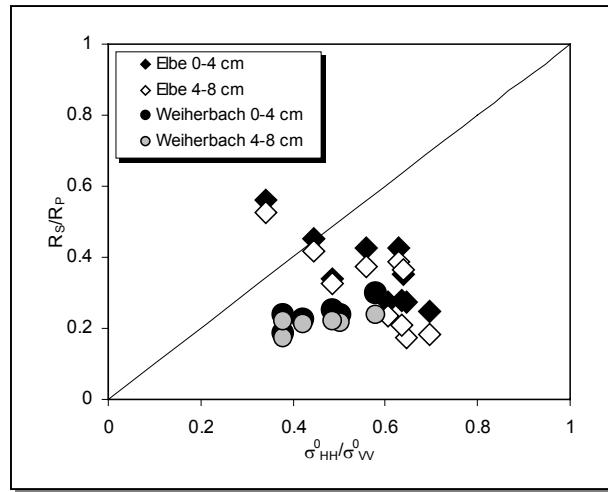
Fig. 6.3:.Measured versus estimated co-polarised ratio for both test sites.

The inversion results for both test sites are shown in Fig. 6.4. The comparison of the measured versus estimated soil moisture values show the same trend as indicated in Fig. 6.3. A significant deviation from the diagonal line with increasing moisture content is obtained, which is in accordance with the already discussed SPM characteristics. The estimation becomes insensitive for m_v values higher than 15 [vol. %], while the significant underestimation of the inverted volumetric moisture content m_v [vol. %] results directly from the underestimated co-polarised ratio.
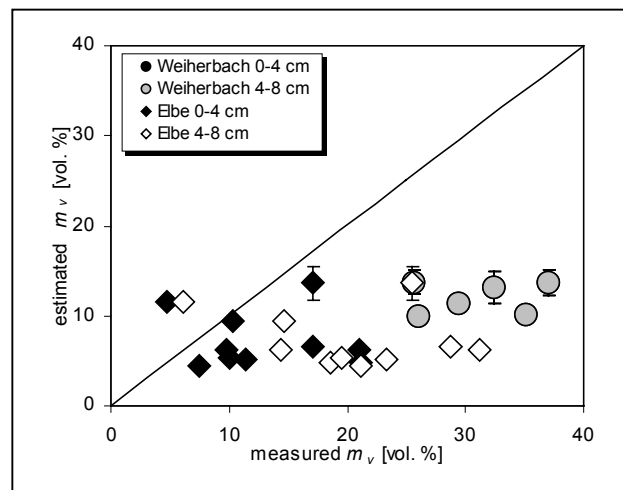
Fig. 6.4: Measured versus estimated volumetric moisture content m_v [vol. %] for both test sites.

Summarising, the main limitations of the SPM are its small surface roughness validity range - below than 0.3 *ks* and the saturation of its sensitivity to soil moisture content above m_v 20 vol. %. However, the robustness of SPM inside its validity range and its relevant physical background led to several investigations to use it as a valuable starting point for the evaluation of semi-empirical and empirical extensions in order to improve its performance. Two of these approaches, relevant for surface parameter estimation from SAR data, will be discussed in the next section.

6.2 Semi-Empirical and Empirical Approaches

Semi-empirical and/or empirical approaches are based on theoretical models, which are extended or modified according to physical considerations or empirical observations in order to increase the performance of the original model to interpret experimental data. In this section, two extensions of the SPM used for the inversion of surface parameters from polarimetric radar data will be introduced and discussed. Compared to the SPM, these models are characterised by a wider validity range regarding surface conditions and, as it will be demonstrated, a higher estimation accuracy.

6.2.1 Semi-Empirical Model Using Oh et al. (1992)

6.2.1.1 Model Description

Y. OH, K. SARABANDI, and F.T. ULABY developed this semi-empirical model at the University of Michigan, in 1992. The radar measurements used for its development were obtained by a truck-mounted scatterometer (LCX POLARSCAT) operating at three frequencies (1.5, 4.5 and 9.5 GHz) in a fully polarimetric mode with an incidence angle range from 10° to 70°.

On the basis of the scatterometer measurements and ground measurements, an empirically determined function for the co- and cross-polarised backscatter ratios was proposed (OH *et al*. 1992)

$$p = \frac{\sigma_{HH}^0}{\sigma_{VV}^0} = \left(1 - \left(\frac{2\theta}{\pi}\right)^{\frac{1}{3\Gamma^0}} \cdot e^{-ks}\right)^2 \tag{6.3}$$

and

$$q = \frac{\sigma_{HV}^0}{\sigma_{VV}^0} = 0.23\sqrt{\Gamma^0}\left(1 - e^{-ks}\right) \tag{6.4}$$

where p and q indicate the co- and cross polarised backscatter ratios, $\dfrac{\sigma^0_{HH}}{\sigma^0_{VV}}$ and $\dfrac{\sigma^0_{HV}}{\sigma^0_{VV}}$ respectively; θ the local incidence angle, ks is the RMS height normalised to the wavelength, and $\Gamma°$ the Fresnel reflectivity coefficient at nadir (i.e., $\theta = 0$) and

$$\Gamma^0 \;=\; \left| \frac{1-\sqrt{\varepsilon'}}{1+\sqrt{\varepsilon'}} \right|^2 \tag{6.5}$$

ε' is the relative dielectric constant. For a known angle of incidence, Eq.(6.3) and Eq.(6.4) constitute a system of two non linear equations with two unknowns: ks and ε'.

The main characteristics of the model are briefly summarised by the following three points:

- The co-polarised ratio p *is always* lower than one for all local incidence angles, surface roughness conditions and soil moisture contents, as shown in Fig. 6.5. It increases monotonically with increasing ks up to $ks \cong 1$ and converges slowly to one, which finally reaches for $ks > 3$. On the other hand, for $ks < 3$, p decreases with increasing local incidence angle and/or with increasing soil moisture content. A significant sensitivity to soil moisture and incidence angle variations can be observed.
- The cross-polarised ratio $q \ll 1$, shows – as compared to the co-polarised ratio - a stronger sensitivity to ks variations and a weaker dependency to soil moisture variations. q increases with increasing ks up to $\cong 1$ and converges slowly to a value, which depends on the soil moisture content and finally reaches it for $ks > 3$. A significant sensitivity of the quotient q to surface roughness and no dependency on the incidence angle can be observed, respectively, as shown in Fig. 6.6.
- In general, the algorithm exhibits a good agreement to the ground measurements in the range of $0.1 \leq ks \leq 6$, $2.5 \leq kl \leq 20$, and $9 \leq m_v \leq 31$.

The fact that p and q are limited to $ks \leq 3$ and $p = \dfrac{\sigma^0_{HH}}{\sigma^0_{VV}} \leq 1$ makes the model more appropriate

for applications at lower frequencies, as for example for the S-, L-, or P-band.
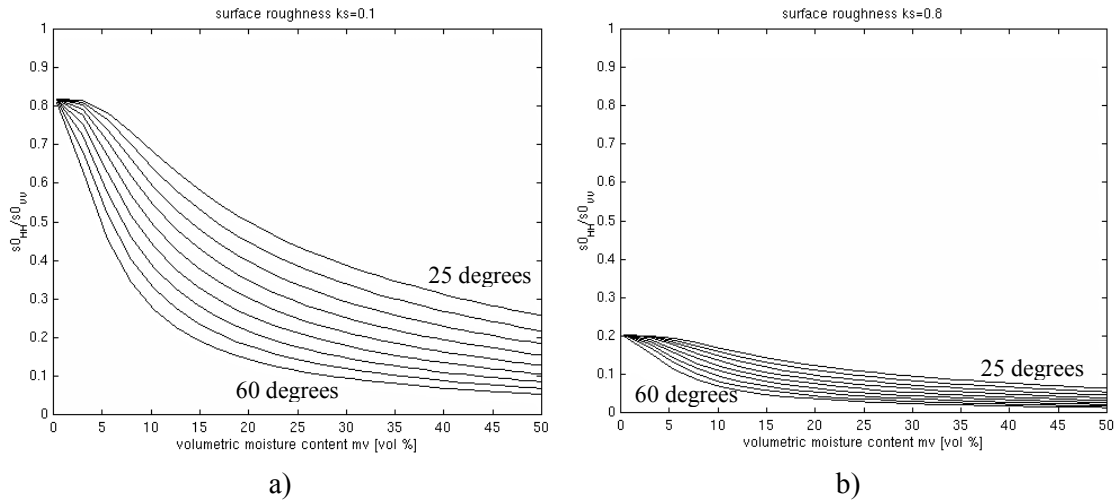
Fig. 6.5: Co-polarised ratio versus volumetric moisture content for varying local incidence angle: a) for a smooth surface $ks = 0.1$ and b) for a rough surface $ks = 0.8$.
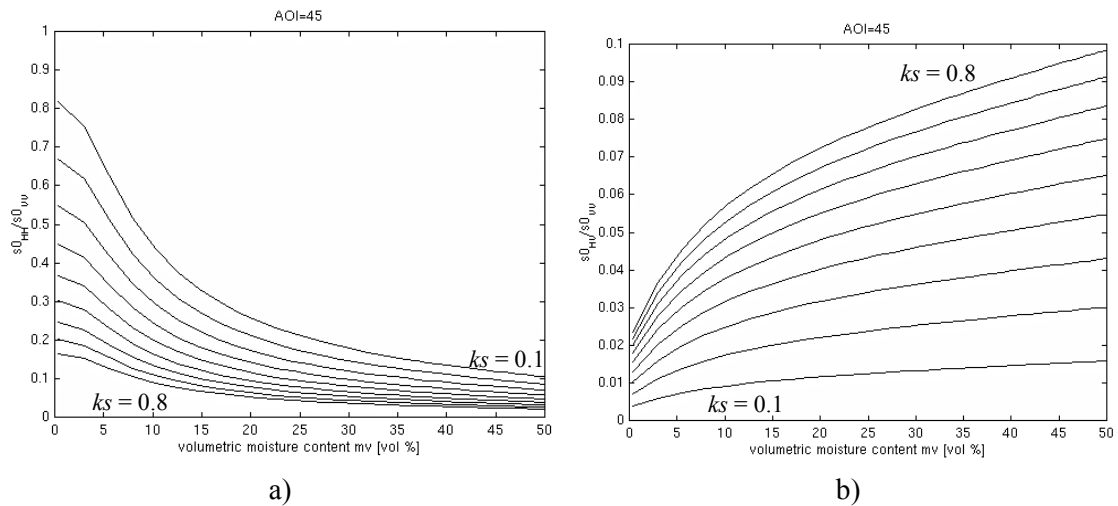
Fig. 6.6: Co- and cross-polarised ratio versus volumetric moisture content for varying surface roughness (from ks=0.1 up to ks=0.8) for a local incidence angle of 45 °.

6.2.1.2 Model Inversion

The inversion of the Oh-Model is based on the solution of Eq. (6.3) and Eq. (6.4) for ks and ε'. In the absence of an analytic solution, ks and ε' have to be estimated by an iterative procedure. In a first step, $\Gamma°$ is evaluated from Eq. (6.3) and Eq. (6.4) after eliminating ks

$$\left(\frac{2\theta}{\pi}\right)^{\frac{1}{\Gamma^{\circ}}}\left[1\frac{q}{0.23\sqrt{\Gamma^{\circ}}}\right]+\sqrt{p}-1=0 \tag{6.6}$$

Using the measured co- and cross-polarised ratios, Γ° can be estimated from Eq. (6.6) using an iterative technique. In this study, the Newton iteration approach was applied. Accordingly, the *n*-th Newton iteration for Γ° is given by

$$x_n = \frac{a^{\frac{(x_{n-1})^2}{3}}\left(1-b\cdot x_{n-1}\right)+c}{\left[\frac{2\cdot x_{n-1}}{3}\cdot\ln(a)\cdot\left(1-b\cdot x_{n-1}\right)-b\right]a^{\frac{(x_{n-1})^2}{3}}} \tag{6.7}$$

where

$$x:=\frac{1}{\sqrt{\Gamma^0}}, \qquad a:=\frac{2\theta}{\pi}, \qquad b:=\frac{q}{0.23}, \qquad c:=\sqrt{p-1} \tag{6.8}$$

In a second step, from the approximated value $x:=\frac{1}{\sqrt{\Gamma^0}}$, Γ^0 is extracted as $\Gamma^0=\left(\frac{1}{x_n}\right)^2$ and used

to retrieve directly from Eq. (6.5) the real part of the dielectric constant

$$\varepsilon' = \left|\frac{1 + \sqrt{\Gamma^0}}{1 - \sqrt{\Gamma^0}}\right| \tag{6.9}$$

The obtained values for ε' are converted into m_v values after TOPP *et al*. (1980). Finally, Γ^0 is used again in Eq. (6.10) to derive the surface roughness value *ks* as

$$ks = \ln\left(\frac{\left(\sqrt{p} + 1\right)}{\left(\frac{2\theta}{\pi}\right)^{\frac{1}{3\Gamma^0}}}\right) \tag{6.10}$$

The iterative procedure converges rather slowly after about 30 iterations.

6.2.1.3 Experimental Data Analysis

As the application of the Oh-Model makes sense only for surface scatterers, non-surface scattering areas have to be masked out. Therefore, the inversion algorithm is applied only on points which satisfy $p < 1$ and q < -11 dB. Both conditions follow from Fig. 6.5 and Fig. 6.6,

and ensure that apart from vegetated areas even surface scatterers affected by multiple scattering, volume scattering, or secondary scattering processes, which are not accounted by the model, are excluded. The application of these conditions on experimental data makes clear that primarily the second condition; and, in second order, the first condition are too strict for many natural bare fields. A high amount of points over bare fields are masked out ranging in the case of the Elbe-Auen from 28 % up to 82 % of points-per-field, while in the case of Weiherbach region the amount of invalid points-per-field is somewhat smaller ranging from 12 % to 55 %. The reason for this high drop-out is once again the roughness conditions as well as secondary scattering and depolarisation effects caused by short surface correlation lengths, as well as the presence of sparse vegetation and/or volume scattering. The two acquisition campaigns took place under different seasonal conditions - the Elbe-Auen campaign during a dry period in August, whereas the Weiherbach campaign during a wet period in April. The fact, that during summer the influence of volume scattering, estimated with the generally higher roughness of the Elbe-Auen test fields, may explain the higher drop out observed over the Elbe-Auen test fields. However, the inversion algorithm is applied by using the mean values of the backscattering coefficients averaged over the entire field. The obtained results are discussed in the following.

Surface Roughness Estimation

The surface roughness inversion results for both test sites are presented in Fig. 6.7. The inversion has been performed, due to the presence of vegetation, for the Elbe-Auen test site only for seven agricultural fields (A5/8, /10, /12, /13, /14, /15, /16). The main RMS error for the Weiherbach test site is about 0.18 and lies on the same order as for the Elbe-Auen test site for which it is about 0.2. On the contrary, the correlation for the Elbe-Auen test site is much higher about 0.6, than for the Weiherbach estimates. It should be noticed that the fields are closely grouped around the zero error line.
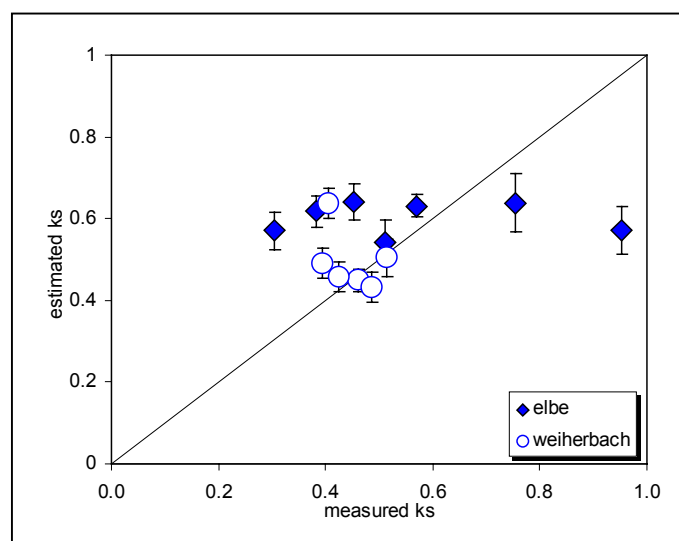
Fig. 6.7: Estimated versus measured surface roughness

Fig. 6.7 shows that the Elbe-Auen fields are overestimated while the Weiherbach fields are fitting very well to the correlation line. However, reasonably good inversion results were achieved up to *ks* = 0.6. The Elbe-Auen test fields cover a wide range of surface roughness values from 0.3 up to 0.95 while the variation of the inverted roughness parameter varies only from 0.46 to 0.64. The rough fields are more effected by the error due to smooth fields. The highest correlation between the measured and the estimated roughness values lies in the range of 0.4 and 0.6, observed for the Elbe-Auen and Weiherbach test fields.
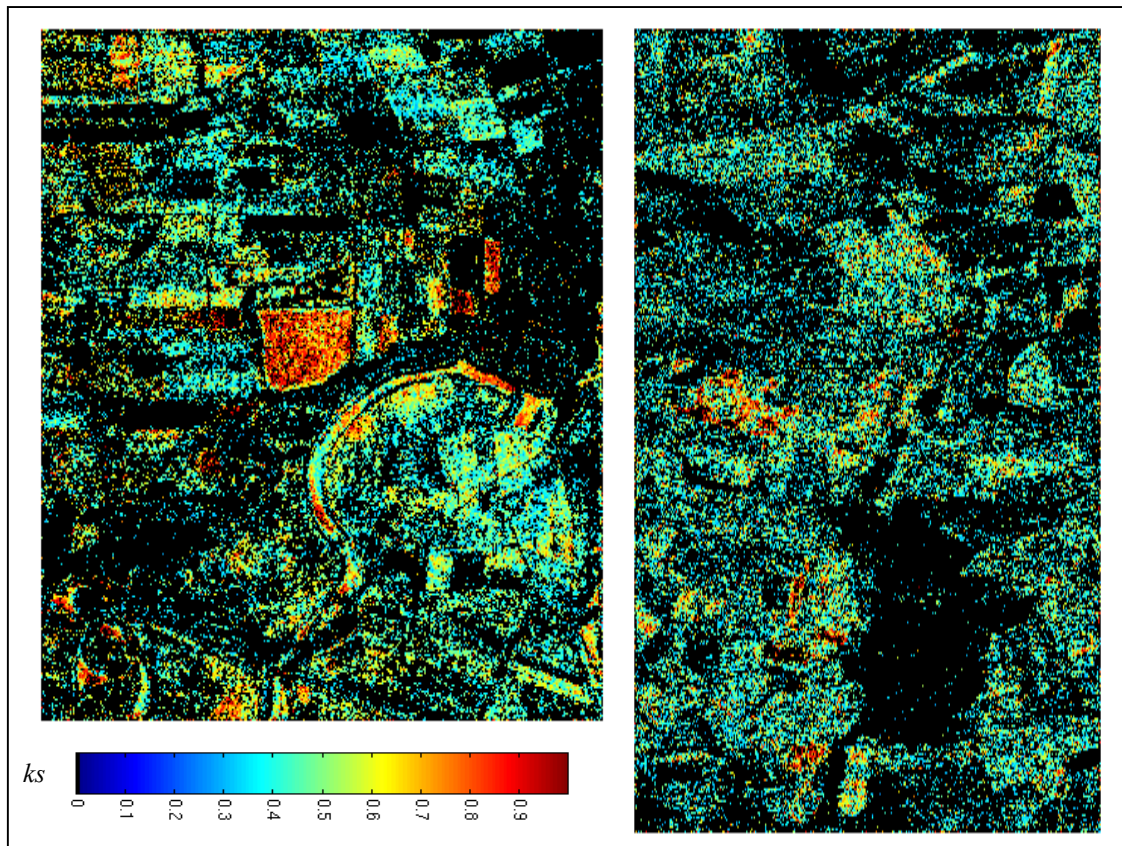
a.) Elbe-Auen   b.) Weiherbach

Fig. 6.8: Surface roughness estimation, ranging from 0 to 1 *ks*.
Areas not satisfying the modelled conditions are black.

In Fig. 6.8, the estimation results are presented as a surface roughness map, where the areas, which are not satisfying the condition, are black. These are mainly areas covered with vegetation.

Soil moisture Estimation

The soil moisture content estimation for the Weiherbach test field for both soil depths are highly underestimated. The RMS error is about 18 for the 0 - 4 cm soil depth and about 25 for the 4 - 8 cm soil depth with a mean correlation 0.6. Significantly better results are obtained from the upper soil layer of the Elbe-Auen test fields with an RMS error of 7. The deeper soil layer indicates a higher RMS error of 12 but is still better estimated than the corresponding value for the Weiherbach fields.
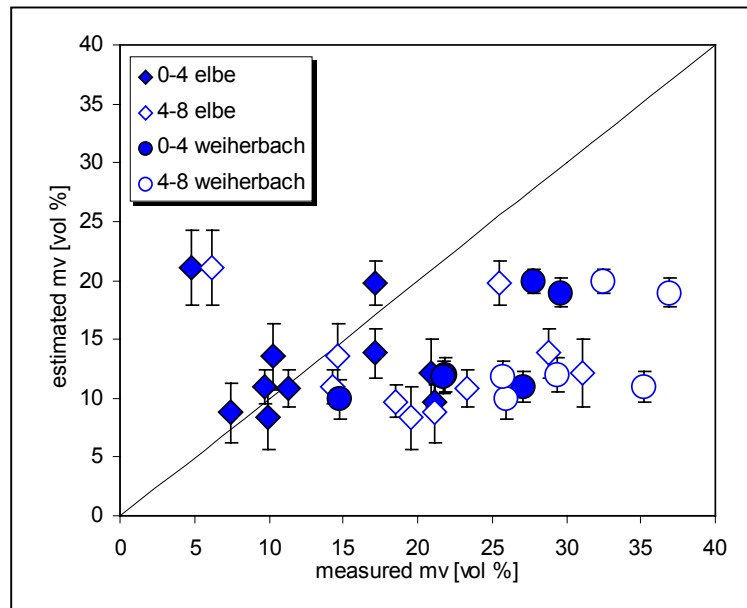
Fig. 6.9: Estimated versus measured soil moisture content m_v [vol %]

Fig. 6.9 shows that the sensitivity of the Oh-Model to soil moisture is higher for dryer soils up to $m_v \leq 25$ vol. %, which extends slightly the saturation limit of the SPM, as predicted from the model (see Fig. 6.5a). Therefore, the validity range of the Oh-Model extends the validity ranges of the SPM for the soil moisture. However, in cases with a high roughness component, as for example field A5/7 of the Elbe-Auen or W5 of the Weiherbach test site, the soil moisture has been significantly overestimated. In general, it can be stated, that the Oh-Model can only be as accurate as the SPM because the Oh-Model is based on the SPM approach.

In Fig. 6.10 the visualised inversion results of the soil moisture content indicates a poor performance for the soil moisture content estimation.
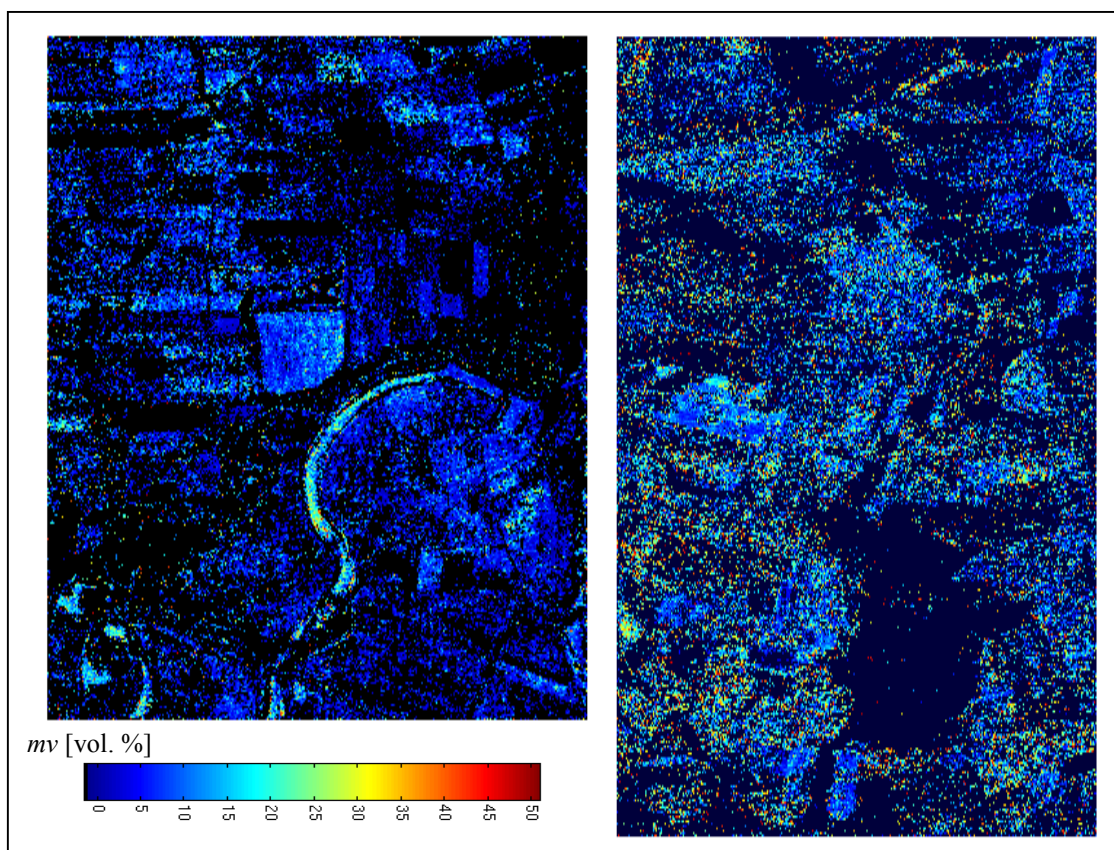
a.) Elbe-Auen   b.) Weiherbach

Fig. 6.10: Soil moisture content estimation, ranging from 0 to 50 m_v [vol %]. Black are the areas which are not satisfying the modelled conditions.

6.2.2 Empirical Model from Dubois et al. (1995)

6.2.2.1 Model Description

The empirical model developed by P. C. DUBOIS, J. VAN ZYL, and T. ENGMAN in 1995 is a simplification of the Oh-Model adressing only co-polarised backscatter coefficient. The data used in the original study, were collected with the scatterometer from the University of Michigan LCX as well as with the University of Bern scatterometer (RASAM) operating at six frequencies between 2.5 GHz and 11 GHz. In later investigations the algorithm was applied to SAR data (AIRSAR and SIR-C) in order to prove the robustness of the algorithm.

Using the scatterometer data and ground measurements, the empirically determined co-polarised backscatter coefficients, σ^0_{HH} and σ^0_{VV} for the horizontal and vertical polarisation, were expressed as a function of system parameters, as the local incidence angle and frequency, and soil parameters, such as dielectric constant and surface roughness. In a first elaborative step, the dependence of the backscattering coefficient ratio on different soil moisture conditions

117

and the local incidence angle was investigated. It was found that the relationship resembles most closely to the tangent of the incidence angle. In a second step, the deviation caused by surface roughness was accounted for by an empirically derived expression for the roughness term $\log(ks \cdot \sin\theta)$. The resulting expressions are given by

$$\sigma^0_{HH} = 10^{-2.75} \frac{\cos^{1.5}\theta}{\sin^5\theta} 10^{0.028\varepsilon' \tan\theta} (ks \cdot \sin\theta)^{1.4} \lambda^{0.7} \tag{6.11}$$

$$\sigma^0_{VV} = 10^{-2.37} \frac{\cos^3\theta}{\sin^3\theta} 10^{0.046\varepsilon' \tan\theta} (ks \cdot \sin\theta)^{1.1} \lambda^{0.7} \tag{6.12}$$

where θ is the local incidence angle, ε' is the real part of the dielectric constant, ks the normalised surface roughness and λ the wavelength. For a known angle of incidence, Eq.(6.11) and Eq.(6.12) constitute a system of two non-linear equations with two unknowns: ks and ε'.

Similar to the prediction of the SPM, the backscatter coefficient of Eq. (6.11) and Eq. (6.12) decreases with increasing local incidence angle and/or with decreasing surface roughness. On the other hand, the backscatter coefficient increases with increasing soil moisture, stronger in σ^0_{VV} than in σ^0_{HH}. Furthermore, the sensitivity to moisture content decreases with increasing local incidence angle.

The empirically determined expressions predict that the ratio $\sigma^0_{HH}/\sigma^0_{VV}$ is roughness-dependent and increases with increasing surface roughness, due to the $\log(ks \cdot \sin\theta)$ term. This is different from the SPM, where the co-polarised term does not depend on roughness.

On the other hand, with increasing soil moisture content, the backscatter ratio $\sigma^0_{HH}/\sigma^0_{VV}$ is steadily increasing, while its sensitivity to moisture content decreases with a decreasing local incidence angle as shown in Fig. 6.11.

The performance of the model may be briefly summarised by the following points (DUBOIS et al. 1995):

- The estimated validity range for the surface parameters are $m_v \leq 35$ % and $ks \leq 2.5$ and their accuracy is ranging for the soil moisture estimation by about 4.2 vol. % and for the surface roughness by about ks of 0.4 for a bare surface (NDVI < 0.4).
- For an inversion accuracy better than 4 vol. % the radar data should be calibrated to within 2 dB absolute and 0.5 dB relative accuracy between the two co-polarised channels.
- If the cross-polarised channel is available, it can be used to exclude disturbing vegetation impacts.
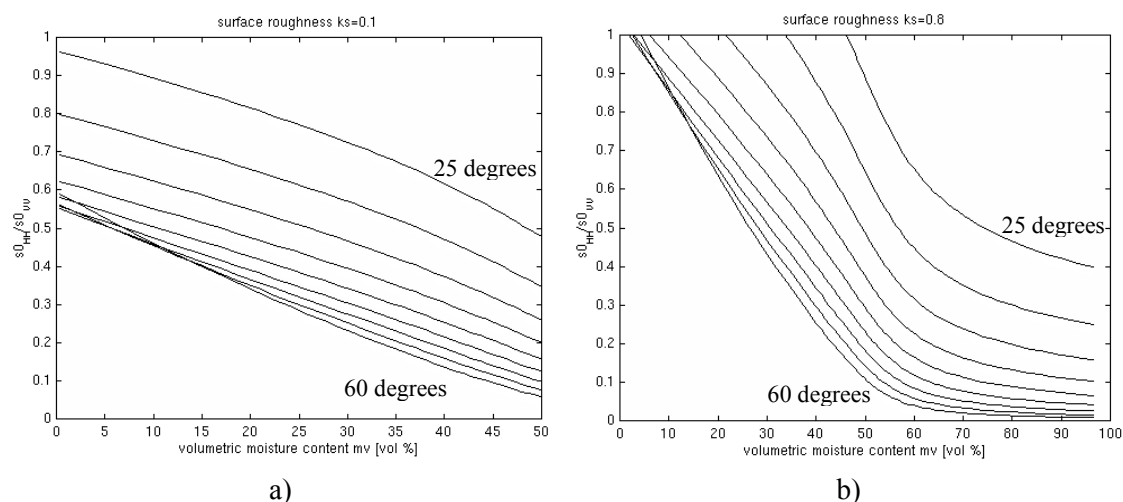
Fig. 6.11: Sensitivity plots of the co-polarised ratio to the volumetric moisture content for varying local incidence angles. a) for a smooth surface $ks = 0.1$; and

b) for a rough surface $ks = 0.8$.

Important aspects which are not considered by the model as stated in Eq. (6.11) and Eq. (6.12), are:

- the influence of the tillage direction on the agricultural fields,
- the influence of the surface correlation length on the fields,
- the influence of topography on the accuracy of the estimated surface parameters.

There are several reasons why the model was developed to include only the co-polarised channels. Co-polarised backscattering coefficients are less sensitive to system noise and cross talk. Consequently, the calibration of the co-polarised returns is simpler to perform and more accurate. In the early 90's, the deployment of effective polarimetric calibration algorithms was still under development. Furthermore, they provide a robust performance to the algorithm even in the presence of sparse vegetation. Finally, the need of only two channels allows the application of the algorithm on data acquired using dual polarised systems instead of fully polarised systems, which are strictly required for the application of the Oh-Model.

6.2.2.2 Model Inversion

The inversion of the empirical algorithm addressed by DUBOIS *et al.*(1995) is much simpler than the inversion of the model proposed by OH *et al.*(1992). Both, dielectric constant as well as surface roughness, can be retrieved directly from the model using the co-polarised backscatter coefficient and the local incidence angle by using the following two step inversion algorithm.

The first step is to retrieve the dielectric constant as

$$\varepsilon' = \frac{\left(\log 10 \left(\frac{\left(\sigma_{HH}^0 \right)^{0.7857}}{\sigma_{VV}^0} \right) 10^{-0.19} \cos^{1.82} \theta \sin^{0.93} \theta \lambda^{0.15} \right)}{-0.024 \tan \theta} \qquad (6.13)$$

and using the estimated dielectric constant, in the second step, to retrieve the surface roughness

$$ks = \sigma_{HH}^0 10^{2.75} \frac{\sin^{2.57} \theta}{\cos^{1.07} \theta} 10^{-0.02 \cdot \varepsilon' \cdot \tan \theta} \lambda^{-0.5} \qquad (6.14)$$

As latter experiments demonstrated, the algorithm is performing relatively well also over sparsely vegetated areas at least at lower frequencies. For the discrimination of vegetated areas the $\sigma_{VH}^0 / \sigma_{VV}^0$ ratio may be used as a good vegetation indication. Ratio values of $\sigma_{VH}^0 / \sigma_{VV}^0 >$ -11 dB indicate the presence of vegetation, and such areas are masked out and remain unconsidered by the inversion. As very well pointed out in DUBOIS et al. (1995); this condition leads to mask out also very rough surfaces, ($ks > 3$), which are mistaken for vegetated areas. Anyway, such fields are too rough to be accounted for by the model and have to be excluded.

The algorithm was applied only on areas where $\sigma_{HH}^0 / \sigma_{VV}^0 < 1$ and $\sigma_{VH}^0 / \sigma_{VV}^0 <$ -11 dB in order to consider only areas lying within the validity range of the model. Also here, for the estimation of the soil moisture content the polynomial relation TOPP et al. (1980) for the conversion from ε' to m_v is used.

6.2.2.3 Experimental Data Analysis

Surface Roughness Estimation

The inversion results for the surface roughness parameter by using the Dubois-Model displayed slightly higher RMS errors as compared to using the Oh-Model for both test sites. For the Weiherbach test fields the RMS error is about 0.25 and for the Elbe-Auen test fields the Dubois-Model leads to the same RMS error of about 0.24. The Weiherbach fields are indicating a high overestimation while for the Elbe-Auen fields no direct trend is observed. In general, the fields are more spread about the zero error line.
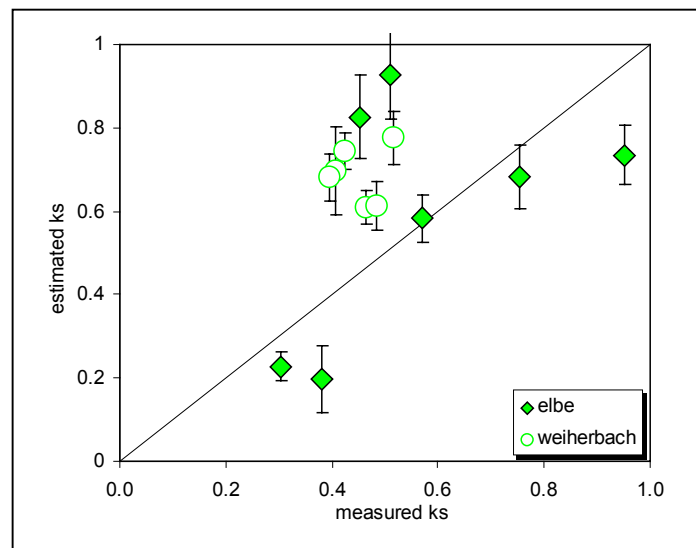
Fig. 6.12: Estimated versus measured surface roughness using the Dubois-Model for two test sites (Elbe-Auen and Weiherbach)
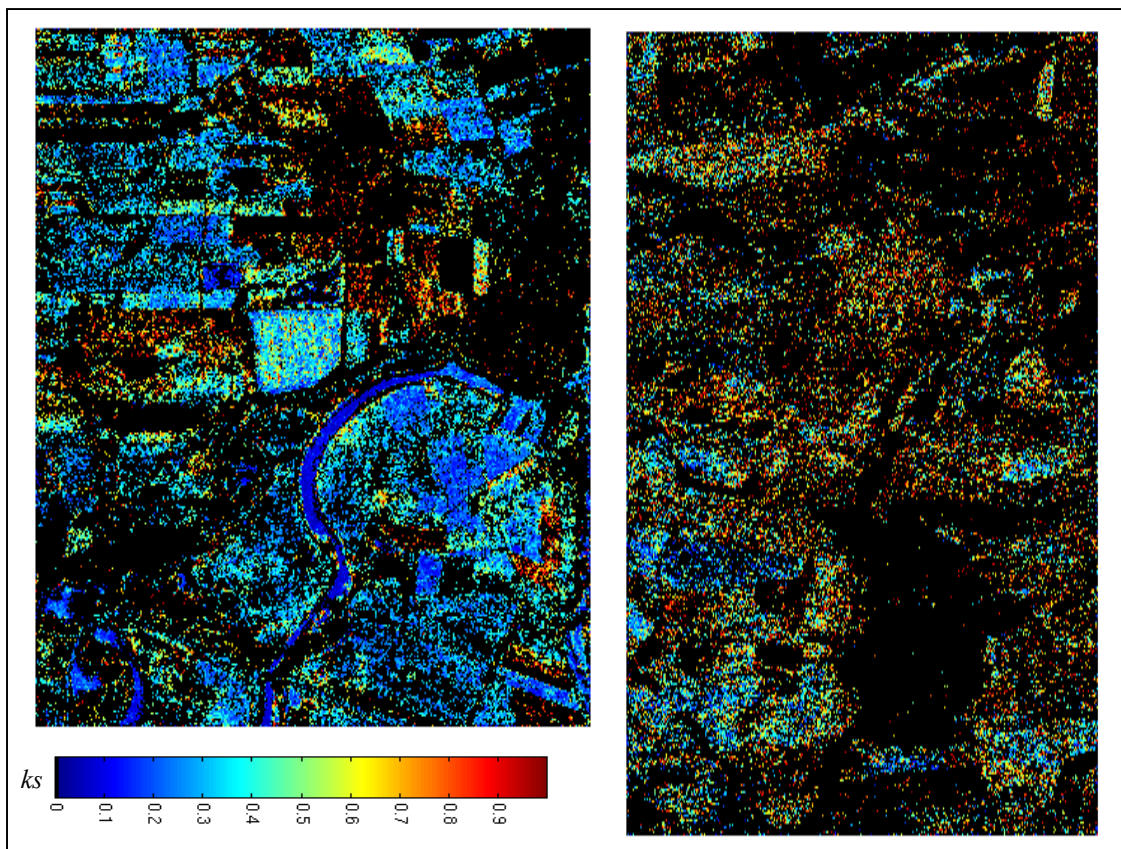
a.) Elbe-Auen   b.) Weiherbach

Fig. 6.13: Surface roughness estimation, ranging from 0 to 1 *ks.*

Black are the areas not satisfying the modelled conditions.

Soil moisture Estimation

The estimated soil moisture values are characterised by a at least better visual performance as compared to the Oh-Model. However, the RMS error for the Elbe-Auen test site is not significantly smaller.
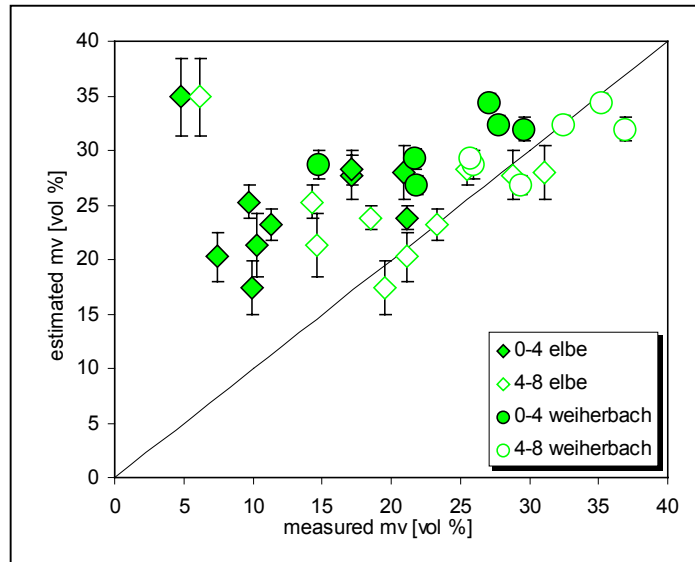
Fig. 6.14: Estimated versus measured soil moisture content m_v [vol. %] using Dubois-Model for two test sites (Elbe-Auen and Weiherbach)

The Weiherbach test site shows a very good performance with a slight overestimation tendency. The RMS error for the upper soil layer is about 8 and much better for the deeper layer at about 3, and it indicates therefore, much better performance than for the Elbe-Auen test site. The Elbe-Auen test site shows nearly the same RMS error for both layers, the deeper soil layer at about 10 and a higher RMS error for the first layer at about 14, contrary to the Oh-Model. The weak correlation for the Elbe-Auen test site results from the field A5/7 which is strongly overestimated. This field behaves in the same way as for the Oh-Model, due to its high roughness and dense cover of vegetation. In contrast, to the Oh-Model, the Dubois-Model is more sensitive to the soil moisture content estimation. Especially, the wetter range between 15 vol. % and 35 vol. % has the highest correlation.
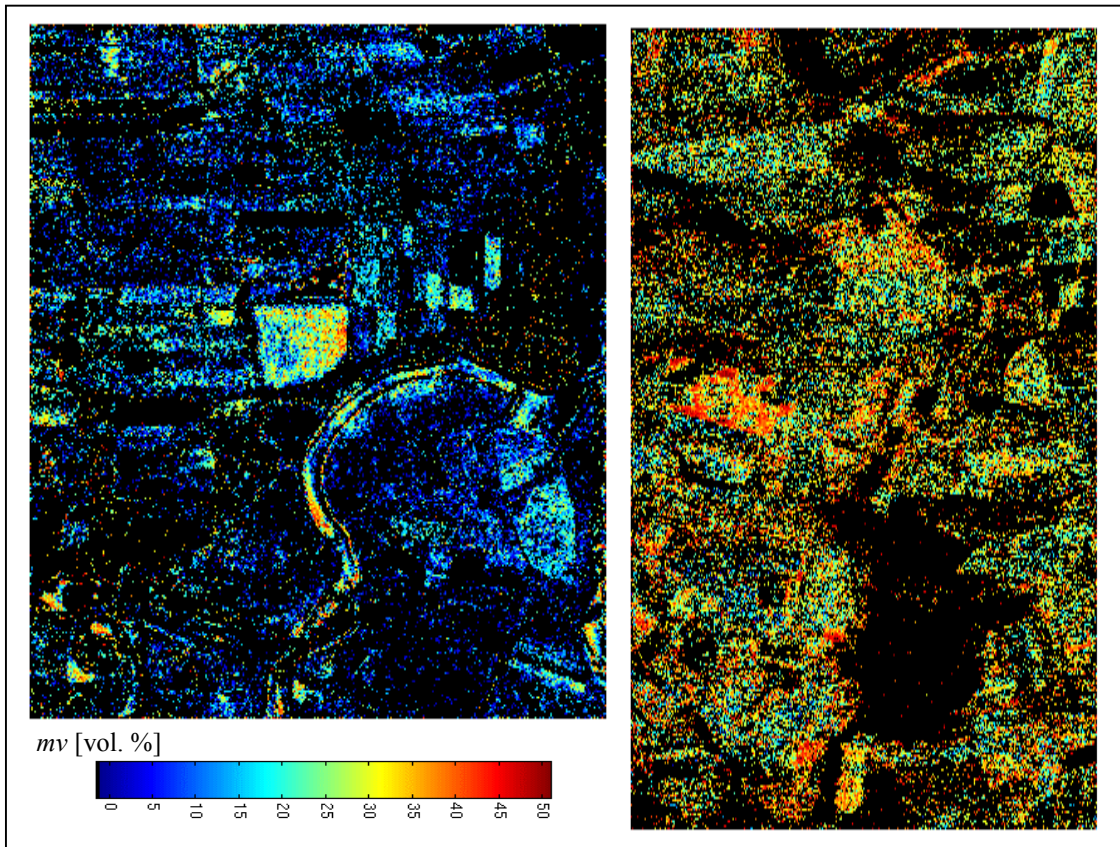
a.) Elbe-Auen   b.) Weiherbach

Fig. 6.15: Soil moisture content estimation, ranging from 0 to 50 m_v [vol %]. Areas not satisfying the modelled conditions are black.

6.3 Synopsis

Up to now, three inversion models were introduced, and their performance was demonstrated on two test sites over fields with different soil conditions. From the three theoretical models tested, the most promising for soil moisture estimation over smooth surfaces is the SPM. However, its inversion performance decreases rapidly with increasing roughness. For test fields with $ks > 0.3$ the estimated soil moisture values are strongly underestimated.

Empirical and semi-empirical models extend the roughness validity range of the SPM based on regressions obtained from experimental data. The Oh-Model considers additionally to the co-polarised channels also the cross-polarised term and obtains thus a higher sensitivity to roughness than the Dubois-Model which uses only the rather limited two co-polarised channel approach. This higher sensitivity is revealed in its better roughness estimation accuracy. In contrast the Dubois-Model has demonstrated an improved performance with respect to moisture content estimation than the Oh-Model. Both models perform best on flat terrain and fields without furrows, while their performance decreases over areas with topography and/or small correlation lengths. The inversion results, expressed in RMS errors and correlations are listed in Table 6.1.

The validity ranges of the three described inversion models are compiled in Table 6.2 and illustrated in Fig. (6.16) with respect to the ground measured fields. For the validity range of the SPM only one of all of the test fields suffices these constrains. The Oh-Model covers the range of surface roughness very well but is limited to cover a wider range of soil moisture. The Dubois-Model covers a wider range of soil moisture but suffers to cover the complete range of surface roughness. However, natural surfaces show, in general, a much wider variety of roughness and of moisture than the ones covered by these first-order models.

Model	Test site	RMS error mv 0-4 [cm]	RMS error mv 4-8 [cm]	ks	Correlation mv 0-4 [cm]	Correlation mv 4-8 [cm]	ks
SPM	Elbe	8.6	15.4	---	-0.1	-0.25	---
	Weiherbach	12.6	19.4	---	0.74	0.6	---
Oh-Model	Elbe	7	12	0.2	-0.1	-0.3	-0.01
	Weiherbach	10.45	17.42	0.18	0.71	0.75	-0.61
Dubois-Model	Elbe	14	10	0.24	0.1	-0.2	0.5
	Weiherbach	7.69	2.95	0.25	0.22	0.1	-0.7

Tab. 6.1: Estimated soil moisture content and surface roughness values,
expressed in RMS error and the correlation r.

Validity range	*ks*	*kl*	θ	*m_v* vol. %	Polarisation
SPM	< 0.3	< 3	20° - 50°	< 20	co-polarised
Oh et al. (1992)	0.1 – 6.0	2.5 - 20	10° - 70°	9 – 31	co- and cross polarised
Dubois et al. (1995)	0.08 – 0.8	2.5 – 20	30° - 60°	0 – 35	co-polarised

Tab. 6.2: Validity range for the semi-empirical/empirical derived Models.
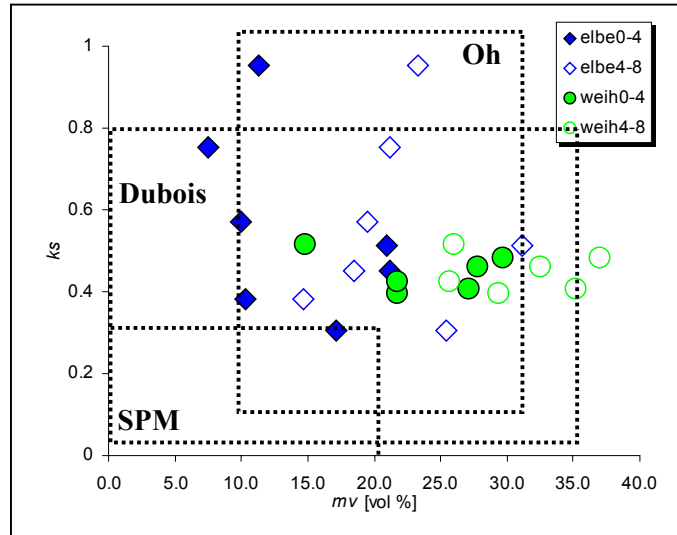
Fig. 6.16: Validity range of the theoretical and semi-empirical/empirical models
in the $ks – m_v$ space.

Further disadvantages of the semi-empirical/empirical models are summarised by the following points:

- Both models consider pure surface scattering and use therefore, ratio based restrictions, $\sigma^0_{HH}/\sigma^0_{VV} < 1$ and $\sigma^0_{VH}/\sigma^0_{VV} < -11$ dB, to discriminate points which cannot be accounted for. The high amount of excluded points indicates the presence of multiple and secondary scattering mechanisms. They are provoked due to sparse vegetation, high roughness and depolarisation effects on the ground. A large class of natural surface scatterers, is characterised by secondary and multiple scattering effects. With increasing surface roughness, relative to the wavelength implied, the effect of multiple scattering becomes stronger, generating an adequate |*HV*| scattering component. Such scatterers are not included in the validity domain of either model, especially not for the Dubois-Model. Also the case of vegetation covered surfaces, makes the application of the two models difficult. Dihedral scattering due to small correlation lengths characterised by |*HH*| > |*VV*|, and/or diffuse scattering (|*HV*| contribution), affect the backscattered signal. Both effects lead to a violation of the requirements, or to a biased estimation of the roughness and moisture parameters.

125

- For the inversion of the two main surface parameters, m_v and ks, the algorithms have to resolve the two unknowns from a system of two non-linear coupled equations. In the first processing step, the first parameter is resolved and used as input for the retrieval of the second parameter. Consequently, the error of the first parameter propagates into the estimation of the second one.

- Because the models are based on the evaluation of absolute coefficients, absolute polarimetric calibration becomes an issue. Absolute calibration is more critical for the Dubois-Model, which uses only two backscattering coefficients for the estimation of two parameters. In contrast, the Oh-Model uses two backscattering ratios and is, therefore, less affected by absolute calibration. DUBOIS *et al.* (1995) pointed out that for an accurate estimation, the limits for relative calibration should be below 0.5 dB and for absolute calibration it should be below 2 dB. Note, that for the E-SAR imaging system relative calibration is about 1 dB and absolute about 3 dB; which are being considered.

- Both models are empirically determined, and they use regression coefficients determined from scatterometer data, as well as SAR data, for the estimation of the surface parameters in the ground-range projection. This limits their transferability to other test sites and sensors.

The two semi-empirical/empirical models in the presented, or in slightly modified versions, have been analysed by a large number of scientists; all of them coming up with approximately the same results. The common problems are posed by the high RMS errors, the large number of regions which are not satisfying the conditions of bare surface scattering, and, the restricted validity range concerning surface conditions, which exclude a wide range of natural surfaces (WANG *et al.* 1997, PRIETZSCH 1998, NEUSCH 2000).

In the conclusion of this chapter, it is important to point out the key role of cross-polarisation for the estimation of soil roughness and moisture estimation. Roughness acts highly depolarising upon the incident wave and thus, generates cross-polarised backscattering and at the same time biases the co-polarised ratio, which is essential for the estimation of the dielectric constant. Hence, cross-polarisation is major for an accurate inversion. But, there is a note of caution concerning its interpretation. Cross-polarisation can be generated from bare surfaces in two ways:

1) The first one is due to the presence of roughness and in this case it is the ratio of the uncorrelated to the co-polarised returns.

2) The second one, is due to surface slope that implies a rotation of the surface about the line-of-sight (SCHULER *et al.* 1998). As stated in *Chapter 5*, line-of-sight rotation introduces cross-polarisation which – in contrast to roughness induced cross-polarisation is correlated to the co-polarised returns.

Under this aspect, it is relevant - and of importance for the interpretation of the obtained inversion results later on in *Chapter 7* - to review the different surface conditions assumed for the application of the three presented models.

1) The SPM assumes a single component non-depolarising surface scatterer, ignoring completely depolarising effects.

2) The Oh-Model, considers surfaces generating cross-polarised backscattering, or in other words, multi-component depolarising surface scatterers.

3) Finally, the Dubois-Model, as it uses only the co-polarised coefficients, is able to handle the non-depolarising single component as well as depolarising multi-component surface scatterers. However, the general performance for roughness estimation is poorer compared to the Oh-Model.

6.4 References to Chapter 6

BECKMANN, P. & SPIZZICHINO A., 'The Scattering of Electromagnetic Waves from Rough Surfaces', Oxford: Pergamon, Reprinted 1978 by Artech House Inc., Norwood, Massachusetts, USA, p. 503, 1963.

CHEN, M. F. & FUNG, A. K., 'A Numerical Study of the Regions of Validity of the Kirchhoff and Small-Perturbation Rough Scattering Models', *IEEE Transactions on Geoscience and Remote Sensing*, vol. 23, no. 2, pp. 163–170, 1988.

DUBOIS, P. C. VAN ZYL, J. J. & ENGMAN, T., 'Measuring Soil Moisture with Imaging Radars*', IEEE Transactions on Geoscience and Remote Sensing*, vol. 33, no. 4, pp. 916-926, 1995.

NEUSCH, T., 'Multi-Frequency and Multi-Polarization Synthetic Aperture Radar Data for Modelling Hydrological Parameters', Aachen: *Shaker Verlag*, Karlsruhe, Universitäre. Dissertation., p. 128, 2000.

OH, Y., SARABANDI, K. & ULABY, F. T., 'An Empirical Model and an Inversion Technique for Radar Scattering from Bare Soil Surfaces', *IEEE Transactions on Geoscience and Remote Sensing*, vol.30, no. 2, pp. 370-381, 1992.

PRIETZSCH, C. C., 'Vergleichende Analyse von SAR-Daten für die Regionalisierung des Wassergehalts im Oberboden*', Dissertation Universität Potsdam*, p.159, 1998.

TOPP, G. C., DAVIS, J. L. & ANNAN, A. P., 'Electromagnetic Determination of Soil Water Content: Measurements in Coaxial Transmission Lines', *Water Resources Research*; vol. 16, no. 3, pp. 574-582, 1980.

VAN ZYL J. J., 'Unsupervised Classification of Scattering Behavior Using Radar Polarimetric Data', IEEE Trans. GRS, GE-27 (1), pp. 36-45, Jan. 1989.

VAN ZYL, J. J., H. Zebker, and C. Elachi, 'Imaging Radar Polarization Signatures: Theory and Application', Radio Science, vol. 22, no. 4, pp. 529-543, 1987.

WANG, J. R., HSU, A., SHI, J. C. O'NEILL, P. E. & ENGMAN, E. T., 'A Comparison of Soil Moisture Retrieval Models Using SIR-C Measurements over the Little Washita River Watershed', *Remote Sensing of Environment*, vol. 59, pp. 308-320, 1997.

Chapter 7

Inversion of Surface Parameters
Using Polarimetric Pre-Processing Techniques

H aving introduced representatives of model-based, empirical, and semi-empirical algorithms for estimating surface parameters from fully- or dual-polarised SAR data, this Chapter investigates the feasibility of polarimetric pre-processing techniques for improving their performance. In the first part of this Chapter, the possibility to utilise polarimetric scatterer decomposition techniques is discussed in order to repress the disturbing influence of secondary scattering processes. The second part treats the problem of the estimation of the local incidence angle in the presence of terrain topography. The potential to estimate terrain slopes from fully polarimetric data alone is investigated and discussed as an alternative to the prevalent method of using available digital elevation models.

7.1 Scattering Decomposition

The main objective of scattering decomposition approaches is to break down the polarimetric backscattering signature of a distributed scatterer – which is in general given by the superposition of different scattering contributions inside the resolution cell - into a sum of elementary scattering contributions related to single scattering processes. In general, scattering decompositions are rendered into two classes:

- The first class includes decompositions performed on the scattering matrix. In this case the received scattering matrix is expressed as the coherent sum of elementary scattering matrices, each related to a single scattering mechanism. Thus, scattering matrix decompositions are often referred in the literature as coherent decompositions. The most common scattering matrix decompositions are the decomposition into the Pauli scattering matrices and the Sphere-Diplane-Helix decomposition first proposed by E. KROGAGER in 1993, and further considered in KROGAGER & BOERNER 1996.
- The second class of decompositions contains decompositions performed on second order scattering matrices. Decompositions of the coherency (or covariance) matrix belong to this class. Such approaches decompose the coherency matrix of a distributed scatterer as the incoherent sum of three coherency matrices corresponding to three elementary orthogonal scattering mechanisms. The decomposition can be addressed, based on a scattering model or on physical requirements, on obtained scattering components, as for example their statistical independence.

An extended review of scattering decomposition approaches can be found in CLOUDE & POTTIER (1996).

Scattering decompositions are widely applied for interpretation, classification, and segmentation of polarimetric data (CLOUDE & POTTIER 1998, LEE *et al.* 1999). They have also been applied for scattering parameter inversion. In the following, their application in the context of surface parameter estimation is considered. Due to of the fact that natural surfaces are distributed scatterers, coherency matrix decompositions are more suited for surface scattering problems than scattering matrix decomposition approaches, and therefore, only such approaches will be treated next.

7.2 Eigenvector Description

In this Section, the polarimetric eigenvector decomposition of the coherency matrix is introduced as a pre-filtering technique, which can be applied on the experimental data in order to improve the performance of the inversion algorithms. As already discussed in Chapter 5, the coherency matrix $[T]$ is obtained from an ensemble of scattering matrix samples $[S_i]$ by forming the Pauli scattering vectors

$$[S_i] = \begin{bmatrix} S_{HH} & S_{HV} \\ S_{VH} & S_{VV} \end{bmatrix} \quad \rightarrow \quad \vec{k}_{P_i} = \frac{1}{\sqrt{2}} \left[S_{HH} + S_{VV}, S_{HH} - S_{VV}, 2S_{HV} \right]^T \tag{7.1}$$

Averaging the outer product of them over the given samples, yields

$$[T] := \left\langle \vec{k}_{P_i} \cdot \vec{k}_{P_i}^+ \right\rangle = \begin{bmatrix} \left\langle |S_{HH} + S_{VV}|^2 \right\rangle & \left\langle (S_{HH} + S_{VV})(S_{HH} - S_{VV})^* \right\rangle & 2\left\langle (S_{HH} + S_{VV})S_{HV}^* \right\rangle \\ \left\langle (S_{HH} - S_{VV})(S_{HH} + S_{VV})^* \right\rangle & \left\langle |S_{HH} - S_{VV}|^2 \right\rangle & 2\left\langle (S_{HH} - S_{VV})S^*_{HV} \right\rangle \\ 2\left\langle S_{HV}(S_{HH} + S_{VV})^* \right\rangle & 2\left\langle S_{HV}(S_{HH} - S_{VV})^* \right\rangle & 4\left\langle |S_{HV}|^2 \right\rangle \end{bmatrix} \tag{7.2}$$

Since the coherency matrix $[T]$ is by definition hermitian positive semi-definite, it can always be diagonalised by an unitary similarity transformation of the form

$$[T] = [U_3][\Lambda][U_3]^{-1} \quad \text{where} \quad [\Lambda] = \begin{bmatrix} \lambda_1 & 0 & 0 \\ 0 & \lambda_2 & 0 \\ 0 & 0 & \lambda_3 \end{bmatrix}, \quad \text{and} \quad [U3] = \begin{bmatrix} | & | & | \\ \vec{e}_1 & \vec{e}_2 & \vec{e}_3 \\ | & | & | \end{bmatrix}. \tag{7.3}$$

$[\Lambda]$ is the diagonal eigenvalue matrix with elements of the real non-negative eigenvalues of $[T], 0 \le \lambda_3 \le \lambda_2 \le \lambda_1$, and $[U_3]$ is a special unitary matrix with the corresponding orthonormal

eigenvectors $\bar{e}_i$. The idea of the eigenvector approach is to use the diagonalisation of $[T]$ obtained from a partial scatterer, which is in general of rank 3, in order to represent it as the non-coherent sum of three deterministic orthogonal scattering mechanisms. Each of the three scattering contributions, expressed in terms of a coherency matrices $[T_1]$, $[T_2]$, and $[T_3]$, is obtained from the outer product of one eigenvector and weighted by its appropriate eigenvalue.

$$[T] = \lambda_1(\bar{e}_1 \cdot \bar{e}_1^+) + \lambda_2(\bar{e}_2 \cdot \bar{e}_2^+) + \lambda_3(\bar{e}_3 \cdot \bar{e}_3^+) = [T_1] + [T_2] + [T_3] \tag{7.4}$$

$[T_1]$, $[T_2]$, and $[T_3]$, are rank one coherency matrices, i.e., they represent deterministic non-depolarising scattering processes and correspond therefore to a single scattering matrix. Furthermore, as they are built up from the orthonormal eigenvectors of $[T]$, they are statistically independent from each other

$$[T] = \begin{bmatrix} t_1 & t_2 & t_3 \\ t_2^* & t_4 & t_5 \\ t_3^* & t_5^* & t_6 \end{bmatrix} = \begin{bmatrix} t_{11} & t_{12} & t_{13} \\ t_{12}^* & t_{14} & t_{15} \\ t_{13}^* & t_{15}^* & t_{16} \end{bmatrix} + \begin{bmatrix} t_{21} & t_{22} & t_{23} \\ t_{22}^* & t_{24} & t_{25} \\ t_{23}^* & t_{25}^* & t_{26} \end{bmatrix} + \begin{bmatrix} t_{31} & t_{32} & t_{33} \\ t_{32}^* & t_{34} & t_{35} \\ t_{33}^* & t_{35}^* & t_{36} \end{bmatrix} \tag{7.5}$$

According to a simplified interpretation, for natural surface scatterers the first scattering component $[T_1]$ represents the dominant anisotropic surface scattering contribution. The second and third components, $[T_2]$ and $[T_3]$, represent secondary dihedral and/or multiple scattering contributions, respectively. In this sense, disturbing secondary scattering effects biasing the original scattering amplitudes can be filtered out by applying the eigenvector decomposition of Eq. (7.4) and omitting one or both secondary contributions for the inversion of the surface parameters.

7.2.1 Application on Experimental Data

In a first step, the eigenvector decomposition is performed according to Eq. (7.4) leading to three contributions $[T_1]$, $[T_2]$, and $[T_3]$. There are two possible options for further implementation. The first one is to consider only the contribution corresponding to the maximum eigenvalue $[T_1]$ and omit both secondary contributions $[T_2]$, and $[T_3]$ assuming a single component non-depolarising surface. The corresponding backscattering coefficients σ_{HH}^0, σ_{VV}^0, and, σ_{HV}^0 are derived from the elements of $[T_1]$ as

$$\sigma_{HH}^0 = 10 \cdot \log 10 \frac{[t_{11} + t_{14} + 2\Re(t_{12})] \cdot \sin(\theta)}{2C} \tag{7.6}$$

$$\sigma_{VV}^0 = 10 \cdot \log 10 \frac{[t_{11} + t_{14} - 2\Re(t_{12})] \cdot \sin(\theta)}{2C} \tag{7.7}$$

$$\sigma_{HV}^0 = 10 \cdot \log 10 \frac{t_{16} \sin(\theta)}{2C} \tag{7.8}$$

where θ is the local incidence angle and C is a calibration factor. In the case of the E-SAR system C=1 000 000 (ZINK 1993, ZINK & KIETZMANN 1995). Note that σ_{HH}^0, σ_{VV}^0 and σ_{HV}^0 are expressed in dB.

The second option is to assume a dual component depolarising surface by considering the first and the second contribution, [T_1] and [T_2], and omit only the third contribution [T_3]. In this case, the corresponding backscattering coefficients σ_{HH}^0, σ_{VV}^0, and, σ_{HV}^0 are obtained from the elements of [T_1] and [T_2] as

$$\sigma_{HH}^0 = 10 \cdot \log 10 \frac{\left[(t_{11} + t_{21}) + (t_{14} + t_{24}) + 2\Re(t_{12} + t_{22})\right] \cdot \sin(\theta)}{2C} \tag{7.9}$$

$$\sigma_{VV}^0 = 10 \cdot \log 10 \frac{\left[(t_{11} + t_{21}) + (t_{14} + t_{24}) - 2\Re(t_{12} + t_{22})\right] \cdot \sin(\theta)}{2C} \tag{7.10}$$

$$\sigma_{HV}^0 = 10 \cdot \log 10 \frac{(t_{16} + t_{26}) \cdot \sin(\theta)}{2C} \tag{7.11}$$

Using these backscattering coefficients now, in a second step, the semi-empirical/empirical inversion algorithms are applied to estimate the moisture content and roughness parameters. Both approaches have been considered and are discussed in the next Sections.

The total power images of the three scattering mechanisms obtained from the eigenvector decomposition are shown in Fig. 7.1 for the Elbe-Auen and in Fig. 7.2 for the Weiherbach test site. The first component represents the dominant scattering mechanism occurring, which in case of surface scatterers may be interpreted as a non-depolarising anisotropic surface scatterering phenomenom. The second and third component correspond to secondary scattering mechanisms, which for low entropy scatterers – such as surface scatterers - are much lower than the first component. Only high entropy scatterers such as forested or urban areas are characterised by significant secondary scattering contributions.

Regarding the test fields now, the contribution of the second and third component for the Elbe-Auen test site is relevant only for fields covered with different crop types or bare fields with a high roughness component (fields A5/7, A5/8, A5/9, A5/11, A5/15 and A5/16). For the Weiherbach test site for which the surface roughness on the test fields is much lower than for the Elbe-Auen test site, only fields covered with vegetation have a noteworthy contribution in the second and third component. Over vegetated fields, the amplitudes of the second component [T_2] show a $|HH_2| > |VV_2|$ behaviour which indicates dihedral type scattering.
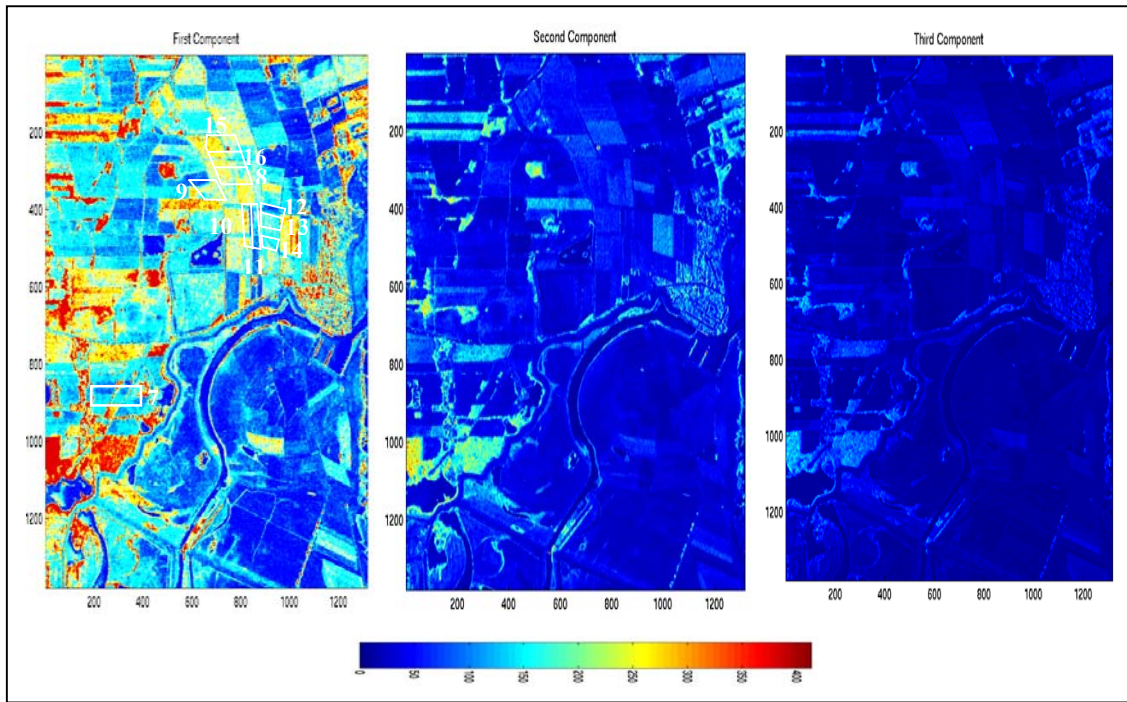
a)   b)   c)

Fig. 7.1: Power images of the a) first, b) second, and, c) third scattering mechanism obtained by applying the eigenvector decomposition on the Elbe-Auen test site.

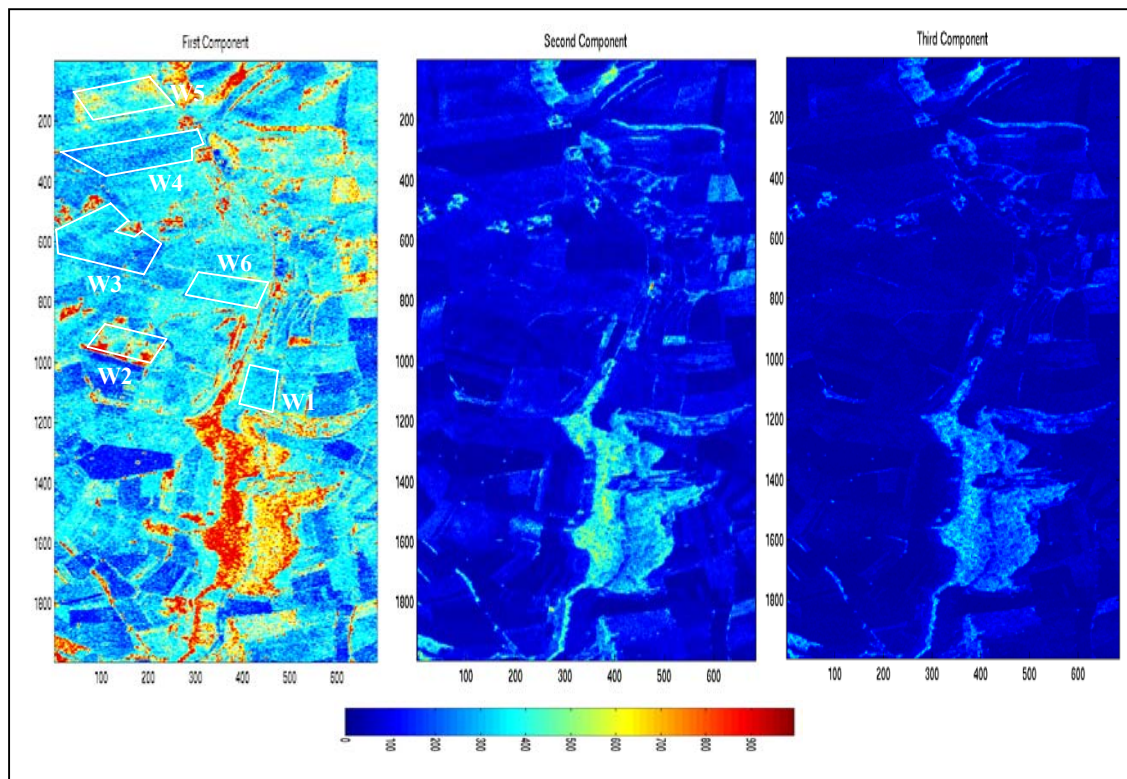a)   b)   c)

Fig. 7.2: Power images of the a) first, b) second, and, c) third scattering mechanism obtained by applying the eigenvector decomposition on the Weiherbach test site.

133

The amplitudes of the third component [T_3], display a significantly higher cross-polarised amplitude as compared to the other two components, verifying the assumption of multiple scattering.

Test fields Elbe	Total Points per field	Valid using [T]	Valid using [T_1]	Gain in [%]	Test fields Weih	Total points per fields	Valid using [T]	Valid using [T_1]	Gain in [%]
A5/7	4991	4975	4984	0.18	W1	9300	5569	7219	22.38
A5/8	1581	1371	1492	8.11	W2	8100	1670	2184	73.04
A5/9	4131	4083	4116	0.80	W3	9000	6292	7635	15.17
A5/10	4141	3343	3448	3.04	W4	10200	4481	5955	41.62
A5/11	3131	2876	2917	1.40	W5	7800	4981	5732	26.51
A5/12	1701	684	1277	46.43	W6	9450	6055	7459	21.07
A5/13	2511	2196	2259	2.78					
A5/14	1846	1264	1338	5.53					
A5/15	4131	1765	3856	54.22					
A5/16	5551	4520	4938	8.46					

Tab. 7.1: Amount of valid points per field which satisfy $\sigma_{HH}^0/\sigma_{VV}^0 < 1$ and $\sigma_{VH}^0/\sigma_{VV}^0 < $ -11 dB.

As already pointed out, one of the main restrictions in the application of the semi-empirical and empirical models is the high number of points which do not satisfy the requirements of $\sigma_{HH}^0/\sigma_{VV}^0 < 1$ and $\sigma_{VH}^0/\sigma_{VV}^0 < $ -11 dB. The decomposition leads to an increase of the amount of points inside one field to be applied for the inversion algorithms.

A quantitative comparison, given in Fig. 7.3. Fig. 7.3a, shows the areas that satisfy the conditions using the original polarimetric amplitudes, while Fig. 7.3b shows the valid point obtained by using the amplitudes corresponding to [T_1]. The highest gain on points is observed over surfaces covered with sparse vegetation or for surfaces with a high roughness component. From an inspection of Tab. 7.1, one finds that for the Weiherbach test site the amount of valid points increases more than for the Elbe-Auen test site. The reason for this is that all Weiherbach fields are covered with sparse vegetation (winter wheat) expect of the fields W2 and W5. For the Elbe-Auen test site the fields A5/12 and A5/15 which are covered with grass; and the fields A5/8, A5/10, A5/14 and A5/16 of a high roughness component, result in the largest gain on valid points.
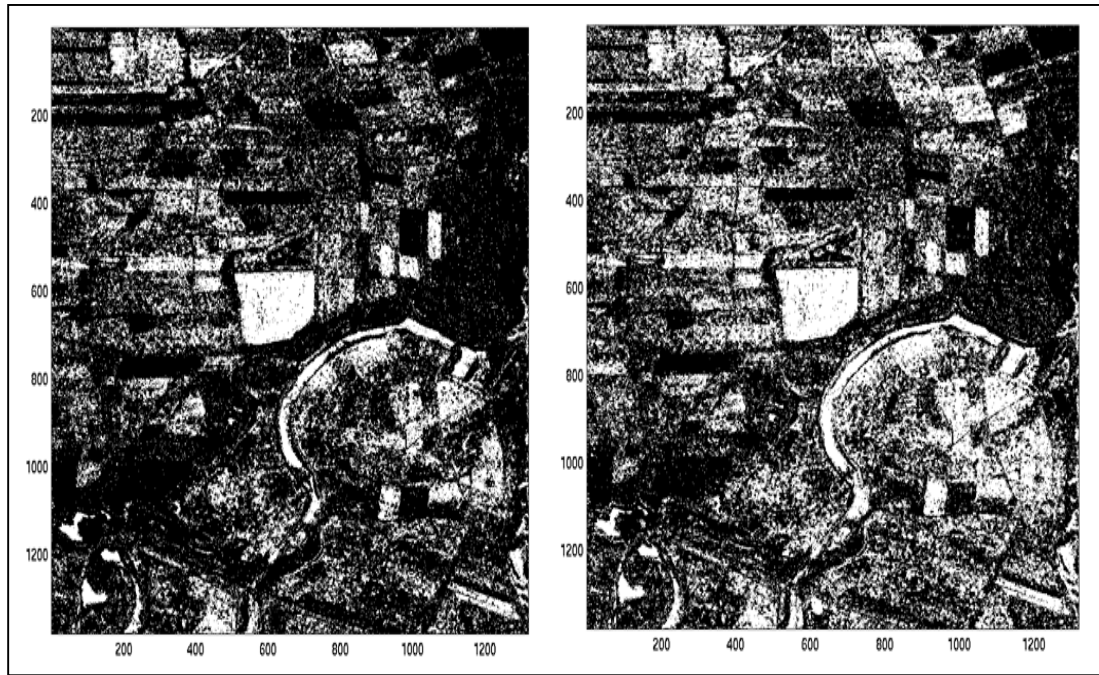
a)   b)
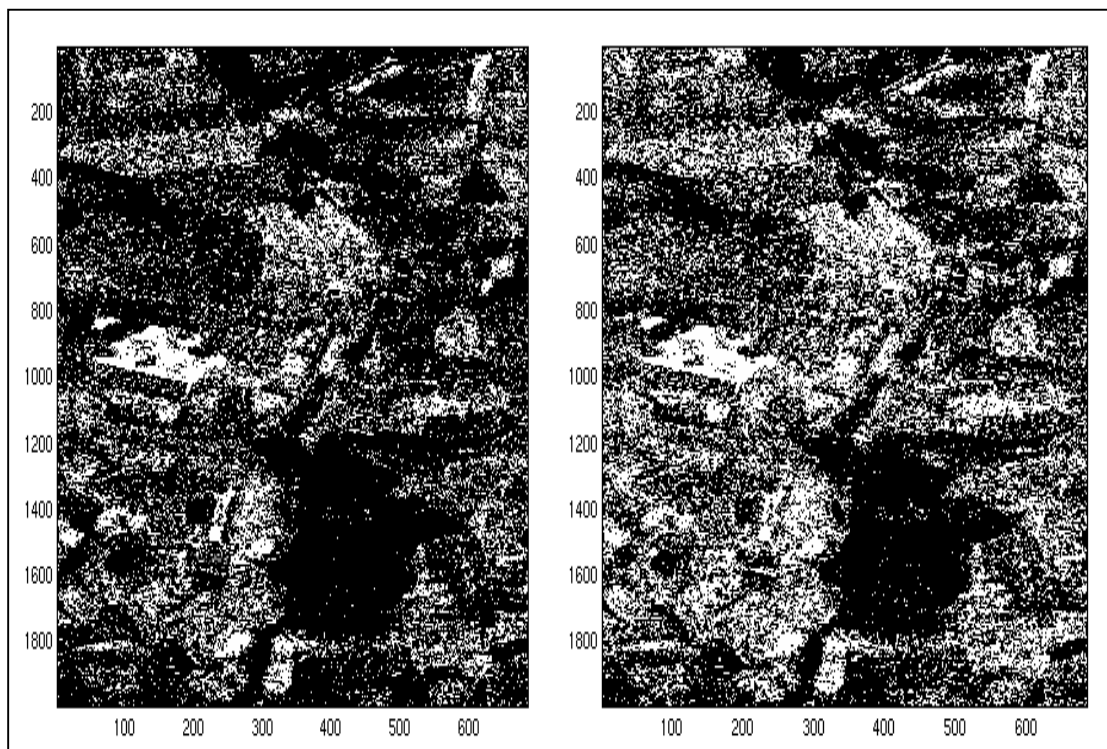
a)   b)

Fig. 7.3: Valid points which satisfy the conditions $\sigma_{HH}^0 / \sigma_{VV}^0 < 1$ and $\sigma_{VH}^0 / \sigma_{VV}^0 < -11$ dB. a) before and b) after decomposition (Top: Elbe-Auen test site and Bottom: Weiherbach test site).

7.2.2 Inversion Results

Surface parameter inversion has been applied for both, the single and the dual-component approach. For the single component approach all three inversion models (SPM, Oh-Model and Dubois-Model) while for the dual component approach only the Oh- and the Dubois-Model were applied. The results are summarised in the following.

7.2.2.1 Single Component Approach

Surface Roughness

The results of surface roughness estimation obtained by applying the Oh- and the Dubois-Model on the dominant scattering mechanism alone are shown in Fig. 7.4. For both models the RMS error is in general at the same level or inessentially higher compared to the estimates obtained from the original data sets. The RMS error for the Dubois-Model is about 0.21 for the Elbe-Auen site, while for the Weiherbach site the RMS error increases up to 0.46. The Oh-Model shows for both test sites a RMS error of about 0.24, the same as obtained by using the original data sets. The main significant improvement compared to the original estimates is the higher correlation obtained from the Dubois-Model; for the Elbe-Auen site at about 0.8 and the Weiherbach site at about 0.5.

a)   b)

Fig. 7.4: Estimated versus measured surface roughness obtained by applying
a) the Oh-Model and b) the Dubois-Model.

Soil Moisture Content

The soil moisture content estimates obtained from the SPM are shown in Fig. 7.5. Even if the mean RMS error - compared to the original data - increases, for some fields the performance is drastically improved. Especially the Elbe-Auen fields A5/7, A5/12, and, A5/15 which are covered with vegetation are shifted closer to the zero RMS error line, with an impressively low RMS error of 4, as shown in Fig. 7.5.

In Fig. 7.6 the Oh model shows a significant degradation in its estimation for both test sites, with a disappointing RMS error of about 10 for the upper and 17 for the deeper soil layer for the Elbe-Auen site and about 8 for the upper and 3 for the deeper soil layer for the Weiherbach site.

Contrary to this observation, significant smaller RMS errors are obtained from the Dubois-Model, which seems to be more affected by the decomposition. The best performance is obtained for the Elbe-Auen test site in the upper soil layer for which the RMS error is reduced down to 5.
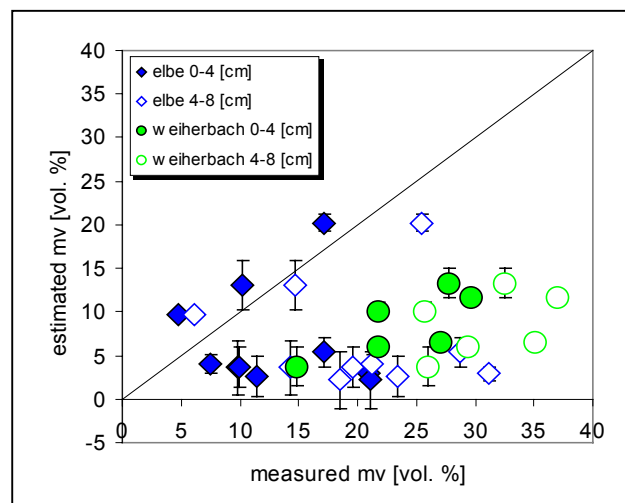
Fig. 7.5: Estimated versus measured soil moisture content in [vol. %]
obtained by using the SPM

The results obtained from the Weiherbach site are similar to the results obtained from the original data. In general the estimated values are slightly overestimated. All estimates are summarised in Fig. 7.6.

The main reason for this behaviour is that the Oh-Model is not suitable to deal with single component surfaces. It considers multi-component natural surfaces, which generate uncorrelated cross-polarised backscattering arising from the depolarising nature of roughness. On the other hand, the Dubois-Model uses only the co-polarised coefficients, a fact that makes this model more insensitive to cross-polarisation effects and limits its application, thus on single component surface contributions only.

However, the general behaviour as well as the sensitivity of the models with respect to soil moisture content remain the same. For example, the underestimation of soil moisture content is still present in the results obtained by using the Oh-Model.

a)   b)

Fig. 7.6: Estimated versus measured soil moisture content in vol % obtained by using a) the Oh-Model and b) the Dubois-Model.

7.2.2.2 Dual Component Approach

Surface Roughness

The Dubois-Model shows a significant improvement of its estimation accuracy for the Weiherbach test site with a reduction of the mean RMS error from 0.46 in the original data down to 0.18. On the Elbe-Auen test site the reduction is not so distinct, as shown in Fig. 7.7. The performance of the Oh-Model is comparable with the estimation performance on the original data sets.
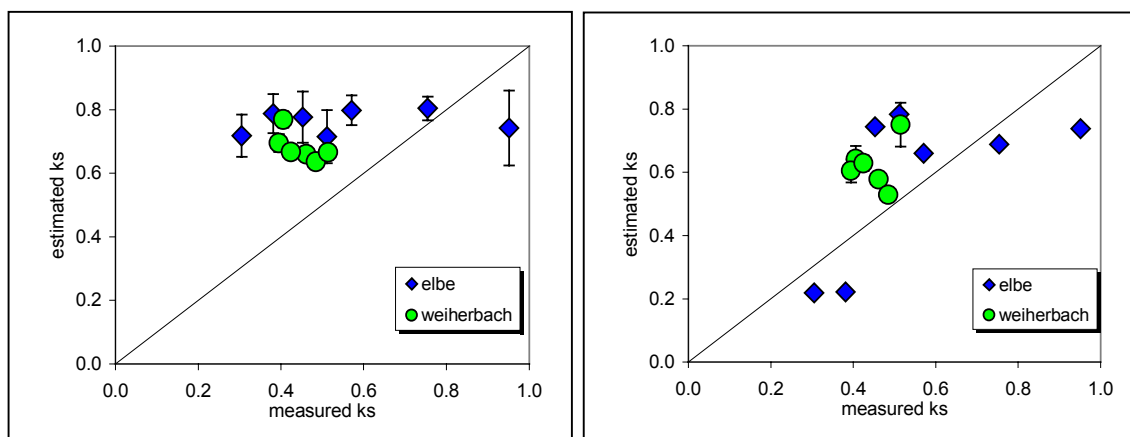
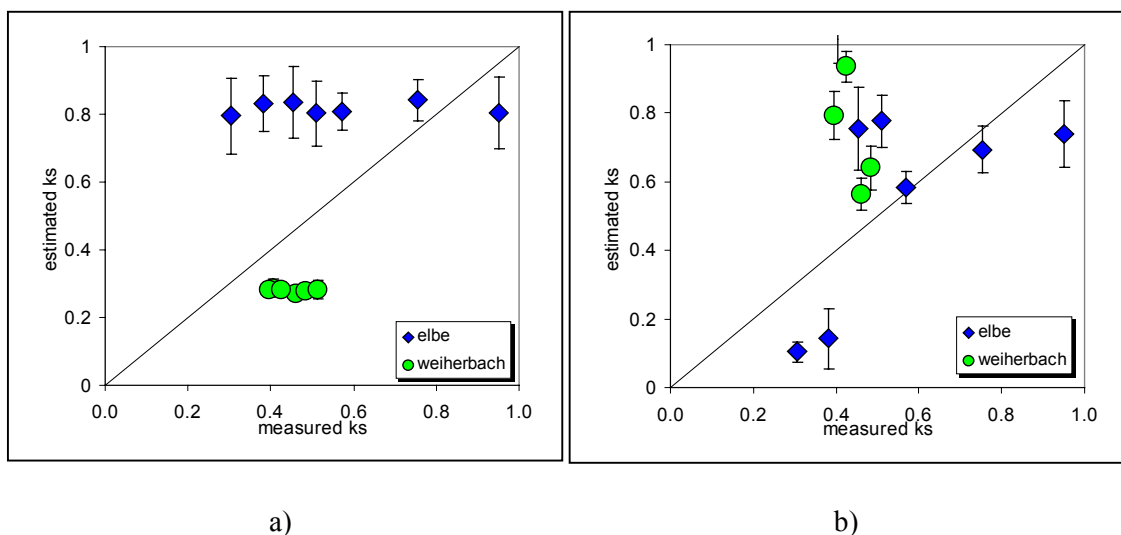a)   b)

Fig. 7.7: Estimated versus measured surface roughness obtained by applying
a)   the Oh-Model and b) the Dubois-Model.

Soil Moisture Content

The estimation of soil moisture content by applying the Dubois-Model is characterised by the same general tendency as the estimation using the single component approach. Nevertheless, the obtained mean RMS error is lower compared to estimates obtained from the single component approach as well as from the original data.

As expected, the application of the Oh-Model on dual component depolarising surfaces improves drastically its estimation performance. This is revealed with the lowest obtained RMS error - compared to all previous approaches - for the Elbe-Auen test site (deeper soil layer), as shown in Fig. 7.8.

These results, allow us to conclude that the eigenvector decomposition of the coherency matrix improves in general the performance of the Oh- and Dubois-Model inversion algorithms. On the one hand, it allows the extension of the applicability of the algorithms on a larger class of natural surfaces. On the other hand, it leads to an improvement of the roughness and soil-moisture estimates. But, even if the main restrictions of both algorithms become partially weaker. Major limitations are still remaining, making the estimation of soil parameters possible only under "idealised" surface conditions.

139

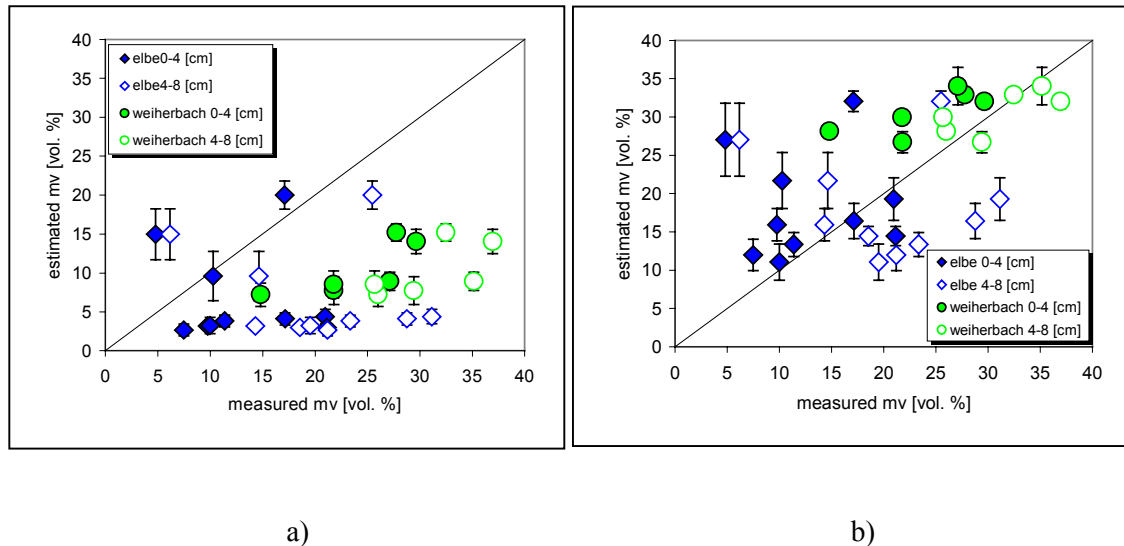a)   b)
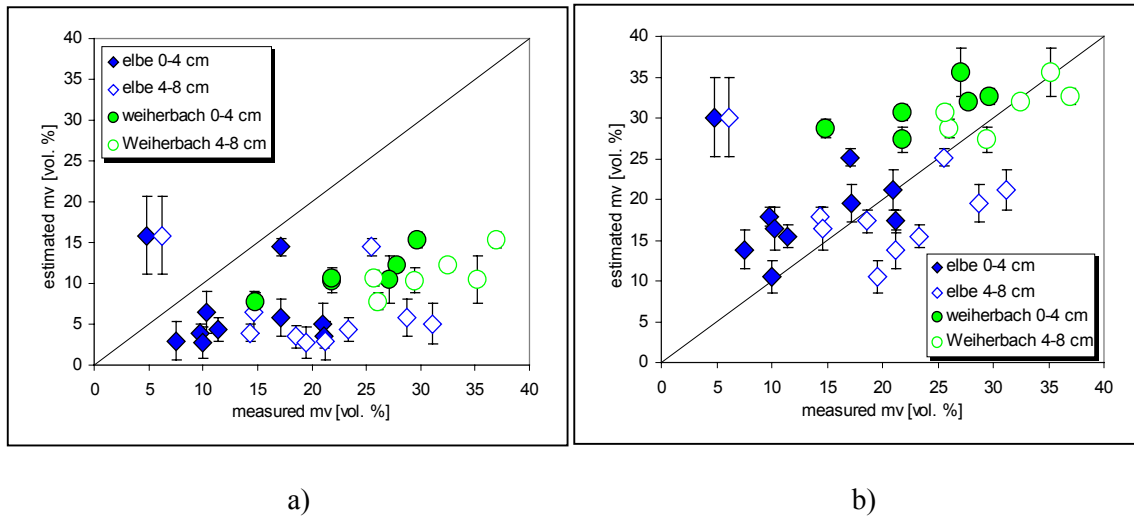
Fig. 7.8: Estimated versus measured soil moisture content in vol % obtained by using a) the Oh-Model and b) the Dubois-Model.

7.3 Model Based Decomposition

A. FREEMAN developed from 1992 to 1998 a three-component scattering model suited for classification and inversion of air- and space-borne polarimetric SAR image data. His decomposition approach belongs to the class of model-based decompositions and uses simple scattering processes to model the scattering behaviour of vegetated terrain. According to this model, backscattering from vegetated terrain can be regarded as the superposition of three single scattering processes: surface scattering, dihedral scattering and volume scattering. Assuming the three processes to be independent from one another, each contributes to the total observed coherency matrix $[T]$ as

$$[T] = [T_S] + [T_D] + [T_V] \tag{7.12}$$

where $[T_S]$ is the coherency matrix for the surface scattering, $[T_D]$ the dihedral scattering, and $[T_V]$ for the volume scattering contribution, respectively.

Surface Scattering Contribution

The first scattering contribution is the surface scattering modelled by a Bragg scatterer (see Fig. 7.8a) with a scattering matrix and a Pauli scattering vector given by
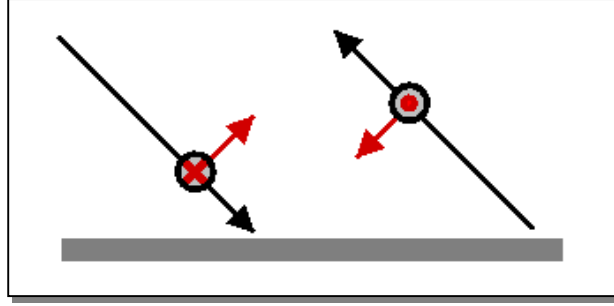
Fig. 7.8a: Bragg scattering mechanism

$$[S_S] = \begin{bmatrix} R_S & 0 \\ 0 & R_P \end{bmatrix} \rightarrow \vec{k}_S = [R_S + R_P, \ R_P - R_S, \ 0]^T \tag{7.13}$$

where R_S is the perpendicular and R_P the vertical to the scattering plane Bragg coefficient

$$R_S = \frac{\cos\theta - \sqrt{\varepsilon_r - \sin^2\theta}}{\cos\theta + \sqrt{\varepsilon_r - \sin^2\theta}} \qquad R_P = \frac{(\varepsilon_r - 1)(\sin^2\theta - \varepsilon_r(1 + \sin^2\theta))}{(\varepsilon_r \cos\theta + \sqrt{\varepsilon_r - \sin^2\theta})^2} \tag{7.14}$$

and ε_r the dielectric constant of the surface. The scattering vector of Eq.(7.14) leads to a coherency matrix of the form

$$[T_S] = f_S \begin{bmatrix} \beta^2 & \beta & 0 \\ \beta & 1 & 0 \\ 0 & 0 & 0 \end{bmatrix} \tag{7.15}$$

Accordingly, the surface contribution is described by two parameters: the real ratio $\beta = \dfrac{R_S + R_P}{R_S - R_P}$ and the backscattering contribution $f_S = |R_S - R_P|^2$.

Dihedral Scattering Contribution

The second scattering mechanism considered by the model is anisotropic dihedral scattering. The scattering matrix of a dihedral scatterer can be expressed as the product of the two scattering matrices describing the forward scattering event occurring at each of the two planes of the dihedral. The model assumes the dihedral to be formed by two orthogonal Bragg scattering planes with the same or different dielectric properties. In this case, the scattering is completely described by the Fresnel reflection coefficients of each reflection plane. For example, the scatering matrix of a soil-trunk dihedral interaction is obtained as

141
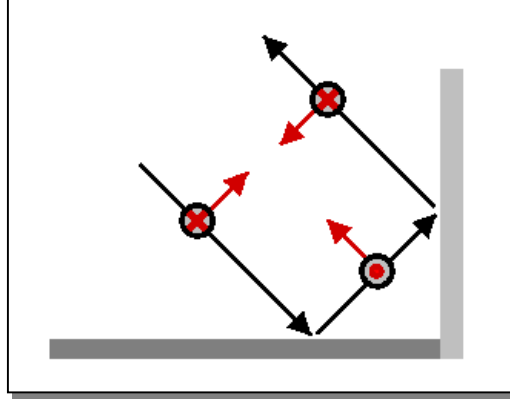
Fig. 7.8b: Dihedral scattering mechanism

$$[S_D] = \begin{bmatrix} 1 & 0 \\ 0 & -1 \end{bmatrix} \begin{bmatrix} 1 & 0 \\ 0 & e^{i\varphi} \end{bmatrix} \begin{bmatrix} R_{SS} & 0 \\ 0 & R_{PS} \end{bmatrix} \begin{bmatrix} R_{ST} & 0 \\ 0 & R_{PT} \end{bmatrix} = \begin{bmatrix} R_{SS} R_{ST} & 0 \\ 0 & -R_{PS} R_{PT} e^{i\varphi} \end{bmatrix} \quad (7.16)$$

The third matrix describes the first forward reflexion at the soil. R_{SS} is the perpendicular and R_{PS} the parallel to the reflection plane Fresnel reflection coefficient for the soil scatterer

$$R_{SS} = \frac{\cos\theta - \sqrt{\varepsilon_S - \sin^2\theta}}{\cos\theta + \sqrt{\varepsilon_S - \sin^2\theta}} \quad \text{and} \quad R_{PS} = \frac{\varepsilon_S \cos\theta - \sqrt{\varepsilon_S - \sin^2\theta}}{\varepsilon_S \cos\theta + \sqrt{\varepsilon_S - \sin^2\theta}} \quad (7.17)$$

and ε_S is the dielectric constant of the soil. The fourth matrix describes the second forward reflection at the trunk, with R_{ST} the perpendicular and R_{PT} the parallel Fresnel reflection coefficient for the trunk scatterer

$$R_{ST} = \frac{\cos\theta - \sqrt{\varepsilon_T - \sin^2\theta}}{\cos\theta + \sqrt{\varepsilon_T - \sin^2\theta}} \quad \text{and} \quad R_{PT} = \frac{\varepsilon_T \cos\theta - \sqrt{\varepsilon_T - \sin^2\theta}}{\varepsilon_T \cos\theta + \sqrt{\varepsilon_T - \sin^2\theta}} \quad (7.18)$$

ε_T the dielectric constant of the trunk. The second matrix accounts for any differential phase φ between HH and VV incorporated by propagation through the vegetation or scattering. Finally, the first matrix performs the transformation from the forward- to the backscattering geometry. The corresponding Pauli scattering vector, follows from Eq. (16) as

$$\vec{k}_D = [R_{SS} R_{ST} - R_{PS} R_{PT} e^{i\varphi}, \ R_{SS} R_{ST} + R_{PS} R_{PT} e^{i\varphi}, \ 0]^T \quad (7.19)$$

leading to a coherency matrix of the form

$$[T_D] = f_D \begin{bmatrix} \alpha^2 & -\alpha & 0 \\ -\alpha & 1 & 0 \\ 0 & 0 & 0 \end{bmatrix} \tag{7.20}$$

Thus, the dihedral contribution is described by the complex ratio $\alpha = \dfrac{R_{SS} R_{ST} - R_{PS} R_{PT} e^{i\varphi}}{R_{SS} R_{ST} + R_{PS} R_{PT} e^{i\varphi}}$,

and, by the real backscattering amplitude $f_D = \left| R_{SS} R_{ST} + R_{PS} R_{PT} \right|^2$.

Volume Scattering Contribution

The third scattering component of the model is a randomly oriented volume of dipoles. The starting point for the evaluation of the corresponding coherency matrix is the scattering matrix of a horizontally oriented dipole

$$[S] = m \begin{bmatrix} 1 & 0 \\ 0 & 0 \end{bmatrix} \tag{7.21}$$

where m is the dipole backscattering amplitude. As described in *Chapter 5*, the scattering matrix obtained by rotating the dipole by an angle of θ about the line-of-sight may be written as

$$[S(\theta)] = \begin{bmatrix} \cos\theta & \sin\theta \\ -\sin\theta & \cos\theta \end{bmatrix} \begin{bmatrix} m & 0 \\ 0 & 0 \end{bmatrix} \begin{bmatrix} \cos\theta & -\sin\theta \\ \sin\theta & \cos\theta \end{bmatrix} = m \begin{bmatrix} \cos^2\theta & \cos\theta\sin\theta \\ \cos\theta\sin\theta & \sin^2\theta \end{bmatrix} \tag{7.22}$$

and the corresponding Pauli scattering vector is given by

$$\vec{k}_P(\theta) = \begin{bmatrix} \cos^2\theta + \sin^2\theta, & \cos^2\theta - \sin^2\theta, & 2\cos\theta\sin\theta \end{bmatrix}^T \tag{7.23}$$

The coherency matrix of a volume of such dipoles is now obtained by averaging the outer product of the scattering vector, as given in Eq. (7.23), over the orientation distribution of the dipoles in the volume

$$[T_V] = \int_0^{2\pi} \vec{k}_P(\theta) \cdot \vec{k}_P^+(\theta) \; P(\theta) \; d\theta \tag{7.24}$$

where $P(\theta)$ is the probability density function of the orientation angle distribution of the dipoles in the volume.
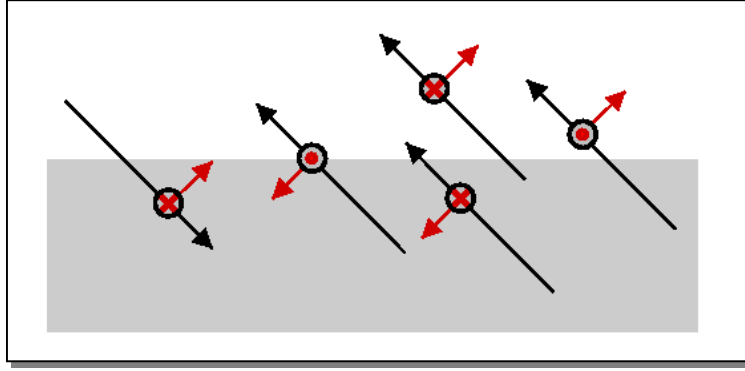
Fig. 7.8c: Volume scattering mechanism

As the volume is assumed to be uniformly randomly oriented, $P(\theta) = 1/(2\pi)$, and from Eq. (7.24) follows

$$[T_V] = f_V \begin{bmatrix} 2 & 0 & 0 \\ 0 & 1 & 0 \\ 0 & 0 & 1 \end{bmatrix} \tag{7.25}$$

Consequently, the random volume contribution is described by a single parameter, namely its backscattering amplitude f_V. Assuming the three scattering processes to be independent from each other, the total coherency matrix is obtained by the superposition of the three corresponding coherency matrices as

$$[T] = f_S \begin{bmatrix} \beta^2 & \beta & 0 \\ \beta & 1 & 0 \\ 0 & 0 & 0 \end{bmatrix} + f_D \begin{bmatrix} \alpha^2 & -\alpha & 0 \\ -\alpha & 1 & 0 \\ 0 & 0 & 0 \end{bmatrix} + f_V \begin{bmatrix} 2 & 0 & 0 \\ 0 & 1 & 0 \\ 0 & 0 & 1 \end{bmatrix} \rightarrow \tag{7.26}$$

$$[T] = \begin{bmatrix} f_S\beta^2 + f_D\alpha^2 + 2f_V & f_S\beta - f_D\alpha & 0 \\ f_S\beta - f_D\alpha & f_S + f_D + f_V & 0 \\ 0 & 0 & f_V \end{bmatrix} \tag{7.27}$$

Tab. 7.1 summarises the scattering contributions for the individual elements of the obtained coherency matrix [T]. The correlations $<(S_{HH} + S_{VV})S_{HV}*>$ and $<(S_{HH} - S_{VV})S_{HV}*>$ vanish as a consequence of the reflection symmetry of all contributions.

Elements of [T]	Surface Scattering		Double Bounce Scattering		Volume Scattering
$\|S_{HH} + S_{VV}\|^2$	$f_S\beta^2$	+	$f_D\|\alpha\|^2$	+	f_V
$\|S_{HV}\|^2$	0	+	0	+	$f_V/3$
$\|S_{HH} - S_{VV}\|^2$	f_S	+	f_D	+	f_V
$(S_{HH} + S_{VV})(S_{HH} - S_{VV})*$	$f_S\beta$	-	$f_D\alpha$	+	f_V

Tab. 7.2: Scattering contributions for the individual elements of [T].

Eq. (7.24) describes the scattering process in terms of five parameters: The three scattering contributions f_S, f_D, and, f_V which are real and positive quantities, the complex coefficient α and the real coefficient β. On the other hand, there are only three real and one complex equations available (obtained from the ($|S_{HH} + S_{VV}|^2$, $|S_{HH} - S_{VV}|^2$, $|S_{HV}|^2$, and $(S_{HH} + S_{VV})(S_{HH} - S_{VV})^*$ elements of $[T]$ respectively) to resolve for the five parameters. Therefore, one of the model parameters has to be fixed. In the case for which the surface contribution is stronger than the dihedral one, α is fixed to be equal 1, while in the opposite case, for which the dihedral contribution is stronger than the surface one, β is fixed to be equal 1. Which of both contributions is stronger is decided according to following empirical rule (VAN ZYL 1992)

$$\text{If} \quad f_S\beta > f_D\alpha \quad \rightarrow \quad \text{Dominant Surface Scattering} \quad \rightarrow \quad \beta = 1$$
$$\text{If} \quad f_S\beta < f_D\alpha \quad \rightarrow \quad \text{Dominant Dihedral Scattering} \quad \rightarrow \quad \alpha = 1$$

Note that, neither the surface scattering nor the dihedral scattering mechanism are contributing to the $|S_{HV}|^2$ term. Thus this term is used to estimate directly the volume scattering contribution which is then subtracted from the $|S_{HH} + S_{VV}|^2$, $|S_{HH} - S_{VV}|^2$ and $(S_{HH} + S_{VV})(S_{HH} - S_{VV})^*$ terms in order to extract the parameters for the surface and dihedral contributions.

There are some important differences between the two decompositions. The first one deals with the statistical independence of the obtained components. While the eigenvector decomposition leads to three rank 1 components, which are orthogonal to each other (i.e. statistically independent), the scattering components of the model-based decomposition are not independent. On the one hand, the surface and the dihedral component are non-depolarising rank 1 scatterers independent from each other. But on the other hand, the volume component has a rank 3 coherency matrix corresponding to a depolarising scatterer present in all polarisations. Further, according to the model based decomposition, cross-polarisation is generated only by depolarisation. For cross-polarisation induced by rotation about the line-of-sight, caused for example by terrain slopes, is not accounted for. Hence, any amount of correlated cross-polarisation becomes misinterpreted as volume scattering contribution. In contrast, due to the statistical independence of the obtained components, the eigenvector decomposition, is able to distinguish correlated from uncorrelated contributions in the polarimetric channels. Finally, while the scattering contributions of the eigenvector decomposition are invariant under line-of-sight rotations, as a consequence of the eigenvector invariance under unitary transformations, the scattering contributions obtained from the model based decomposition are not.

7.3.1 Application on Experimental Data

For the inversion of surface parameters only the first scattering component, corresponding to the surface scattering mechanism, is of interest. In a first step, the formed coherency matrix $[T]$ is decomposed into the three scattering mechanisms according to Eq (7.26). The co-polarised backscattering coefficients σ_{HH}^0 and σ_{VV}^0, corresponding to the Bragg scattering term, are reconstructed from f_S and β as:

$$\sigma_{HH}^0 = 10 \cdot \log 10 \frac{(f_s \cdot \beta^2)\sin(\theta)}{C} \tag{7.28}$$

$$\sigma_{VV}^0 = 10 \cdot \log 10 \frac{(f_s \cdot \sin(\theta))}{C} \tag{7.29}$$

where θ is the local incidence angle and C is a calibration factor. In case of the E-SAR system is C=1,000,000 (ZINK 1993, ZINK & KIETZMANN 1995). σ_{HH}^0, and, σ_{VV}^0 are both expressed in dB.

Because the surface contribution is modelled as a Bragg scatterer, parameter inversion using the corresponding separated contribution makes sense only in terms of the SPM. The inversion of the SPM is applied, as described in Section 6.1.1.1, by using the co-polarised scattering coefficients of Eqs.(7.28-7.29).

The total power images of the three scattering contributions obtained from the model-based decomposition are shown in Fig. 7.9 and Fig. 7.10 for the Elbe-Auen and the Weiherbach test sites, respectively. Forested and dense vegetated areas are characterised by a dominant volume, a reasonably dihedral and a small surface scattering contribution. However, more interesting – in the context of this study - is the behaviour of the fields. For the flat Elbe-Auen test site, relatively smooth bare fields have a dominant surface and negligible dihedral and volume contributions. Rougher fields show additionally to the surface also a non-negligible volume scattering contribution, while vegetated fields show an additional double bounce contribution as expected.

The situation changes for the hilly Weiherbach test site, where also smooth fields show suddenly a significant volume component. It results from correlated slope induced cross-polarisation, which is erroneously interpreted as volume scattering. This interpretation deficiency concerning the cross-polarisation contribution leading to an overestimation of volume scattering becomes even clearer by comparing the volume scattering component with the third scattering component obtained from the eigenvector decomposition displayed in Fig. 7.9 and Fig. 7.10, respectively.
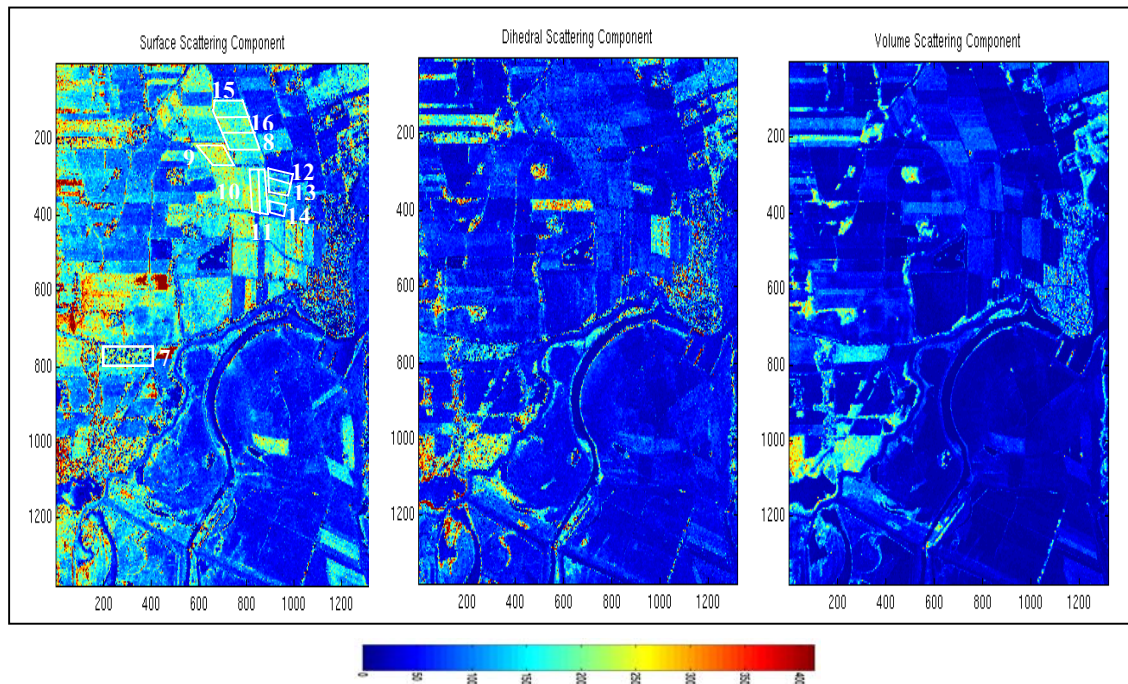
a)   b)   c)

Fig. 7.9: Power images of the a) surface, b) dihadral, and, c) volume scattering component obtained by applying the Freeman decomposition on the Elbe test site.
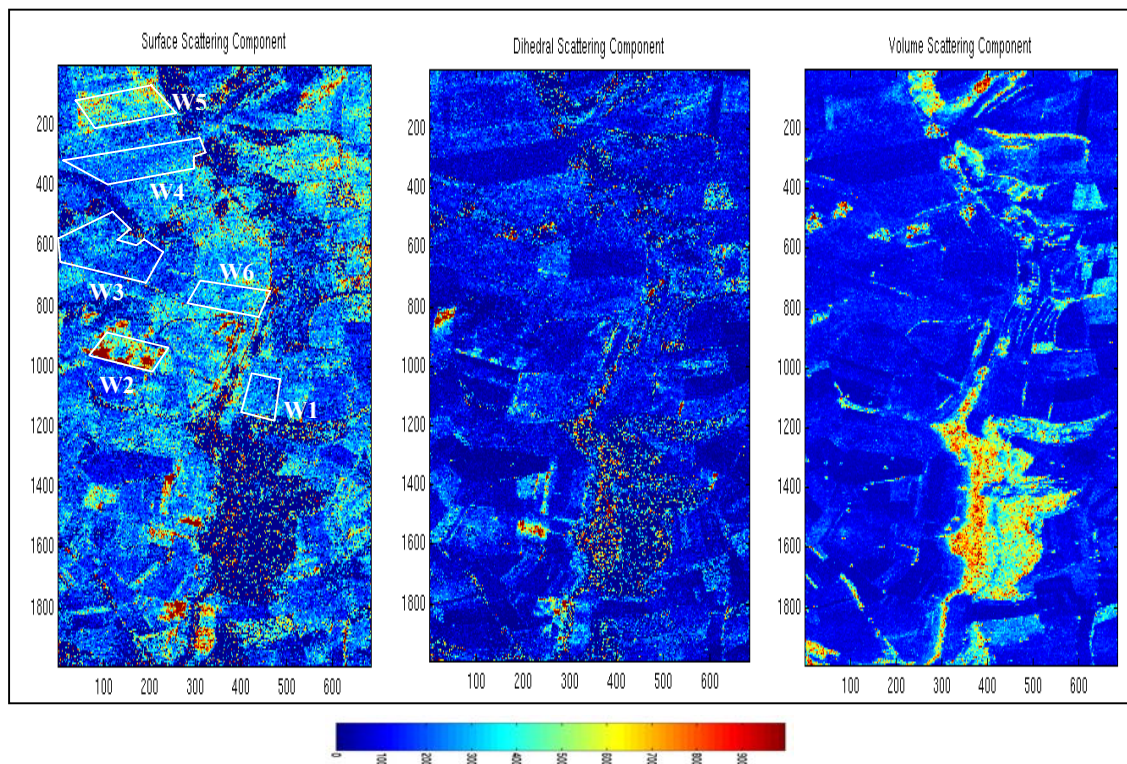
a)   b)   c)

Fig. 7.10: Power images of the a) surface, b) dihedral, and, c) volume scattering component obtained by applying the Freeman decomposition on the Weiherbach test site.

7.3.2 Inversion Results

Soil Moisture Content

The RMS error for the Weiherbach is in general higher than for the Elbe-Auen test site as also observed from the SPM inversion from the original data set. The RMS error for the Weiherbach test site for the upper layer with 11 is lower than for the deeper soil layer with 18. The best performance with the lowest RMS error is given by the upper layer of the Elbe-Auen test site, the deeper layer has an RMS error of 12.9.

The results demonstrate a clear improvement of the quantitative estimation of soil moisture content from SPM. By using the model based decomposition approach the estimation of the surface roughness is no longer possible, just because the disturbing influence of higher surface roughness, *ks* > 0.3, has been filtered out.
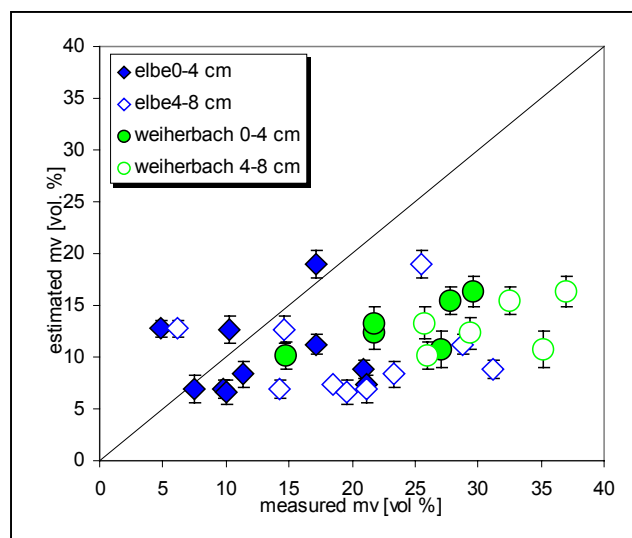

Fig. 7.11: Estimated versus measured soil moisture content using SPM
applied on decomposed intensity data.

7.4 Terrain Slope Correction
Using Schuler-Lee-Pottier Approach

The backscattering characteristics of surface scatterers depend apart from roughness and the dielectric constant also on the incidence angle in a very sensitive way. Therefore, the knowledge of the correct local incidence angle is essential for quantitative estimation of soil moisture and roughness from polarimetric SAR data. In the absence of topography the incidence angle equals the radar look angle and can be estimated from the imaging geometry straightforwardly. This is no longer true for terrain with topographic variations for which the local incidence angle becomes a function of the radar look angle and the local terrain slope. Consequently, in this case, additionally to the imaging geometry the terrain topography has to be known for the estimation of the local incidence angle. The most common approach used for accounting for the influence of topography variations on the incidence angle is the use of a digital elevation model (DEM) of the imaged area (VAN ZYL *et al.* 1993, LUCKMANN 1998). However, availability of a high resolution DEM is not always guaranteed, and thus the estimation of surface parameters from SAR data in the presence of topography is still rather problematic.

Recently, a technique which allows the estimation of terrain slope from the scatterer orientation angle from fully polarimetric SAR data has been proposed, offering for the first time the possibility to correct for topographic effects without any additional terrain information (SCHULER *et al.* 1998, POTTIER *et al.* 1999, LEE *et al.* 2000). In the remainder of this Chapter, the potential utilisation of this new technique with respect to the quantitative estimation of surface parameters is examined. The performance of the correction for topographic effects by using the polarimetric orientation angle is evaluated and compared against the conventional method of using the incidence angle derived from an actual DEM.

To analyse the performance of the inversion techniques under the presence of topography, only the polarimetric SAR data acquired over the Weiherbach test site are useful, because the Elbe-Auen test site is very flat. As already discussed in *Chapter 3*, the Weiherbach test site is a hilly terrain with gentle topographic variations and, as indicated in *Chapter 6*, the obtained inversion results are in general characterised by a higher RMS error compared to the results obtained from the Elbe-Auen test site.

7.4.1 Local Incidence Angle

For the derivation of the local incidence angle (LIA) the scattering geometry of Fig. 7.12 is considered. A local right-handed coordinate system $(\vec{e}_x, \vec{e}_y, \vec{e}_z)$, located at a point *P* on the surface, is defined with its *y*-axis alignment with the ground range direction and its *x*-axis with
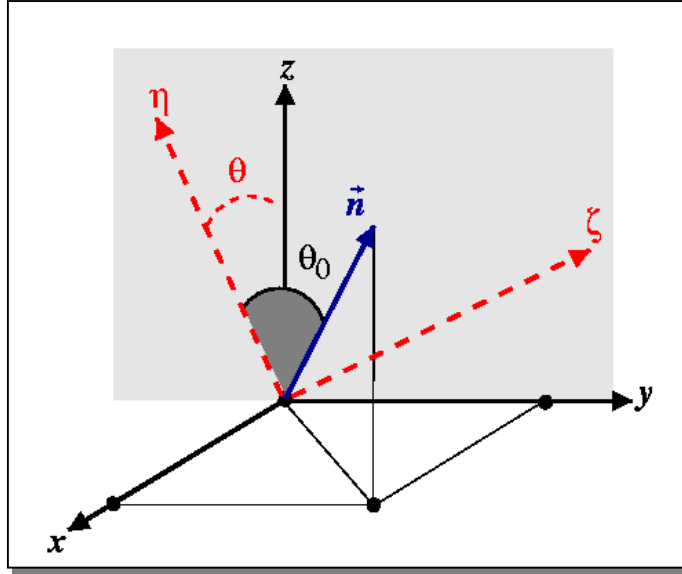
Fig. 7.12: Scattering Geometry and local incidence angle.

the azimuth imaging direction, respectively. The surface normal vector $\vec{n}$ is defined orthogonal to the tangential plane at P and can be expressed in the $(\vec{e}_x, \vec{e}_y, \vec{e}_z)$ coordinate system as

$$\vec{n} = n_x \vec{e}_x + n_y \vec{e}_y + n_z \vec{e}_z \tag{7.30}$$

In terms of the surface normal vector, the local ground range and azimut slopes, α_{rg} and α_{az}, at P are defined as

$$\tan(\alpha_{rg}) := \frac{\partial n_y}{\partial n_z} = -\frac{n_y}{n_z} \quad \text{and} \quad \tan(\alpha_{az}) := \frac{\partial n_x}{\partial n_z} = -\frac{n_x}{n_z} \tag{7.31}$$

To express $\vec{n}$ in the radar geometry, a second right-handed coordinate system $(\vec{e}_x, \vec{e}_\eta, \vec{e}_\varsigma)$ with origin at P is defined with its η-axis alignment with the line-of-sight (or slant range) direction, and its x-axis with the azimuth imaging direction, respectively.

The transformation of the surface normal vector $\vec{n}$ form the $(\vec{e}_x, \vec{e}_y, \vec{e}_z)$ into the $(\vec{e}_x, \vec{e}_\eta, \vec{e}_\varsigma)$ coordinate system corresponds to its rotation by the radar look angle θ about the azimuth axis

$$\vec{n}_{(\vec{e}_x, \vec{e}_\eta, \vec{e}_\varsigma)} = \begin{bmatrix} n_x \\ n_\eta \\ n_\varsigma \end{bmatrix} = \begin{bmatrix} 1 & 0 & 0 \\ 0 & -\sin\theta & \cos\theta \\ 0 & \cos\theta & \sin\theta \end{bmatrix} \begin{bmatrix} n_x \\ n_y \\ n_z \end{bmatrix} = \begin{bmatrix} n_x \\ -n_y \sin\theta + n_z \cos\theta \\ n_y \cos\theta + n_z \sin\theta \end{bmatrix} \tag{7.32}$$

Fig. 7.13: Local incidence angle versus azimuth slope at different radar look angles in the presence of a) a low (1 [degree]) and b) a high (15 [degree]) range slope.

The local incidence angle is defined as the angle between the line-of sight direction and the surface normal

$$\cos(\theta_0) := \vec{e}_\eta \cdot \vec{n} = -n_y \sin\theta + n_z \cos\theta \qquad (7.33)$$

and using Eq (7.32) in Eq.(7.33), the local incidence angle projection is defined as $\cos(\theta_0)$, respectively. It is obtained as a function of the radar look angle, and the local range and azimuth slopes (LEE *et al*. 2000) as

$$\cos(\theta_0) = \frac{\tan\alpha_{rg} \sin\theta + \cos\theta}{\sqrt{1 + \tan^2\alpha_{rg} + \tan^2\alpha_{az}}} \qquad (7.34)$$

From Eq. (7.34) follows that the presence of range and/or azimuth slopes makes the local incidence angle to be different from the radar look angle. Their influence is shown in Fig. 7.13, in which the local incidence angle is plotted as a function of azimuth terrain slope for different incidence angles in the presence of a) low and b) high range slopes, respectively . Accordingly, the influence of the azimuth slope decreases with increasing radar look angle and/or decreasing range slopes. Only in the absence of topography, $\alpha_{rg} = \alpha_{az} = 0$ and $\theta = \theta_0$. The estimation of the local incidence angle from Eq. (7.34) requires apart from the radar look angle, the local ground range and azimuth terrain slopes. All needed parameters can be extracted by transforming an available DEM - applying backward geocoding - into the ground-range/azimuth image coordinates and the knowledge of the actual flight trajectory (SCHREIER 1993).

7.4.2 Local Orientation Angle

As shown in Fig. 7.14, the local orientation angle is defined as the surface normal projected into the radar basis or in other words, as the angle that rotates the surface normal $\vec{n}$ about the line-of-sight to the incidence plane $(\vec{e}_\eta, \vec{e}_\varsigma)$. Using the representation of $\vec{n}$ in the $(\vec{e}_x, \vec{e}_\eta, \vec{e}_\varsigma)$ coordinate system as given in Eq.(7.32), it follows
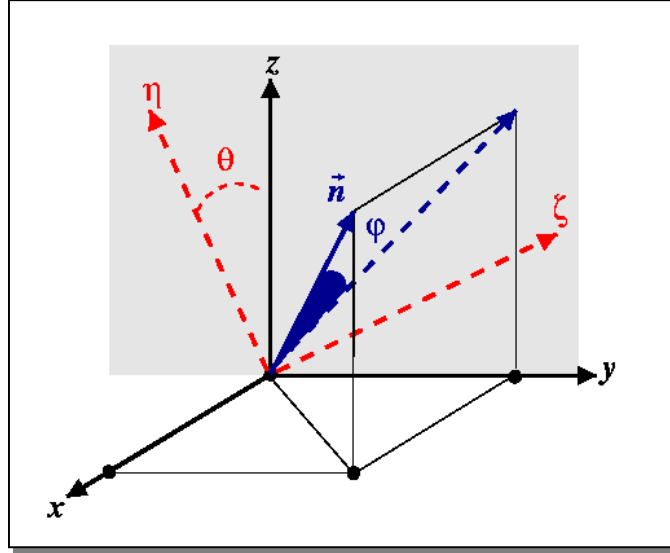
Fig. 7.14: Scattering geometry and local orientation angle.

$$\vec{n}(\varphi)_{(\vec{e}_x, \vec{e}_\eta, \vec{e}_\varsigma)} = \begin{bmatrix} \cos\varphi & 0 & -\sin\varphi \\ 0 & 1 & 0 \\ \sin\varphi & 0 & \cos\varphi \end{bmatrix} \begin{bmatrix} n_x \\ n_\eta \\ n_\varsigma \end{bmatrix} = \begin{bmatrix} n_x \cos\varphi + n_y \sin\varphi\cos\theta - n_z \sin\varphi\sin\theta \\ n_y \sin\theta + n_z \cos\theta \\ n_x \cos\varphi - n_y \cos\varphi\cos\theta + n_z \cos\varphi\sin\theta \end{bmatrix} \quad (7.35)$$

Because $\vec{n}(\varphi)_{(\vec{e}_x, \vec{e}_\eta, \vec{e}_\varsigma)}$ lies in the $(\vec{e}_\eta, \vec{e}_\varsigma)$ plane, its x-component has to be zero, leading to the following expression for the local orientation angle

$$n_x \cos\varphi + n_y \sin\varphi\cos\theta - n_z \sin\varphi\sin\theta = 0 \quad \rightarrow \quad \tan\varphi = \frac{n_x}{-n_y \cos\theta + n_z \sin\theta} \quad (7.36)$$

Substituting, Eq.(7.35) in Eq.(7.36), the local orientation angle can be stated as a function of the radar look angle, the local range and the local azimuth slope as

$$\tan\varphi = \frac{\tan\alpha_{az}}{-\tan\alpha_{rg} \cos\theta + \sin\theta} \quad (7.37)$$
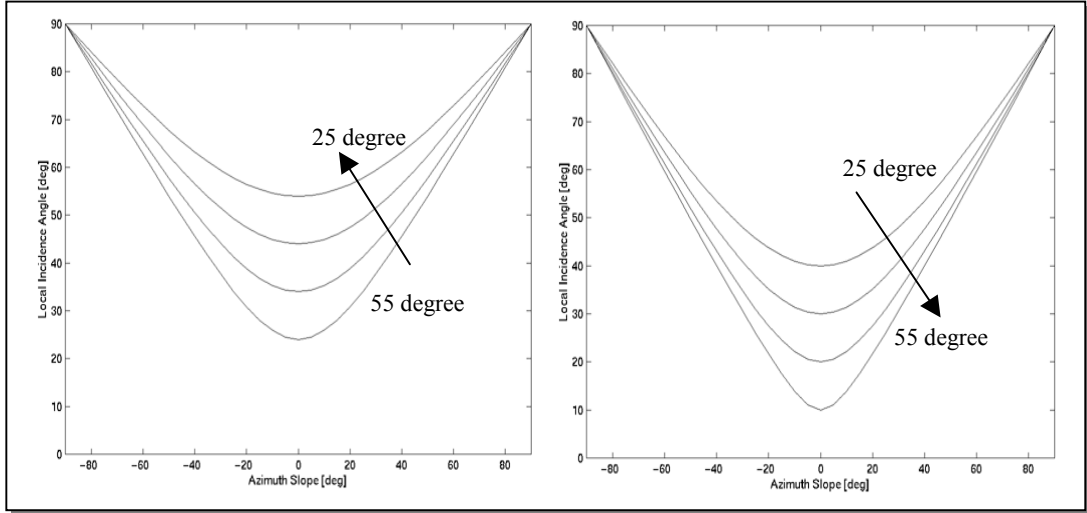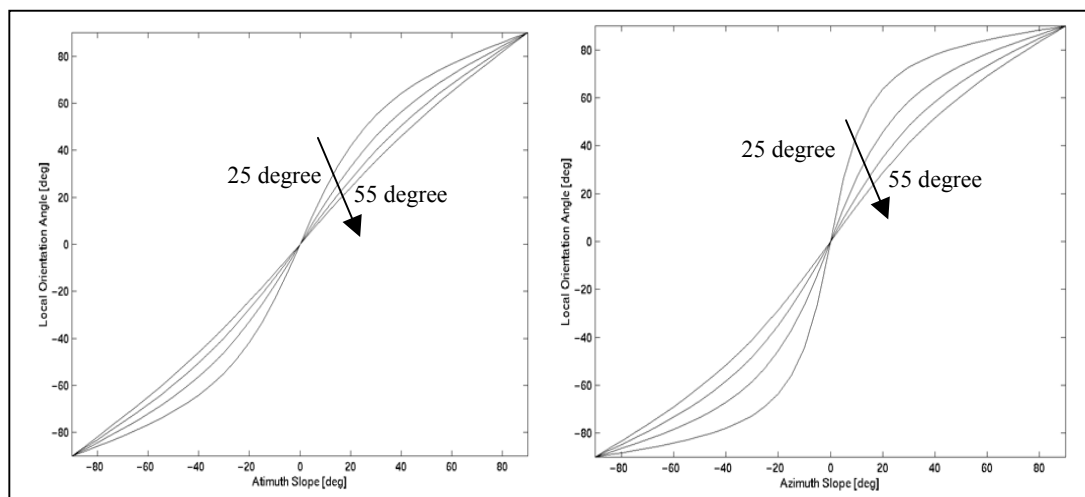
Fig. 7.15: Local orientation angle versus azimuth slope at different radar look angles in the presence of a) a low (1 [degree]) and b) a high (15 [degree]) range slope.

The effect is shown in Fig. 7.15 in which the orientation angle is plotted as a function of azimuth terrain slope for different incidence angles in the presence of a low a) and a high b) range slope.

The dependency of the orientation angle on azimuthal slopes increases with decreasing incidence angle and with decreasing range slopes. For flat terrain, $\alpha_{rg} = \alpha_{az} = 0$ and $\varphi = 0$. Note that, according to Eq.(7.37) the orientation angle depends much stronger on azimuth than on range slopes.

The local orientation angle can be interpreted as the angle about which the antenna has to be rotated in order to align its horizontal polarisation axis to the tangential plane of the surface. The presence of topography variations - and especially slopes in the azimuth direction - induce a local orientation angle, which causes a misalignment between the horizontal polarisation axis and the terrain tangential plane. This leads to a falsification of the measured surface signature that can be corrected by rotating the measured data by the negative of the orientation angle about the line of sight (LEE *et al*. 2000). This correction cannot supersede the incidence angle correction but has the advantage that it may be always applied due to the fact that the orientation angle can be estimated directly from the measured scattering matrix data, as it is shown in the next Section.

7.4.3 Orientation Angle Correction

Several methods have been proposed to extract the orientation angle from polarimetric data (SCHULER *et al*. 1998, POTTIER *et al*. 1999, LEE *et al*. 2000). The most promising results were

obtained by using the phase difference between circular polarisations. According to this approach, the extraction of the orientation angle can be addressed by the following steps (LEE *et al.* 2000): Starting once more from the scattering matrix [S] and the corresponding Pauli scattering vector

$$[S] = \begin{bmatrix} S_{HH} & S_{HV} \\ S_{VH} & S_{VV} \end{bmatrix} \quad \Rightarrow \quad \vec{k}_3 = \frac{1}{\sqrt{2}} \begin{bmatrix} S_{HH} + S_{VV}, S_{HH} - S_{VV}, 2S_{HV} \end{bmatrix}^T \tag{7.38}$$

the 3x3 complex coherence matrix is formed as

$$[T] = < \vec{k}_3 \cdot \vec{k}_3^+ > = \begin{bmatrix} T_{11} & T_{12} & T_{13} \\ T_{12}^* & T_{22} & T_{23} \\ T_{23}^* & T_{23}^* & T_{33} \end{bmatrix} \tag{7.39}$$

From [T] the orientation angle φ is obtained directly within the range of $-\pi/4$ to $\pi/4$ as (LEE *et al.* 2000)

$$\varphi = \frac{\phi + \pi}{4} \tag{7.40}$$

where ϕ is the phase difference between the right-right and left-left circular polarisations which can be expressed in terms of the elements of [T] as

$$\phi = \arctan\left(\frac{2\Re\{T_{23}\}}{T_{33} - T_{22}} \right) \tag{7.41}$$

To account for negative orientation angles the above equation has to be modified

$$For \ \theta \ \rangle \frac{\pi}{4} \ , replace \ \theta \ by \ \left(\theta - \frac{\pi}{2} \right) \tag{7.42}$$

After the estimation of the orientation angle the correction of the coherency matrix can be performed rotating the original coherency matrix about the line-of-sight by the negative of the induced orientation angle

$$[T_{cor}] = [R(-2\theta)] \ [T] \ [R(-2\theta)]^{-1} \tag{7.43}$$

where [R(...)] is the 3x3 unitary LOS rotation matrix (see *Chapter 5*)

$$[R(-2\theta)] = \begin{bmatrix} 1 & 0 & 0 \\ 0 & \cos(-2\theta) & \sin(-2\theta) \\ 0 & -\sin(-2\theta) & \cos(-2\theta) \end{bmatrix} \quad \text{and} \quad [R(-2\theta)]^{-1} = [R(-2\theta)]^T \quad (7.44)$$

Eq.(7.43) represents a rotation of the antenna about the line-of-sight by an angle that forces the horizontal polarisation components to be parallel to the slope terrain surface. The horizontal polarisation component is known as azimuth slope which induces the polarisation orientation shift.

7.4.4 Model Inversion Using Oh- and Dubois-Model

After SAR processing and polarimetric calibration the scattering matrix data were on the one hand corrected using the DEM and on the other hand corrected using the POL-DEM procedure of SCHULER et al. 1998, 1999, described in Section 7.2.1 and 7.2.2, respectively.

The extracted orientation angle map obtained by applying the slope estimation technique is compared with the corresponding map derived from the DEM in Fig. 7.16. The good overall performance of the slope estimation technique is apparent, as the same topographic structures over the entire test site are clearly reconstructed. The noisy parts are over the forested areas which induces phase noise to the elements of the coherency matrix.

a)   b)
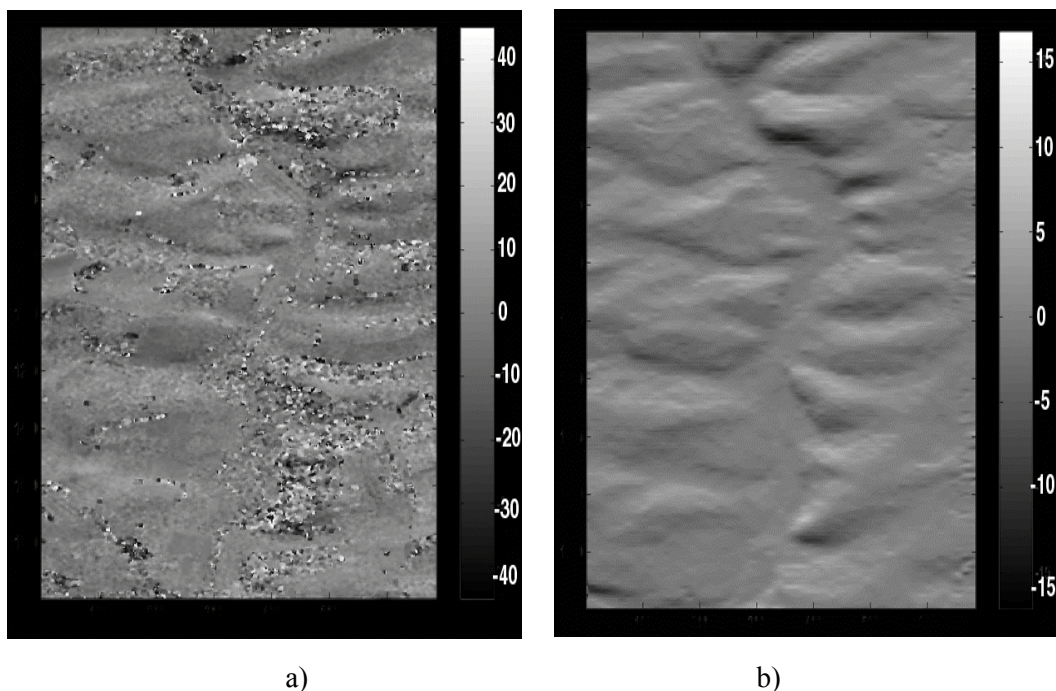
Fig. 7.16: Orientation angle representation extracted from polarimetric data and from the DEM expressed in degree.

The quantitative comparison of the mean slopes for each particular test field is shown in Fig. 7.17. As one can see, the same tendency of decreasing (values in the minus region) or increasing (values in the plus region) is sustained. The only exception is the field W4, where a opposite signed slope is estimated. This field is characterised by the smallest slope in azimuth and range direction and reaches the limit of estimation accuracy of the technique. The highest orientation slope values are observed for the fields W5, W2, and, W6 in accordance to values obtained from the DEM. In general, the orientation angle extracted from the polarimetric data shows a higher standard variation than the one extracted from the DEM mainly due to the phase noise.
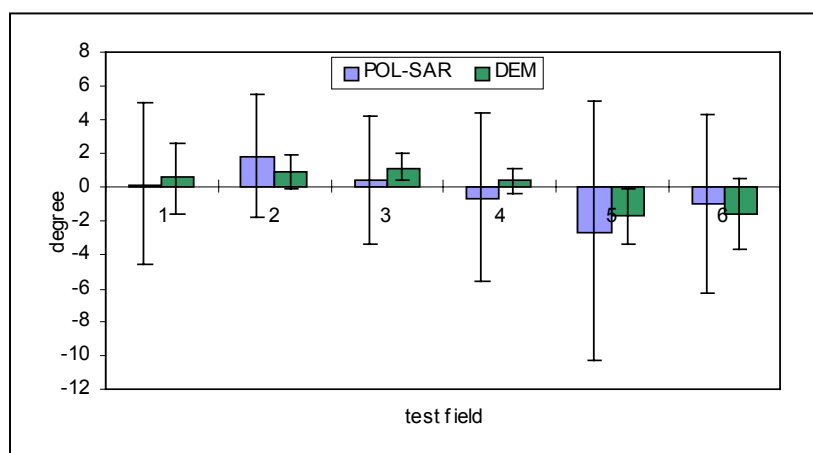
Fig. 7.17: Quantitative comparison of the orientation angle extracted from polarimetric data and from a DEM for each test field.

Local Incidence Angle Corrected Data

Surprisingly, the impact of terrain correction by using the local incidence angle evaluated from the DEM is different for the two inversion algorithms. The roughness estimation for the Oh-Model shows a significant improvement with a decrease of the mean RMS error up to 50 % compared to the uncorrected estimates. For the soil moisture estimates the RMS error of the Dubois-Model reduces slightly for the upper soil layer down to 7.09 [vol. %] compared to the uncorrected estimates. The expected, sensitivity of the quantitative soil moisture inversion to the incidence angle variation is observed. On the other hand, the Oh-Model shows a surprising increase in the mean RMS error.

a)   b)

Fig. 7.18: Estimated versus measured for a) soil moisture content and b) surface roughness
achieved from two semi-empirical/empirical models.

Orientation Angle Corrected Data

The roughness estimates using the orientation angle corrected data shows for the Oh-Model a
decrease in the RMS error of up to 45 [%] and a slight increase of the RMS error for the
Dubois-Model estimates compared to the original data. This is the same trend as observed for
the local incidence angle corrected data. The moisture content estimates are also in general
better with reduced RMS errors. However, the improvement is smaller than obtained by using
the local incidence angle corrected data. For the Dubois- and the Oh-Model a RMS error of 0.3
[vol. %] for the upper soil layer is obtained.

a)   b)

Fig. 7.19: Estimated versus measured for a) soil moisture content and b) surface roughness
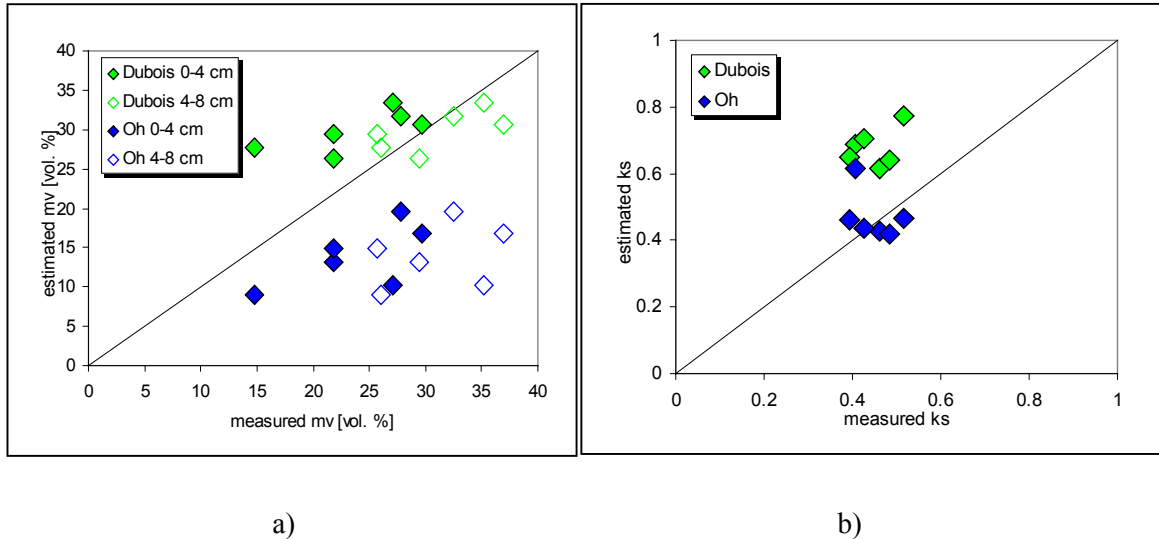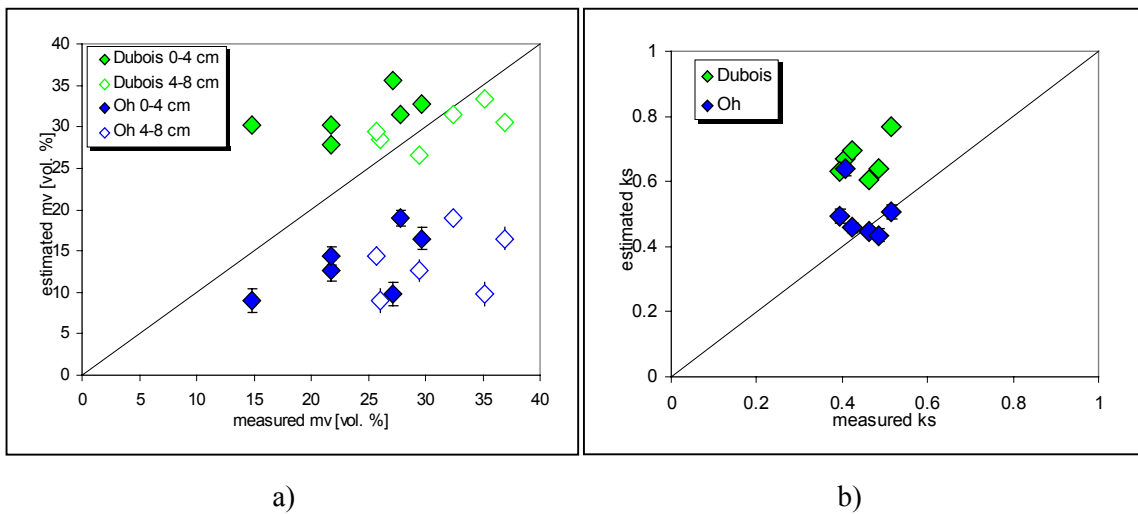achieved from two semi-empirical/empirical models.

The results underline the importance of terrain correction for a quantitative surface parameters extraction. In terms of their performance sensitivity to the presence of terrain slopes the two inversion models show a different behaviour. For the surface roughness estimation the Dubois-Model is less sensitive to terrain variation but its estimates have a larger RMS error compared to the Oh-Model. The Oh-Model reacts very sensitively to slope variations and shows the highest improvement with respect to the corrections. The soil moisture estimation is in general much more problematic for both models than the roughness estimation which is indicated by the relative large RMS errors. Both empirical models show the same sensitivity to terrain variations: A variation of about 1 degree in terrain slope leads approximately to RMS error variation of the order of 0.5 [vol. %]. The Dubois-Model shows a higher sensitivity to the soil moisture content estimation than to the surface roughness estimation. In contrast, the Oh-Model is more sensitive to surface roughness estimation than to soil moisture content estimation.

This different behaviour indicates once more the importance of the *HV* scattering component for roughness estimation. As the Dubois-Model is based only on the |*HH*| and |*VV*| amplitude information, it demonstrates a poorer roughness estimation accuracy compared to the Oh-Model, which uses information from all three polarisations. The rotation of the surface with respect to the radar line of sight (caused by the slope component in azimuth) introduces additionally to the *HV* component generated by the surface - that is uncorrelated to the *HH* and *VV* components - a *HV* component which is correlated to the *HH* and *VV* components; (see Eq.(7.43)). As the Oh-Model uses only amplitude information, it can not distinguish between correlated and uncorrelated *HV* information and overestimates the surface roughness in the presence of slopes. This is the main reason for the improvement of the Oh-Model performance after applying the slope corrections.

However, the effectiveness of the orientation angle correction cannot be compared with the correction by using the local incidence angle derived from a DEM. Nevertheless, it leads to significantly better estimates compared to completely uncorrected data. It can be used as a good first order correction in the case where a DEM is not available. As expected, the correction is particularly efficient for fields with a large topographic height variation leading for the Dubois-Model to the highest improvement of soil moisture content estimates. The quantitative value for the correction varies in the two empirical models. On one of the steepest test fields of the Weiherbach test site (W5) the Dubois-Model shows after applying the orientation angle correction, an improvement up to 0.5 [vol. %]. A fair point to note here is the fact that our test site has a much higher variation in the range slope component than in the azimuthal component. This reduces the performance of the orientation angle correction compared to the DEM based correction as it accounts mainly for azimuthal slopes.

7.5 Synopsis

In this *Chapter 7*, polarimetric pre-processing techniques for improving the estimation performance of the introduced surface parameter inversion techniques have been tested.

In the first part, the eigenvector decomposition of the coherency matrix was applied to decompose the scattering process into three components. As discussed in Section 6.3, the performance of the semi-empirical/empirical models is limited by secondary scattering processes, which leads to a biased estimation of moisture content and roughness. The intention was to improve their performance, filtering out such effects, by considering only the first, or the first and second component obtained from the eigenvector decomposition. A quantitative overview of the estimation results is summarised in Tab. 7.3.

Single Component Approach

- The obtained results demonstrate an increase of the amount of valid points that are satisfying the requirements of the models.

- **SPM**: The soil moisture estimates indicate a decrease of the RMS error compared to the estimation results obtained from the original data. The performance increases drastically for vegetated fields.

- **Oh-Model**: For both estimated surface parameters the performance is at the same level or poorer compared to estimates obtained from the original data. This is because accounting only the first contribution leads practically to a cancellation of the cross-polarisation, and the performance of the Oh-Model for surface roughness estimation is strongly dependent on it.

- **Dubois-Model**: For the surface roughness estimates a significant increase of the correlation up to 0.8 is obtained, while for the moisture content estimates a slight decrease of the mean RMS error is observed as compared to the original data.

Dual Component Approach

The poor estimation performance obtained from the single component approach, leads to the conclusion that – apart from the SPM – a depolarising model is needed. Therefore, the inversion models have been applied on combined first and second components obtained from the eigenvector decomposition.

- **Oh-Model**: As expected, the soil moisture content estimation improved significantly, while the surface roughness estimation behaves at the same performance level as obtained by using the original data.

- **Dubois-Model**: Surprisingly, for both surface parameters, a significant improvement of the estimation error is obtained.

Model/ Elbe-Auen Weiherbach	RMS error			Correlation		
RADAR LOOK ANGLE	*mv* 0-4 cm	*mv* 4-8 cm	*ks*	*mv* 0-4 cm	*mv* 4-8 cm	*ks*
Eigenvector and Eigenvalue Decomposition – Single Component						
SPM						
Elbe-Auen	10	16	---	-0.07	-0.1	---
Weiherbach	16	23	---	-0.7	0.4	---
Oh-Model						
Elbe-Auen	10	17	0.24	-0.15	-0.3	0.8
Weiherbach	14	21	0.24			0.5
Dubois-Model						
Elbe-Auen	8	3	0.21	0.7	0.8	0.5
Weiherbach	8	3	0.46	0.8	0.71	0.1
Eigenvector and Eigenvalue Decomposition – Dual Component						
Oh-Model						
Elbe-Auen	9	11	0.28	-0.16	-0.31	0.6
Weiherbach	13	20	0.24	0.9	0.8	-0.6
Dubois-Model						
Elbe-Auen	9	9	0.18	-0.21	0.04	0.14
Weiherbach	8.1	3.02	0.18	0.7	0.7	0.25

Tab. 7. 3: Estimation results for the three inversion models for different pre-processing constellations - single and dual component of [*T*]

In the second part, a model based decomposition approach was applied for improving the performance of the SPM model. The three-component scattering model decomposes the scattering signature into a Bragg surface scatterer, a dihedral scattering and a volume scatterer of randomly oriented dipoles. Each of these scattering mechanism is contributing to the total backscattering signal. From the obtained surface scattering contribution the two scattering coefficients, σ^0_{HH} and σ^0_{VV}, were reconstructed and used for the inversion with the SPM. The obtained results demonstrate a better estimation performance than the original data and better than the eigenvector and eigenvalue approach. The lowest RMS error is obtained from the upper layer of the Elbe-Auen, with about 7 vol. %.

In the third part, the potential of a new technique for the compensation of terrain variations is discussed and investigated for the application of inversion models. The usual way to compensate the topographic variations is to extract the local incidence angle from a DEM. Alternatively, the terrain slopes are estimated from the polarimetric data itself by extracting the orientation angle from [T] and correcting for it. The orientation angle is by definition more sensitive to the azimuth slopes. A quantitative comparison of two semi-empirical/empirical inversion models on the original data using the local incidence angle and on orientation angle corrected polarimetric SAR data using the radar look angle was performed. The quantitative estimation results are summarised in Tab. 7.4.

- **Oh-Model**: The estimation results for the surface roughness parameter improves with the orientation angle correction and reaches the best performance of all estimation approaches with the local incidence angle. The performance with respect to moisture content was much poorer.

- **Dubois-Model**: Contrary to the Oh-Model, the performance of the Dubois-Model with respect to the soil moisture content seems to be more sensitive to the applied terrain slope compensation, and relatively insensitive with respect to surface roughness.

Model/ Weiherbach	RMS error			Correlation		
	mv 0-4 cm	*mv* 4-8 cm	*ks*	*mv* 0-4 cm	*mv* 4-8 cm	*ks*
RLA						
Oh-Model	10	17	0.18	0.7	0.6	-0.4
Dubois-Model	8	3	0.25	0.7	0.8	0.5
OAC						
Oh-Model	11	18	0.1	0.6	0.3	-0.4
Dubois-Model	7	3	0.2	0.6	0.6	0.5
LIA						
Oh-Model	11	18	0.09	0.6	0.3	-0.5
Dubois-Model	7	3	0.24	0.7	0.7	0.3

Tab. 7. 4: Estimation results for the two semi-empirical/empirical models for different topography correction approaches: RLA- Radar Look Angle (no-correction), OAC – Orientation Angle Correction, LIA - Local Incidence Angle.

7.6 References to Chapter 7

BOERNER, W.-M. ET AL., 'Polarimetry in Radar Remote Sensing: Basic and Applied Concepts', Chapter 5 in F. M. Henderson and A.J. Lewis (ed.), 'Principles and Applications of Imaging Radar', vol. 2 of Manual of Remote Sensing, (ed. R. A. Reyerson), Third Edition, John Willey & Sons, New York, 1998.

CLOUDE, S. R., 'Polarimetry: The Characterisation of Polarimetric Effects in EM Scattering', PhD. Thesis, University of Birmingham, Faculty of Engineering, UK, October 1986

CLOUDE, S. R. & POTTIER, E.,'An Entropy Based Classification Scheme for Land Applications of Polarimetric SAR', *IEEE Transactions on Geoscience and Remote Sensing*, vol. 35, no. 1, pp. 68-78, 1997.

CLOUDE, S. R. & POTTIER, E., 'A Review of Target Decomposition Theorems in Radar Polarimetry', *IEEE Transactions on Geoscience and Remote Sensing*, vol. 34, no. 2, pp. 498–518, 1996.

DUBOIS, P. C. VAN ZYL, J. J. & ENGMAN, T., 'Measuring Soil Moisture with Imaging Radars*', IEEE Transactions on Geoscience and Remote Sensing*, vol. 33, no. 4, pp. 916-926, 1995.

FREEMAN, A. & DURDEN, S. L., 'A three-component scattering model to describe polarimetric SA Data', in Proceedings SPIE Conference Radar Polarimetry, San Diego, CA, pp. 213-224, 1992

FREEMAN, A. & DURDEN, S. L., 'A Three-Component Scattering Model for Polarimetric SAR Data', *IEEE Transactions on Geoscience and Remote Sensing*, vol. 36, no. 3, pp. 963-973, 1998.

HAJNSEK, I., CLOUDE, S. R., LEE, J. S. & POTTIER, E., 'Terrain Correction for Quantitative Moisture and Roughness Retrieval Using Polarimetric SAR Data', *Proceedings IGARSS'00*, Honolulu, Hawaii, pp. 1307-1309, July 2000.

HAJNSEK, I., POTTIER, E. & CLOUDE, S. R., 'Slope Correction for Soil Moisture and Surface Roughness Retrieval', *Proceedings of third European Conference on Synthetic Aperture Radar EUSAR 2000*, pp. 273-276, May 2000.

KROGAGER, E., 'Aspects of Polarimetric Radar Imaging', Thesis Danish Defense Research Establishment, p. 235, 1993

KROGAGER, E, & W.M. BOERNER, ,On the Importance of Utilizing Polarimetric Information in Radar Imaging Classification', AGARD Proc. 582-17, 1-13, April 1996.

LEE, J. S., JURKEVICH, I., DEWAELE, P., WAMBACQ, P. & COSTERLINCK, A., 'Speckle filtering of synthetic aperture radar images: A review', *Remote Sens. Rev.*, vol. 8, pp 311-340, 1994.

LEE, J. S., GRUNES, M. R. & DE GRANDI, G., 'Polarimetric SAR Speckle Filtering and its Impact on Classification', *IEEE Transactions on Geoscience and Remote Sensing*, vol. 37, no. 5, pp. 2363 – 2373, 1997.

LEE, J. S., GRUNES, M. R., AINSWORTH, T. L., DU, L. J., SCHULER, D. L. & CLOUDE, S. R., 'Unsupervised Classification Using Polarimetric Decomposition and the Complex Wishart Classifier', *IEEE Transactions on Geoscience and Remote Sensing*, vol. 37, no. 5, pp. 2249 – 2258, 1999.

LEE, J. S., D. L. SCHULER & T. L. AINSWORTH, 'Polarimetric SAR Data Compensation for Terrain Azimuth Slope Variation', *IEEE Transactions on Geoscience and Remote Sensing*, vol. 38, no. 5, part I, pp. 2153-2163, 2000.

LUCKMANN, A., 'Correction of SAR Imagery for Variation in Pixel Scattering Area Caused by Topography', *IEEE Transaction of Geoscience and Remote Sensing*, vol. 36, no. 1, 1998, pp. 344-350, 1998

OH, Y., SARABANDI, K. & ULABY, F. T., 'An Empirical Model and an Inversion Technique for Radar Scattering from Bare Soil Surfaces', *IEEE Transactions on Geoscience and Remote Sensing*, vol.30, no. 2, pp. 370-381, 1992.

POTTIER, E., SCHULER, D. L., LEE, J.-S., & AINSWORTH, T. L., 'Estimation of the Terrain Surface Azimuthal/Range Slopes Using Polarimetric Decomposition of Polsar Data', Proceeding IGARSS'1999, Hamburg, pp. 2212-2214, 1999

SCHREIER, G., 'SAR Geocoding: Data and System', Karlsruhe: Wichmann, p.435, 1993.

SCHULER, D. AINSWORTH, T., LEE, J. S. & DE GRANDI, G., 'Topographic Mapping Using Polarimetric SAR data', *International Journal of Remote Sensing*, vol. 34, no. 5, pp. 1266-1277, 1998

SCHULER, D., LEE, J.-S., & AINSWORTH, T. L., 'Compensation of Terrain Azimuthal Slope Effects in Geophysical Parameter Studies Using Polarimetric SAR Data', Remote Sensing of Environment, vol. 69, pp. 139-155, 1999

TOPP, G. C., DAVIS, J. L. & ANNAN, A. P., 'Electromagnetic Determination of Soil Water Content: Measurements in Coaxial Transmission Lines', *Water Resources Research*; vol. 16, no. 3, pp. 574-582, 1980.

VAN ZYL, J. J. On the Importance of Polarization in Radar Scattering Problems, Ph.D. thesis, California Institute of Technology, Pasadena, CA, December 1985.

VAN ZYL, J. J., CHAPMAN, B. D., DUBOIS, P. & SHI, J., 'The Effect of Topography on SAR Calibration ', *IEEE Transactions on Geoscience and Remote Sensing*, vol. 31, no. 5, pp. 1036-1043, 1993

VAN ZYL, J. J., 'Application of Cloude's Target Decomposition Theorem to Polarimetric Imaging Radar Data', Radar Polarimetry, San Diego, CA SPIE'92, vol. 1748, pp. 184-212, 1992.

ZINK, M., 'Kalibration von SAR-Systemen', Deutsche Forschungsanstalt für Luft- und Raumfahrt, Forschungsbericht DLR-FB 93-18, p. 168, 1993

ZINK, M, & KIETZMANN, H., 'Next Generation SAR-External Calibration', Deutsche Forschungsanstalt für Luft- und Raumfahrt, Forschungsbericht, DLR 95-4, , p. 45, 1995.

Chapter 8

Inversion of Surface Parameters
Using Extended Bragg Scattering Model

I n this chapter a new model for the inversion of surface roughness and soil moisture from polarimetric SAR data is introduced. In the two previous chapters the applicability of three inversion models and methods for their extensions have been investigated. A second promising approach for the extraction of surface parameters started with the analysis of second order statistics of surface scatterers (BORGEAUD & NOLL 1994, MATTIA *et al*. 1997). The correlation coefficient between different polarisation states has been observed to correlate with complex dielectric constant and/or surface roughness measurements. These observations depict the first step to an independent estimation of the observed surface parameters, but their investigations are still not sufficient for quantitative estimation. Recently, observations based on experimental data collected in an anechoic chamber, indicated a relationship between surface roughness and the eigenvalues of the polarimetric coherency matrix, which themselves have a physical significance in terms of scattering amplitudes (CLOUDE & PAPATHANASSIOU 1999, CLOUDE 1999, CLOUDE *et al*. 1999). Furthermore, their ratio can be interpreted in terms of generalised polarimetric coherence coefficients. An alternative model for the investigation of surface parameters from polarimetric SAR data will be introduced arising from these experimental observations. The proposed model is a two component model including a Bragg term and a roughness induced rotation symmetry term. In order to decouple the real part of the complex dielectric constant from the surface roughness, the model is formulated in terms of the polarimetric entropy H, alpha angle α, and anisotropy A, which are derived from the eigenvalues and eigenvectors of the polarimetric coherency matrix.

8.1 Model Based Eigenvector Decomposition

8.1.1 Model Description

As discussed in *Chapter 7*, the limitation of the Small Perturbation Model (SPM) for the interpretation and inversion of experimental data from natural surfaces arises from its inability to describe non-zero *cross-polarised* backscattering and depolarisation effects. To circumvent this shortcoming, a configurational average of the SPM solution is proposed, which introduces cross-polarised energy and at the same time forces the polarimetric coherence to be less than one.

The rotation of the Bragg coherency matrix [T] about an angle β in the plane perpendicular to the scattering plane (see Fig. (8.1)) can be written as

$$[T(\beta)] = \begin{bmatrix} 1 & 0 & 0 \\ 0 & \cos 2\beta & \sin 2\beta \\ 0 & -\sin 2\beta & \cos 2\beta \end{bmatrix} \begin{bmatrix} \langle |R_S + R_P|^2 \rangle & \langle (R_S - R_P)(R_S + R_P)^* \rangle & 0 \\ \langle (R_S + R_P)(R_S - R_P)^* \rangle & \langle |R_S - R_P|^2 \rangle & 0 \\ 0 & 0 & 0 \end{bmatrix} \begin{bmatrix} 1 & 0 & 0 \\ 0 & \cos 2\beta & -\sin 2\beta \\ 0 & \sin 2\beta & \cos 2\beta \end{bmatrix} \quad (8.1)$$

Fig. 8.1: Uniform distribution of surface slope

Performing now configurational averaging over a given distribution $P(\beta)$ of β, the coherency matrix becomes

$$[T] = \int_0^{2\pi} [T(\beta)] P(\beta) d\beta \quad (8.2)$$

Assuming P (β) to be a uniform distribution about zero with width β_1 (see Fig. (8.1))

$$P(\beta) = \begin{cases} \dfrac{1}{2\beta_1} & |\beta| \leq \beta_1 \\ 0 \leq \beta_1 \leq \dfrac{\pi}{2} \end{cases} \quad (8.3)$$

the coherency matrix for the rough surface becomes

$$[T] = \begin{bmatrix} T_{11} & T_{12} & T_{13} \\ T_{21} & T_{22} & T_{23} \\ T_{31} & T_{32} & T_{33} \end{bmatrix} = \begin{bmatrix} C_1 & C_2 \sin c(2\beta_1) & 0 \\ C_2 \sin c(2\beta_1) & C_3(1 + \sin c(4\beta_1)) & 0 \\ 0 & 0 & C_3(1 - \sin c(4\beta_1)) \end{bmatrix}$$ (8.4)

with $\mathrm{sinc}(x) = \sin(x)/x$. The coefficients C_1, C_2, and, C_3 describe the Bragg component of the surface, and are given by

$$C_1 = |R_S + R_P|^2 \qquad C_2 = (R_S + R_P)(R_S^* - R_P^*) \qquad C_3 = \frac{1}{2}|R_S - R_P|^2$$ (8.5)

The width of the distribution β_1 describes the roughness component and controls both the polarimetric coherence and the level of cross-polarised power.

From Eq. (8.4), the polarimetric coherence between the Left-Left and Right-Right circular polarisations (CLOUDE 1999) follows as

$$\gamma_{LLRR} := \frac{T_{22} - T_{33}}{T_{22} + T_{33}} = \sin c(4\beta_1)$$ (8.6)

and depends only on the surface roughness. This is in accordance with former experimental observations reported in (MATTIA *et al.* 1997). On the other hand, the polarimetric anisotropy can be interpreted as a generalised rotation invariant expression for γ_{LLRR}. Consequently, the anisotropy is independent on the dielectric properties of the surface.

This fact allows a straightforward separation of roughness and moisture effects inside $[T]$ and represents one of the major advantages of the proposed model. Note that this result is independent of the choice of slope distributions. The form of $P(\beta)$ affects only the mathematical expression of the anisotropy.

Fig. 8.2 shows the variation of polarimetric coherence (dotted line) and normalised cross-polarised power (solid line). For $\beta_1 = 0$ the *HH-VV* coherence is unity and the *HV* power zero, as expected in the limit of a smooth surface, and the coherency matrix reduces to the form given by Eq. (6.1). As β_1 increases, the HV power increases, while the coherence reduces monotonically from 1 for a smooth surface to zero for $\beta_1 = 90$ degrees. In this second limiting case of high surface roughness the surface becomes azimuthally symmetric. Note that the increase in *HV* power is faster than the fall-off in coherence, and, therefore, for small β_1 values the anisotropy will be high (close to 1). As β_1 increases the anisotropy falls monotonically to zero.
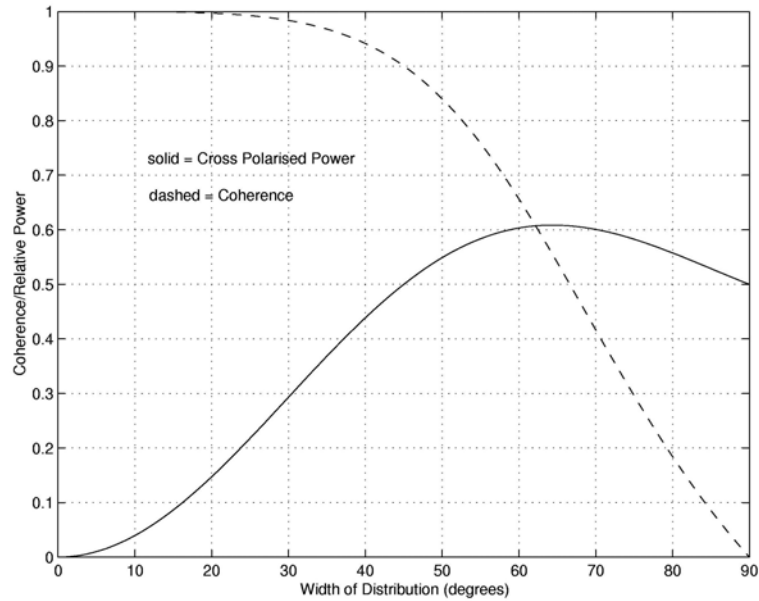
167

Fig. 8.2: Variation of cross-polarisation and coherence with model parameter β_1

Fig. 8.3 shows how this fall in the anisotropy coefficient A occurs as a function of β_1 for a range of dielectric constant values. For $ks < 1$, i. e. up to $\beta_1 = 90°$, we can see an almost linear relation between A and ks, which is independent of the dielectric constant, and hence of the soil moisture content. Finally, A becomes insensitive to a further increase of roughness above $ks = 1$. Again, it is important to note that the value of A at any β_1 is independent on the surface dielectric constant and on the local incidence angle. Similar studies show that A is also independent of the angle of incidence (HAJNSEK *et al.* 2000).

Further structure in Eq. (8.4), can be exposed, by plotting the entropy/alpha loci of points for different dielectric constant values and widths of slope distribution β_1 for a fixed local incidence angle of $\theta = 45$ degrees as shown in Fig. 8.4. The loci are best interpreted in a polar co-ordinate system centred on the origin. In this sense, the radial co-ordinate corresponds to the dielectric constant while the azimuthal angle represents changes in roughness. These loci can be used to provide an estimate of the surface dielectric constant, independent of surface roughness. The corresponding entropy/alpha values are evaluated from the coherency matrix [T] as given in Eq. (8.4).

Fig. 8.3: Anisotropy versus Roughness for 45 degree local incidence angle (AOI)

In the limiting case of a smooth surface, the entropy becomes zero and the alpha angle corresponds directly to the dielectric constant through Eq. (6.1). However, as the entropy increases with increasing roughness, the apparent alpha angle value decreases, leading to an underestimation of the dielectric constant. Using Eq. (8.5), it is possible to compensate this roughness induced underestimation of the alpha angle by tracking the loci of constant ε' back to the H = 0 line. In this way both, the entropy and alpha values, are required in order to obtain a corrected estimate of the surface moisture.

Fig. 8.4: Entropy/Alpha diagram for 45 degree AOI plotted for varying dielectric constant

Hence, by estimating three parameters, the entropy H, the anisotropy A and the alpha angle α, we obtain a separation of roughness from surface dielectric constant. The roughness inversion is then performed directly from A, while the dielectric constant estimation arises from using combined H and α values.
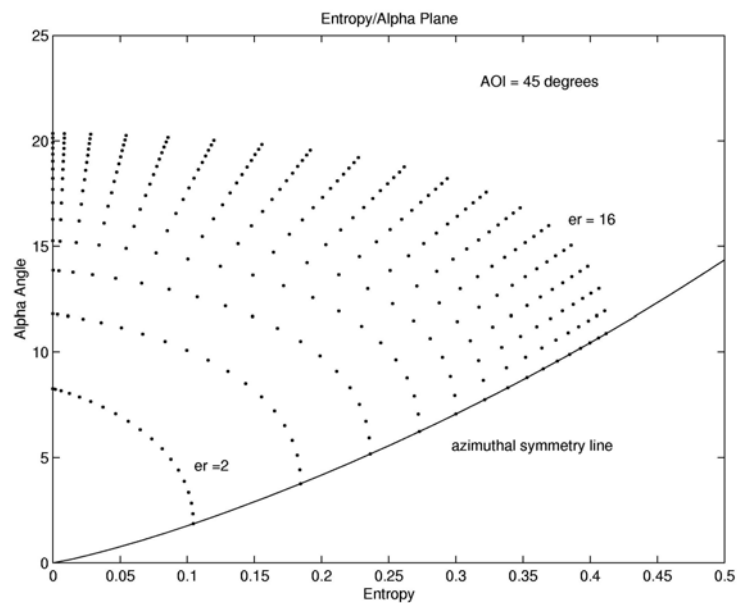
8.1.2 Model Inversion

After SAR processing and polarimetric calibration, the scattering matrix data are transformed into a coherency matrix form. In order to reduce multiplicative noise induced effects, i.e. speckle, an adaptive polarimetric Lee-filter with a window size of 7 by 7 is applied (Lee et al. 1997). Then the eigenvector decomposition is performed, followed by the computation of entropy H, anisotropy A, and alpha angle α (CLOUDE & POTTIER 1996). In a pre-selection step, areas where H > 0.5 and alpha > 45 degrees are masked out in order to select only surface scatterers.

For the estimation of the dielectric constant the following approach is used: For a range of dielectric constant values and local incidence angle values, the coherency matrix is modelled according to Eq.(8.4) and used for the evaluation of the corresponding entropy/alpha angle values, which are stored into a look-up table. Then, using this look-up table, the dielectric constant values are obtained directly from the estimated entropy and alpha angle values.

8.1.3 Experimental Data Analyses

To be up to the mark, three of the seven Elbe-Auen test fields (A5/7, 9, 11) violate the requirement of dominant surface scattering, and therefore, will not be considered in the following. To reduce the estimation variation, the anisotropy A and the alpha angle α have been estimated by averaging a minimum number of 1500 independent samples over each field. The results of the polarimetric surface scattering model inversion for surface roughness and volumetric moisture content are shown in Fig 8.5 and Fig. 8.6, respectively.

Surface Roughness Estimation

For the remaining regions, the *ks* values are obtained directly from their anisotropy values by using a linear approximation of the relationship (CLOUDE 1999), see Fig. 8.3

$$ks = 1 - A \tag{8.7a}$$

The correlation between estimated and measured *ks* values is shown in Fig. (8.5a). It is high for the Elbe-Auen test site, about 0.8; and low for the Weiherbach test site, about 0.36. The RMS error for the Elbe-Auen test site is much lower with 0.14 as for the Weiherbach test site with 0.21. The relative RMS error, which is defined as the variation in percent between the estimated and measured values, is for both test sites low, for the Elbe-Auen test site 23 % and for the Weiherbach test site 29 %, which underlines the good performance of the proposed method for roughness estimation. The fact that the lower *ks* values are overestimated and the higher underestimated, indicates that the use of a modified linear relation between A and *ks* may lead to even better inversion results. In fact, for small *ks* values another regression can be used according to (CLOUDE & LEWIS 2000).

$$(ks = 1.25 - 2A) \tag{8.7b}$$

Because of the lack of a simple analytical relationship between A and *ks* the optimum regression is still not resolved. This pertinent property has to be investigated in the future under the consideration of more experimental data. Nevertheless, the inversion formula of Eq. (8.7) leads to good estimates for the majority of the test fields, which cover a large spectrum of natural surface conditions.

a)   b)

Fig. 8.5: Estimated versus measured surface roughness for a) both test sites and b) the Weiherbach site, containing additionally additive noise filtering

Surface scattering is characterised by a strong dominant scattering mechanism, represented by the first eigenvalue. The amplitudes of the secondary scattering effects, expressed by the second and third eigenvalues may in comparison be very small, down to –25 dB or even less. As they are close to the system noise floor, they are more affected by noise effects. Hence, in contrast to the entropy, the anisotropy coefficient A is a "noisy" parameter, especially in low entropy areas. The presence of noise leads to an underestimation of A and, according to Eq.

(8.7), to an overestimation of roughness. This behaviour can be clearly recognised in Fig. (8.5a). Even after applying polarimetric speckle filtering, a remaining noise level biases the estimates. To remove the remaining noise effects, additive noise filtering has to be applied (LEE *et al*. 1994). A alternate and original additive noise filtering algorithm for polarimetric, data which is based on the variation of the <HV VH*> channel correlation, was developed and applied to the data.

The principle of the developed additive noise filter is explained in the following. The scattering matrix for backscattering problems is symmetric, i.e., *HV = VH* (BOERNER *et al*. 1998). Consequently, the 4 x 4 scattering coherency matrix $[T_4]$, formed using the outer product of the four dimensional scattering vector $\vec{k}$ as

$$[T_4] = \left\langle \vec{k} \cdot \vec{k}^+ \right\rangle \quad \text{where} \quad \vec{k} = \frac{1}{\sqrt{2}} [S_{HH} + S_{VV}, S_{HH} - S_{VV}, S_{HV} + S_{VH}, i(S_{HV} - S_{VH})]^T \tag{8.8}$$

is a hermitian positive semi-definite matrix of rank 3. The eigenvector decomposition of $[T_4]$ leads to three real non-negative eigenvalues, while the fourth one is zero

$$[T_4] = [U] \begin{bmatrix} \lambda_1 & 0 & 0 & 0 \\ 0 & \lambda_2 & 0 & 0 \\ 0 & 0 & \lambda_3 & 0 \\ 0 & 0 & 0 & \lambda_4 \end{bmatrix} [U]^{*T}, \qquad \lambda_1 \geq \lambda_2 \geq \lambda_3 \geq \lambda_4 = 0 \tag{8.9}$$

The *HV* and *VH* polarisation channels are measured independently by the polarimetric SAR system. In the absence of noise, the correlation coefficient between these two channels is 1. However, as noise increases, the correlation coefficient decreases and $[T_4]$ becomes a rank 4 matrix with $\lambda_4 > 0$. Hence, the estimation of λ_4 allows us to assess the noise level in the data. As the coherency matrix represents a second order average of the scattering amplitudes, λ_4 corresponds to the average noise power σ_N. In order to remove the estimated noise level, and assuming the noise power to be equal in all four channels, we subtract the known σ_N from the diagonal form of the 3x3 coherency matrix $[T]$ to obtain a noise filtered coherence matrix estimate

$$[T_3]_F = [T_3] - \sigma_N [I_3] \tag{8.10}$$

where $[I_3]$ is the 3x3 identity matrix. All eigenvector decomposition parameters are now obtained from the matrix $[T_3]_F$, where F stands for filtered. Note that the 4x4 eigen-decomposition of Eq. (8.9) has to be applied after cross-talk removal and phase calibration but before the cross-channel symmetrisation.

The roughness estimates finally obtained, are shown in Fig. (8.5b) and demonstrate clearly the reduction of the roughness overestimation, down to a RMS error of 19 %. Since the additive noise filter requires both cross-polarised channels, it has been applied only to the Weiherbach test site because the data from the Elbe-Auen test site were available only in a symmetrised format.

Soil Moisture Estimation

In a second step, the computed entropy and alpha values are used to estimate the dielectric constant. The estimation is performed - as already mentioned - by using a lookup table, which delivers the dielectric constant as a function of the entropy/alpha values and the local incidence angle. In this way, the range and topography induced variation of the local incidence angle across the image can be accounted for. The correlation between the estimated and measured values at different soil depths for the two test sites is compiled in Fig. 8.6.
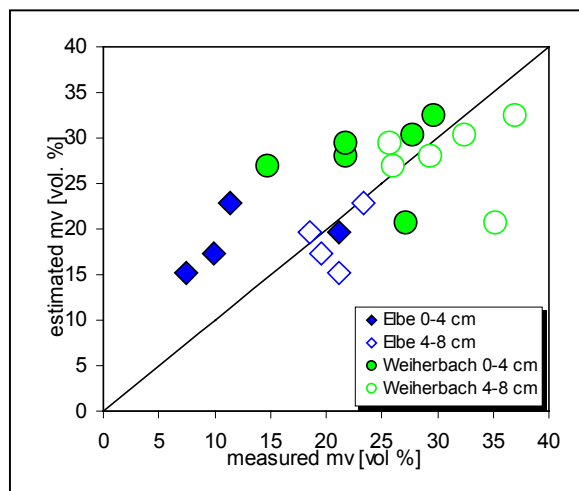

Fig. 8.6: Estimated versus measured dielectric constant.

As expected for L-band observations, the mean RMS error is smaller for the ground measurements performed at the deeper soil layer (4-8 cm). Fig. 8.6 shows the correlation between estimated and measured volumetric moisture values for all soil depths. The inverted m_v values correlate better with the ground measurements at a depth of 4-8 cm. The corresponding correlation for this depth is shown in Fig. 8.7. In this case, the RMS error for the Elbe-Auen test site is about 7.8 for the top soil layer, and 3.2 for the deeper soil layer; whereas for the Weiherbach test site the values are about 5.8 for the top layer, and 10.4 for the deeper layer. Useful for the comparison, the relative RMS error for the volumetric moisture content is of the order of 14 [vol. %] for the Elbe, and 19 [vol. %] for the Weiherbach site. Both test sites show a slight underestimation of the mean value at about 2 [vol. %]. The standard deviation is about 3 for the Elbe-Auen test site, while for the Weiherbach test site it is significantly higher, on the

order of 6. The main reason for this is the presence of one single, strongly heterogeneous bare field, for which the obtained estimates are uncorrelated. By ignoring this field, the RMS error decreases to 8 [vol. %] and the correlation coefficient rises to 0.85.

The presented polarimetric surface scattering model is based on the SPM. Therefore, the two models are characterised by a similar behaviour concerning their sensitivity to soil moisture. As already described in *Chapter 6* (see Fig. (6.1)) the inversion of moisture content using the SPM for slightly rough surfaces begins to saturate above $m_v = 20$ [vol. %]. The proposed model extends significantly the soil moisture sensitivity range, allowing accurate estimations up to $m_v = 35$ [vol. %]. Above 35 [vol. %] the estimation performance is successively decreasing.

a)   b)

Fig. 8.7: Estimated versus measured complex dielectric constant (a) and volumetric soil moisture (b) at 4-8 cm soil depth for two test sites (Elbe-Auen and Weiherbach)

The estimated surface parameters are visualised in Fig. 8.8 for surface roughness and in Fig. 8.9 for soil moisture content. The number of regions, which satisfies the condition for applying the inversion model, is for the Elbe-Auen test site higher than for the Weiherbach site. Nevertheless, the number of second and multiple scattering mechanisms, causes still a problem for an accurate surface parameter estimation. The main reason for this is the presence of vegetation. Therefore, further methods have to be developed for facing the vegetation problem and to minimise the estimation error.

Fig. 8.8: Surface Roughness ranging from 0 to 1; black: not valid areas

Fig. 8.9: Soil moisture content ranging from 0 to 40 [vol. %]; black: not valid areas
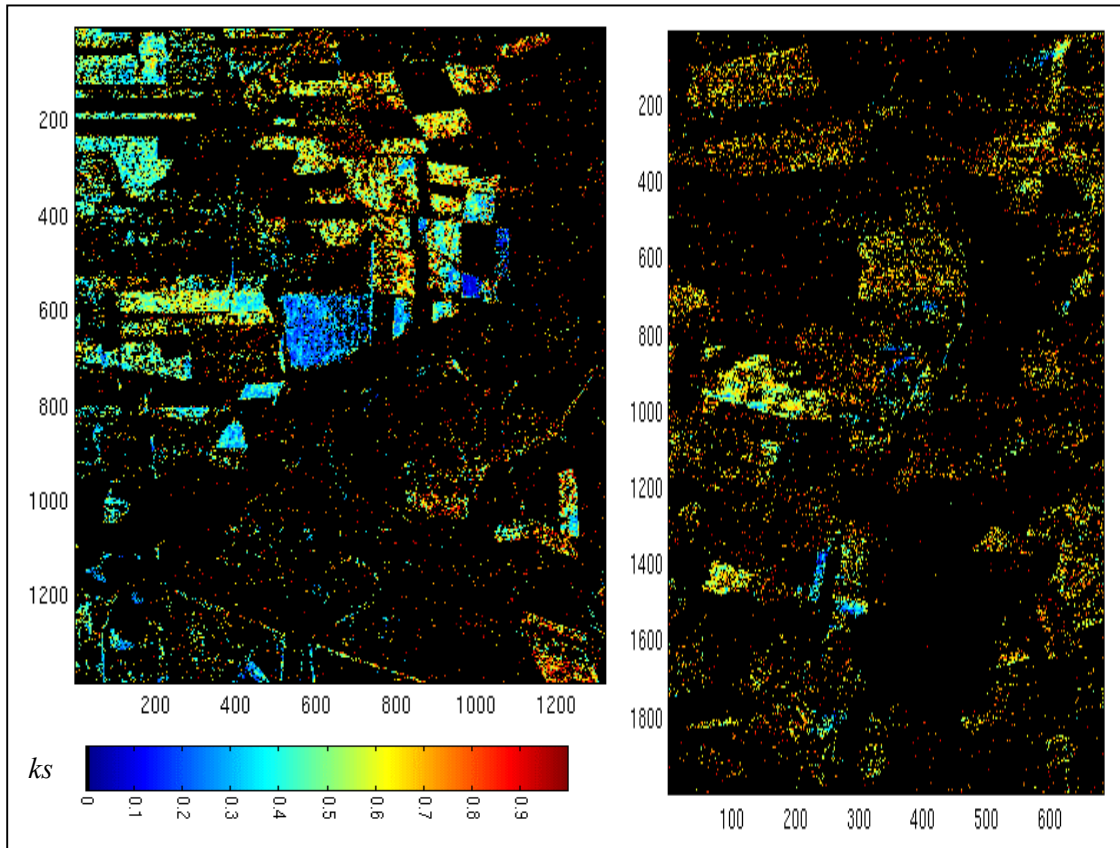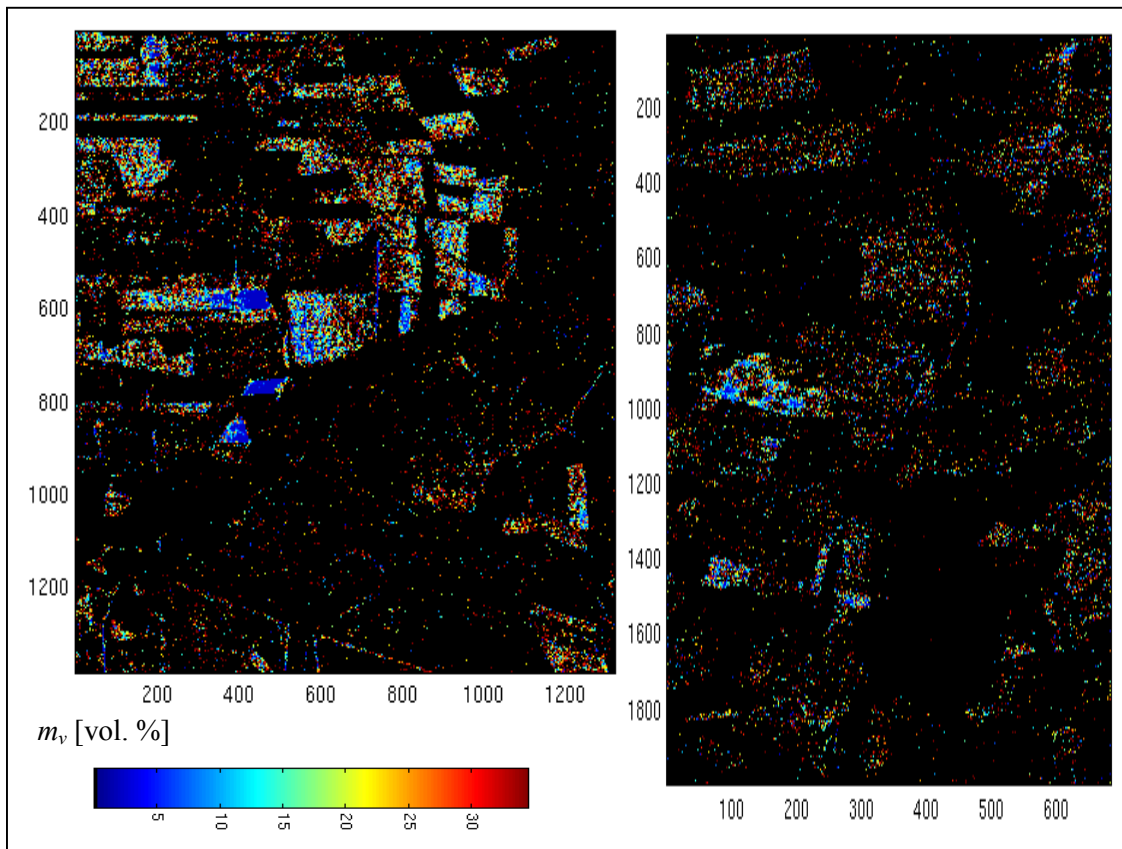
8.2 Synopsis

In this Chapter, an alternate new general parametric model, which enables the quantitative estimation of roughness and dielectric constant over a wide range of natural bare surfaces from polarimetric SAR data, has been introduced. The model is an extension of the SPM and assumes reflection symmetric surfaces, where the mean normal to the surface vector defines the axis of symmetry. It allows the *HH* and *VV* back-scattering coefficients to be different and account for non-zero cross-polarised, backscattering as well as depolarisation effects. The application of the model to experimental data shows good agreement between inverted values and ground measurements for *ks*, *ε'* and m_v. The low RMS errors for *ks* about 0.14 for the Elbe-Auen, and about 0.11 for the Weiherbach test site and for m_v ranging from 5 to 10 [vol. %] considering both test sites, indicates that the structure of the data is in accordance with the predictions of the model over a large range of surface conditions. Even the seasonal impact on the estimation is observed due to the fact that the RMS errors for the Weiherbach test site are much smaller in the upper soil layer, when flight campaign in March, and for the Elbe-Auen test site the RMS error is much smaller in the deeper soil layer, during the flight campaign in August, respectively.

The main advantage of the proposed inversion model is the straightforward separation of roughness and dielectric constant estimation, which can be performed without any data based regression. Furthermore, as the three key observables: entropy, anisotropy and alpha angle, are invariant under LOS (Line-of Sight) rotations the inversion becomes independent of azimuthal slope variations. This makes the application of the technique possible also over terrain with variable topography without the need of additional topographic information. The robust behaviour of the proposed algorithm over hilly terrain was confirmed, and it has been shown that it permits robust roughness estimation widely independent of topographic variations. However, the moisture content estimation is much more sensitive to incidence angle variations. Sensitivity analyses with respect to terrain variations have shown that 1 degree in terrain slope variation leads to an RMS error variation in the order of 0.25 [vol. %] (HAJNSEK *et al*. 2000).

Absolute calibration of the scattering matrix data is not strictly required, while for the *ks* estimation only cross-talk and relative channel calibration are sufficient, for the estimation of *ε'* the relative copolar-phase calibration is essential. The high dependency of the *ε'* estimation on the alpha angle values combined with the fact that any copolar-phase imbalance $\Delta \phi$ affects directly the alpha angle estimation ($\Delta\alpha \approx \Delta \Phi/ 2$), forces the demand on accurate phase calibration. Further, the effect of noise on the smaller eigenvalues leads to an overestimation of surface roughness. This can be avoided by applying multiplicative as well as additive noise filtering. However, one note of caution is required: the applied filtering techniques must always preserve the polarimetric information content of the data (LEE *et al*. 1997).

The influence of surface correlation length, remains unknown as it does not appear explicitly in the model. Small correlation lengths lead to multiple scattering effects, which are biasing the alpha angle α estimation by increasing the HH/VV ratio.

The presence of vegetation on the one hand increases the entropy and decreases the anisotropy, leading to overestimation of the surface roughness. On the other hand, it increases the alpha angle leading also to overestimated complex dielectric constant values.

8.3   References to Chapter 8

BOERNER, W.-M. et al., 'Polarimetry in Radar Remote Sensing: Basic and Applied Concepts', Chapter 5 in F.M. Henderson and A.J. Lewis (ed.), 'Principles and Applications of Imaging Radar', vol. 2 of Manual of Remote Sensing, (ed. R.A. Reyerson), Third Edition, Jhon Willey & Sons, New York, 1998.

BORGEAUD, M. & NOLL, J., 'Analysis of Theoretical Surface Scattering Models for Polarimetric Microwave Remote Sensing of Bare Soils', *International Journal of Remote Sensing*, vol. 15, no. 14, pp. 2931-2942, 1994.

CLOUDE, S. R., & PAPATHANASSIOU, K. P., 'Surface Roughness and Polarimetric Entropy', *Proceedings IGARSS'99*, Hamburg 1999, pp. 2443-2445,1999.

CLOUDE, S. R., 'Eigenvalue Parameters for Surface Roughness Studies', *Proceedings of SPIE Conference on Polarization: Measurement, Analysis and Remote Sensing II*, vol. 3754, Denver, Colorado, USA, July 1999.

CLOUDE, S. R., HAJNSEK, I. & PAPATHANASSIOU, K. P., 'An Eigenvector Method for the Extraction of Surface Parameters in Polarimetric SAR', *Proceedings of the CEOS SAR Workshop*, Toulouse 1999, ESA SP-450, pp. 693 – 698, 1999.

CLOUDE, S. R. & LEWIS, G. D., 'Eigenvalue Analysis of Mueller Matrix for Bead Basted Aluminium Surfaces', SPIE Polarisation Analysis and Measurement III, *Proceedings of SPIE*, vol. AM107, July-Aug 2000.

DAVIDSON, M. W.J., LE TOAN, T., MATTIA, F. SATALINO, G. MANNINER, T. & BORGEAUD, M., 'On the Characterization of Agricultural Soil Roughness for Radar Remote Sensing Studies', *IEEE Transactions on Geoscience and Remote Sensing*, vol. 38, no. 2, pp. 630–640, 2000.

DUBOIS, P. C. VAN ZYL, J. J. & ENGMAN, T., 'Measuring Soil Moisture with Imaging Radars', *IEEE Transactions on Geoscience and Remote Sensing*, vol. 33, no. 4, pp. 916-926, 1995.

HAJNSEK, I., CLOUDE, S. R., J.S. LEE, E. POTTIER, 'Inversion of Surface Parameters from Polarimetric SAR Data', *Proceedings IGARSS'00*, vol. III, pp. 1095-1097, p. 2001.

HAJNSEK, I., CLOUDE, S. R., LEE, J. S. & POTTIER, E., 'Terrain Correction for Quantitative Moisture and Roughness Retrieval Using Polarimetric SAR Data', *Proceedings IGARSS'00*, Honolulu, Hawaii, pp. 1307-1309, July 2000.

HAJNSEK, I., POTTIER, E. & CLOUDE, S. R., 'Slope Correction for Soil Moisture and Surface Roughness Retrieval', *Proceedings of third European Conference on Synthetic Aperture Radar EUSAR 2000*, pp. 273-276, May 2000.

LEE, J. S., GRUNES, M. R. & DE GRANDI, G., 'Polarimetric SAR Speckle Filtering and its Impact on Classification', *IEEE Transactions on Geoscience and Remote Sensing*, vol. 37, no. 5, pp. 2363 – 2373, 1997.

LEE, J. S., JURKEVICH, I., DEWAELE, P., WAMBACQ, P. & COSTERLINCK, A., 'Speckle filtering of synthetic aperture radar images: A review', *Remote Sens. Rev.*, vol. 8, pp 311-340, 1994.

MATTIA, F., LE TOAN, T., SOUYRIS, J. C., DE CAROLIS, G., FLOURY, N., POSA, F. & PASQUARIELLO, G., 'The Effect of Surface Roughness on Multi-Frequency Polarimetric

SAR data', *IEEE Transactions on Geoscience and Remote Sensing*, vol. 35, no. 4, pp. 954-965, 1997.

OH, Y., SARABANDI, K. & ULABY, F. T., 'An Empirical Model and an Inversion Technique for Radar Scattering from Bare Soil Surfaces', *IEEE Transactions on Geoscience and Remote Sensing*, vol.30, no. 2, pp. 370-381, 1992.

TOPP, G. C., DAVIS, J. L. & ANNAN, A. P., 'Electromagnetic Determination of Soil Water Content: Measurements in Coaxial Transmission Lines', *Water Resources Research*; vol. 16, no. 3, pp. 574-582, 1980.

Chapter 8

Inversion of Surface Parameters
Using Extended Bragg Scattering Model

In this chapter a new model for the inversion of surface roughness and soil moisture from polarimetric SAR data is introduced. In the two previous chapters the applicability of three inversion models and methods for their extensions have been investigated. A second promising approach for the extraction of surface parameters started with the analysis of second order statistics of surface scatterers (BORGEAUD & NOLL 1994, MATTIA *et al.* 1997). The correlation coefficient between different polarisation states has been observed to correlate with complex dielectric constant and/or surface roughness measurements. These observations depict the first step to an independent estimation of the observed surface parameters, but their investigations are still not sufficient for quantitative estimation. Recently, observations based on experimental data collected in an anechoic chamber, indicated a relationship between surface roughness and the eigenvalues of the polarimetric coherency matrix, which themselves have a physical significance in terms of scattering amplitudes (CLOUDE & PAPATHANASSIOU 1999, CLOUDE 1999, CLOUDE *et al.* 1999). Furthermore, their ratio can be interpreted in terms of generalised polarimetric coherence coefficients. An alternative model for the investigation of surface parameters from polarimetric SAR data will be introduced arising from these experimental observations. The proposed model is a two component model including a Bragg term and a roughness induced rotation symmetry term. In order to decouple the real part of the complex dielectric constant from the surface roughness, the model is formulated in terms of the polarimetric entropy H, alpha angle α, and anisotropy A, which are derived from the eigenvalues and eigenvectors of the polarimetric coherency matrix.

8.1   Model Based Eigenvector Decomposition

8.1.1   Model Description

As discussed in *Chapter 7*, the limitation of the Small Perturbation Model (SPM) for the interpretation and inversion of experimental data from natural surfaces arises from its inability to describe non-zero *cross-polarised* backscattering and depolarisation effects. To circumvent this shortcoming, a configurational average of the SPM solution is proposed, which introduces cross-polarised energy and at the same time forces the polarimetric coherence to be less than one.

The rotation of the Bragg coherency matrix $[T]$ about an angle β in the plane perpendicular to the scattering plane (see Fig. (8.1)) can be written as

$$[T(\beta)] = \begin{bmatrix} 1 & 0 & 0 \\ 0 & \cos 2\beta & \sin 2\beta \\ 0 & -\sin 2\beta & \cos 2\beta \end{bmatrix} \begin{bmatrix} \left\langle |R_S + R_P|^2 \right\rangle & \left\langle (R_S - R_P)(R_S + R_P)^* \right\rangle & 0 \\ \left\langle (R_S + R_P)(R_S - R_P)^* \right\rangle & \left\langle |R_S - R_P|^2 \right\rangle & 0 \\ 0 & 0 & 0 \end{bmatrix} \begin{bmatrix} 1 & 0 & 0 \\ 0 & \cos 2\beta & -\sin 2\beta \\ 0 & \sin 2\beta & \cos 2\beta \end{bmatrix} \quad (8.1)$$

Fig. 8.1: Uniform distribution of surface slope

Performing now configurational averaging over a given distribution $P(\beta)$ of β, the coherency matrix becomes

$$[T] = \int_0^{2\pi} [T(\beta)] P(\beta) d\beta \quad (8.2)$$

Assuming $P(\beta)$ to be a uniform distribution about zero with width β_1 (see Fig. (8.1))

$$P(\beta) = \begin{cases} \dfrac{1}{2\beta_1} & |\beta| \le \beta_1 \\ 0 \le \beta_1 \le \dfrac{\pi}{2} \end{cases} \quad (8.3)$$

the coherency matrix for the rough surface becomes

$$[T] = \begin{bmatrix} T_{11} & T_{12} & T_{13} \\ T_{21} & T_{22} & T_{23} \\ T_{31} & T_{32} & T_{33} \end{bmatrix} = \begin{bmatrix} C_1 & C_2 \sin c(2\beta_1) & 0 \\ C_2 \sin c(2\beta_1) & C_3(1 + \sin c(4\beta_1)) & 0 \\ 0 & 0 & C_3(1 - \sin c(4\beta_1)) \end{bmatrix} \quad (8.4)$$

with $\text{sinc}(x) = \sin(x)/x$. The coefficients C_1, C_2, and, C_3 describe the Bragg component of the surface, and are given by

$$C_1 = |R_S + R_P|^2 \qquad C_2 = (R_S + R_P)(R_S^* - R_P^*) \qquad C_3 = \frac{1}{2}|R_S - R_P|^2 \qquad (8.5)$$

The width of the distribution β_1 describes the roughness component and controls both the polarimetric coherence and the level of cross-polarised power.

From Eq. (8.4), the polarimetric coherence between the Left-Left and Right-Right circular polarisations (CLOUDE 1999) follows as

$$\gamma_{LLRR} := \frac{T_{22} - T_{33}}{T_{22} + T_{33}} = \sin c(4\beta_1) \qquad (8.6)$$

and depends only on the surface roughness. This is in accordance with former experimental observations reported in (MATTIA *et al.* 1997). On the other hand, the polarimetric anisotropy can be interpreted as a generalised rotation invariant expression for γ_{LLRR}. Consequently, the anisotropy is independent on the dielectric properties of the surface.

This fact allows a straightforward separation of roughness and moisture effects inside [*T*] and represents one of the major advantages of the proposed model. Note that this result is independent of the choice of slope distributions. The form of *P*(*ß*) affects only the mathematical expression of the anisotropy.

Fig. 8.2 shows the variation of polarimetric coherence (dotted line) and normalised cross-polarised power (solid line). For $\beta_1 = 0$ the *HH-VV* coherence is unity and the *HV* power zero, as expected in the limit of a smooth surface, and the coherency matrix reduces to the form given by Eq. (6.1). As β_1 increases, the HV power increases, while the coherence reduces monotonically from 1 for a smooth surface to zero for $\beta_1 = 90$ degrees. In this second limiting case of high surface roughness the surface becomes azimuthally symmetric. Note that the increase in *HV* power is faster than the fall-off in coherence, and, therefore, for small β_1 values the anisotropy will be high (close to 1). As β_1 increases the anisotropy falls monotonically to zero.
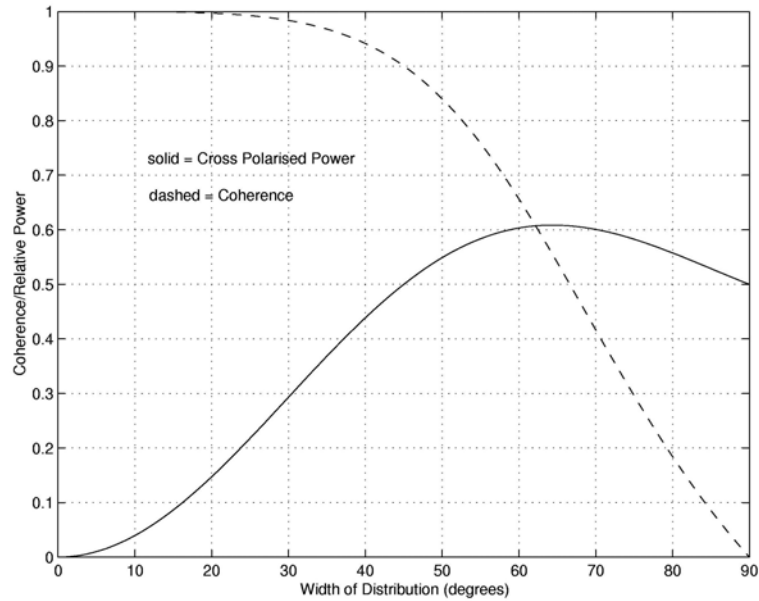
Fig. 8.2: Variation of cross-polarisation and coherence with model parameter β_1

Fig. 8.3 shows how this fall in the anisotropy coefficient A occurs as a function of β_1 for a range of dielectric constant values. For $ks < 1$, i. e. up to $\beta_1 = 90°$, we can see an almost linear relation between A and ks, which is independent of the dielectric constant, and hence of the soil moisture content. Finally, A becomes insensitive to a further increase of roughness above $ks = 1$. Again, it is important to note that the value of A at any β_1 is independent on the surface dielectric constant and on the local incidence angle. Similar studies show that A is also independent of the angle of incidence (HAJNSEK *et al*. 2000).

Further structure in Eq. (8.4), can be exposed, by plotting the entropy/alpha loci of points for different dielectric constant values and widths of slope distribution β_1 for a fixed local incidence angle of $\theta = 45$ degrees as shown in Fig. 8.4. The loci are best interpreted in a polar co-ordinate system centred on the origin. In this sense, the radial co-ordinate corresponds to the dielectric constant while the azimuthal angle represents changes in roughness. These loci can be used to provide an estimate of the surface dielectric constant, independent of surface roughness. The corresponding entropy/alpha values are evaluated from the coherency matrix [*T*] as given in Eq. (8.4).
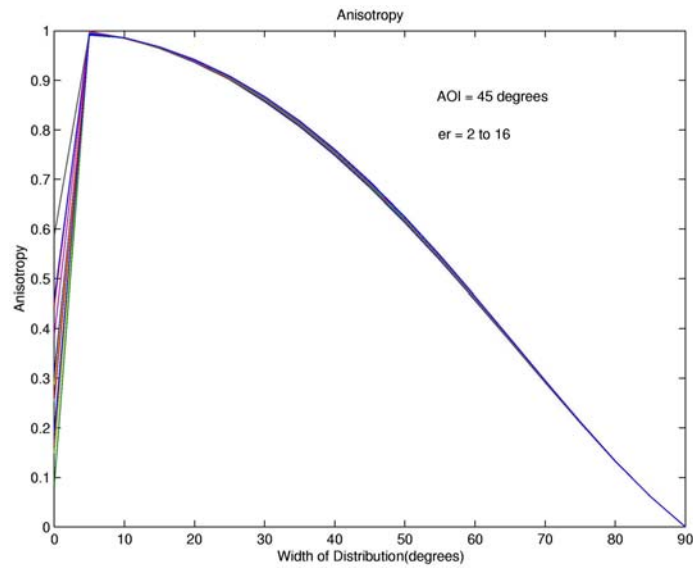
Fig. 8.3: Anisotropy versus Roughness for 45 degree local incidence angle (AOI)

In the limiting case of a smooth surface, the entropy becomes zero and the alpha angle corresponds directly to the dielectric constant through Eq. (6.1). However, as the entropy increases with increasing roughness, the apparent alpha angle value decreases, leading to an underestimation of the dielectric constant. Using Eq. (8.5), it is possible to compensate this roughness induced underestimation of the alpha angle by tracking the loci of constant ε' back to the H = 0 line. In this way both, the entropy and alpha values, are required in order to obtain a corrected estimate of the surface moisture.
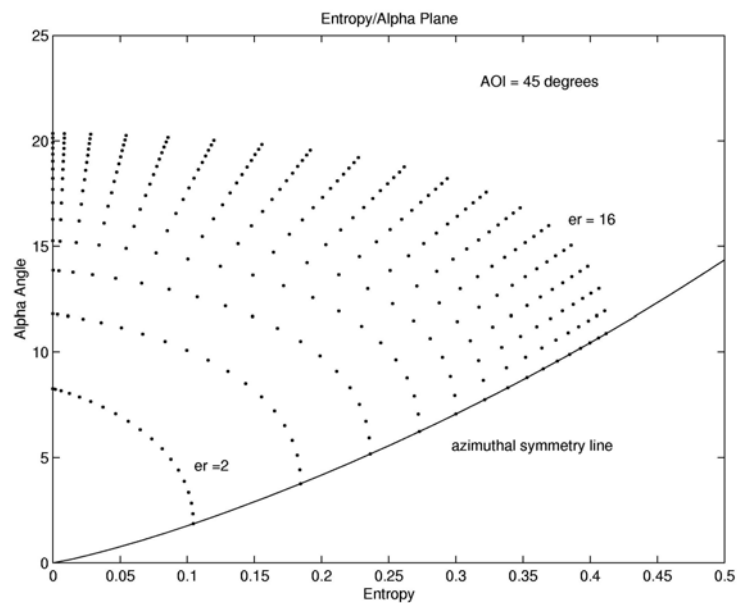

Fig. 8.4: Entropy/Alpha diagram for 45 degree AOI plotted for varying dielectric constant

Hence, by estimating three parameters, the entropy H, the anisotropy A and the alpha angle α, we obtain a separation of roughness from surface dielectric constant. The roughness inversion is then performed directly from A, while the dielectric constant estimation arises from using combined H and α values.

8.1.2 Model Inversion

After SAR processing and polarimetric calibration, the scattering matrix data are transformed into a coherency matrix form. In order to reduce multiplicative noise induced effects, i.e. speckle, an adaptive polarimetric Lee-filter with a window size of 7 by 7 is applied (Lee et al. 1997). Then the eigenvector decomposition is performed, followed by the computation of entropy H, anisotropy A, and alpha angle α (CLOUDE & POTTIER 1996). In a pre-selection step, areas where H > 0.5 and alpha > 45 degrees are masked out in order to select only surface scatterers.

For the estimation of the dielectric constant the following approach is used: For a range of dielectric constant values and local incidence angle values, the coherency matrix is modelled according to Eq.(8.4) and used for the evaluation of the corresponding entropy/alpha angle values, which are stored into a look-up table. Then, using this look-up table, the dielectric constant values are obtained directly from the estimated entropy and alpha angle values.

8.1.3 Experimental Data Analyses

To be up to the mark, three of the seven Elbe-Auen test fields (A5/7, 9, 11) violate the requirement of dominant surface scattering, and therefore, will not be considered in the following. To reduce the estimation variation, the anisotropy A and the alpha angle α have been estimated by averaging a minimum number of 1500 independent samples over each field. The results of the polarimetric surface scattering model inversion for surface roughness and volumetric moisture content are shown in Fig 8.5 and Fig. 8.6, respectively.

Surface Roughness Estimation

For the remaining regions, the *ks* values are obtained directly from their anisotropy values by using a linear approximation of the relationship (CLOUDE 1999), see Fig. 8.3

$$ ks \ = 1 - \ A \qquad\qquad (8.7a) $$

The correlation between estimated and measured *ks* values is shown in Fig. (8.5a). It is high for the Elbe-Auen test site, about 0.8; and low for the Weiherbach test site, about 0.36. The RMS error for the Elbe-Auen test site is much lower with 0.14 as for the Weiherbach test site with 0.21. The relative RMS error, which is defined as the variation in percent between the estimated and measured values, is for both test sites low, for the Elbe-Auen test site 23 % and for the Weiherbach test site 29 %, which underlines the good performance of the proposed method for roughness estimation. The fact that the lower *ks* values are overestimated and the higher underestimated, indicates that the use of a modified linear relation between A and *ks* may lead to even better inversion results. In fact, for small *ks* values another regression can be used according to (CLOUDE & LEWIS 2000).

$$(ks = 1.25 - 2A) \qquad\qquad (8.7b)$$

Because of the lack of a simple analytical relationship between A and *ks* the optimum regression is still not resolved. This pertinent property has to be investigated in the future under the consideration of more experimental data. Nevertheless, the inversion formula of Eq. (8.7) leads to good estimates for the majority of the test fields, which cover a large spectrum of natural surface conditions.

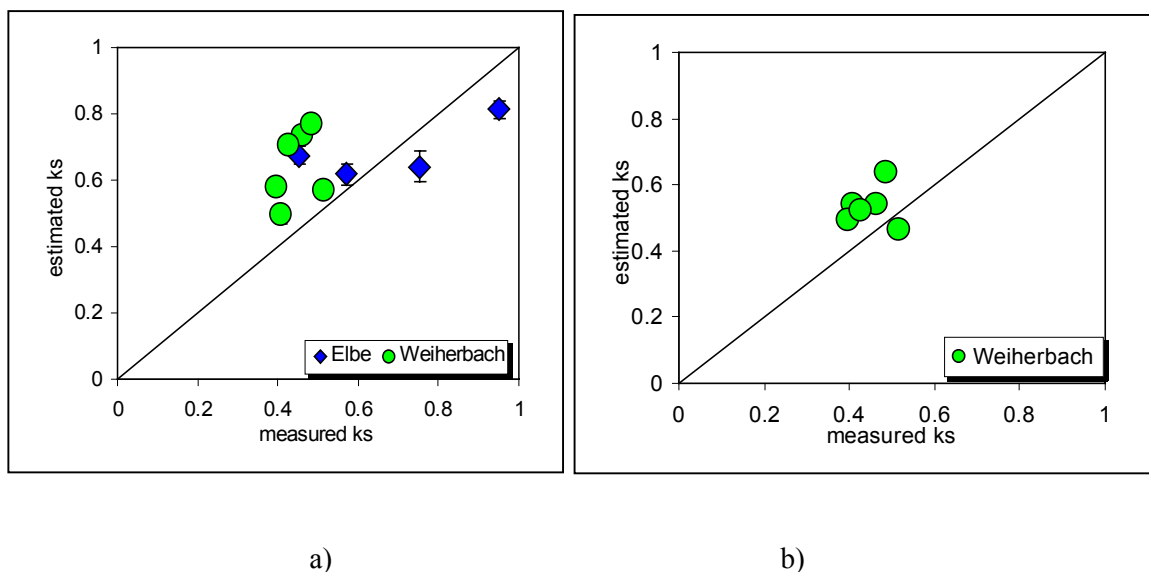a)   b)

Fig. 8.5: Estimated versus measured surface roughness for a) both test sites and b) the Weiherbach site, containing additionally additive noise filtering

Surface scattering is characterised by a strong dominant scattering mechanism, represented by the first eigenvalue. The amplitudes of the secondary scattering effects, expressed by the second and third eigenvalues may in comparison be very small, down to –25 dB or even less. As they are close to the system noise floor, they are more affected by noise effects. Hence, in contrast to the entropy, the anisotropy coefficient A is a "noisy" parameter, especially in low entropy areas. The presence of noise leads to an underestimation of A and, according to Eq.

(8.7), to an overestimation of roughness. This behaviour can be clearly recognised in Fig. (8.5a). Even after applying polarimetric speckle filtering, a remaining noise level biases the estimates. To remove the remaining noise effects, additive noise filtering has to be applied (LEE *et al*. 1994). A alternate and original additive noise filtering algorithm for polarimetric, data which is based on the variation of the <HV VH*> channel correlation, was developed and applied to the data.

The principle of the developed additive noise filter is explained in the following. The scattering matrix for backscattering problems is symmetric, i.e., *HV = VH* (BOERNER *et al*. 1998). Consequently, the 4 x 4 scattering coherency matrix $[T_4]$, formed using the outer product of the four dimensional scattering vector $\vec{k}$ as

$$[T_4] = \left\langle \vec{k} \cdot \vec{k}^+ \right\rangle \quad \text{where} \quad \vec{k} = \frac{1}{\sqrt{2}} \left[S_{HH} + S_{VV}, S_{HH} - S_{VV}, S_{HV} + S_{VH}, i(S_{HV} - S_{VH}) \right]^T \tag{8.8}$$

is a hermitian positive semi-definite matrix of rank 3. The eigenvector decomposition of $[T_4]$ leads to three real non-negative eigenvalues, while the fourth one is zero

$$[T_4] = [U] \begin{bmatrix} \lambda_1 & 0 & 0 & 0 \\ 0 & \lambda_2 & 0 & 0 \\ 0 & 0 & \lambda_3 & 0 \\ 0 & 0 & 0 & \lambda_4 \end{bmatrix} [U]^{*T}, \qquad \lambda_1 \geq \lambda_2 \geq \lambda_3 \geq \lambda_4 = 0 \tag{8.9}$$

The *HV* and *VH* polarisation channels are measured independently by the polarimetric SAR system. In the absence of noise, the correlation coefficient between these two channels is 1. However, as noise increases, the correlation coefficient decreases and $[T_4]$ becomes a rank 4 matrix with $\lambda_4 > 0$. Hence, the estimation of λ_4 allows us to assess the noise level in the data. As the coherency matrix represents a second order average of the scattering amplitudes, λ_4 corresponds to the average noise power σ_N. In order to remove the estimated noise level, and assuming the noise power to be equal in all four channels, we subtract the known σ_N from the diagonal form of the 3x3 coherency matrix $[T]$ to obtain a noise filtered coherence matrix estimate

$$[T_3]_F = [T_3] - \sigma_N [I_3] \tag{8.10}$$

where $[I_3]$ is the 3x3 identity matrix. All eigenvector decomposition parameters are now obtained from the matrix $[T_3]_F$, where F stands for filtered. Note that the 4x4 eigen-decomposition of Eq. (8.9) has to be applied after cross-talk removal and phase calibration but before the cross-channel symmetrisation.

The roughness estimates finally obtained, are shown in Fig. (8.5b) and demonstrate clearly the reduction of the roughness overestimation, down to a RMS error of 19 %. Since the additive noise filter requires both cross-polarised channels, it has been applied only to the Weiherbach test site because the data from the Elbe-Auen test site were available only in a symmetrised format.

Soil Moisture Estimation

In a second step, the computed entropy and alpha values are used to estimate the dielectric constant. The estimation is performed - as already mentioned - by using a lookup table, which delivers the dielectric constant as a function of the entropy/alpha values and the local incidence angle. In this way, the range and topography induced variation of the local incidence angle across the image can be accounted for. The correlation between the estimated and measured values at different soil depths for the two test sites is compiled in Fig. 8.6.
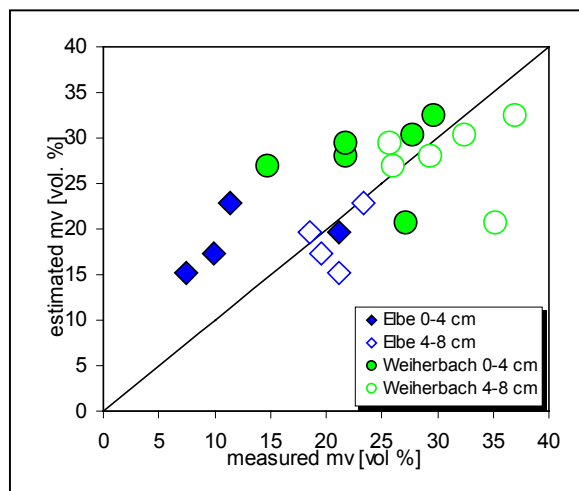

Fig. 8.6: Estimated versus measured dielectric constant.

As expected for L-band observations, the mean RMS error is smaller for the ground measurements performed at the deeper soil layer (4-8 cm). Fig. 8.6 shows the correlation between estimated and measured volumetric moisture values for all soil depths. The inverted m_v values correlate better with the ground measurements at a depth of 4-8 cm. The corresponding correlation for this depth is shown in Fig. 8.7. In this case, the RMS error for the Elbe-Auen test site is about 7.8 for the top soil layer, and 3.2 for the deeper soil layer; whereas for the Weiherbach test site the values are about 5.8 for the top layer, and 10.4 for the deeper layer. Useful for the comparison, the relative RMS error for the volumetric moisture content is of the order of 14 [vol. %] for the Elbe, and 19 [vol. %] for the Weiherbach site. Both test sites show a slight underestimation of the mean value at about 2 [vol. %]. The standard deviation is about 3 for the Elbe-Auen test site, while for the Weiherbach test site it is significantly higher, on the

order of 6. The main reason for this is the presence of one single, strongly heterogeneous bare field, for which the obtained estimates are uncorrelated. By ignoring this field, the RMS error decreases to 8 [vol. %] and the correlation coefficient rises to 0.85.

The presented polarimetric surface scattering model is based on the SPM. Therefore, the two models are characterised by a similar behaviour concerning their sensitivity to soil moisture. As already described in *Chapter 6* (see Fig. (6.1)) the inversion of moisture content using the SPM for slightly rough surfaces begins to saturate above $m_v = 20$ [vol. %]. The proposed model extends significantly the soil moisture sensitivity range, allowing accurate estimations up to $m_v = 35$ [vol. %]. Above 35 [vol. %] the estimation performance is successively decreasing.

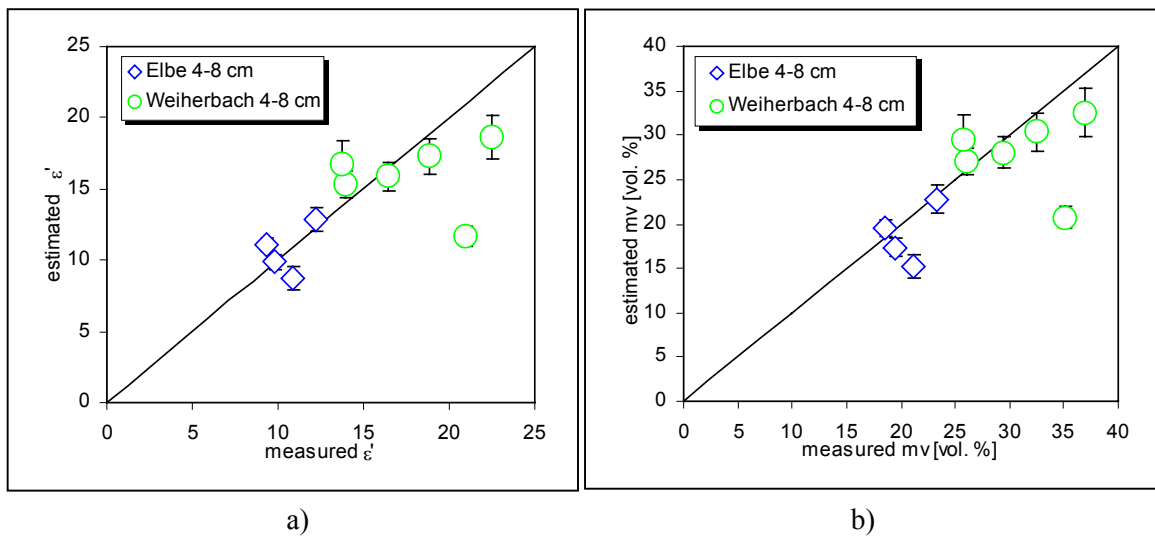a)   b)

Fig. 8.7: Estimated versus measured complex dielectric constant (a) and volumetric soil moisture (b) at 4-8 cm soil depth for two test sites (Elbe-Auen and Weiherbach)

The estimated surface parameters are visualised in Fig. 8.8 for surface roughness and in Fig. 8.9 for soil moisture content. The number of regions, which satisfies the condition for applying the inversion model, is for the Elbe-Auen test site higher than for the Weiherbach site. Nevertheless, the number of second and multiple scattering mechanisms, causes still a problem for an accurate surface parameter estimation. The main reason for this is the presence of vegetation. Therefore, further methods have to be developed for facing the vegetation problem and to minimise the estimation error.
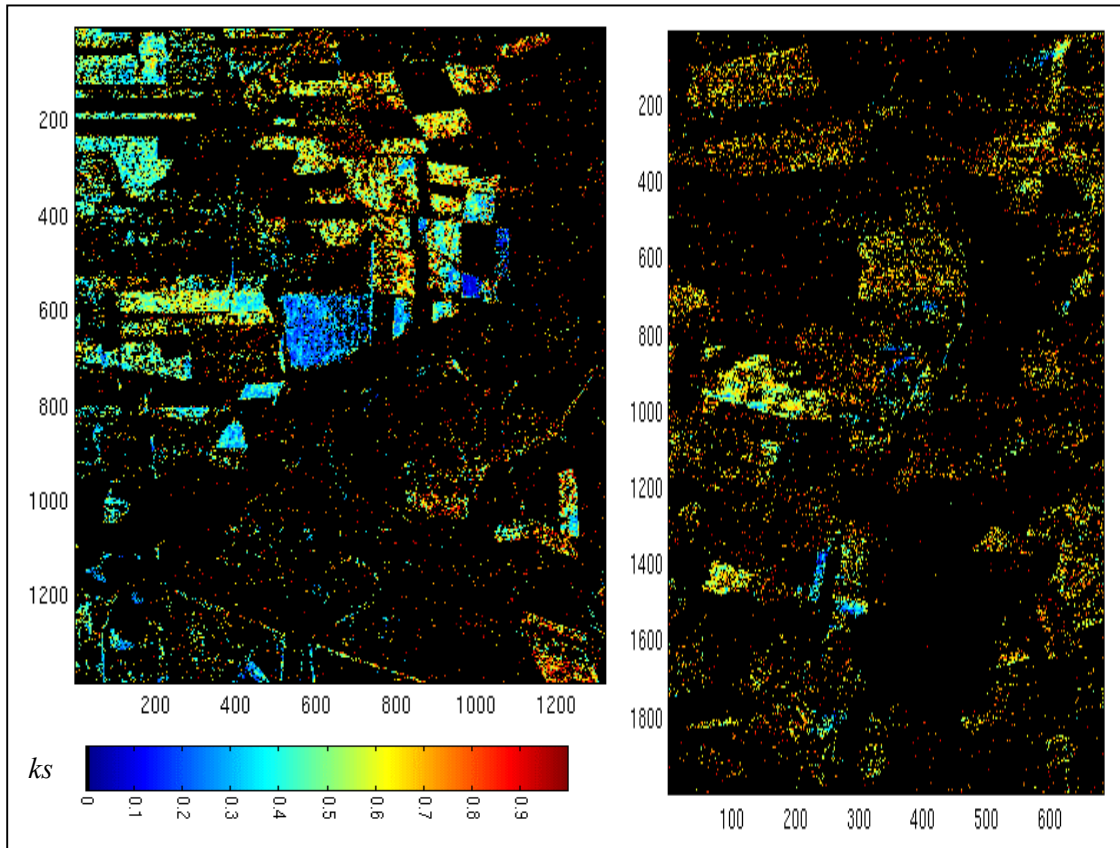
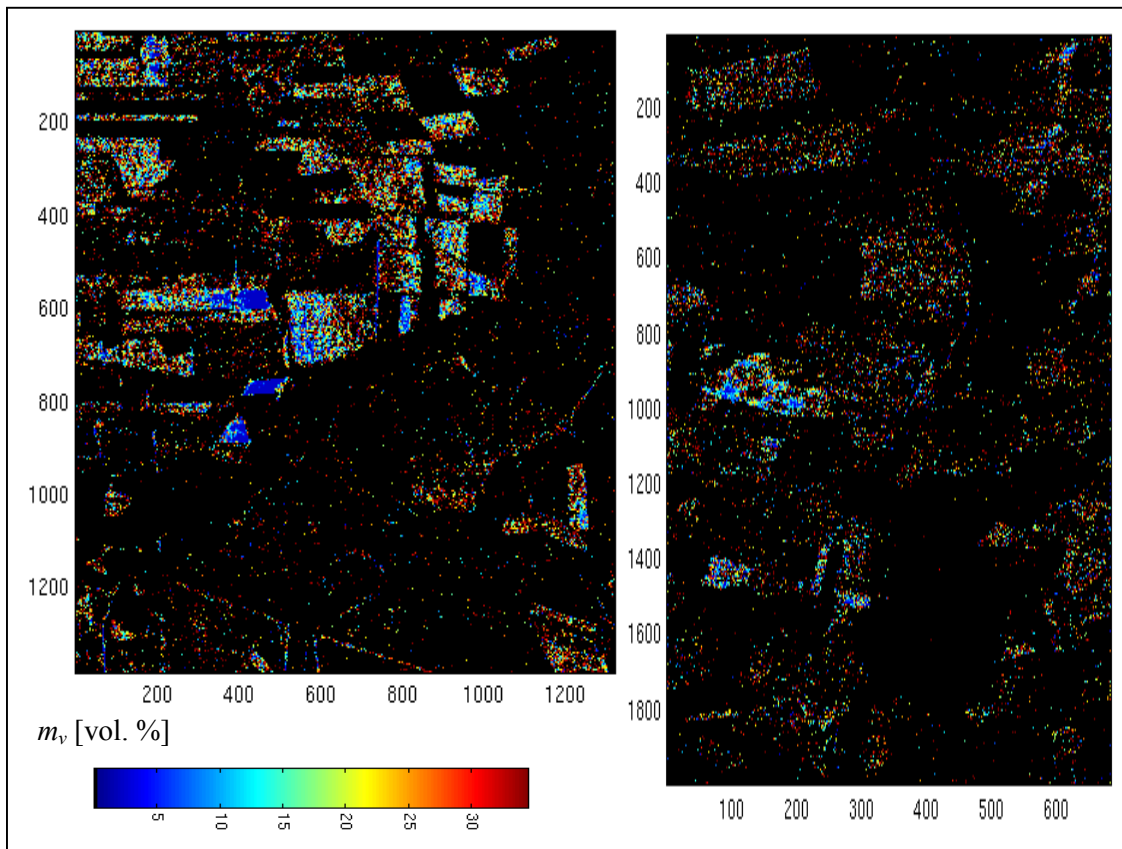Fig. 8.8: Surface Roughness ranging from 0 to 1; black: not valid areas

Fig. 8.9: Soil moisture content ranging from 0 to 40 [vol. %]; black: not valid areas

8.2 Synopsis

In this Chapter, an alternate new general parametric model, which enables the quantitative estimation of roughness and dielectric constant over a wide range of natural bare surfaces from polarimetric SAR data, has been introduced. The model is an extension of the SPM and assumes reflection symmetric surfaces, where the mean normal to the surface vector defines the axis of symmetry. It allows the *HH* and *VV* back-scattering coefficients to be different and account for non-zero cross-polarised, backscattering as well as depolarisation effects. The application of the model to experimental data shows good agreement between inverted values and ground measurements for ks, ε' and m_v. The low RMS errors for ks about 0.14 for the Elbe-Auen, and about 0.11 for the Weiherbach test site and for m_v ranging from 5 to 10 [vol. %] considering both test sites, indicates that the structure of the data is in accordance with the predictions of the model over a large range of surface conditions. Even the seasonal impact on the estimation is observed due to the fact that the RMS errors for the Weiherbach test site are much smaller in the upper soil layer, when flight campaign in March, and for the Elbe-Auen test site the RMS error is much smaller in the deeper soil layer, during the flight campaign in August, respectively.

The main advantage of the proposed inversion model is the straightforward separation of roughness and dielectric constant estimation, which can be performed without any data based regression. Furthermore, as the three key observables: entropy, anisotropy and alpha angle, are invariant under LOS (Line-of Sight) rotations the inversion becomes independent of azimuthal slope variations. This makes the application of the technique possible also over terrain with variable topography without the need of additional topographic information. The robust behaviour of the proposed algorithm over hilly terrain was confirmed, and it has been shown that it permits robust roughness estimation widely independent of topographic variations. However, the moisture content estimation is much more sensitive to incidence angle variations. Sensitivity analyses with respect to terrain variations have shown that 1 degree in terrain slope variation leads to an RMS error variation in the order of 0.25 [vol. %] (HAJNSEK *et al.* 2000).

Absolute calibration of the scattering matrix data is not strictly required, while for the ks estimation only cross-talk and relative channel calibration are sufficient, for the estimation of ε' the relative copolar-phase calibration is essential. The high dependency of the ε' estimation on the alpha angle values combined with the fact that any copolar-phase imbalance $\Delta\phi$ affects directly the alpha angle estimation ($\Delta\alpha \approx \Delta\Phi/2$), forces the demand on accurate phase calibration. Further, the effect of noise on the smaller eigenvalues leads to an overestimation of surface roughness. This can be avoided by applying multiplicative as well as additive noise filtering. However, one note of caution is required: the applied filtering techniques must always preserve the polarimetric information content of the data (LEE *et al.* 1997).

The influence of surface correlation length, remains unknown as it does not appear explicitly in the model. Small correlation lengths lead to multiple scattering effects, which are biasing the alpha angle α estimation by increasing the HH/VV ratio.

The presence of vegetation on the one hand increases the entropy and decreases the anisotropy, leading to overestimation of the surface roughness. On the other hand, it increases the alpha angle leading also to overestimated complex dielectric constant values.

8.3   References to Chapter 8

BOERNER, W.-M. et al., 'Polarimetry in Radar Remote Sensing: Basic and Applied Concepts', Chapter 5 in F.M. Henderson and A.J. Lewis (ed.), 'Principles and Applications of Imaging Radar', vol. 2 of Manual of Remote Sensing, (ed. R.A. Reyerson), Third Edition, Jhon Willey & Sons, New York, 1998.

BORGEAUD, M. & NOLL, J., 'Analysis of Theoretical Surface Scattering Models for Polarimetric Microwave Remote Sensing of Bare Soils', *International Journal of Remote Sensing*, vol. 15, no. 14, pp. 2931-2942, 1994.

CLOUDE, S. R., & PAPATHANASSIOU, K. P., 'Surface Roughness and Polarimetric Entropy', *Proceedings IGARSS'99*, Hamburg 1999, pp. 2443-2445,1999.

CLOUDE, S. R., 'Eigenvalue Parameters for Surface Roughness Studies', *Proceedings of SPIE Conference on Polarization: Measurement, Analysis and Remote Sensing II*, vol. 3754, Denver, Colorado, USA, July 1999.

CLOUDE, S. R., HAJNSEK, I. & PAPATHANASSIOU, K. P., 'An Eigenvector Method for the Extraction of Surface Parameters in Polarimetric SAR', *Proceedings of the CEOS SAR Workshop*, Toulouse 1999, ESA SP-450, pp. 693 – 698, 1999.

CLOUDE, S. R. & LEWIS, G. D., 'Eigenvalue Analysis of Mueller Matrix for Bead Basted Aluminium Surfaces', SPIE Polarisation Analysis and Measurement III, *Proceedings of SPIE*, vol. AM107, July-Aug 2000.

DAVIDSON, M. W.J., LE TOAN, T., MATTIA, F. SATALINO, G. MANNINER, T. & BORGEAUD, M., 'On the Characterization of Agricultural Soil Roughness for Radar Remote Sensing Studies', *IEEE Transactions on Geoscience and Remote Sensing*, vol. 38, no. 2, pp. 630–640, 2000.

DUBOIS, P. C. VAN ZYL, J. J. & ENGMAN, T., 'Measuring Soil Moisture with Imaging Radars', *IEEE Transactions on Geoscience and Remote Sensing*, vol. 33, no. 4, pp. 916-926, 1995.

HAJNSEK, I., CLOUDE, S. R., J.S. LEE, E. POTTIER, 'Inversion of Surface Parameters from Polarimetric SAR Data', *Proceedings IGARSS'00*, vol. III, pp. 1095-1097, p. 2001.

HAJNSEK, I., CLOUDE, S. R., LEE, J. S. & POTTIER, E., 'Terrain Correction for Quantitative Moisture and Roughness Retrieval Using Polarimetric SAR Data', *Proceedings IGARSS'00*, Honolulu, Hawaii, pp. 1307-1309, July 2000.

HAJNSEK, I., POTTIER, E. & CLOUDE, S. R., 'Slope Correction for Soil Moisture and Surface Roughness Retrieval', *Proceedings of third European Conference on Synthetic Aperture Radar EUSAR 2000*, pp. 273-276, May 2000.

LEE, J. S., GRUNES, M. R. & DE GRANDI, G., 'Polarimetric SAR Speckle Filtering and its Impact on Classification', *IEEE Transactions on Geoscience and Remote Sensing*, vol. 37, no. 5, pp. 2363 – 2373, 1997.

LEE, J. S., JURKEVICH, I., DEWAELE, P., WAMBACQ, P. & COSTERLINCK, A., 'Speckle filtering of synthetic aperture radar images: A review', *Remote Sens. Rev.*, vol. 8, pp 311-340, 1994.

MATTIA, F., LE TOAN, T., SOUYRIS, J. C., DE CAROLIS, G., FLOURY, N., POSA, F. & PASQUARIELLO, G., 'The Effect of Surface Roughness on Multi-Frequency Polarimetric

SAR data', *IEEE Transactions on Geoscience and Remote Sensing*, vol. 35, no. 4, pp. 954-965, 1997.

OH, Y., SARABANDI, K. & ULABY, F. T., 'An Empirical Model and an Inversion Technique for Radar Scattering from Bare Soil Surfaces', *IEEE Transactions on Geoscience and Remote Sensing*, vol.30, no. 2, pp. 370-381, 1992.

TOPP, G. C., DAVIS, J. L. & ANNAN, A. P., 'Electromagnetic Determination of Soil Water Content: Measurements in Coaxial Transmission Lines', *Water Resources Research*; vol. 16, no. 3, pp. 574-582, 1980.

Chapter 9

Conclusion and Outlook

The sensitivity of microwave scattering to the dielectric properties and the geometric structure of bare soil surfaces make radar remote sensing a challenge for a wide range of environmental issues related to the condition of natural surfaces. Especially, the potential for retrieving soil moisture with a high spatial and/or temporal resolution represents a significant contribution to hydrological and meteorological modelling, as well as to economical optimisation of agricultural procedures.

Surfaces are characterised in terms of their material and geometrical properties. One of the main parameters describing the material properties of surfaces is the volumetric soil moisture content. The relation to the radar backscatter signal is assumed to be given primarily by the dielectric constant. The geometric properties are described by the spatial roughness scales in both, horizontal and vertical directions, in terms of the surface RMS height s and the surface correlation length, l respectively. In the scattering problem both parameters are scaled by the actual wavelength λ in terms of ks and kl ($k = 2\pi / \lambda$).

The classical way to measure volumetric soil moisture content and surface roughness is by using gravimetric sampling and the needle board. Both methods were used for ground measurements performed over two test sites: the flat terrain of Elbe Auen along the River Elbe, characterised by dry and rough surface conditions; and the hilly terrain of the Weiherbach watershed, characterised by wet and slight to moderate surface roughness conditions. Considering both test sites together, the ground measurements cover a wide range of soil moisture values, $7 < m_v$ [vol. %] < 37, (i.e., $7 < \varepsilon' < 22.5$), and surface roughness, $1 < s$ [cm] < 3.5 (i.e. $0.3 < ks < 0.95$ for L-band conditions) (HAJNSEK 2001, NEUSCH 2000. Uncertainties of ground measurements caused during samples collection should be accounted. As discussed in Section 2.1.4.1, the accuracy of soil moisture measurements is about 10 vol. % due to uncertainties of the gravimetric soil sample drying method and due to the water loss during the measurement process. Thus, inaccurate or deficient ground measurements may sometimes be one of the reasons for a low correlation between measured and estimated parameters.

The challenge is to perform accurate large scale surface parameter estimation with high spatial resolution by means of radar remote sensing. Data acquisition has been done with the experimental airborne synthetic aperture radar (E-SAR) system, developed by the German Aerospace Center, Institute of Radio Frequency Technology and Radar Systems (HORN et al. 1999, SCHEIBER et al. 1999). For the investigations presented in this work, only the L-band configuration - in a fully polarimetric mode - was used.

The main problem for the quantitative estimation of soil moisture and/or surface roughness from SAR data lies in the separation of their individual effects on the backscattered signal. Polarimetry plays an important role as it allows a direct or indirect separation of roughness and moisture induced effects. Hence, most of the developed inversion models are based on the estimation of dual or fully polarimetric SAR image data takes. The basic concepts of wave and scattering polarimetry have been summarised in *Chapter 5*.

A large number of surface scattering models for the estimation of surface parameters of bare surfaces have been addressed over the last decades. In *Chapter 6*, three representative inversion models have been introduced. Their performance was tested against ground measurements from the two test sites. The Small Perturbation Model (SPM) is the first scattering model, which was discussed and applied to an inversion of volumetric soil moisture content. The main limitations of the SPM are its small surface roughness validity range for *ks* values below 0.3*, and the saturation of its sensitivity to soil moisture content above m_v values of about 20 [vol. %]. Thus, for most natural bare surfaces the validity range of roughness conditions for the SPM is too limited to be of practical importance. Nevertheless, the robustness of the SPM inside its validity range, and its physical background has led to several semi-empirical or empirical approaches using it as a starting point in order to extend the inversion over a larger range of surface conditions. The main advantage of such approaches is their simple implementation - in general they are based on the evaluation of backscattering amplitude ratios - while the main limitation arises from their empirical nature.

Two such empirical extensions of the SPM model have been discussed: The first one is the semi-empirical model introduced by OH *et al*. (1992) which additionally considers next to the co-polarised also the cross-polarised channel, and it is therefore more sensitive to roughness than to the volumetric soil moisture content. The second is the empirical model addressed by DUBOIS *et al*. (1995), which considers only the co-polarised amplitude ratio revealing a higher sensitivity to soil moisture than to the surface roughness. Both models consider pure surface scattering and use ratio-based conditions - $\sigma_{HH}^0 / \sigma_{VV}^0 < 1$ and $\sigma_{VH}^0 / \sigma_{VV}^0 < -11$ dB - for discriminating patches, which cannot be resolved. The high proportion of excluded patches for both test sites indicates the insufficiency of these models to deal with secondary scattering processes, depolarisation effects caused by roughness, and the presence of noise. Such effects, are only indirectly accounted by empirically determined regression coefficients. However, both models improve the performance of the SPM drastically, but on the same time the obtained inversion uncertainties are still high for accurate quantitative surface parameter estimation.

In *Chapter 7*, two approaches for repressing the disturbing secondary scattering processes are introduced. The main idea is to use polarimetric scattering decomposition techniques to decompose the polarimetric backscattering signature obtained from natural surfaces. Two decomposition techniques, the eigenvector decomposition and the model-based decomposition have been tested as polarimetric pre-processing techniques in order to improve the performance of the SPM, the Oh-Model and the Dubois-Model.

The eigenvector decomposition of the coherency matrix (CLOUDE 1986) leads to three independent deterministic scattering contributions: The first represents the dominant anisotropic surface scattering process, while the second and third correspond to secondary dihedral and/or multiple scattering contributions. Using only the first for inversion, the estimation of the volumetric moisture content by the SPM, especially for vegetated areas, improved drastically. Also the Dubois-Model show a significant improvement in the surface roughness estimation performance, while the Oh-Model yielded a degradation of its estimation accuracy.

This is because by using the first contribution only, the surface scattering is approximated as a non-depolarising process with an non-essential cross-polarised component. This is especially critical for the Oh-Model, for which the surface roughness estimation is strongly dependent on the cross-polarised backscattering. To approximate the surface by a more realistic depolarising scattering process, the *Oh* and *Dubois* inversion model was applied on the sum of the first two contributions – *omitting only the third contribution* - with an improved estimation for both surface parameters.

The model-based decomposition decomposes the scattering signature into three scattering components each specified by a simple scattering model (FREEMAN & DURDEN 1998). The first scattering contribution corresponds to a Bragg scatterer and can be, therefore, directly inverted using the SPM and omitting the two other components. The results obtained demonstrate the best performance for volumetric moisture content estimation, compared to the original data and the eigenvector approach.

Due to the high dependency of the polarimetric scattering signature on the local incidence angle, compensation for topographic variations is essential for quantitative estimation of surface parameters, and is discussed in *Chapter 7*. Usually, the compensation is performed using the local incidence angle obtained from an existing DEM. Alternatively, terrain slopes can be estimated from the polarimetric data itself by extracting the local orientation angle (SCHULER *et al*. 1998, POTTIER *et al*. 1999, LEE *et al*. 2000). The local orientation angle can be interpreted as the angle about which the antenna has to be rotated in order to align its horizontal polarisation axis to the tangential plane of the surface. In this sense, the polarimetric backscattering signature can be corrected rotating the corresponding coherency matrix by the negative of the orientation angle about the line of sight. This latter approach was compared in Chapter 7 against a DEM based on the local incidence angle correction (SCHULER *et al*. 1998, POTTIER *et al*. 1999, LEE *et al*. 2000). As expected, the orientation angle correction leads to an improved parameter estimation performance but remains still inferior compared to the incidence angle correction. Nevertheless, it leads to a good first order correction in the case for which a DEM is not available.

Finally in *Chapter 8*, a novel surface scattering model, the *Extended Bragg Scattering Model* (EX-Bragg), is introduced. It is based on second order statistics of the surface scattering

process expressed in terms of eigen-parameters of the coherency matrix. It is a two-component scattering model, with a Bragg scattering term and a roughness-induced perturbation term, and it is able to deal with roughness-induced depolarisation and cross-polarised backscattering contributions. The EX-Bragg model extends significantly the validity range of the original SPM, to ks values close to one and volumetric moisture content estimates up to m_v 35 [vol. %]; and it is therefore applicable over a wider range of natural bare surfaces. The main advantage of this model is that it allows a straightforward separation of roughness and dielectric constant estimation. The EX-Bragg-Model shows the best performance overall as compared with all tested algorithms. It permits robust roughness estimates, widely independent on incidence angle variation. The expected invariance for azimuthal rotation and, therefore, the reduced sensitivity to topographic slope variations has been verified. On the other hand, the soil moisture content estimation is highly sensitive to the incidence angle.

For bare surfaces with small ks values the presence of additive noise is a problematic factor for its application as it affects strongly the anisotropy estimation and subsequently the roughness estimates. Up to a certain noise level, this can be resolved satisfactorily by combining multiplicative as well as additive noise filtering, as discussed in *Chapter 8*. In future, the EX-Bragg scattering model has to be further validated over an even wider range of surface conditions and at different frequencies in order to assess more accurately its performance.

The results of this dissertation research lead to the conclusion that moisture content and roughness of bare surfaces can be estimated with an accuracy of about 5 % to 10 % for bare or sparse vegetated surfaces with moisture content ranging from 0 up to 40 [vol. %] and with roughness scales up to ks < 1.

Outside this range, the estimation performance decreases rapidly. The achieved accuracy satisfies the requirements for most geophysical and environmental applications. For example the modelling of land surface processes and interactions a relative accuracy of soil moisture is required about 10 % (RAST 1999). Also, the given range of moisture content is adequate. Concerning the valuable roughness range now, radar sensors operating at lower frequencies as S- or L-band allow the coverage of a sufficiently wide range of natural surfaces.

The main limitation for surface parameter estimation from polarimetric SAR data is the presence of vegetation. This combined with the fact that most natural surfaces are temporarily or permanently covered by vegetation restricts significantly the importance of radar remote sensing for a wide spectrum of geophysical and environmental applications. However, the evolution of radar technology and techniques allows optimism concerning the vitiation of this limitation.

One often proposed approach for solving the problem of surface parameter inversion under vegetation cover is to use longer wavelengths (lower frequencies). P-band is for example such a potential frequency candidate with sufficient high penetration into and through vegetation

layers. However, first experimental results at P-band indicate that this approach solves only one part of the problem. In the case of dense vegetation the efficient separation of vegetation scattering from surface scattering contributions - required for the extraction of the underlying surface characteristics - is not possible. Furthermore, the fact that the effective roughness is scaled by the wavelength makes moderate rough bare surfaces to appear very smooth at P-band, implying low backscattering coefficients often close to the system noise floor (HAJNSEK *et al.* 2001). In this case, additive noise becomes a significant limitation. Thus, single frequency and conventional polarimetry alone seems to be unable to resolve satisfactory the problem. More promising appears the option of dual frequency (for example L- and P-band) fully polarimetric configurations (MOGHADDAM & SAATCHI 2000). The combination of two or more frequencies promises on the one hand the coverage of a wider class of natural surface conditions and on the other hand more robust estimates. However, a note of caution is required: A changing of wavelength may also imply a change of the scattering process, and affects the applicability of the inversion algorithms (HAJNSEK *et al.* 2001).

The second challenging way is the new technique of polarimetric interferometry (CLOUDE & PAPATHANASSIOU 1998, PAPATHANASSIOU & CLOUDE 1999, PAPATHANASSIOU and CLOUDE 2000). The sensitivity of the interferometric phase plus coherence to the location of the effective scattering center inside the resolution cell, combined with the strong influence of ground scattering on the location of the scattering-center, provides for the first time a sensible way to estimate even weak ground scattering under vegetation. Additionally, the variation of the interferometric coherence as a function of baseline allows conclusions about the vegetation layer over the surface. On the other hand, polarimetry is important for the inversion of the surface scattering problem. Thus, the combination of polarimetry and interferometry, in terms of polarimetric interferometry, has a very promising application for the extraction of surface information under vegetation.

Arrived at the end of this work, and looking back, I have the feeling that the understanding of polarimetry and the methodology of surface parameter retrieval was less time and energy consuming than to write it down:

> *You know that I write slowly.*
> *This is chiefly because I am never satisfied*
> *until I have said as much as possible in a few words,*
> *and writing succinctly takes far more time than writing at length.*
> **Karl Friedrich Gauss**

Looking forward, I am certain that it is the beginning rather than the end of a long promising path.

9.1 References to Chapter 9

CLOUDE, S. R., 'Polarimetry: The Characterisation of Polarimetric Effects in EM Scattering', PhD. Thesis, University of Birmingham, Faculty of Engineering, UK, October 1986.

CLOUDE, S. R. & PAPATHANASSIOU, K. P., 'Polarimetric SAR Interferometry', *IEEE Transactions on Geoscience and Remote Sensing*, vol. 36, no. 5, pp. 1551-1565, 1998.

DUBOIS, P.C. ,VAN ZYL, J. J. & ENGMAN, T., 'Measuring Soil Moisture with Imaging Radars*', IEEE Transactions on Geoscience and Remote Sensing*, vol. 33, no. 4, pp. 916-926, 1995.

FREEMAN, A. & DURDEN, S. L., 'A Three-Component Scattering Model for Polarimetric SAR Data', *IEEE Transactions on Geoscience and Remote Sensing*, vol. 36, no. 3, pp. 963-973, 1998.

HAJNSEK, I., 'Pilotstudie Radarbefliegung der Elbaue', Endbericht TP. I.2, p. 93, 1999, in: Verbundvorhaben Morphodynamik der Elbe, FKZ 0339566 des BMBF, in: *Interner Bericht* DLR 551-1/2001.

HAJNSEK, I., K. P. PAPATHANASSIOU & S. R. CLOUDE, 'L- and P-Band for Surface Parameter Estimation', Proceedings of IGARSS'01, Sydney, in print.

HORN, R. SCHEIBER, R., BUCKREUß, S., ZINK, M., MOREIRA, A., SANSOSTI, E. & LANARI, R., 'E-SAR Generates Level –3 SAR Products for ProSmart', *Proceedings IGARSS'99*, Hamburg, vol. II, pp. 1195-1199, 1999.

LEE, J. S., D. L. SCHULER & T. L. AINSWORTH, 'Polarimetric SAR Data Compensation for Terrain Azimuth Slope Variation', *IEEE Transactions on Geoscience and Remote Sensing*, vol. 38, no. 5, part I, pp. 2153-2163, 2000.

MOGHADDAM, M. & SAATCHI, S., 'Estimating subcanopy soil moisture with radar', *J. Geophys. Res.*, 2000, in press.

NEUSCH, T., 'Multi-Frequency and Multi-Polarization Synthetic Aperture Radar Data for Modelling Hydrological Parameters', Aachen: *Shaker Verlag*, Karlsruhe, Universitäre. Dissertation., p. 128, 2000.

OH, Y., SARABANDI, K. & ULABY, F. T., 'An Empirical Model and an Inversion Technique for Radar Scattering from Bare Soil Surfaces', *IEEE Transactions on Geoscience and Remote Sensing*, vol. 30, no. 2, pp. 370-381, 1992.

PAPATHANASSIOU, K. P., CLOUDE, S. R. & REIGBER, A., 'Estimation of Vegetation Parameters using Polarimetric SAR Interferometry Part I and Part II', *Proceedings of CEOS SAR Workshop 1999*, CNES, Toulouse, France, 26-29 October 1999.

PAPATHANASSIOU, K. P. & CLOUDE, S. R., 'Single-Baseline Polarimetric SAR Interferometry, *IEEE Transactions on Geoscience and Remote Sensing*, submitted 2001.

POTTIER, E., SCHULER, D. L., LEE, J.-S., & AINSWORTH, T. L., 'Estimation of the Terrain Surface Azimuthal/Range Slopes Using Polarimetric Decomposition of Polsar Data', *Proceeding IGARSS'99*, Hamburg, pp. 2212-2214, 1999.

RAST, M (ED.), 'Land-Surface Process and Interaction Mission', ESA, Noordwijk, SP-1233, vol. 2, 1999.

SCHEIBER, R., REIGBER, A., ULBRICHT, A., PAPATHANASSIOU, K. P., HORN, R., BUCKREUß, S. & MOREIRA, A., 'Overview of Interferometric Data Acquisition and Processing Modes of

the Experimental Airborne SAR System of DLR', *Proceedings IGARSS'99*, Hamburg, vol. I, pp. 35-37, 1999.

SCHULER, D. AINSWORTH, T., LEE, J. S. & DE GRANDI, G., 'Topographic Mapping Using Polarimetric SAR data', *International Journal of Remote Sensing*, vol. 34, no. 5, pp. 1266-1277, 1998

Index

SHORT FORM CURRICULUM VITAE

Irena Hajnsek

June 2001

PERSONAL DATA

Surname: **Hajnsek**

Christian Name: **Irena**

Date of Birth: 22th April 1970

Place of Birth: Ljubljana, Slovenia

Nationality: German

Marital Status: Single

Home Address: Auweg 12
D-82234 Wessling, Germany

Present Position: **German Aerospace Centre (DLR) e. V.**
Institute for Radio Frequency and Radar Systems
P.O. BOX 1116, Münchener Str. 20, Geb. 102
D-82230 Wessling / Oberpfaffenhofen
Tel./Fax: +[49] (8153) 28-2363/1449
Email: irena.hajnsek@dlr.de

EDUCATION

Primary School: **1976-1982, Elementary School,** Berlin-Charlottenburg, Germany

Secondary School: **1982-1990, Anne-Freud Gymnasium,** Berlin-Charlottenburg, Germany
06/1990 Abitur (Matura: University Entrance Examination)

University: **10/1990-07/1996** Study of Geography at the Freie Universität Berlin-Dahlem, Main subjects: Geology and Biology
07/1996 Diploma Thesis: "*Quantifizierung der Drift an einem Fließgewässer unter Berücksichtigung naturnaher und ferner Bereiche*" ('*Drift Quantization in Riversystems with respect to the natural landscape*')
10/1998-06/2001 Doctoral Thesis at the Friedrich-Schiller University Jena, Institute of Geography, Department of Geomatics
Thesis title: *Inversion of Surface Parameter from Polarimetric SAR Data.*

AREAS OF RESEARCH INTEREST

Hydrology and River Ecosystems, Geographic Information Systems, Radar Remote Sensing, Geoscience Application of Synthetic Aperture Radar (SAR), Physical Parameter Inversion Techniques and Modelling, Applied SAR Interferometry and Radar Polarimetry.

RESEARCH EXPERIENCE

02/1994-07/1994 Université Louis Pasteur, Strasbourg, France. Scientific traineeship within the project: Repartition du Phosphore dans trois Compartiments d'un Ecosysteme Aquatique „*Eau-Plante-Sedimént*": Etude comparative dans le cas particulier de deux espèces aquatiques appartenant au genre Elodea ('Phosphorus sources for aquatic macrophytes in running water').

10/1996-10/1999 German Aerospace Centre, Institute of Radio Frequency Technology, Oberpfaffenhofen, Germany. Research investigations in the frame of a Compound Project by the German Ministry of Research and Education on "*Floodplain Mapping with Multi-frequency and Polarimetric Airborne-SAR Data Takes*". Main activities: Project management; organisation and coordination of ground measurement campaigns; Extraction of surface parameters (soil moisture and roughness) from SAR data for hydrodynamic modelling; Landuse classification; Integration, management and combination of SAR data with collected ground data into a geographical information system (GIS).

08/1999-10/1999 Applied Electromagnetics (AEL), St. Andrews, Scotland. Scientific research in the frame of the EC-TMR and under an ONR-NICOP Project on "*The estimation of surface parameters from polarimetric SAR data. Establishment and validation of a new polarimetric scattering model suitable for surface parameters extraction*".

11/1999-07/2000 Université de Rennes I, Rennes, France. Scientific studies and reseaarch in the frame of the EC-TMR Polarimetry Network Project on "*The influence and correction of topography for the quantitative estimation of surface parameters*".

08/2000-10/2000 Applied Electromagnetics (AEL), St. Andrews, Scotland. Scientific research in the frame of the EC-TMR Polarimetry Network Project on "*The validation of surface parameters extraction and accuracy assessment of surface parameter inversion techniques*".

Since 11/2001 German Aerospace Centre (DLR), Oberpfaffenhofen, Germany, Institute of Radio Frequency Technology and Radar Systems, Department SAR Technology. Research and studies on "*Geoscience applications and parameter inversion techniques from multi-frequency, polarimetric and interferometric air- and space-borne SAR Data*".

WORK EXPERIENCE

02/1993-04/1993 Federation for Environment and Nature Protection Berlin (Bund für Umwelt und Naturschutz Berlin) Project on "*The design and realisation of Berlin's Greenbelt*". Report in comprehensive brochure entitled: 'Ein Grüngürtel für Berlin'

06/1993-09/1996 Skilled student assistant: Management of the Library of the Geomorphologic Institute at the Freie Universitaet Berlin

04/1994-10/1995 Climate Project Paleomonsoon (research trainee in ongoing research projects)

08/1994 Work in the organisation committee of the '*International Congress for Quaternary Research XIV*'

10/1996-09/1998 Research Assistant at the Freie Universität Berlin in collaboration with the German Aerospace Center (DLR e.V.), Institute of Radio Frequency Technology in Oberpfaffenhofen, Germany.

10/1998-10/1999 Employee at the German Aerospace Centre (DLR e.V.), Institute of Radio Frequency Technology, Oberpfaffenhofen, Germany.

11/1999-06/2000 EC-Fellowship at the Université de Rennes I, France, in the Frame of EC-TMR Polarimetry Network.

07/1999-10/2000 EC-Fellowship Applied Electromagnetics (AEL), St. Andrews, Scotland, in the Frame of EC-TMR Polarimetry Network.

since 11/2001 Research Assistant at the German Aerospace Centre (DLR e.V.), Institute of Radio Frequency Technology and Radar Systems, Department SAR Technology, Oberpfaffenhofen, Germany.

COURSES TAUGHT

08/1998 Summer School Alpbach on '*Our Solid and Liquid Planet'* organised by the Austrian Space Agency (ASA), Alpbach, Austria.

09/1998 Carl-Cranz-Gesellschaft (CCG)-Course on '*SAR Principles and Application'*, Oberpfaffenhofen, Germany.

02/2000 TMR Training Workshop on '*Foundation of Polarimetry and Basic Principles of Polarimetric Radar-Observations and Analysis'*, Joint Research Centre, ISPRA, Italy.

TEACHING EXPERIENCE

I) Supervision of Graduation Theses at DLR/ HR:

Ilka Schulze, 1998, Freie Universität Berlin, Institute of Geography, Berlin-Dahlem, Germany.
Diploma Project: „*Auswertung multifrequenter Echtzeit-prozessierter ESAR Daten am Beispiel zweier Testgebiete an der Elbe*" (Analysis of multifrequency real-time ESAR data in case of two test sites on the river Elbe).

Thomas Busche, 1999, Universität Göttingen, Institute of Geography, Göttingen ,Germany.
Diploma Project: „*Bestimmung von Oberflächenparametern aus ESAR Daten am Beispiel unbedeckter Felder im Bereich der Unteren Mittelelbe-Niederung*" (Estimation of surface parameters using E-SAR data on bare fields in the area of Mittelelbe).

Steffen Allgyer, 1999, Universität Erlangen, Institute of Geography, Erlangen-Zentrum, Germany.

Diploma Project: "*Vegetations- und Landnutzungsklassifikation mit Hilfe eines multifrequenten, multipolarisierten E-SAR Datensatzes am Beispiel der Unteren Mittelelbe*" (Vegetation and land-cover mapping with multi-frequency and multi-polarimetric ESAR data on the river Elbe).

II) Lecture activities:

02/2001 Radar-Course for Students on: '*Polarimetric Application of Radar Remote Sensing*', DLR, Oberpfaffenhofen, Germany.

06/2001 20 hours course on *Polarimetric Radar Remote Sensing for Land Applications*', University of Jena, Department of Geoinformatik, Germany.

10/1996-10/1999 Supervision of more than 10 student trainees from various German and European universities at the German Aerospace Centre, Oberpfaffenhofen.

PUBLICATIONS

I) Theses

Diploma Thesis: "Quantifizierung der Drift an einem Fließgewässer unter Berücksichtigung naturnaher und ferner Bereiche" ('Drift Quantization in Riversystems with respect to the natural landscape'), Freie Universität Berlin, Institute of Geography, Berlin-Charlottenburg, Germany, 1996 July

Doctoral Thesis: Inversion of Surface Parameter from Polarimetric SAR Data, Friedrich-Schiller University Jena, Institute of Geography, Department of Geoinformatik, Jena, Germany, (September 2001)

II) Reviewed Journal Publications

ROBACH, F., HAJNSEK, I., EGLIN, I., & TREMOILERES, M., 'Phosphorus sources for aquatic macrophytes in running waters: water or sediment ?' *Acta botanica Gallica*, no.142, vol.6, pp. 719-731, 1995.

HAJNSEK, I., POTTIER, E. & CLOUDE, S.R., 'Inversion of Surface Parameters from Polarimetric SAR', *IEEE Transactions on Geoscience and Remote Sensing*, submitted 2000.

III) Refereed Conference Publications

HAJNSEK, I., BUSSE, L., & GUNKEL, G., 'Die Bedeutung vieler Parameter auf die Quantität und Zusammensetzung der Drift und des Sestons', *Deutsche Gesellschaft für Limnologie*, Berlin, Germany, Band I, pp. 52-56, 1996.

GUNKEL, G., HAJNSEK, I., & BUSSE, L., 'Verfrachtung und Sedimentation von partikulaeren Wasserinhaltsstoffen in kleinen Fließgewaessern des Flachlandes', DFG-Rundgespräch, pp. 39-45, 1997.

HAJNSEK, I., ERGENZINGER, P., & SCHMULLIUS, C. C., 'Flood-Plain Mapping of the River Elbe with Multi-Frequency and Multi-Polarisation Airborne-Radar Data', *Proceedings IGARSS'98*, Seattle, USA, vol. II, pp. 998-1000, 1998.

HAJNSEK, I., ERGENZINGER, P., & SCHMULLIUS, C. C., 'Pilotprojekt Radarbefliegung der mittleren Elbtalaue', *8. Magdeburger Gewässerschutzseminar*, Poland, 1998.

HAJNSEK I., PAPATHANASSIOU K. P., REIGBER A., & CLOUDE S., 'Soil-Moisture Estimation Using Polarimetric SAR Data', *Proceedings IGARSS'99*, Hamburg, Germany, vol. V, pp. 2440-2442, 1999.

HAJNSEK I., BUSCHE T., SCHMULLIUS C., & ERGENZINGER P., 'Determination of Hydrological Parameters Using Airborne-Radar Data (DLR E-SAR)', *Proceedings IGARSS'99*, Hamburg, Germany, vol. II, pp. 1108-1110, 1999.

HAJNSEK I., ALLGEYER S., SCHMULLIUS C., & ERGENZINGER P., 'Landnutzungs-klassifikation mit Hilfe der Radarfernerkundung am Beispiel der mittleren Unterelbe', *Tagungsband: Fachtagung Elbe*, Wittenberge, Germany, pp. 113-114, 1999.

HAJNSEK I., BUSCHE T., SCHMULLIUS C., & ERGENZINGER P., 'Vergleich von Algorithmen zur Modellierung von hydrologischen Parametern mit Hilfe von flugzeuggetragenen Radarsensoren (DLR E-SAR)', *Tagungsband: Fachtagung Elbe*, Wittenberge, Germany, pp. 115-116, 1999.

CLOUDE S. R., HAJNSEK I. & PAPATHANASSIOU, K. P., 'Eigenvector Methods for the Extraction of Surface Parameters in Polarimetric SAR', *Committee on Earth Observation Satellites, SAR-Workshop*, Toulouse, France, pp. 693-698, 1999.

HAJNSEK I., POTTIER E.,& CLOUDE S. R., 'Slope Correction for Soil Moisture and Surface Roughness Retrieval', *Proceedings of the European Conference on Synthetic Aperture Radar, EUSAR'2000*, Munich, Germany, pp. 273-276, May 2000.

HEROLD, M., SCHMULLIUS, C. C. & HAJNSEK, I., 'Multifrequency and Polarimetric Radar Remote Sensing of Grassland, Geobiophysical and Landcover Parameter Retrieval with E-SAR Data', *European Association of Remote Sensing EARSel*, Dresden, Germany, in print, 2000.

HAJNSEK, I., CLOUDE, S. R., LEE, J.-S. & POTTIER, E., 'Inversion of Surface Parameter from Polarimetric SAR Data' *Proceeding of IGARSS'2000*, Honolulu, Hawaii, vol. III, pp. 1095-1097, 2000.

HAJNSEK, I. & POTTIER, E., 'Terrain Correction for Quantitative Moisture and Roughness Retrieval Using Polarimetric SAR Data', *Proceeding of IGARSS'00*, Honolulu, Hawaii, vol. III, pp. 1307-1309, 2000.

HAJNSEK, I., PAPATHANSSIOU, K.P. & CLOUDE, S. R., 'L- and P-Band for Surface Parameter Estimation', *Proceedings IGARSS'01*, Sydney, Autralia, in print, 2001.

HAJNSEK, I., PAPATHANSSIOU, K. P. & CLOUDE, S. R., 'Additive Noise Filtering for Polarimetric Eigenvalue Processing', *Proceedings IGARSS'01*, Sydney, Autralia, in print, 2001.

HAJNSEK, I., PAPATHANASSIOU, K. P., HORN, R., SCHEIBER, R., & MOREIRA, A., 'Neue Methoden zur Bestimmung von Bodenoberflächen-Vegetationsparametern entwickelt aus polarimetrischen und interferometrischen E-SAR Daten', DFD-Nutzerseminar, Konstanz, Germany, in print, 2001.

IV) Study Reports

HAJNSEK, I., '*Pilotstudie über Radarbefliegung der Elbauen*', Endbericht TP. I.2, Verbundvorhaben Morphodynamik der Elbe, FKZ 0339566 des BMBF, in: *Internal Report* DLR 551-1/2001, p. 116, 1999.

HAJNSEK, I., '*Inversion of Surface Parameters from Polarimetric SAR Image Data Takes collected with the E-SAR at L-Band*', Internal Report DLR, in print 2001.